University of Southampton Research Repository

University of Southampton

Faculty of Engineering and Physical Sciences
Institute of Sound and Vibration Research

Aerodynamic noise simulation of high-speed train bogie

By

Yuan He

ORCID ID https://orcid.org/0000-0003-3768-519X

Thesis for the degree of Doctor of Philosophy

January 2023

University of Southampton

Abstract

Faculty of Engineering and Physical Sciences
Institute of Sound and Vibration Research

Doctor of Philosophy

Aerodynamic noise simulation of high-speed train bogie

by Yuan He

Aerodynamic noise from high-speed trains becomes more and more important as the train speed increases. Of the various sources, the train bogies contribute significantly to the overall aerodynamic noise, especially the leading bogie. This research aims to reveal the aerodynamic noise generation mechanisms from bogies of high-speed trains and propose suitable noise reduction measures. Numerical simulation has been a great challenge for the simulation of the aerodynamic noise of bogies. This is due to the complex geometry, which makes the discretization very difficult and, meanwhile, the grid will be very large. To overcome these challenges, a hybrid grid system is explored, which can guarantee a high-quality grid in the boundary layer while maintaining the overall number of cells in the grid at an acceptable level; the model size and flow speed are both scaled down to further reduce the number of the grid cells. The Delayed Detached Eddy Simulation is used to investigate the flow and obtain the noise source information to feed into the Ffowcs Williams-Hawkings acoustic analogy for far-field noise prediction. The hybrid grid system and the numerical methods are validated by simulations for a circular cylinder, square cylinder and an isolated wheelset. After that, the hybrid grid system is applied and further developed for the simulations of a bogie in a simplified cavity. The results show that the rear part of the bogie and cavity have strong pressure fluctuations and the noise generated by the cavity is much greater than that by the bogie. A more complex model of a bogie under a leading car is then investigated. It is found that the bottom of the cowcatcher and the bogie, the cavity rear surface, and the side dampers, which are directly flapped by the highly turbulent wake and detached shear layer, form strong pressure fluctuations. The far-field noise levels and the sound power levels emitted by the cavity are greater than that of the bogie. The effect on the aerodynamics and aeroacoustics of the lateral position of the bogie's side components relative to the car body is investigated. The flow field results show that the protruded side components shield the detached shear layer from upstream, preventing it from impinging on the rear part of the cavity. The pressure fluctuation on the side components increases, while it reduces at the rear surface of the cavity, as a result of which only a small difference in the sound power is found between the various cases. Based on the analysis of the flow field and pressure fluctuation distribution of the simulated cases, a noise control technique based on a dual staggered jet is developed to reduce the noise level of the leading car. The wake at the bottom and the detached shear layer at the two sides of the cavity is pushed away by the jets, which reduces the pressure fluctuations on the bogie and the cavity. A reduction of 2 dB for the sound pressure levels and 3.5 dB for the sound power levels is obtained. Finally, to reduce further the computational cost of the models, a novel decomposition method for CFD simulation is developed. A model of tandem square cylinders is adopted to validate the method showing good agreement between the decomposed model and the complete model. The computational time of the decomposed model is 29.6% less than that of the complete model. The collected inflow data is compressed by a convolutional Variational AutoEncoder neural network and the compression ratio achieves 63.5. The decomposition method then is applied to the simulation of a half-width leading car model.

Table of Contents

Table of Tables

Table of Figures

Research Thesis: Declaration of Authorship

Print name: Yuan He

Title of thesis: Aerodynamic noise simulation of high-speed train bogie

I declare that this thesis and the work presented in it are my own and has been generated by me as the result of my own original research.

I confirm that:

1. This work was done wholly or mainly while in candidature for a research degree at this University;
2. Where any part of this thesis has previously been submitted for a degree or any other qualification at this University or any other institution, this has been clearly stated;
3. Where I have consulted the published work of others, this is always clearly attributed;
4. Where I have quoted from the work of others, the source is always given. With the exception of such quotations, this thesis is entirely my own work;
5. I have acknowledged all main sources of help;
6. Where the thesis is based on work done by myself jointly with others, I have made clear exactly what was done by others and what I have contributed myself;
7. Parts of this work have been published as

He, Y., D. Thompson, and Z. Hu, *Numerical Investigation of Flow-Induced Noise around a High-Speed Train Bogie in a Simplified Cavity*, in *International Conference on Rail Transportation, Chengdu, China*. June 2021. p. 65-72.

Signature: .... Date:...........................

Acknowledgements

Pursuing a PhD is a good journey to know more and deeper about the objective world as well as myself. The experience of four years' research is not only beneficial to my expertise but also to my will when some difficult time comes in the future. It has become a good wealth in my future life and career. During this journey, there are many people who I should express my gratitude to.

First and foremost, I would like to thank my supervisors, Prof. David Thompson and Dr. Zhiwei Hu. I wish to thank them for the consistent guidance, support and patience during this special period of years of the global pandemic. Their sense of responsibility, hardworking, professional supervision and erudite academic knowledge will definitely be the model in my future career. I also would like to thank Prof. Xiaozhen Sheng, who is the manager of the sponsoring project, for giving me a lot of care about the life and research during the study.

I appreciate the help from my classmates Dr. Yanan Wang and Dr. Dong Zhao, who helped me at the beginning of my PhD. I gratefully acknowledge the help from Dr. Xiaowan Liu and Dr. Xianying Zhang, thank you for those patient and supportive discussions.

The work described here has been supported by the Ministry of Science and Technology of China under the National Key R&D Programme grant 2016YFE0205200, 'Joint research into key technologies for controlling noise and vibration of high-speed railways under extremely complicated conditions'. I deeply appreciate the financial support and assistance from the Ministry of Science and Technology of China and from Prof. David Thompson, Prof. Xiaozhen Sheng and Dr. Shumin Zhang.

Last but not the least, I thank my family for their understanding and support. Sincere love and gratitude to my wife, Li Gui, and my little son for your love, support and giving.

Definitions and Abbreviations

Roman symbols

A	Reference area (m^2)
A_i	The area of the cell on let surface
A_j	The area of the jet inlet(m^2)
A_m	The area of the inlet of the main stream(m^2)
c_0	Speed of sound (m/s)
C_d	Drag force coefficient
C_l	Lift force coefficient
C_s	Side force coefficient
$C_{d,rms}$	Root mean square of drag force coefficient
$C_{l,rms}$	Root mean square of lift force coefficient
$C_{s,rms}$	Root mean square of side force coefficient
C_p	Pressure coefficient
$C_p(t)$	Time varying pressure coefficient
C_{pb}	Base pressure coefficient
$C_{p,rms}$	Root mean square of pressure coefficient
d	Wall distance (m)
$\tilde{d}$	Modified length scale in DES model (m)
D	Diameter of the cylinder (m)
D_1	Dimension of original model (m)
D_2	Dimension of scaled model (m)
D_w	Diameter of the wheel (m)
dp/dt	The change rate of the pressure(Pa/s)
ds	The area of each sphere segment
f	Frequency (Hz)
f_1	Frequency of original model (Hz)
f_2	Frequency of scaled model (Hz)
F_{drag}	Drag force(N)
F_{lift}	Lift force(N)
G	Filter kernel
h	The length of the slot(m)
H_0	The height of the train(m)
$H(f)$	Heaviside function
L	Cavity length(m)
$L_{\dot{p}}$	The pressure fluctuation strength level

$L_{\dot{p}\_total}$	The total pressure fluctuation strength level
L_s	The position of the sampling surface
M	Mach number
M_c	Convective Mach number
nusgs	The sub-grid viscosity in OpenFOAM (m^2/s)
k	Turbulence kinetic energy
p	Pressure (Pa)
p'	Pressure fluctuation (Pa)
P_{ij}	Compressive stress tensor (N/ m^2)
p_{ref}	Reference acoustic pressure (Pa)
p_{rms}	The rms of acoustic pressure(Pa)
Q	Q criterion (second invariant of the velocity gradient)
r	Radius of receiver (m)
r_1	Radius of original model receivers (m)
r_2	Radius of scaled model receivers (m)
R_e	Reynolds number
R_j	The injected momentum flux ratio of the jet
S	The surface of the sphere
S_{ij}	Mean strain rate tensor (1/s)
S_t	Strouhal number
t	Time (s)
t^*	Dimensionless time
T_{ij}	Lighthill stress tensor (N/m^2)
Tu	Turbulence intensity
U_0	Freestream velocity (m/s)
U_1	Velocity of original model (m/s)
U_2	Velocity of scaled model (m/s)
u_j	The local inlet speed of the jet (m/s)
u_{jMax}	The maximum magnitude of the jet speed(m/s)
U_n	Velocity normal component (m/s)
U_t	The total velocity(m/s)
U_∞	Free stream velocity (m/s)
$\bar{U}$, U_mean	Time-averaged velocity (m/s)
$\bar{u}_j$	The mean speed of the jet
w	The width of the slot(m)
W_0	The width of the train (m)
w_j	The width of the jet (m)
W_{ref}	Reference sound power, 10^{-12} W

x, y, z	Cartesian coordinate system
x^+, y^+, z^+	Dimensionless first-cell spacing
x_p	The distance to centre of the jet inlet (m)
Δt	Physical time step (s)
$\Delta x, \Delta y, \Delta z$	Cell dimensions in x, y, and z directions (m)
Δ	Cut off width (m)
$\delta(f)$	Dirac delta function
δ_{ij}	Kronecker delta
ρ	Density (kg/ m^3)
ρ'	Density fluctuation (kg/ m^3)
μ	Dynamic viscosity (Ns/ m^2)
γ	geometry factor
v	Kinematic viscosity (m^2/s)
θ	Separation angle (degrees)
$\emptyset$	the collected variable value
ε	Turbulence dissipation rate
v_t	Turbulent viscosity (m^2/s)
v_{sgs}	Sub-grid-scale viscosity (m^2/s)
$\tilde{v}$	Modified turbulent eddy viscosity (m^2/s)
∇	Gradient operator
u_τ	Friction velocity (m/s)
τ_{ij}	Stress tensor (N/ m^2)
τ_w	Wall shear stress (N/ m^2)
τ_{ij}^{sgs}	Sub-grid stress tensor

Abbreviations

2D	Two-dimensional
3D	Three-dimensional
CAA	Computational Aeroacoustics
CFD	Computational Fluid Dynamics
CFL	Courant-Friedrichs-Lewy
dB	Decibel
DDES	Delayed Detached Eddy Simulation
DES	Detached Eddy Simulation
DNS	Direct Numerical Simulation
ETR 500	Elettro Treno Rapido 500
FW-H	Ffowcs Williams and Hawkings
ICE3	Intercity-Express 3

LBM	Lattice Boltzmann Method
LES	Large Eddy Simulation
PIMPLE	PISO-SIMPLE
PISO	Pressure-Implicit Split Operator
PSD	Power Spectra Density
RANS	Reynolds-Averaged Navier-Stokes
RNG	Re-Normalisation Group
S-A	Spalart-Allmaras turbulence model
SPL	Sound pressure level
SWL	Sound power level
RMS	Root mean square
SGS	Sub-Grid-Scale
SIMPLE	Semi-Implicit Method Pressure Linked Equations
TKE	Turbulence kinetic energy
URANS	Unsteady Reynolds-Averaged Navier-Stokes
KL loss	Kullback-Leibler divergence

Subscripts

0	Ambient freestream quantities
i	Spatial or summation index
∞	Free stream quantities
min	Minimum value
max	Maximum value

Superscripts

_	Mean value
‘	Fluctuating component
*	Non-dimensional value

Chapter 1 Introduction

1.1 Background and motivation

High-speed trains have become a popular mode of intercity transportation, especially in Europe and Asia. The maximum speed of trains in service has been increasing in many countries since the first modern high-speed train service commenced in Japan in the 1960s with an operational speed of 210 km/h. Compared with the rolling noise, the aerodynamic noise increases more rapidly as the train speed increases (Thompson et al. 2015). Therefore, the aerodynamic noise becomes more and more important as the speed of the trains increases.

One of the most important parts of a high-speed train is the bogie, which has multiple functions, such as to bear the load from the train body, to guide the train along the tracks, and at the same time to attenuate the vibration caused by the movement. Therefore, as shown in Figure 1.1, many components are contained in the bogie region including frame, wheels and axles, dampers, suspensions, air springs, brake systems, and in motor bogies the motors and gear boxes. These components make the structure of the bogie extremely complex. More details about the components can be found in Appendix A. Furthermore, the bogie is located in a cavity underneath the train, with high-speed flow coming from beneath and beside the train. This inevitably induces impact, ejection and recirculation zones in the bogie area, especially for the front bogie (Talotte 2000), which makes the flow field very complex as well. Thompson et al. (2015) pointed out that aerodynamic noise generated from the bogie areas has been estimated to contribute 15 dB more than that from pantograph to the overall sound power of the train. Therefore, studying and understanding the generation mechanisms of the aerodynamic noise of bogies under different circumstances and configurations is important for the purpose of reducing high-speed train noise. Although some experiments as well as numerical studies have been carried out to investigate the aerodynamic noise generated by the bogie, the flow field and characteristics of the noise still need to be further revealed. Therefore, numerical simulations of the bogie with more realistic geometry are very meaningful to understand the mechanisms of the noise generation of the bogie. In addition, the development of noise reduction measures based on the understanding of the noise generation is useful in reducing the overall noise generated by the whole train.

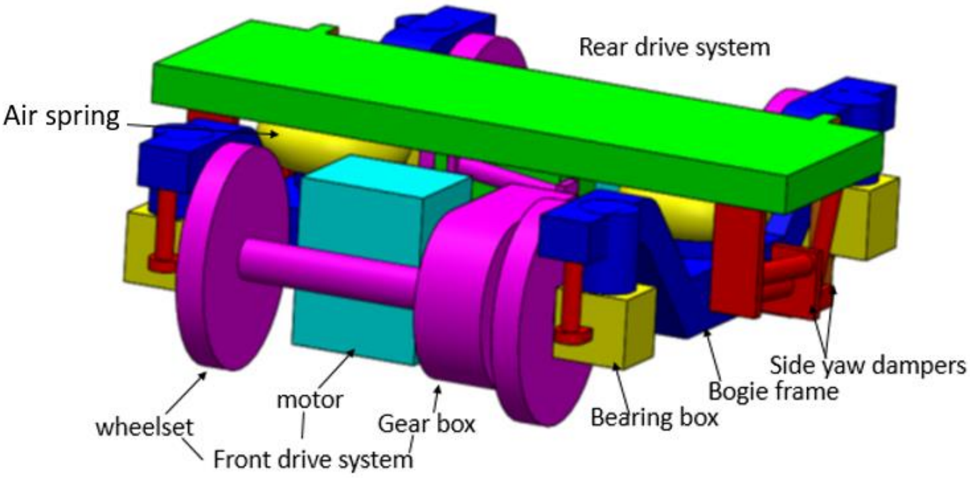

Figure 1.1 Simplified 3D model of a typical high-speed train bogie

1.2 Research objectives

This project aims to extend the understanding of the mechanism of aerodynamic noise generation around the leading bogie of a high-speed train. The relationship between the flow physics and the aerodynamic noise of the bogie and the critical factors influencing its generation are expected to be determined. Based on this, noise reduction measures will be developed. More specifically, the research objectives are as follows:

1. To explore a feasible grid generation procedure that can provide a fine enough grid with good quality in the boundary layer area of a complex bogie structure with complete components, which includes the complex geometry, while maintaining an acceptable quantity in the volume grid.
2. To investigate the aerodynamic and aeroacoustic characteristics of the bogies in a simplified cavity and under a more realistic leading car geometry. The strong dipole noise source components should be identified and the relationship between the noise generation and the flow physics should be clarified. The noise contributions from different components of the bogie and the cavity should be quantified.
3. To assess the effect of the relative lateral distance between the side components of the bogie and the car body. The effect on the flow field and on the aerodynamic noise should be studied.
4. To develop a feasible aerodynamic noise reduction method, which can effectively reduce the aerodynamic noise and meanwhile will not increase extra devices on the train.
5. To explore a CFD method that can be used to simulate some particular areas of concern on the train. Since the model size of a whole train is very large and it requires very high computational cost, simulation of a small zone of it becomes attractive. However, the boundary conditions for the small zone will be a subject that needs to be explored.

The results of this research could improve the understanding of the aerodynamic noise generated in the train bogie area. A feasible noise reduction method developed based on the numerical simulation results of the bogie model can provide a concept that could be further applied in the railway industry. Moreover, the proposed decomposition method may shed light in the field of aerodynamic noise simulation of trains, which is usually very expensive and time-consuming.

The far field noise prediction procedure used in this research is the hybrid method of Computational Fluid Dynamics (CFD) and Computational AeroAcoustics (CAA). The surface pressure data obtained by the Delayed Detached Eddy simulation (DDES) method is used in the Ffowcs William-Hawkings (FW-H) equation to predict the far field noise.

1.3 Structure of the thesis

In Chapter 2, previous experimental and numerical work related to the aerodynamic noise of high-speed trains, especially of the train bogies, is reviewed. Then, Chapter 3 presents the computational methodology used in this research including the CFD methods, turbulence models, and the CAA techniques. The CFD methods and the proposed hybrid mesh concept are validated in Chapter 4. Then the validated numerical methods are used to simulate the aerodynamic noise of a bogie in a simplified cavity and under the car body of a leading vehicle in Chapter 5 and Chapter 6 respectively. The effect of the relative position of the side components of the bogie will be investigated in Chapter 7. In Chapter 8, a noise reduction method based on introducing jet flow is developed to reduce the aerodynamic noise of the train bogie. Chapter 9 gives the details of the proposed CFD decomposition methods and its application. Finally, the main conclusions and proposed future work are outlined in Chapter 10.

1.4 Original contributions

The main original contributions of this research can be summarised as follows:

1. Although some previous numerical research has been carried out to study the aerodynamic noise of the train bogie, either the geometry of the model is greatly simplified or the grid, especially in the boundary layer, is not fine enough. The present research applies a hybrid grid system, whose concept is originally proposed by Nakahashi and Obayashi (1987), to discretise the complex bogie geometry. A particular contribution of present research is the combination of a pure hexahedral grid near the solid surface and a pure polyhedral grid in the rest of the volume; another one is the procedure developed for the generation of this hybrid grid. This hybrid grid guarantees a high quality of the grid in the boundary layer and meanwhile, the overall number of cells in the grid is

maintained at an acceptable level. By using this hybrid grid, a bogie model, which has relatively complete geometry, can be simulated and it becomes feasible to detect more phenomena. Such an approach is more realistic and helpful to understand the generation mechanism of the aerodynamic noise from the bogie.

2. The flow field around the bogie in a simplified cavity and under a more realistic leading car body is investigated. Detailed explanations of the mechanisms of bogie noise generation based on the flow physics are carried out, which extends the understanding on this topic. Moreover, useful information of the characteristics of the aerodynamic noise of the bogie and its cavity are provided and the sound power contributions from the different model components are also investigated. These research results can provide useful information for the train design and its aerodynamic noise reduction.

3. The relative positions between the bogie and the cavity are different in some railways because of the limitations of the loading gauge. The effects of the lateral position of the bogie side components are calculated and the drag, lift, and side forces and the noise levels are compared. This study can provide useful information for the assessment of the aerodynamics and aeroacoustics of the bogie in certain conditions.

4. The noise control technique of introducing a secondary jet is applied to reduce the sound power emitted by a leading car. Cases with different jet slots are simulated and the flow physics associated with the noise reduction by the jet is provided. This proposed technique can provide a concept that has a great potential to reduce the aerodynamic noise from the first bogie area.

5. A CFD decomposition method is proposed to reduce the size of the model and its feasibility is investigated. The concept of modularization, by assembling different zones of the model with identical interfaces, and the method of inflow data preparation are the original contributions. By using this decomposition method, instead of simulating the whole model, which usually requires high computational cost, only the zone of concern, which is smaller than the whole model, needs to be simulated. Both the simulation time and computational cost can be reduced by using this decomposition method. It is useful in the geometry parameter study and geometry optimization of the train. In addition, the application of a convolutional variational autoencoder, which is based on the one proposed by Laubscher and Rousseau (2020) to compress the inflow data is another contribution..

Chapter 2 Literature review

2.1 Aerodynamic noise of high-speed trains

2.1.1 Aerodynamic noise sources of high-speed trains

The noise emitted from a high-speed train mainly contains two parts: rolling noise caused by the interaction of the wheels and rails, and aerodynamic noise caused by the interaction between air flow and train components (Thompson et al. 2015). As the speed of the train V increases, the sound power of rolling noise increases at a rate of V^3, while the sound power of aerodynamic noise increases more rapidly. The aerodynamic noise sources of a high-speed train can be divided into two types: dipole and quadrupole. The dipole sources are generated by the pressure fluctuations on solid surfaces, and their output sound power is approximately proportional to V^6 (Curle 1955). The quadrupole sources are produced by the turbulent flow and their sound power is proportional to V^8 (Lighthill 1952). Depending on the weighting method applied to the total sound pressure, the speed dependence can be even higher than these values. When the train speed exceeds approximately 350 km/h, as shown in Figure 2.1, the aerodynamic noise will become the main contributor to the total noise of a high-speed train (Thompson et al. 2015).

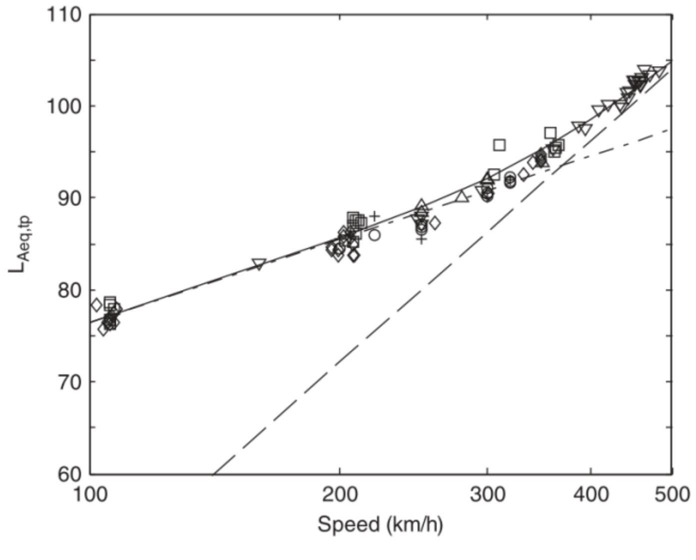

Figure 2.1 $L_{Aep,tp}$ measured at 25 m from TGV-A (▿,□,◇),TGV-Duplex (○, Δ) and Thalys (+) . (–·–·) Straight line with slope of 30 $\log_{10}$V to represent rolling noise; (——) straight line with slope of 80 $\log_{10}V$ to represent aerodynamic noise; (—) total (Thompson et al. 2015).

Generally speaking, all components in contact with the air flow on a moving high-speed train emit aerodynamic noise, but the main source regions are the train nose, bogies, pantographs , inter-coach spacings, rear power car, and car body surfaces(Talotte 2000; Nagakura 2006; Martens et al. 2009).

Nagakura (2006) conducted a wind tunnel test using a 1/5 scale Shinkansen train model. The noise source distribution was estimated according to the data measured by an acoustic mirror, both in wind tunnel tests and field tests. Figure 2.2 shows the estimated contribution of individual noise sources to the total noise level at a point 25 m away from the track when the train speed is 300 km/h. The cowcatcher area beneath the front of the leading car is the strongest noise source and followed by the leading bogie, the door of the drivers' cab, and the bogie of the trailing car. The high noise source strength from the lower part of the leading car is caused by the shear layer at the cowcatcher, which dominates the noise at frequencies of 2 kHz or over.

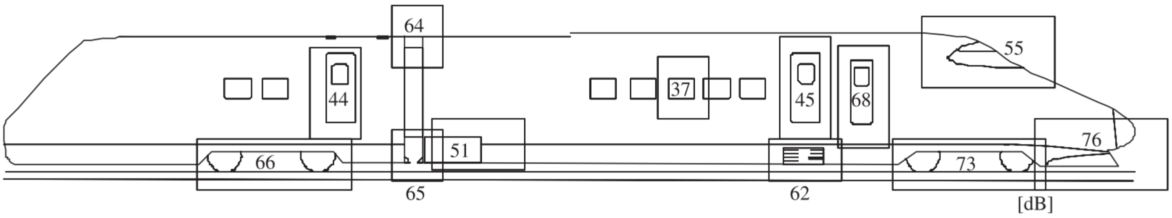

Figure 2.2 Estimated sound pressure level of noise generated by individual parts of Shinkansen train (full scale equivalent U = 300 km/h, measured at a point 25 m away from the track without sound barriers) (Nagakura 2006)

Lauterbach et al. (2012) used a microphone array to identify the sound sources of a 1:25 scaled model of ICE 3 (Inter City Express 3) in a wind tunnel test. Figure 2.3 illustrates the sound power level distribution obtained in the wind tunnel at different frequencies. For the scaled model, the noise from the bogie section is dominant for frequencies below 5 kHz while the pantograph is the dominant sound source for frequencies above 5 kHz.

It should be noted that the noise generated from the lower part of the train can be shielded by trackside noise barriers. Therefore, the noise sources on the upper part of the train, such as the pantographs and the gaps between cars, become more influential when barriers are present. The noise spectra generated by the pantograph consist of significant peaks, which are produced by the vortex shedding from the circular rods of the pantograph (Talotte 2000).

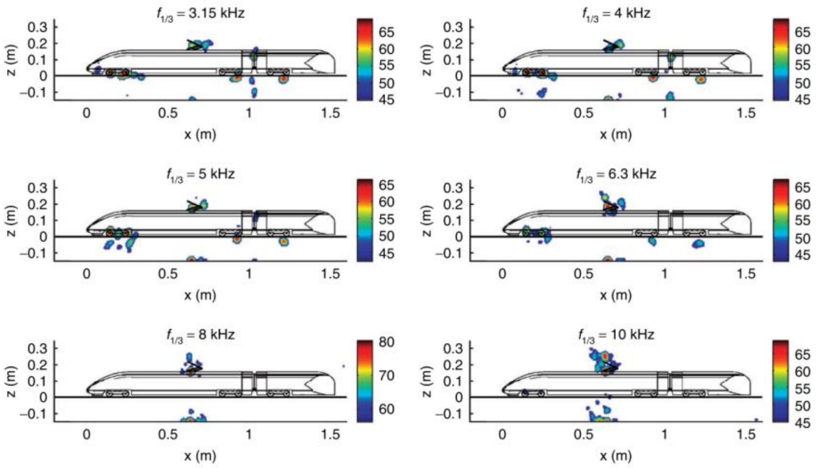

Figure 2.3 One-third octave source maps of the 1/25 scale ICE 3, measured in the aeroacoustic wind tunnel Braunschweig (AWB) at U = 60 m/s. Sound power level is given colour-coded over a dynamic range over 24 dB; with reference power $P_0 = 1 \times 10^{-12}$ W. (Lauterbach et al. 2012)

2.1.2 Reynolds number effect in the research of high-speed trains

For high-speed train aerodynamics and aeroacoustics, many investigations have been carried out on scaled models in wind tunnels. Through the dimensional analysis, the results from scaled-model measurements can be applied to full-scale trains. Wind tunnel tests using scaled models have the advantages of lower cost, fewer interference factors, and the ability to control the inflow parameters. However, compared to full scale models, the scaled models have much lower Reynolds numbers, which may introduce a significant effect when applying the results to full scale trains. The definition of Reynolds number (*Re*) is

$$Re = \frac{UD}{v} \tag{2.1}$$

where U is freestream velocity, D is the characteristic length, v is the molecular viscosity.

According to the theory of flow similarity, when the Reynolds number exceeds a critical value, its effect becomes very small. However, due to differences in geometry and flow, this critical value can vary. Baker et al. (2019) point out that bluff bodies like high-speed trains are insensitive to Reynolds number because their geometry constrains the flow separation and they proposed that as long as the Reynolds number, based on the train height and free stream velocity, is greater than at least 2×10^5 the results of scaled models can be applied to full scale trains. Kwon et al. (2001) measured drag coefficients of two train models, for Reynolds numbers 4×10^5 to 8.5×10^5, with different moving ground simulation technologies in a wind tunnel and found that the drag coefficients were almost independent of Reynolds number. However, some other researchers found different levels of influence of Reynolds number on the aerodynamic drag and pressure coefficient on the train surface (Baker and Brockie 1991; Willemsen 1997; Niu et al. 2016). Cheli et al. (2013) and Niu et al. (2016) studied changes in force and pressure coefficient on the train model based on different Reynolds numbers as well as yaw angles of inlet flow and found that under different yaw angles the dependence level on the Reynolds number is different because the yaw angle governs the flow separation on the car body (Baker et al. 2019).

Similar to the aerodynamic properties, the aeroacoustics of high-speed trains is also affected by the model scale used in wind tunnel tests because the aerodynamic noise is a product of the flow around the trains. Lauterbach et al. (2012) used a 1:25 scaled model of ICE 3 to conduct an aeroacoustic test, in which a wide range of Reynolds numbers are covered, up to 4.6×10^5 in an aeroacoustic wind tunnel and 3.7×10^6 in a cryogenic wind tunnel (Reynolds number based on the width of the train, which is about 80%-90% of the height of the train). In the cryogenic wind tunnel tests, the Mach number (M) and Reynolds number can be varied independently by adjusting the temperature of Nitrogen used for the flow. The definition of M is

$$M = \frac{U}{c_0} \tag{2.2}$$

where U is the flow speed, c_0 is the local sound speed.

The results show that there was only a weak dependence on the Reynolds number of the noise generated at the front bogie. In addition, from the shape of the spectra, the noise source was also independent of the Mach number.

2.2 Aerodynamic noise of high-speed train bogie

2.2.1 Experimental research

Many researchers have pointed out that the aerodynamic noise generated by a bogie is highly dependent on the incoming flow (Thompson et al. 2015; Zhu et al. 2016; Latorre Iglesias et al. 2017; Uda et al. 2018). Uda et al. (2018) used a series of hot-wire anemometers installed along the on the track slab to measure the velocity distribution under an operational train. They found that the flow velocity under the front bogie is higher than under the rear ones because the boundary layer on the train floor grows gradually towards the rear of the train; this leads to the aerodynamic noise generated by the front bogie being higher than that from other bogies.

Yamazaki et al. (2019) conducted tests for a 1/7 scaled model in a wind tunnel and arranged the components in the bogie cavity to estimate the contribution of each component to the total aerodynamic noise. The results show that the motor and the brake, which are exposed to the shear layer shedding from the car body, significantly influence the aerodynamic noise of the high-speed train bogie. Latorre Iglesias et al. (2017) studied the aerodynamic noise from a 1/7 scaled motor bogie and trailer bogie, as shown in Figure 2.4, and found that the spectra from the two configurations are quite similar. The explanation is the components exposed to the shear layer from the car body and the incoming flow of the two bogies are almost the same and the other components shielded by the bogie cavity are not the main aerodynamic noise sources. It was also shown that the relative position of the side frame, as shown in Figure 2.5, with respect to the bogie cavity is important. Figure 2.6 depicts the effect of the side frame position on the noise spectra for a 1/7 scale model bogie. Case C represents the case of an empty cavity with rounded edge (to suppress noise from the rear step of the cavity), MB is the case with the motor bogie, MB+S50, MB+S75, and MB+S100 mean the configurations of the bogie model, shown in Figure 2.5, with the side frame displaced further out laterally by 50 mm, 75 mm, and 100 mm, respectively. As the shafts are extended, more components are exposed to the slipstream. Thus, the noise level increases as the extension is increased from 0 mm to 100 mm. The noise increases in all frequency bands but the increase is smaller at low frequencies. The yaw damper and the front of the side frame were regarded as the two main contributors to the increase of the noise (Latorre Iglesias et al. 2017).

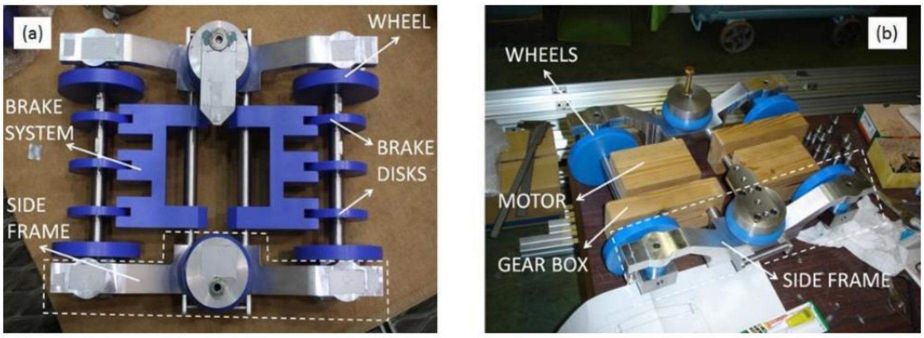

Figure 2.4 1/7 scale simplified bogie mock-up, left is a trailer bogie, right is a motor bogie (Latorre Iglesias et al. 2017)

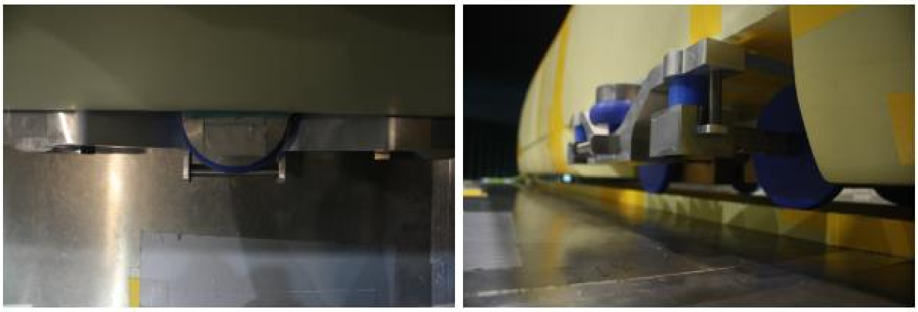

(a) Top view.

(b) Front view.

Figure 2.5 The images of the motor bogie mock-up with the wheel shafts extended by 100 mm ((Latorre Iglesias et al. 2017).

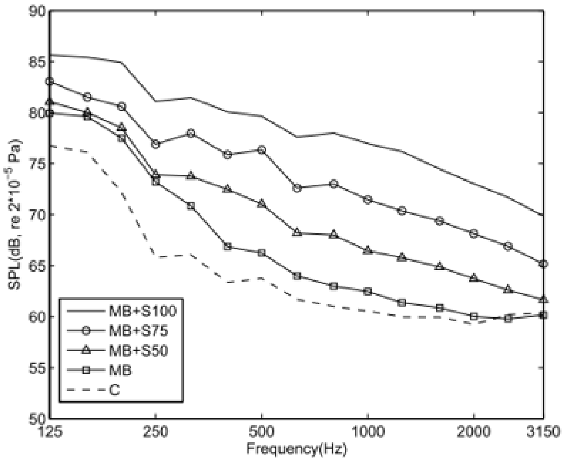

Figure 2.6 Noise spectra radiated by the different bogie side noise configurations for a flow speed of 89 m/s plotted against full scale frequency(Latorre Iglesias et al. 2017).

Whereas pantograph noise contains tonal components, the aerodynamic noise generated by the bogies is broadband and predominantly in the lower frequencies. The incoming flow of the bogie is turbulent due to the wake generated by the components further upstream. This prevents regular vortex shedding and the noise spectra, therefore, become more broadband. In order to study the interaction noise of bogie components, the noise of two cubes in a tandem arrangement with different separation distances was tested by (Latorre Iglesias 2015). The results indicated that when the second cube was immersed in the wake of the upstream cube, the low frequency noise significantly increased while the higher frequency noise did not change. It can be inferred that the changes at low frequencies are due to the wake from the upstream cube impinging on the downstream cube. However, the high frequency noise is associated with small eddies such as from the separation points which probably are not affected by the wake of the upstream cube. This study strongly implied that the noise generation mechanism of a bogie is quite different from that of a pantograph and the low frequency noise is related to those components immersed in the wake flow, such as the yaw dampers and the components located at the rear part of a bogie. In order to estimate the aerodynamic noise generated by a high-speed train bogie and pantograph, Latorre Iglesias (2015) developed a semi-empirical component-based model. The bogie and the pantograph were divided into different components and then the noise spectra from the individual components were combined to obtain the overall noise. For the bogie case, the motor was modelled as a cube, the gear box was modelled as a rectangular cuboid, and the wheel was simplified to a circular disc. Noise spectra of these simple shapes were measured in an anechoic wind tunnel to determine the empirical constants for the model. The result of the prediction model seems to provide good agreement with the test spectra, but to improve the accuracy interaction noise needs to be included in the model.

Sawamura et al. (2018) conducted a wind tunnel test for a 1/7 scaled model to investigate the noise generated in the bogie region. A two-dimensional (2D) microphone array was placed under the bogie as shown in Figure 2.7. An acoustic transmission plate, which allows the sound waves to pass through and prevents the airflow entering the microphone area, was set in the ground surface below the bogie. Figure 2.8 shows the noise source distribution at different frequencies. It is noticeable that at low frequencies the main noise sources are located at the rear part of the bogie. Uda et al. (2018) used wind tunnel tests to simulate the flow distribution under a train car, to match results obtained through field tests, and estimated the aerodynamic noise of the train bogie by a two-dimensional microphone array. The noise spectra obtained were then superposed with estimated rolling noise and machinery noise. The final result was validated by the total measured noise obtained in the field test. It was shown that, for frequencies below 500 Hz, the aerodynamic noise of the bogie is greater than both rolling noise and machinery noise.

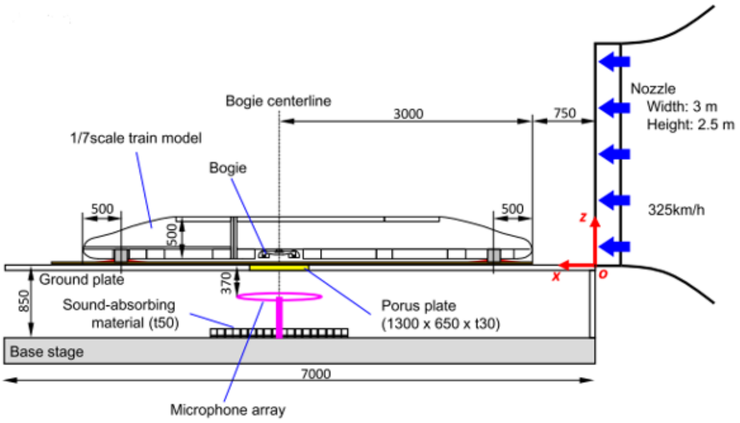

Figure 2.7 Schematic side view of the test setup used by Sawamura et al. (2018)

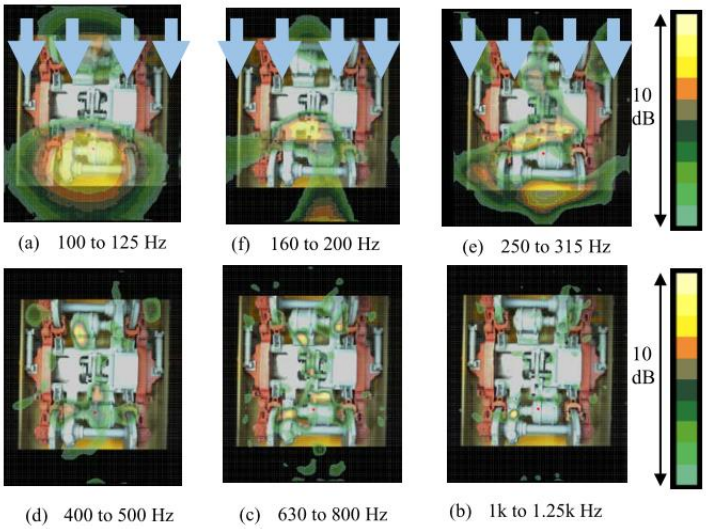

(a) 100 to 125 Hz (f) 160 to 200 Hz (e) 250 to 315 Hz

(d) 400 to 500 Hz (c) 630 to 800 Hz (b) 1k to 1.25k Hz

Figure 2.8 Noise source distribution of the bogie’s aerodynamic noise(bottom view of 1/7th scale model, the frequencies are converted to full scale ones) (Sawamura et al. 2018)

Nagakura (2006) used the acoustic mirror technology to measure the aerodynamic noise of a high-speed train. In the field test, it was found that for frequencies below 2000 Hz, the noise sources located at the lower part of the train including the cowcatcher and the bogies are stronger than those at other regions. Similar conclusions were found in the wind tunnel test results from Lauterbach et al. (2010) and Lauterbach et al. (2012). However, the role of each component in the aerodynamic noise contribution in the frequency domain could not be clearly determined. In Figure 2.9, the noise spectra of the front bogie with different inflow velocities have similar shapes and the tonal components remained at the frequencies of 2417 Hz and 3406 Hz (at 1/25 scale). This phenomenon is different from that observed in the pantograph noise spectra in which the peak frequencies scale with the wind speed. Lauterbach et al. (2012) proposed that a characteristic dimension of the bogie cavity is probably responsible for the tonal components. Minelli et al. (2020) used a CFD method to calculate the aerodynamic noise from an ICE3 train leading car scale model without a bogie present in the cavity. They also detected the spectral peak at 3406 Hz, which seems to be related to the distance between the ground and the top of the cavity, although not the one at 2417 Hz. However, it is still an open issue whether this phenomenon will occur in the test of a different type of train or at higher Reynolds numbers and Mach numbers.

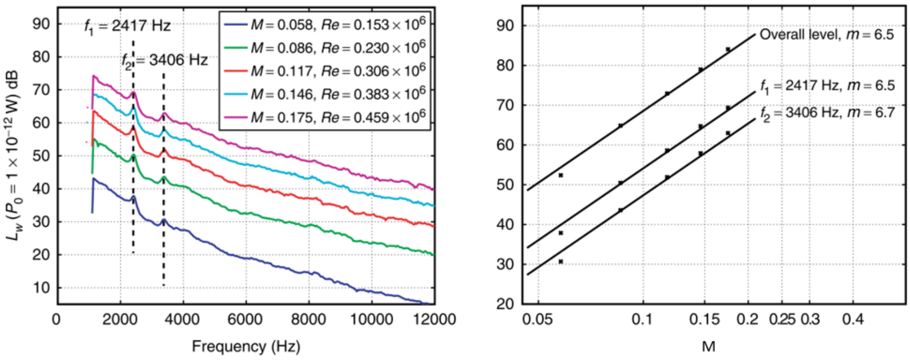

(a) (b)

Figure 2.9 Characterisation of the noise of the front bogie in 1/25 scale model for different Mach numbers, measured in the aeroacoustic wind tunnel Braunschweig. (a): Narrowband spectra (Δf = 36.6 Hz) for different Mach numbers; (b): Relation between sound power level and Mach number M, m is the speed exponent. (Lauterbach et al. 2012)

The bogies are also one of the main sources of aerodynamic drag of a high-speed train, which contribute to the energy consumption significantly. The bogie itself, any fairing, and the shape of bogie cut outs (cavities) are all factors that affect the aerodynamic drag. Mancini (2001) investigated the effects of bogie fairings on the aerodynamic drag of an ETR 500 high-speed train.

By optimising the external surface of the fairings, the drag was reduced by 20% in wind tunnel tests, as shown in Figure 2.10.

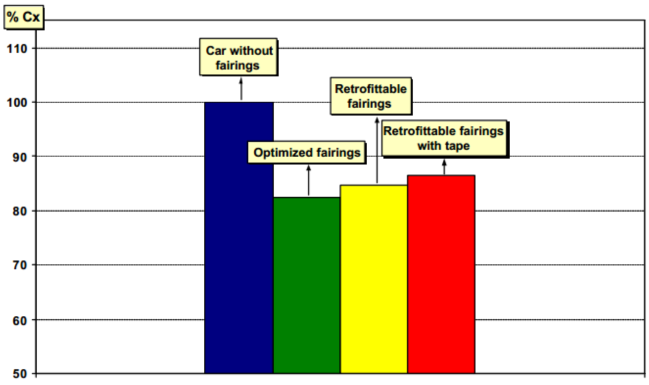

Figure 2.10 Effects of bogie fairings on the drag coefficient in wind tunnel tests of the ETR 500 (Mancini et al. 2001).

2.2.2 Numerical research

Due to the complex structure of the bogie geometry and flow phenomena, simulations of bogie aerodynamics and aeroacoustics are extremely difficult. When choosing the turbulence model to use, the flow field information, the limitations of the turbulence models, and the available computational resources should be carefully considered. The resolution of the grid, especially the boundary layer grid, should meet the requirement of the selected turbulence models. Dévéhat (1996) used Reynolds-averaged Navier–Stokes (RANS) method with the Re-Normalisation Group (RNG) $k-\varepsilon$ turbulence model to calculate the turbulence production around a train car with a bogie under it. Due to the limitation of computational capability, the boundary layer grid was not refined and the bogie surface was set to be free-slip. The anti-yaw dampers at the side of bogie were identified to produce high turbulence, which was also demonstrated by the experiments of Latorre Iglesias et al. (2017). You et al. (2015) utilized the Realizable $k-\varepsilon$ model to calculate the effects of rotating wheels on the underbody flow of a high-speed train. A hexahedral mesh was used away from the train body and a tetrahedral one near the train surface. However, the information about the boundary layer grid is not clearly presented. There are few flow field simulations of a whole bogie by using large eddy simulation (LES) because it requires extremely high grid resolution. Detached eddy simulation (DES), which is a hybrid method of RANS and LES, has a higher accuracy to solve the separated flow compared with RANS, and a lower grid requirement for resolution of the boundary layer compared with LES. Thus, it is used by many researchers to calculate the flow field around a high-speed train (Yang and Liu 2017; Zhang et al. 2018; Liu et al. 2019).

Zhu et al. (2014) simulated a reduced scale (1:10) isolated wheelset of a high-speed train by using the Spalart-Allmaras DDES (delayed detached eddy simulation) model. The surface pressure data is then fed to predict the far field noise using FW-H analogy. The results show that for an isolated wheelset, the vortex shedding from the wheel and axle is the main reason of the generation of the tonal noise. The model was then extended to tandem wheelsets, a simplified bogie and a simplified bogie in a cavity (Zhu et al. 2016; Zhu et al. 2018). For the simplified bogie, as shown in Figure 2.11(a), the incoming flow with higher energy impinges on the front part of the bogie and generates flow separation and vortex shedding, and then decays to the wake containing vortices which are convected downstream and impinge on the rear part of the bogie. Therefore, for the cases of tandem wheelsets or where the bogie is in a cavity, shown in Figure 2.11(b), the wake flow from upstream components disturbs the vortex shedding and makes it not regular anymore, which is the main reason that the noise spectra of a bogie tend to be broadband (Zhu et al. 2016; Zhu et al. 2018).

The aerodynamic and aeroacoustic effects from a moving ground and fairing were investigated by Zhu et al. (2017). It shows that both the fairing and the ground can reinforce the pressure fluctuation of the bogie in the cavity. However, the aeroacoustic results calculated by the convective Ffowcs Williams and Hawkings (FW-H) equation show that the fairing is able to reduce the noise while the moving ground reinforces the noise.

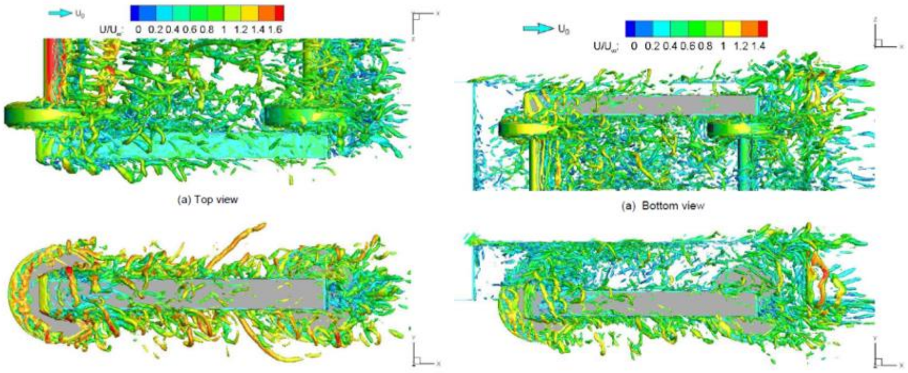

(a) without cavity (b) with cavity

Figure 2.11 Iso-surface of the instantaneous normalized Q of simplified bogie without and with cavity (Zhu 2015).

Minelli et al. (2020) used compressible improved delayed detached eddy simulation (IDDES) to investigate the aerodynamic noise of an ICE3 high-speed train nose. The bogie components in the cavity were removed and the focus was on the train nose and bogie cavity. By comparing the aeroacoustic and the flow structure visualizations, the shear layer from the car body surface and the underbody jet flow are regarded as the main noise sources, as shown in Figure 2.12.

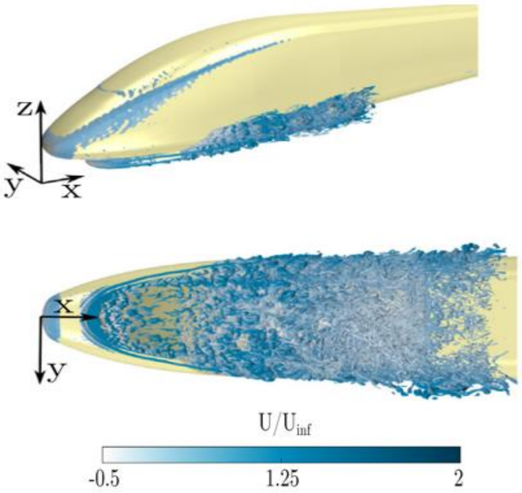

Figure 2.12 Flow structures of the front part of a simplified train model without a bogie in the cavity represented by the second invariant of the velocity gradient Q=1×10^6. The structures are coloured by the streamwise velocity component (Minelli et al. 2020).

Meskine et al. (2013) used Lattice Boltzmann methods (LBM) to simulate the flow around a full-scale high-speed train with bogies. Figure 2.13 illustrates that the vortices from the upstream edge of the front bogie are convected by the high-speed flow and then impinge the downstream bogies. This impingement between the flow and solid surfaces generates pressure fluctuations which are the main source of aerodynamic noise from the bogie. The leading bogie forms a higher aerodynamic noise source than the other bogies because it has the highest inflow velocity (Nagakura 2006; Thompson et al. 2015; Zhu et al. 2016). In order to improve the performance of the train nose, Masson et al. (2012) and Paradot et al. (2008) combined LBM and the FW-H method to study the flow field and aerodynamic noise of two types of French high-speed train. They also confirmed that the front bogie forms a stronger aerodynamic noise source than other bogies. In the optimization study, the train nose, cowcatcher area, bogie components, and underbelly zone of front bogie were modified and the noise spectra were compared with that of the original configuration.

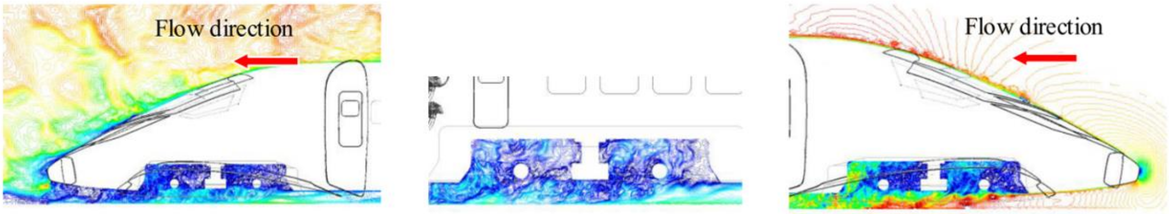

Figure 2.13 Instantaneous velocity magnitude contours. From right to left: 1st, 4th and rear bogie cavities (Meskine et al. 2013).

Although some numerical studies have been performed to investigate the flow field and aerodynamic noise of the train bogie, most of them focus on the general flow field or the influence from some parts of the bogie. Further work is required to reveal the noise generation mechanism of the bogie with more components and features. In addition, the grid used in the boundary layer is critical in the simulation of wall bounded flows, especially the ones with separation (Spalart and Allmaras 1992; Shur et al. 1999; Spalart and Streett 2001). However, the grid in the boundary layer used in many numerical simulations of high-speed trains is not fine enough due to the computational cost (Sima et al. 2008; Dong et al. 2019; Guo et al. 2020). Therefore, exploring a grid system, which can be used to discretise the domain with complex geometry and meanwhile guarantee that the generated grid has a good quality and an acceptable quantity, becomes necessary.

To discretise complex geometries in CFD model, Nakahashi and Obayashi (1987) proposed a hybrid grid system, which combines the advantages of the hexahedral and tetrahedral grid. The word ‘hybrid’ here implies the two types of grid are used to discretize the appropriate parts of the computational domain. It has been applied to investigations of the flow field of aircraft (Shaw and Peace 2002; Tysell 2010) and turbomachinery (Becker et al. 2010). In such a hybrid grid system, although the tetrahedral grid is more flexible than the hexahedral one, it cannot provide results as accurate as a hexahedral grid with the same number of cells and its total number of cells is larger than a hexahedral grid with the same cell size (Juretić and Gosman 2010; Yu et al. 2012). To overcome the drawbacks of the tetrahedral grid, as discussed above, a polyhedral grid has been developed as an alternative (Garimella et al. 2014; Lee 2015). The polyhedral grid possesses several advantages, the most significant one being that it has more adjacent edges or faces, which makes the approximation of gradients much better than when using tetrahedral meshes (Chen et al. 2022). Another significant advantage is that the polyhedral cells are less sensitive to stretching and thus reduce the degree of meshing distortion (Peric and Ferguson 2005). Besides, for the same level of simulation errors, the polyhedral grid has the smallest number of cells and the lowest consumption of computing resources (Juretić and Gosman 2010; Liu et al. 2022). In industrial simulations, the polyhedral grid has been successfully applied in the studies of railway aerodynamics (Sima et al. 2008), building environment (Chen et al. 2022; Liu et al. 2022) and turbine flow (Galindo et al. 2013; Chen et al. 2021).

Therefore, in the following simulations, a hybrid grid system, which is based on a hexahedral grid close to the wall and a polyhedral grid in the rest of the region, will be built to discretise the complex geometry of the bogie. Its generation procedure, validation by benchmark cases and development in different complex models will be carried out.

2.3 Reduction of bogie aerodynamic noise

Research has indicated that the origin of aerodynamic noise generated by the bogie area is the large pressure and velocity fluctuations in the flow field around the bogie and on its solid surface (Thompson et al. 2015; Zhu et al. 2016; Latorre Iglesias et al. 2017). In the control of the aerodynamic noise of the train bogies, no research is found on the application of active control techniques; passive noise control techniques, such as the flow control and the use of noise-isolating materials, are more popular.

In the 1/7 scaled train body measurements of Latorre Iglesias (2015), the noise was reduced by rounding the edges of the downstream edge, without which the noise from the bogie cavity itself was more significant than the bogie components shielded by it. Yamazaki et al. (2019) installed different deflectors along the edge of the cavity and different sized under-covers beneath the bogie to reduce the aerodynamic noise. It was found that the aerodynamic noise was reduced by about 3 dB when the deflector was installed and by 4 dB when the bogie cavity was fully covered. Zhu et al. (2018) compared the aerodynamic noise generated by the bogie with and without faring. The results show that a strong unsteady flow around the bogie area is generated because of the discontinuity of the car body sidewalls, whereas when the faring is installed, the flow interactions are limited inside the bogie cavity and its development outside the fairing is also weakened greatly. Therefore, the far field noise is reduced by 5 dB. On the prototype Shinkansen high-speed train FASTECH360S, side covers, as shown in Figure 2.14, were installed to improve the shape of the side walls of the car body and thus, the aerodynamic noise can be reduced (Kurita 2011). Similar noise reduction measures were also applied on the Shinkansen 500S and 700S high-speed trains (Torii and Ito 2000). Although fairings are beneficial to reduce the drag and aerodynamic noise, they can increase the instability and tendency to overturn in the presence of side winds due to the increased side force and rolling moment (Ali et al. 2017). In addition, the fairing makes the maintenance of the bogie more difficult and obstructs things like hot axle box detectors.

Besides the sides of the bogie, the bottom of the bogie is also in contact with the air. The impingement produced by the turbulent flow from upstream is another source of noise (Zhu et al. 2016). Yamazaki et al. (2019) used deflectors and under-covers with different widths to prevent the flow inside the bogie cavity and compared the effect of varying their widths. The deflector was installed at the upstream cavity rim. The results show that when the width of the under-cover and the deflector exceeds 75% of the sleeper, the noise reduction becomes significant and if the side gaps are also covered, the noise level can be reduced more.

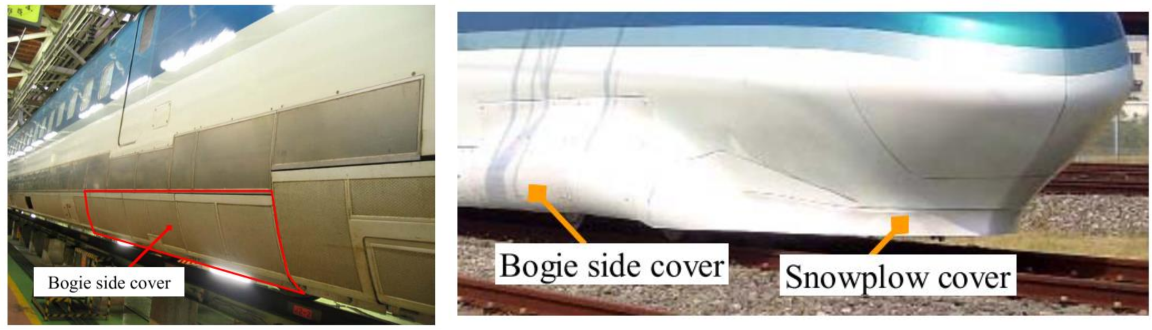

Figure 2.14 Side covers installed at the bogie side (Kurita 2011)

As shown in Figure 2.15, another passive noise control measure is the use of sound-absorbing panels (Kurita 2011). The panels are installed on the cavity surface and the side and bottom area. The noise generated inside the bogie cavity, and that reflecting between the lower part of the train and the noise barriers, can be absorbed.

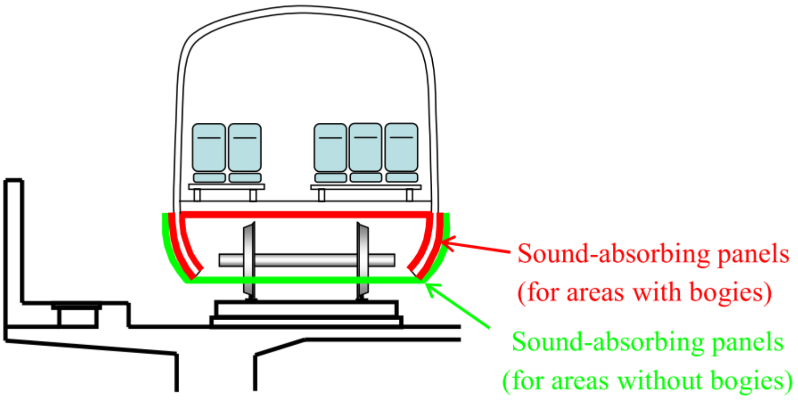

Figure 2.15 Sound absorption panels installed at the bogie region (Kurita 2011)

Although these noise reduction techniques can reduce the aerodynamic noise effectively and are even applied on some real high-speed trains, there are some disadvantages that affect the running of the train or its cost. For example, the application of fairings (side covers) can reduce the flow oscillation inside the cavity and then, reduce the noise but they increase the risk of overturning of the train in the presence of side winds (Ali et al. 2017). In addition, the installed side covers, under-covers and sound-absorbing panels will increase the weight of the car body and increase the running cost. The sound-absorbing panels are made using penetrable plates, honeycomb and porous material, which are easily blocked by the dust around the railway. Moreover, the panels are hard to maintain, and thus, increase the maintenance cost.

In investigations of aerodynamic noise reduction of aircraft landing gear, Oerlemans and De Bruin (2009) first applied a kind of planar jet (air curtain) to reduce the noise. The planar jet can produce a low-speed zone behind it and shield the landing gear from the high-speed air flow. Thus, the sound power of dipole sources, which is proportional to 6th power of the incoming velocity, can be considerably reduced. Therefore, after understanding more about the generation mechanism of the aerodynamic noise of the bogie, appropriate application of planar jets can be considered to reduce the bogie noise.

2.4 Summary

At the beginning of this chapter, literature on the aerodynamic noise of high-speed trains has been reviewed. The main source regions of aerodynamic noise are located at the train nose, bogies, pantographs, inter-coach spacing, rear power car, and car body surfaces. The aerodynamic noise generated by the leading bogie is greater than the others because it faces the strongest incoming flow. Therefore, the project will be focused on the leading bogie. Then, dependency of the aerodynamics and aeroacoustics of high-speed trains on the Reynolds number is investigated. The critical Reynolds number of the self-similarity of the high-speed train is still an open issue. Thus, attention should be paid to this when studying reduced-scale models of the high-speed train bogie.

The noise spectra of train bogies tend to be broadband because the flow around the bogie is highly turbulent and the regular vortex shedding is disturbed. According to some experimental research, the noise energy is higher in the low frequency region and the configuration and position of the components are very important factors that affect the aerodynamic noise generation. More effort should be put to numerical research which can be used to explain the noise generation mechanisms. However, numerical investigations are extremely difficult to carry out reliably because of the complex structure of the train bogies. Accounting for the computational cost, RANS and DES are commonly used to simulate the flow field of train bogie because their grid resolution requirement is much lower than LES. It is worth noting that Lattice Boltzmann methods, which are suitable for the simulation of situations with extremely complex structures, are also used by some authors. Hybrid approaches, which are a combination of CFD and CAA, are used to calculate the far field noise of train bogies.

Various aerodynamic noise reduction measures have been attempted by controlling the flow, such as fairings at the sides of the bogie cavity, deflectors at the front rim of the bogie cavity and an under-cover at its bottom. The basic mechanism of the noise reduction with these measures is to isolate the bogie area and to prevent the highly turbulent flow from contact with it. Another passive noise control measure is the use of sound-absorbing panels that are installed on the surface of the bogie cavity and its side and bottom area. The noise generated around the bogie area can be absorbed by these panels.

In noise control in aviation, a secondary jet flow has been proposed to reduce the noise of the landing gear (Oerlemans and De Bruin 2009; Zhao et al. 2015). The concept is to introduce a jet flow at the front of the landing gear to create a low speed zone behind it, reducing the noise sources on the landing gear. Therefore, it is worth considering jet flow as a potential noise reduction measured for the bogie, as no literature has been found on this topic.

Chapter 3 Computational methodology

The simulation of the flow field is the basis of noise simulations, as the information describing the sound source comes from the result of the flow field. Before calculating the sound field, turbulence models, grid systems, and boundary conditions should be carefully chosen and validated. Different turbulence models require different grid resolution which means that the computational cost should be taken as an important factor when choosing a turbulence model. Therefore, RANS, LES, and DES methods are described.

3.1 Computational fluid dynamics

The Navier-Stokes (NS) equations, which are based on the continuum assumption, are well established as the governing equations for viscous fluids, developed from the conservation statements for mass, momentum and energy. The equations using tensor index notion are given as

$$\frac{\partial \rho}{\partial t}+\frac{\partial}{\partial x_j}\left(\rho U_j\right)=0 \tag{3.1}$$

$$\frac{\partial \rho U_i}{\partial t}+\frac{\partial}{\partial x_j}\left(\rho U_i U_j+P\delta_{ij}-\tau_{ij}\right)=0 \tag{3.2}$$

$$\frac{\partial \rho(e+\frac{1}{2}U_iU_i)}{\partial t}+\frac{\partial}{\partial x_i}\left(\rho U_i\left(e+\frac{P}{\rho}+\frac{1}{2}U_iU_i\right)-\tau_{ij}U_j+q_i\right)=0 \tag{3.3}$$

where $\tau_{ij}=2\mu S_{ij}-\frac{2}{3}\mu\delta_{ij}S_{kk}$ is the viscosity stress tensor, μ is molecular viscosity, δ_{ij} is the Kronecker delta, $S_{ij}=\frac{1}{2}\left(\frac{\partial U_i}{\partial x_j}+\frac{\partial U_j}{\partial x_i}\right)$ is the strain rate tensor. In the energy equation (3.3), $e+\frac{1}{2}U_iU_i$ is the total energy, e is the internal energy, $q_i=-K\frac{\partial T}{\partial x_i}$ is the heat flux, K is the thermal conductivity, and T is the temperature.

There are six variables in the compressible N-S equations and five independent equations (equation (3.2) consists of three equations). The equations can achieve closure by adding the gas state equation, which is as follows for a perfect gas

$$p=\rho RT \tag{3.4}$$

Usually, when the Mach number Ma is low (<0.3) the elastic forces in the fluid are relatively small compared with the inertial forces, which means compressibility of the flow can be neglected, and the flow can be considered as incompressible with constant density (Young et al. 2010). Moreover, for incompressible flow, the thermodynamic field can be decoupled from the hydrodynamic field.

Therefore, the energy equation (3.3) is not required when the flow is incompressible. The N-S equations for incompressible flow are simplified as follows:

$$\frac{\partial U_j}{\partial x_j} = 0 \tag{3.5}$$

$$\frac{\partial U_i}{\partial t} + \frac{\partial U_i U_j}{\partial x_j} + \frac{\partial}{\rho \partial x_j}(P\delta_{ij} - \tau_{ij}) = 0 \tag{3.6}$$

where $\tau_{ij} = 2\mu S_{ij}$.

3.1.1 Reynolds-averaged Navier-Stokes equations

The instantaneous variables in equations (3.5) and (3.6) can be decomposed as follows

$$U_i = \langle U_i \rangle + u_i' \tag{3.7}$$

$$P = \langle P \rangle + p' \tag{3.8}$$

where $\langle U_i \rangle$ and $\langle P \rangle$ are the averaged velocity and pressure, and u_i' and p' are the fluctuating components of velocity and pressure.

Then the Navier-Stokes equations can be rewritten as

$$\frac{\partial \langle U_i \rangle}{\partial x_i} = 0 \tag{3.9}$$

$$\frac{\partial \langle U_i \rangle}{\partial t} + \frac{\partial \langle U_i \rangle \langle U_j \rangle}{\partial x_j} + \frac{1}{\rho}\frac{\partial P}{\partial x_i} - v\frac{\partial^2 \langle U_i \rangle}{\partial x_j^2} + \frac{\partial \langle u_i' u_j' \rangle}{\partial x_j} = 0 \tag{3.10}$$

where $\langle u_i' u_j' \rangle$ is the Reynolds stress component which can be expressed in terms of the mean velocity gradient according to the Boussinesq hypothesis:

$$-\langle u_i' u_j' \rangle = \frac{1}{2} v_t \left(\frac{\partial \langle U_i \rangle}{\partial x_j} + \frac{\partial \langle U_j \rangle}{\partial x_i}\right) - \frac{2}{3} k \delta_{ij} \tag{3.11}$$

where v_t is the turbulence kinematic eddy viscosity, k is the turbulence energy, and δ_{ij} is the Kronecker delta.

Several models can be used for v_t, such as the one-equation Spalart-Allmaras (SA) model, the two-equation $k - \varepsilon$ and $k - \omega$ shear stress transport (sst) models and others.

Spalart and Allmaras (1992) derived the SA turbulence model by establishing the transport equation of a modified turbulent kinematic viscosity $\tilde{v}$.

$$\frac{\partial \tilde{v}}{\partial t} + U_j \frac{\partial \tilde{v}}{x_j} = c_{b1} \tilde{S} \tilde{v} + \frac{1}{\sigma}\left[\frac{\partial}{\partial x_j}\left((v + \tilde{v})\frac{\partial \tilde{v}}{x_j}\right) + c_{b2}\frac{\partial \tilde{v}}{x_i}\frac{\partial \tilde{v}}{x_i}\right] - c_{\omega 1} f_{\omega} \left(\frac{\tilde{v}}{d}\right)^2 \tag{3.12}$$

The turbulence viscosity is calculated as follows:

$$v_t = \tilde{v} f_{v1} \tag{3.13}$$

where $f_{v1} = \frac{\chi^3}{\chi^3 + c_{v1}^3}$, $\chi = \frac{\tilde{v}}{v}$, v is the molecular viscosity, f_{v1} is a damping coefficient in the near-wall region. Other terms in Equation (3.12) are defined as follows:

$$\tilde{S} = \Omega + \frac{\tilde{v}}{k^2 d^2} f_{v2} \tag{3.14}$$

$$f_\omega = g\left(\frac{1 + c_{\omega 3}^6}{g^6 + c_{\omega 3}^6}\right)^{1/6} \tag{3.15}$$

where Ω is the vorticity magnitude $\Omega = \sqrt{2\omega_{ij}\omega_{ij}}$, d is the distance to the wall, which is used as the length scale to determine the destruction level in the equation; $f_{v2} = 1 - \frac{\chi}{1+\chi f_{v1}}$, $g = r + c_{\omega 2}(r^6 - r)$, and $r = \min\left[\frac{\tilde{v}}{\tilde{S}k^2 d^2}, 10\right]$. The constants in the equations are c_{b1}=0.1355, σ =2/3, c_{b2}=0.622, k=0.41, c_{w2}=0.3, c_{w3}=2, c_{v1}=7.1 and $c_{w1} = \frac{c_{b1}}{k^2} + \frac{1+c_{b2}}{\sigma}$.

In a statistically steady flow, $\overline{U}_i$ and $\overline{P}$ are time-averaged values and independent of time. Therefore, the unsteady term in Equation (3.10) is zero. However, when the flow is unsteady the mean values are ensemble averaged. Thus, the unsteady term remains, which is the main difference between RANS and unsteady RANS (URANS).

3.1.2 Large eddy simulation

According to Richardson's basic concept of energy cascade, turbulence contains different scales of eddies; the large eddies are unstable and break up, at the same time transferring energy to the smaller eddies (Richardson 1922). The smaller eddies repeat the breaking up and energy transfer process until the smallest eddies, which are called the Kolmogorov scale, can be dissipated by the molecular viscosity (Kolmogorov 1941). The basic concept of LES is to calculate the large scale eddies, which contain most of the energy, and to model the influence of small scale eddies on the resolved scales. Therefore, the computational cost of LES is lower than Direct Numerical Simulation (DNS), which resolves all eddies in turbulence (Smagorinsky 1963).

The scales of eddies are separated by a filtering operation, which is defined as:

$$\overline{f}(x) = \int f(x')G(x, x', \Delta)dx' \tag{3.16}$$

G is the filter kernel and Δ is the cut-off width. The filtered mass and momentum equations in conservative form are as follows (Pope 2000):

$$\frac{\partial \bar{U}_i}{\partial x_i} = 0 \tag{3.17}$$

$$\frac{\partial \bar{U}_i}{\partial t} + \frac{\partial \bar{U}_i \bar{U}_j}{\partial x_i} = 2v\frac{\partial \bar{S}_{ij}}{\partial x_i} - \frac{1}{\rho}\frac{\partial \bar{p}}{\partial x_i} + \frac{1}{\rho}\frac{\partial \tau_{ij}^R}{\partial x_i} \tag{3.18}$$

where $\bar{S}_{ij} = \frac{1}{2}(\frac{\partial \bar{U}_i}{\partial x_j} + \frac{\partial \bar{U}_j}{\partial x_i})$ is the filtered strain rate. The residual stress tensor is defined as

$$\tau_{ij}^R = -\rho(\overline{U_i U_j} - \bar{U}_i \bar{U}_j) \tag{3.19}$$

The anisotropic residual-stress is defined by

$$\tau_{kl}^{sgs} = \tau_{ij}^R - \frac{1}{3}\tau_{ii}^R \delta_{ij} \tag{3.20}$$

τ_{kl}^{sgs} is also called the Sub-Grid Stress tensor (SGS). In order to close the equations, a model is needed for τ_{kl}^{sgs}. The simplest model was proposed by Smagorinsky (1963).

$$\tau_{kl}^{sgs} = 2\mu_{sgs}\bar{S}_{ij} \tag{3.21}$$

$$\mu_{sgs} = \rho(C_{sgs}\Delta)^2\sqrt{\bar{S}_{ij}\bar{S}_{ij}} \tag{3.22}$$

μ_{sgs} is the subgrid-scale turbulence viscosity, C_{sgs} is the Smagorinsky constant and has different values for different flow configurations. $\Delta = (\Delta_x \Delta_y \Delta_z)^{1/3}$ is the filter length scale where Δ_x, Δ_y, and Δ_z are the grid lengths in the three coordinate directions. A problem with the Smagorinsky model is that μ_{sgs} is greater than it should be in the near-wall viscous sublayer. One solution is to apply the van Driest damping which has been used in RANS models (Moin and Kim 2006).

$$\Delta_v = \min\,(D_L, \Delta) \tag{3.23}$$

$$D_L = \frac{\kappa y}{C_s}(1 - e^{\frac{-y^+}{A^+}}) \tag{3.24}$$

where Δ_v is the damped filter length scale, D_L is the filter length scale based on the distance from the grid to the wall, Δ is grid filter length scale, κ is the von Karman constant which is equal to 0.41, A^+=26. Compared to the original Smagorinsky model, the Van Driest damping method can return smaller sub-grid turbulence viscosity in the near-wall region.

Nicoud and Ducros (1999) proposed a model called the Wall-Adapting Local Eddy-Viscosity (WALE) model. An advantage of this model is that it returns zero sub-grid turbulence viscosity in laminar zones, which includes the viscous sublayer in the boundary layer. The sub-grid scale turbulence viscosity is defined as

$$\mu_{sgs} = \rho {\Delta_s}^2 \frac{(S_{ij}^d S_{ij}^d)^{1.5}}{(\overline{S}_{ij}\overline{S}_{ij})^{2.5} + (S_{ij}^d S_{ij}^d)^{1.25}} \tag{3.25}$$

$$S_{ij}^d = \frac{1}{2}\left(\overline{g}_{ij}^2 + \overline{g}_{ji}^2\right) - \frac{1}{3}\delta_{ij}\overline{g}_{kk}^2 \tag{3.26}$$

where $\Delta_s = C_w\Delta$, C_w is recommended as 0.325. $\overline{g}_{ij}^2 = \overline{g}_{ik}\overline{g}_{kj}$ and $\overline{g}_{ij}$ is the filtered velocity gradient $\frac{\partial \overline{U}_i}{\partial x_j}$.

3.1.3 Detached eddy simulation

Detached eddy simulation (DES) is a combination of LES and URANS, which was proposed by Spalart et al. (1997). Regions near solid boundaries are simulated by URANS and outside these regions LES is applied. Therefore, compared with LES, the computational cost of DES is considerably reduced. In addition, the DES method is not a zonal approach because the switch between URANS and LES is not decided by a predetermined parameter setting for the zones but by the local grid near the wall region. The switch is applied by replacing the length scale d in Equation (3.12) by the following equation:

$$\tilde{d} = \min\,(d, C_{des}\Delta) \tag{3.27}$$

where C_{des} is an empirical constant, for homogeneous turbulence it is 0.65 (Shur et al. 1999), and $\Delta = (\Delta_x\Delta_y\Delta_z)^{1/3}$. When $d < C_{des}\Delta$, the URANS model is applied to simulate the near wall region and, when $d > C_{des}\Delta$, the LES model is triggered to resolve the filtered flow field. Therefore, the near-wall grid region is very important. In separation or transition flow, which are sensitive to the grid and turbulence models, grid-induced separation will be introduced if the grid is ambiguous at the edge of boundary layer (Menter et al. 2003; Menter and Kuntz 2004). Spalart et al. (2006) proposed a new treatment to resist the ambiguous mesh, which is known as delayed detached-eddy simulation (DDES). The length scale $\tilde{d}$ is redefined as

$$\tilde{d} \equiv d - f_d \max(0, d - C_{des}\Delta) \tag{3.28}$$

where

$$f_d = 1 - \tanh((8r_d)^3) \tag{3.29}$$

$$r_d = \frac{v_t + v}{\sqrt{U_{i,j}U_{i,j}}\,k^2 d^2} \tag{3.30}$$

$U_{i,j}$ is the velocity gradient. Compared with Equation (3.27) the length scale is not only dependent on the grid but also on the flow field variables.

3.2 Computational aeroacoustics (CAA)

Generally, acoustic calculation methods can be categorized into three types: analytical approaches, numerical approaches, and hybrid methods (Harwood 2014).

The first type is the exclusively analytical approaches, especially the acoustic analogy which separates the propagation of the acoustic disturbances from the sources of these disturbances. Many studies (Sarkar and Hussaini 1993; Witkowska et al. 1997) using Lighthill's analogy (Lighthill 1952) ignore the viscous and non-isentropic behaviour effect to simplify the acoustic source stress tensor. There are also some extensions or reformations of Lighthill's analogy, such as Curle's analogy (Curle 1955), Ffowcs Williams and Hawking's analogy (Ffowcs Williams and Hawkings 1969), Goldstein's analogy (Goldstein 2003) and Howe's vortex sound formulation (Howe 1975). It is difficult to find analytical expressions without the introduction of simplifying assumptions for the realistic applications, especially for applications in which the source includes turbulence (Harwood 2014).

Fully numerical approaches can solve the full nonlinear N-S equations or simplified versions to compute the acoustic sources as well as to predict the propagation of acoustic fluctuations to the observer. In consideration of the fact that the effect of viscosity on acoustic waves appears only when the propagation distance is large, viscosity is usually ignored when studying noise propagation and the N-S equations are simplified to what is known as the full Euler equations. In practice, the variables are split into the background mean flow and the fluctuating components and the non-linear terms are neglected to obtain the Linearized Euler Equations (LEE) which can be used to describe the velocity, density and pressure fluctuations convected with the mean flow (vorticity, entropy and acoustic waves) (Zhang 2012). Because of the large computational domain and high order discretisation scheme required, these exclusively numerical approaches usually require tremendous computer resources to capture small acoustic fluctuations (Lyrintzis 2003).

In the hybrid methods, the noise source region is calculated by the numerical approaches and the sound propagation to far field is predicted by the analytical approaches. Thus, the hybrid methods, which combine the strengths of the numerical and analytical approaches (Harwood and Dupère 2016), have become the most popular choice to handle aerodynamic noise problems.

3.2.1 Lighthill's acoustic analogy

The first acoustic analogy was proposed by Lighthill (1952), who rearranged the Navier-Stokes equations to form an inhomogeneous acoustic wave equation that can describe the aeroacoustic waves. After some algebraic manipulations, the mass and momentum conservation equations (3.1) and (3.2) can be written as:

$$\frac{\partial^2 \rho'}{\partial t^2} - c_0^2 \nabla^2 \rho' = \frac{\partial^2 T_{ij}}{\partial x_i \partial x_j} \tag{3.31}$$

with

$$T_{ij} = \rho U_i U_j + (p' - c_0^2 \rho')\delta_{ij} - \tau_{ij} \tag{3.32}$$

where $\rho' = \rho - \rho_0$ is the density fluctuation and $p' = p - p_0$ is the pressure fluctuation, c_0 is the local sound speed, and T_{ij} is the Lighthill stress tensor. The left-hand side of equation (3.31) is the standard wave operator and the right-hand side term can be regarded as equivalent noise sources. $\rho U_i U_j$ represents the source from non-linear effects, $p' - c_0^2 \rho'$ is the source related to the non-isentropic effects which can be ignored if there is no unsteady heat source, and τ_{ij} describes the source associated by viscosity which is also negligible in low Mach number flow.

Equation (3.31) is the inhomogeneous wave equation which can be solved by applying the Green's function in free space. After integrating the contribution from every source point, which is expressed using the Green's function, the far field acoustic density fluctuation can be obtained as

$$\rho'(\mathbf{x}, t) = \frac{1}{4\pi c_0^2} \frac{\partial^2}{\partial x_i \partial x_j} \int_V \frac{T_{ij}\left(\mathbf{y}, t - \frac{r}{c_0}\right)}{r} dV(\mathbf{y}) \tag{3.33}$$

where $\mathbf{x}$ is the observer position in the far field, $\mathbf{y}$ is the source position, $r = |\mathbf{x} - \mathbf{y}|$ is the distance between the observer and the noise source position.

3.2.2 Curle's equation

When solving Lighthill's equation (3.31), the presence of solid boundaries in the flow is not considered. Curle (1955) extended Lighthill's general theory by taking into account the influence of solid boundaries. A dipole source term, which is due to the interaction between the solid boundaries and the flow, is added into the equation (3.33):

$$\rho'(\mathbf{x}, t) = \frac{1}{4\pi c_0^2} \frac{\partial^2}{\partial x_i \partial x_j} \int_V \frac{T_{ij}\left(\mathbf{y}, t - \frac{r}{c_0}\right)}{r} dV(\mathbf{y}) + \frac{1}{4\pi c_0^2} \frac{\partial}{\partial x_i} \int_S \frac{P_i\left(\mathbf{y}, t - \frac{r}{c_0}\right)}{r} dS(\mathbf{y}) \tag{3.34}$$

where S is the integral surface on the solid boundaries; $P_i = l_i p_{ij}$ is the force per unit area exerted on the fluid by the solid boundaries in the x_i direction, l_i is the unit normal vector of the solid boundaries, and $p_{ij} = p\delta_{ij} - \tau_{ij}$ is the compressive stress tensor.

In low Mach number flow, the first term on the right side of equation (3.34) can be ignored and in the acoustic far field the spatial derivative in the second term can be converted to a time derivative term,

$$\rho'(\mathbf{x}, t) = \frac{(x_i - y_i)}{4\pi c_0^3} \frac{\partial}{\partial t} \int_S \frac{P_i\left(\mathbf{y}, t - \frac{r}{c_0}\right)}{r^2} dS(\mathbf{y}) \tag{3.35}$$

In equation (3.35) the sound pressure $p'(\mathbf{x}, t) = c_0^2 \rho'(\mathbf{x}, t)$ is proportional to the integral of the pressure fluctuation rate $\frac{\partial p}{\partial t}$ on the solid surface. Therefore, the sound pressure produced by a single point source is proportional to the pressure fluctuation rate $\frac{\partial p}{\partial t}$ (Curle 1955),

$$p'(x_i, t) \propto \frac{dP_i\left(\mathbf{y}, t - \frac{r}{c_0}\right)}{dt} \tag{3.36}$$

where $p'(x_i, t)$ is the sound pressure generated by the point source at the position $\mathbf{y}$. When the focus is on the far field noise, equation (3.36) can be used to assess the sound source strength. In order to investigate the distribution of the dipole noise sources on the solid surface, the following equation is used to calculate the pressure fluctuation strength:

$$L_{\dot{p}} = 10 \log_{10}\left(\sum_{i=1}^{n} PSD_i \times df\right) \tag{3.37}$$

where PSD_i is the power spectral density of the dp/dt signal at the i^{th} frequency, df is the frequency interval and n is the number of frequencies.

To quantify the total sound source strength of a component, the following equation is used to sum the power of every element of the component:

$$L_{\dot{p},total} = 10 \log_{10}\left(\sum_{j=1}^{m} \left(\sum_{i=1}^{n} (PSD_{ji} \times df) \times dA_j\right)\right) \tag{3.38}$$

where m is the total number of grid elements associated with the component, A_j is the area of the j^{th} grid element.

3.2.3 Ffowcs Williams-Hawkings equation

In Curle’s equation, the solid boundary is considered as stationary, whereas arbitrary motion of the solid boundary is taken into account by Ffowcs Williams and Hawkings (1969).

In order to consider the enclosed volume formed by the solid boundaries, a generalized density function is set up that is equal to the fluid density $\rho(\mathbf{x},t)$ outside the boundaries and the constant density ρ_0 inside the boundaries.

$$\bar{\rho}(\mathbf{x},t) = \rho_0 + [\rho(\mathbf{x},t) - \rho_0]H(f) = \begin{cases} \rho(\mathbf{x},t) & f > 0 \\ \rho_0 & f < 0 \end{cases} \tag{3.39}$$

$H(f)$ is the Heaviside unit function which is defined as

$$H(f) = \begin{cases} 1 & \text{for } f > 0 \\ 0 & \text{for } f < 0 \end{cases} \tag{3.40}$$

where f is a function that is positive in the region of interest, negative inside the boundaries, and 0 on the boundaries; the divergence ∇f is the normal vector of the surface and the time derivative $\partial f/\partial t$ is the component of the solid surface velocity in the normal direction ∇f.

Taking the gradient and the time derivative of equation (3.39),

$$\frac{\partial \bar{\rho}}{\partial t} = H(f)\frac{\partial \rho}{\partial t} - (\rho - \rho_0)\delta(f)v_n \tag{3.41}$$

$$\nabla\bar{\rho} = H(f)\nabla\rho + (\rho - \rho_0)\delta(f)\mathbf{n} \tag{3.42}$$

The second term on the right-hand side in equations (3.41) and (3.42) is only present on the boundaries where $\delta(f) = 1$. Replacing the density ρ in the conservation equations (3.1) and (3.2) with the generalized density $\bar{\rho}$, the following equations can be obtained:

$$\frac{\partial \overline{\rho - \rho_0}}{\partial t} + \frac{\partial \overline{\rho U_{\boldsymbol{i}}}}{\partial x_i} = [\rho U_n - (\rho - \rho_0)V_n]\delta(f) = Q\delta(f) \tag{3.43}$$

$$\frac{\partial \overline{\rho U_{\boldsymbol{i}}}}{\partial t} + \frac{\partial \overline{\rho U_\imath U_\jmath}}{\partial x_i}(\overline{\rho U_\imath U_\jmath} + \bar{p}\delta_{ij} - \bar{\tau}_{\boldsymbol{ij}}) = F_i\delta(f) \tag{3.44}$$

where $Q = \rho u_n - (\rho - \rho_0)V_n$ is the mass source distributed on the surface, $F_i = \rho U_i(U_n - V_n) + Pn_i - \tau_{ij}n_j$ is the force distribution on the surface. U_n is the fluid velocity component in the surface normal direction. Similar to the derivation of Lighthill’s equation, rearranging equations (3.42) and (3.43), the inhomogeneous wave equation can be derived as:

$$\frac{\partial^2 \bar{\rho}'}{\partial t^2} - c_0^2\nabla^2\bar{\rho}' = \frac{\partial^2}{\partial x_i \partial x_j}[T_{ij}H(f)] - \frac{\partial}{\partial x_i}[F_i\delta(f)] + \frac{\partial}{\partial t}[Q\delta(f)] \tag{3.45}$$

The first term in the right-hand side is the quadrupole source in the fluid region, the second term is the dipole source on the boundaries, and the third term is the monopole source generated by the unsteady flow through the boundaries. Applying the Green's function, equation (3.44) can be solved,

$$\rho'(\mathbf{x},t) = \frac{\partial^2}{\partial x_i \partial x_j} \int_V \frac{T_{ij}\left(\mathbf{y}, t - \frac{|\mathbf{x}-\mathbf{y}|}{c_0}\right)}{4\pi c_0^2 |\mathbf{x}-\mathbf{y}|} d\mathbf{y} - \frac{\partial}{\partial x_i} \int_S \frac{F_i\left(\mathbf{y}, t - \frac{|\mathbf{x}-\mathbf{y}|}{c_0}\right)}{4\pi c_0^2 |\mathbf{x}-\mathbf{y}|} d\mathbf{y} + \frac{\partial}{\partial t} \int_S \frac{Q\left(\mathbf{y}, t - \frac{|\mathbf{x}-\mathbf{y}|}{c_0}\right)}{4\pi c_0^2 |\mathbf{x}-\mathbf{y}|} d\mathbf{y} \tag{3.46}$$

When it is low Mach number flow, the volume integral, which is the quadrupole term, can usually be ignored. The monopole source term also can be dropped because for a high-speed train bogie, the solid surface is rigid which cannot induce mass fluctuation. The dipole source is related to the pressure fluctuation on the solid surface, which can be calculated by CFD approaches.

3.3 Summary

In the current study, there are two major steps in the aerodynamic noise simulation. The first one is to obtain the aerodynamic information, using CFD techniques. The second one is to calculate the far-field noise using the FW-H equation with the input of the surface pressure fluctuations sampled from the first step. For the aerodynamic simulations, the RANS, DDES and LES methods are reviewed. Their computational cost is from the cheapest to the highest but their accuracy successively increases. In the current study, the open-source CFD solver OpenFOAM 2.4.0 is used. Since the purpose of the study is to achieve an engineering model rather than high-fidelity flow simulations, the DDES method, which is a compromise between the computational cost and accuracy, is chosen to simulate the aerodynamic flow field. To reduce the flow convergence time, the RANS method is used to initialize the flow field before running for the DDES simulations. In addition, Equations (3.37) and (3.38), which are derived from Curle's equation, are adopted to assess the dipole noise source strength. For the far-field noise calculation, the FW-H method is used and it is performed in ANSYS FLUENT.

Chapter 4 Validation cases for CFD and CAA

Bogies consist of many different components with cross-sections that can be approximated as circular, square, or rectangular. In this chapter, benchmark cases are calculated, including the flow over circular and square cylinders, an isolated wheelset, and an open cavity. The aims are to validate the CFD methods, grid systems and turbulence models used for the subsequent simulations of the whole bogie and its components.

4.1 Circular and square cylinder flow

4.1.1 Computational domain and grid type

In this section, the flow field over a circular cylinder and over an approximately square cylinder are calculated. The free stream velocity in both cases is 30 m/s. The diameter of the circular cylinder is 50 mm, corresponding to a Reynolds number $Re = 1 \times 10^5$ based on the cylinder diameter and freestream velocity. The height of the square cylinder, which faces the incoming flow, is 41 mm, corresponding to $Re = 8.2 \times 10^4$ based on the height. The cylinder is not exactly square, having a width in the streamwise direction of 43.1 mm. These cases are chosen to allow direct comparison with the results given by Liu (2017).

As shown in Figure 4.1, two types of grid system are tested for the circular and square cylinders. The inspiration for type I, which is a structured mesh, is from Liu (2017). As shown in Figure 4.1, the boundaries of the domain have sufficient distance from the cylinder. The upstream inlet, the top and bottom surfaces are located at 10*D* from the cylinder axis and the downstream outlet is located at 20*D* where *D* is the diameter or height. Liu (2017) studied the spanwise correlation of the pressure fluctuation on a circular cylinder surface and pointed out that simply replicating the data in the spanwise direction will produce unphysical correlations. However, increasing the length in the spanwise direction will increase the computational cost. Therefore, a length in the spanwise direction of 3*D* for the circular cylinder and 4*D* for the square cylinder are used, as in Liu (2017).

The structured grid system has the merits of high orthogonality and easy-to-control grid growth, by which the simulation can achieve higher precision than an unstructured grid system when using the same numerical schemes. Therefore, the structured grid system is recommended in many academic papers, especially for flow that is largely affected by walls, where a grid system with good quality and appropriate spacing growth near the walls is crucial for the flow simulation (Spalart et al. 1997; Spalart and Streett 2001). However, for a model with a complex geometry like a train bogie, the discretization by a structured grid is an extremely difficult task. Compared with the structured grid, the unstructured grid system has the opposite characteristics; it is relatively easy to generate and very flexible for models with complex geometry, but high quality is hard to achieve. An alternative is therefore studied, referred to as Type II, which combines the merits of the structured and unstructured grid systems. This is a hybrid grid system which is based on a structured grid close to the wall and a polyhedral grid in the rest of the region.

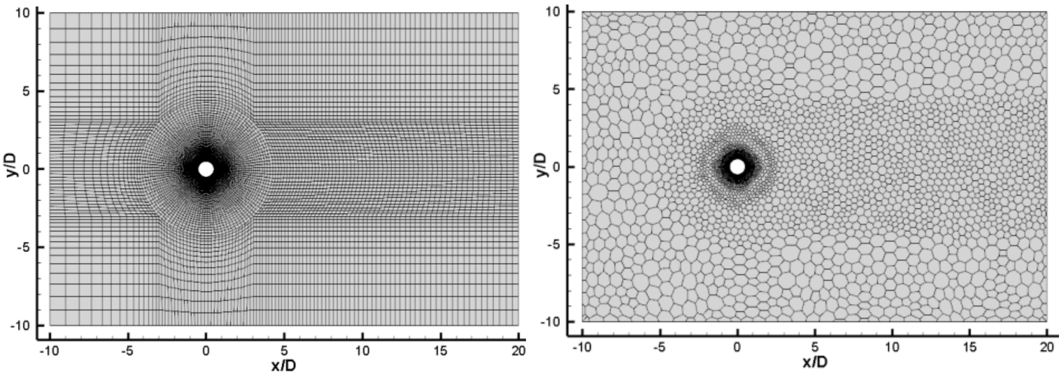

(a) type I: structured (b) type II: hybrid

Figure 4.1 Two types of grid system used for cylinder flow

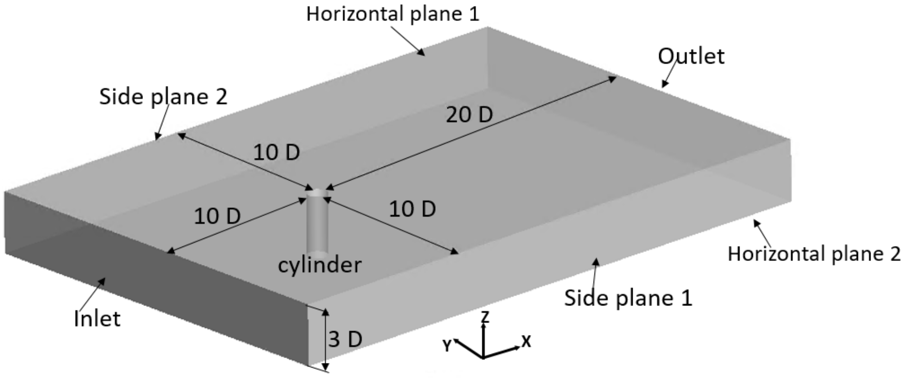

Figure 4.2 The three dimensional computational domain

The procedure used to generate the hybrid grid is shown in Figure 4.3 and some examples are shown in Figure 4.4 and Figure 4.5. It starts from the creation of the hexahedral mesh near the cylinder surface using ANSYS IcemCFD. Some mesh blocks are created to cover the cylinder surface and the mesh distribution and resolution can be adjusted by setting the parameters on the block edges. The maximum aspect ratio, the height of the first layer and the expansion ratio of the boundary layer grid are all the same as the one of the structured grid, which are the same as the parameters used by (Liu 2017). After generating the structured grid, an unstructured tetrahedral grid is generated in the rest of the computational domain. The grid is refined by setting a refinement box in the region near the cylinder. In order to merge the hexahedral grid with the tetrahedral grid, an interface is specified between the two types of grid. The grid size and distribution on the interface should be similar. Finally, a conversion from the tetrahedral grid to a polyhedral grid is performed in ANSYS Fluent 14.8. Compared with the tetrahedral cells, the polyhedral cells are less sensitive to stretching (Peric and Ferguson 2005). The reason for the conversion is the need to improve the quality and reduce the total number of the grid cells.

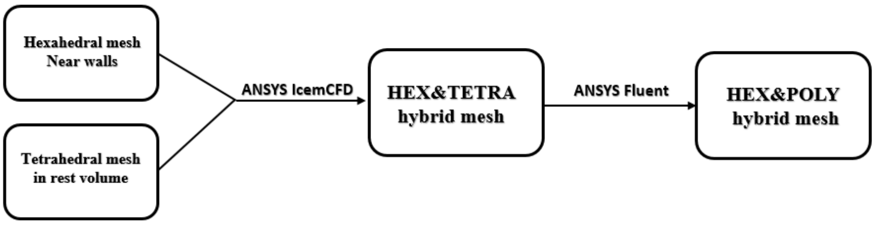

Figure 4.3 The procedure of hybrid mesh generation

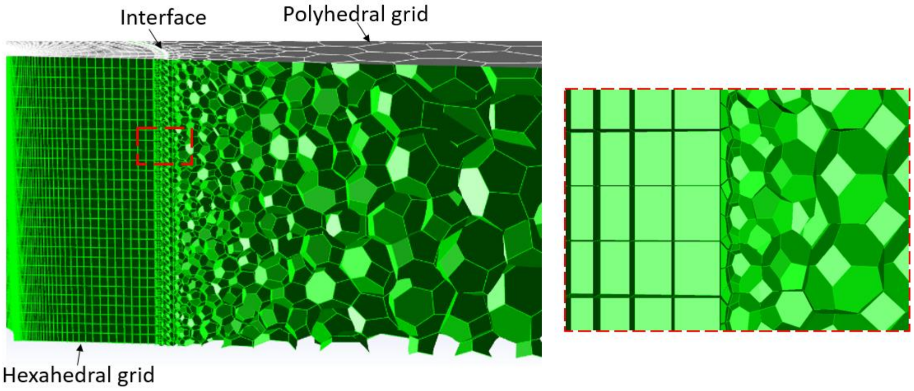

Figure 4.4 The hybrid mesh connection area

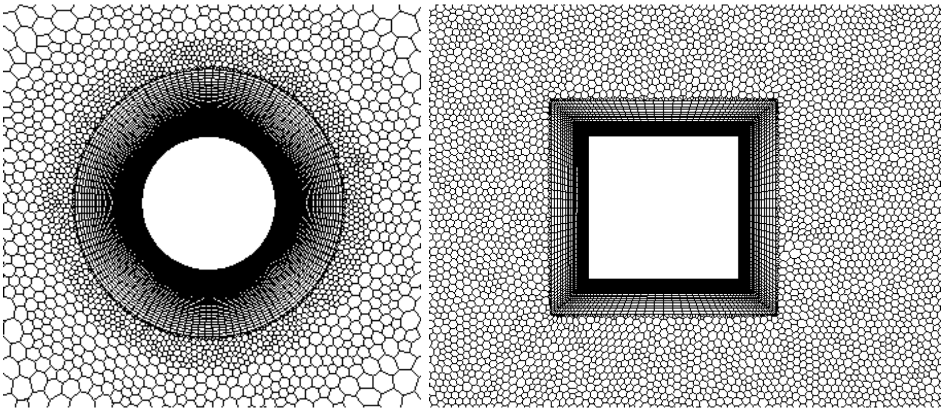

Figure 4.5 The grid configuration near the cylinder surface of type II

4.1.2 Numerical setup

The simulations are conducted in the software OpenFOAM 2.4.0. The DDES method with S-A model proposed by Spalart and Allmaras (1992) is tested. Table 4.1 shows the boundary conditions used for the simulations.

Table 4.1 Boundary conditions for S-A DDES

Boundary	Inlet	Outlet	Cylinder	Horizontal planes	Side planes
nusgs	zero gradient	zero gradient	fixed value	periodic	symmetry
$\tilde{v}$	1.0e-4	zero gradient	fixed value	periodic	symmetry
U	fixed value	zero gradient	fixed value	periodic	symmetry
P	zero gradient	fixed value	zero gradient	periodic	symmetry

For separated flows, the boundary layer should be well resolved, otherwise the separation parameters, such as the position of the separation point, cannot be calculated accurately. Use is made of x^+, $y^+$and z^+, the normalized grid resolutions in circumferential, normal, and spanwise directions respectively, which are defined as:

$$x^+ = \frac{u_\tau \Delta x}{v} \tag{4.1}$$

$$y^+ = \frac{u_\tau \Delta y}{v} \tag{4.2}$$

$$z^+ = \frac{u_\tau \Delta z}{v} \tag{4.3}$$

where $u_\tau = (\frac{\tau_w}{\rho})^{0.5}$ is the friction velocity at the cylinder surface, $\tau_w = \mu \left(\frac{\partial u}{\partial n}\right)\Big|_w$ is the wall shear stress, μ is dynamic viscosity, and $\frac{\partial u}{\partial n}\Big|_w$ is the normal velocity gradient at the wall, $\Delta x, \Delta y$, and Δz are the grid resolutions in the three local coordinate directions. The viscous sublayer will be simulated in the cases. Therefore, the values of y^+ in the grid layer adjacent to the solid surface should all be smaller than 1 (Spalart 2000).

In order to reduce the calculation time, the following second order implicit temporal scheme, which is called “backward” time marching in OpenFOAM (Curtiss and Hirschfelder 1952), is used:

$$\frac{\partial \varphi_n}{\partial t} = \frac{1}{\Delta t}(\frac{3}{2}\varphi_n - 2\varphi_{n-1} + \frac{1}{2}\varphi_{n-2}) \tag{4.4}$$

where φ_n is the current variable, φ_{n-1} is the variable at the previous time step Δt, φ_{n-2} is the variable at two time steps before the current one.

For the convection term, Gauss linear is used in the DDES simulation; this has high precision but requires a grid with high quality and uniform distribution (Greenshields 2015). For the velocity and pressure coupling term, the PIMPLE algorithm is used, which combines the SIMPLE and PISO algorithms (Greenshields 2015).

CFL is the Courant-Friedrichs-Lewy number which is defined as (Courant et al. 1928)

$$CFL = \frac{\Delta t U_\infty}{\Delta l} \tag{4.5}$$

where Δt is the time step, U_∞ is the freestream velocity, and Δl is the cell size in the velocity direction. For an explicit temporal scheme, CFL should be less than 1 to resolve the flow physics; but for implicit temporal schemes, there is no clear requirement for the CFL value (Mockett et al. 2010). In general, a small value of CFL is beneficial to the numerical stability and the capture of small-scale features in the flow but leads to an increase in the calculation time. Therefore, as a compromise, an upper limit of 2 is used for CFL in the simulations.

4.1.3 Results of circular cylinder flow

The bogie contains several circular cylinders such as the axles and the various dampers, see Figure 1.1 and Appendix A. For a DDES model of flow over a circular cylinder, refining the grid does not guarantee a grid convergence as demonstrated by Travin (2000), Zhu (2015) and Liu (2017). Liu (2017) has studied the effects of the grid spatial resolution, the temporal resolution and the numerical schemes at $Re = 10^5$; then the same parameters were successfully applied to a range of Reynolds numbers. Therefore, in Table 4.2, the height and maximum aspect ratio in the first boundary layer follow the previous research by Liu (2017). Case c-I refers to circular cylinder with structured grid, as shown in Figure 4.1(b) and Case c-II refers to circular cylinder with hybrid grid, as shown in Figure 4.1(b). In case c-II the near-wall grid, whose number of cells is 1.37 million, is the same as that in case c-I. The tetrahedral grid is connected to the structured grid close to the boundary layer. After converting the tetrahedral grid into a polyhedral one, the number of cells in the rest of the volume reduces by about half to 0.39 million, which makes the number of cells for case c-II 29.6% less than that of case c-I.

Table 4.2 Grid parameters of structured grid and hybrid grid for circular cylinder

Grid Type	Grid Type-Case number	Number of cells (M)	Expansion Ratio	x^+	y^+	z^+
Structured	c-I	2.5	1.05	140	1	140
Hybrid	c-II	Hexa: 1.37 Poly: 0.39	1.05	140	1	140

Figure 4.6 shows the drag coefficient C_d and lift coefficient C_l obtained in case c-I, plotted against a non-dimensional time $t^* = tU_\infty/D$ (i.e. $t^* = 1$ corresponds to the time taken for the flow to pass the diameter of the cylinder). C_d and C_l are defined as follows:

$$C_d = \frac{F_{drag}}{\frac{1}{2}\rho U_\infty^2 A} \tag{4.6}$$

$$C_l = \frac{F_{lift}}{\frac{1}{2}\rho U_\infty^2 A} \tag{4.7}$$

where F_{drag} is the drag force of the cylinder, F_{lift} is the lift force of the cylinder; ρ is air density, 1.225 kg/m^3. U_∞ is the free stream velocity and A is the frontal area of the cylinder.

Before sampling the flow parameters, the statistical steady state is achieved after an initial transient calculation with a time scale of about *t** = 360. The value of *Re* in this simulation is in the subcritical region, and the regular vortex shedding from the cylinder generates oscillating lift and drag forces (Liu 2017). In addition, the magnitude of the lift force fluctuations is clearly higher than that of drag force, which makes it more influential on the aerodynamic noise when the cylinder is regarded as a compact source.

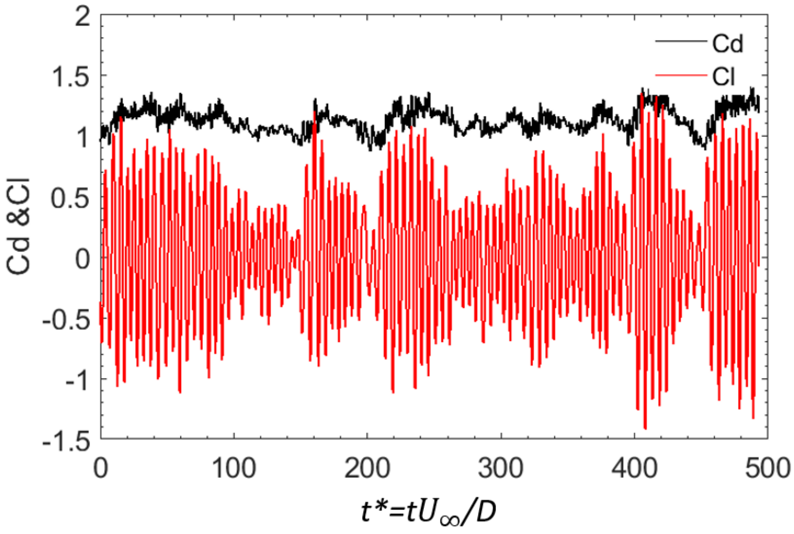

Figure 4.6 Force coefficients for case c-I, after the initial transient of t*=360

The power spectral densities (PSDs) of the lift force coefficient for case c-I and case c-II are presented in Figure 4.7 and plotted against Strouhal number, *St*, which is defined as,

$$St = \frac{fD}{U_\infty} \tag{4.8}$$

where *f* is the frequency, *D* is the component characteristic length and U_∞ is the freestream velocity. The calculations are based on a signal of length 0.75 s, corresponding 450 passage times of the cylinder diameter. The calculation is based on Welch's method with a Hanning window. The width of the window is about 0.25 s; five segments with 50% overlap are used. The frequency resolution is 4 Hz, corresponding to ΔSt= 0.0067. The vortex shedding frequency at $St = 0.2$ and its harmonic at $St = 0.6$ are captured by both types of grid, which has good agreement with the numerical simulation from Liu (2017) . The main fluctuation energy is focused near the main vortex shedding frequency, as the distribution of the dynamic energy in the flow is always closely related to a certain physical process. The vortex shedding produced by the Kelvin-Helmholtz type instabilities on detached shear layer is an important cause of the generation of dipole noise and the mode of its interaction with the solid surface determines the characteristics of the noise spectra and the noise source distribution (Lockard et al. 2007; Liu et al. 2019)

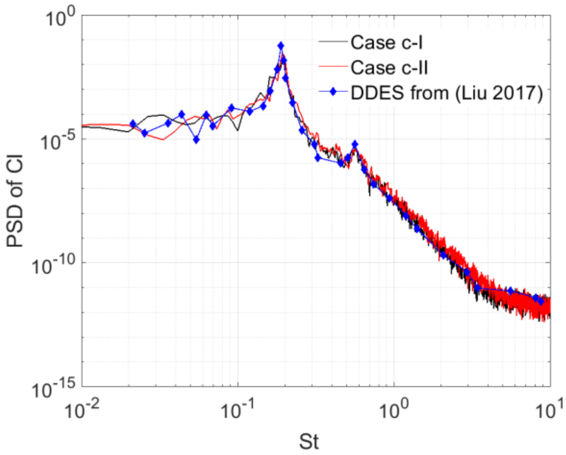

Figure 4.7 The comparison of power spectral density of C_l, comparison of case c-I , c-II and numerical result from Liu (2017)

A comparison is given in Table 4.3 between various important parameters obtained in the current numerical results and published experimental and numerical data. θ_{SEP} is the angle of the separation point, where the friction coefficient C_f becomes zero. The friction coefficient is defined as

$$C_f = \frac{\tau_w}{0.5\rho U_\infty^2} \tag{4.9}$$

where τ_w is wall shear stress, which defined as,

$$\tau_w = \mu \left(\frac{\partial u}{\partial y}\right)_{y=0} \tag{4.10}$$

where μ is the dynamic viscosity, u is the flow velocity parallel to the wall.

The definition of θ is the same as used by Liu (2017), in which θ is zero at the front stagnation point and 180° at the rear stagnation point. The mean drag coefficient C_d and the Strouhal number of the peak St of cases c-I and c-II are the same, and the root mean square (rms) value of C_l and the separation angle θ_{SEP} are also close, which indicates that the hybrid grid system performs as well as the structured one.

Table 4.3 Comparison of results of case c-I and c-II at Re = 10^5.

Grid Type	Case	C_d	$C_{l,rms}$	St	θ_{SEP} (°)
Structured	c-I	1.17	0.53	0.19	82.0
Hybrid	c-II	1.17	0.56	0.19	82.5
Exp.	Schewe (1983)	1.21	0.29	0.20	-
Exp.	Norberg (2001)	-	0.51	0.19	-
Num.	Liu (2017)	1.23	0.73	0.19	84.0

Figure 4.8 shows the distribution around the cylinder of the time-averaged pressure coefficient C_p which is defined as:

$$C_p = \frac{\bar{p} - p_\infty}{\frac{1}{2}\rho U_\infty^2} \tag{4.11}$$

where $\bar{p}$ is the time-averaged pressure on the surface, $p_\infty = 0$ is the reference pressure, ρ is a constant of the air density and U_∞ is the free stream velocity. These results are compared with experimental data from Weidman (1968) and LES simulation results from Cheng et al. (2017).

The value of C_p from Cheng et al. (2017) is equal to 1 at the stagnation point. However, the current calculated values are all slightly higher. This is probably caused by an insufficient distance between the inlet surface and the cylinder (Breuer 1998; Cheng et al. 2017). The lowest pressure values calculated by case c-I and c-II are both close to the experimental data as shown in Figure 4.8. After the inflection point, the pressure starts to increase, but the ranges of the calculated adverse pressure gradients are all longer than the experimental results from Weidman (1968) and the simulation of Cheng et al. (2017). In addition, the mean pressure values at the rear of the cylinder are higher than the experimental data. The reason for these differences may due to the limitation of the turbulence models which makes it very difficult to capture the correct transition position which in turn affects the variables in the wake region.

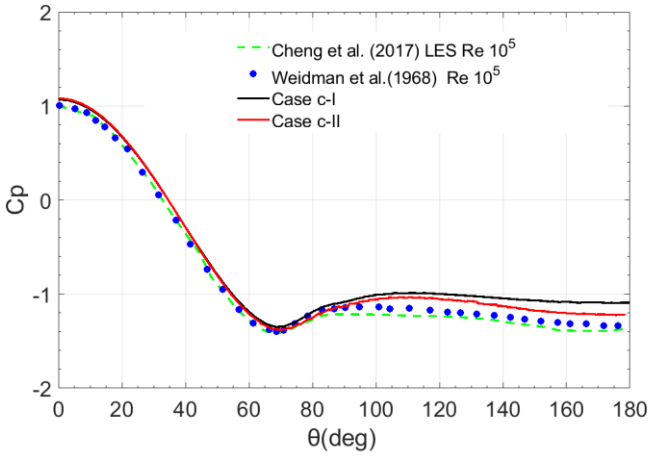

Figure 4.8 The distribution of mean pressure coefficient along the cylinder surface: simulation results and experimental data (Weidman 1968; Cheng et al. 2017).

In order to assess the pressure fluctuation on the cylinder surface, the rms pressure coefficient $C_{p_{rms}}$ is investigated:

$$C_{p_{rms}} = \frac{p_{rms}}{\frac{1}{2}\rho U_{\infty}^{2}} \tag{4.12}$$

where p_{rms} is the rms value of the pressure. Figure 4.9 shows the distribution of $C_{p_{rms}}$ on the cylinder surface, which is compared with experimental results from (West and Apelt 1993; Norberg 2003). The simulation results are similar to the experimental data. The position of the first peaks is close to the separation points as listed in Table 4.3, where the value of C_f is zero. The second peaks are close to the bubble positions, as shown in Figure 4.10, where the C_f is also zero according to the simulation from (Travin et al. 2000; Liu 2017). It should be noticed that in the simulations the second peaks are not as significant as in the experimental data. The reason may also be due to the limitation of the turbulence models. The pressure fluctuation value of the second peak is induced by the counter-rotating vortex formed by the reattachment of the detached turbulent flow, which cannot be precisely predicted by the adopted turbulence models, and is under predicted (Liu 2017).

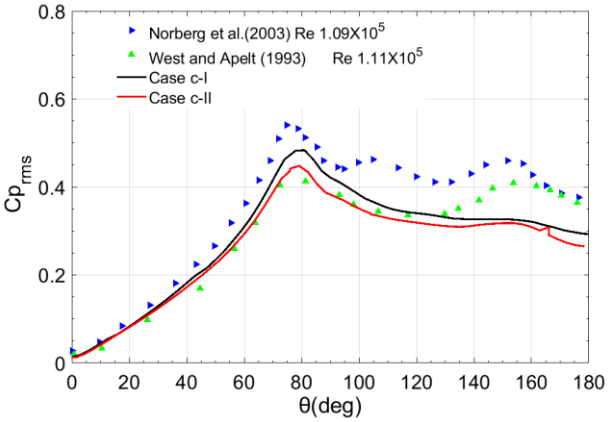

Figure 4.9 The distribution of $C_{p_{rms}}$ around the cylinder surface: simulation results and experimental data (West and Apelt 1993; Norberg 2003)

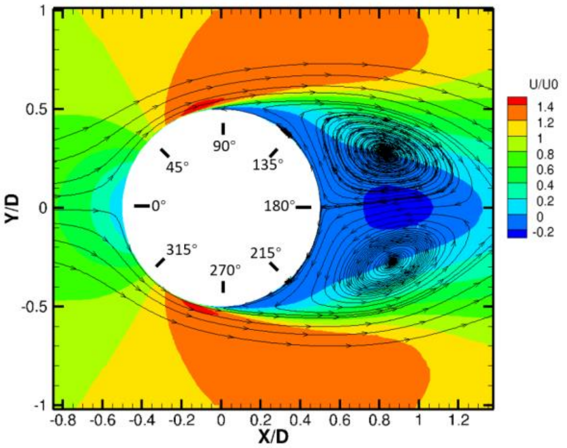

Figure 4.10 Time-averaged streamwise velocity contours together with mean streamlines, *D* is the diameter of the circular cylinder

4.1.4 Results of square cylinder flow

Square and rectangular shapes are typical cross-sections of the components of the bogie used in the simulation, such as the motor, the bogie frame, and the simplified endplates of dampers, see Figure 1.1 and Appendix A. Compared with the circular cylinder flow, the square cylinder flow is more independent of the Reynolds number because the separation point is fixed at the corner. In this section, simulations for a square cylinder are studied to compare the simulations of the hybrid grid and the structured grid.

As in the simulations of circular cylinders, DDES with the S-A turbulence model is used in this work. The height of the first boundary layer mesh should guarantee $y^+ \leq 1$ to resolve the flow within the boundary layer. Since the separation point is stable at the front leading edge of the square cylinder, the grid resolution in the spanwise direction can be coarser than that used for circular cylinder flow simulation. Table 4.4 lists the grid parameters used for the structured grid case s-I and hybrid grid case s-II. Liu (2017) studied the influence of different resolution in the spanwise direction and pointed out that z^+=550 is adequate. The grid resolution of case s-I follows the results from Liu (2017). The grid parameters of the structured part of the mesh in case s-II are the same as case s-I. When generating the tetrahedral volume mesh, a refinement box, with a maximum size of twice the mesh size of the structured grid on the interface, is set near the square cylinder. After converting to the tetrahedral mesh to the polyhedral mesh, the total number of cells in case s-II is about 1.47 million, which is 30% less than the purely structured grid case s-I.

Table 4.4 The grid parameters used for DDES simulations of square cylinder.

Grid Type	Grid Type-Case number	Number of cells (M)	Expansion Ratio	x^+	y^+	z^+
Structured	s-I	2.2	1.05	180	1	550
Hybrid	s-II	Hexa: 1.12 Poly: 0.35	1.05	180	1	550

A summary of the simulation results is listed in Table 4.5 and compared with experimental results, from Vickery (1966) and Norberg (1993), and DDES results from (Liu 2017). The force data used to determine the average is obtained from 0.3 s to 0.7 s; its length corresponds to 290 times the flow-through time for the cylinder width. The simulation results of cases s-I and s-II are similar, which demonstrates that the hybrid grid also has a good performance in the simulation of the square cylinder flow. Compared with the experimental data, there is a significant derivation between the current results for the force coefficients and the published ones. The simulated results from Liu (2017) considered round chamfered corners (with a radius of 0.5 mm) on the cylinder and set a very fine grid near the corners. This overcomes problems with high skewness of the cells close to the corners and may be the reason that these results are closer to the experimental data. To confirm this, a hybrid grid case with rounded corner is calculated. It can be noted that the results are closer to the experimental data and numerical results from Liu (2017) than the other two cases with sharp corners. However, in the subsequent simulations of the bogie components, round corners will not be considered because it will make the grid generation much more difficult.

Table 4.5 Summary of flow parameters of square cylinder cases.

Grid Type-Case number.	C_d	$C_{d,rms}$	$C_{l,rms}$	St
s-I	2.39	0.238	1.48	0.130
s-II	2.38	0.195	1.47	0.130
Round corner	2.06	0.199	1.39	0.128
Vickery (1966)	2.05	0.170	1.30	0.120
Norberg (1993)	2.10	-	-	0.130
Liu (2017)(DDES)	2.08	0.210	1.38	0.129

Figure 4.11 shows the PSDs of the lift coefficient for case s-I, case s-II and a summary of the numerical result from (Liu 2017). Good agreement is found: the spectra shapes are similar, and the differences between the peak values and peak frequencies are both smaller than 5%. As for the circular cylinder, the calculation is based on Welch's method with a Hanning window. The width of the window is about 0.2 s, giving a frequency resolution of 5 Hz, corresponding to ΔSt= 0.0068; three segments are used with 50% overlap. The primary vortex shedding frequency at $St = 0.13$ and its harmonic at 0.39 are captured by both types of grid.

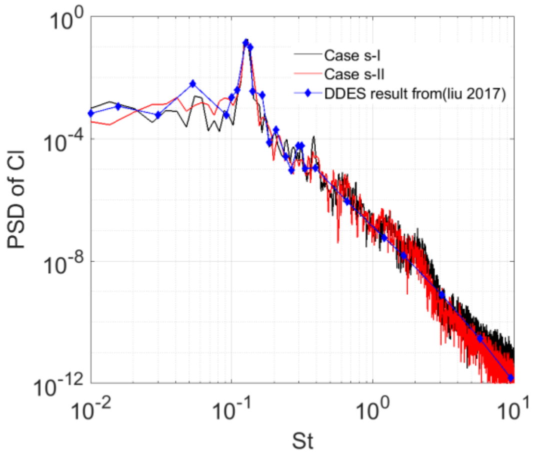

Figure 4.11 PSD of C_l of cases s-I , case s-II and DDES result from (Liu 2017)

Figure 4.12 and Figure 4.13 show the time-averaged and rms values of the pressure coefficient C_p on the cylinder surface. The simulation results are close to the experimental data of Vickery (1966) except for the values at the cylinder corners. The jump in the time-averaged value of pressure coefficient can be eased by using a round chamfer at the cylinder corner (Liu 2017).

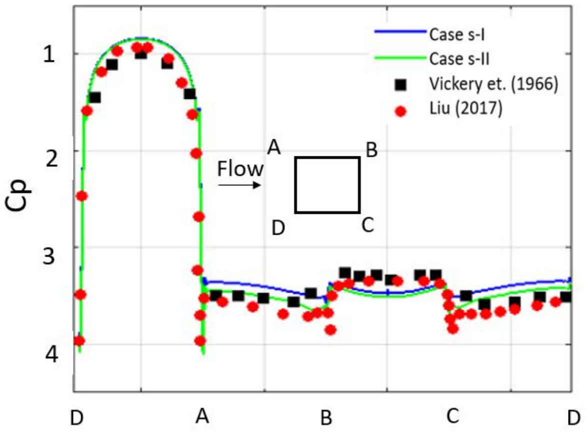

Figure 4.12 The distribution of C_p around the square cylinder surface: simulation results and experimental data (Vickery 1966; Liu 2017).

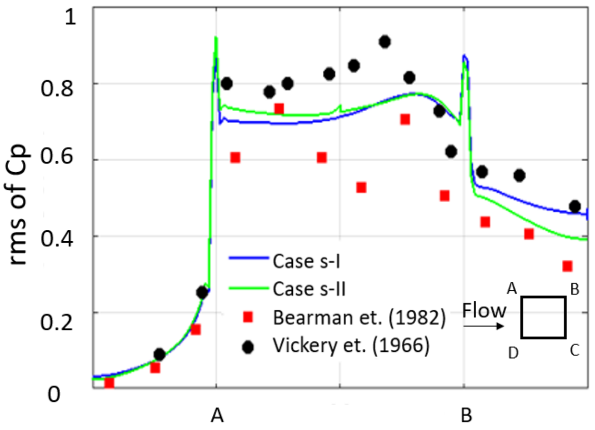

Figure 4.13 The distribution of rms value of C_p around the cylinder surface: simulation results and experimental data (Vickery 1966; Bearman and Obasaju 1982).

The sampled time-varying pressure data on the cylinder surface is used as the input to the FW-H equation to calculate the far-field noise. The far-field receivers are located in the mid-span of the cylinder, which is parallel to the incoming flow direction, and distributed at a radial distance R = 5 m from the cylinder axis. Figure 4.14 shows the one-third octave band noise spectra and directivity of overall sound pressure level (OASPL) calculated for the case s-II (polyhedral grid). These results are compared with the simulation and experimental data from (Liu 2017), which is scaled to the receivers with radius of 5 m. The noise spectra in Figure 4.14(a) are for a receiver in the direction normal to the flow, i.e. at $\theta = 90°$. There is a good agreement between the peaks, with the difference between the peak values smaller than 0.5 dB. When the overall level is plotted against angle Figure 4.14(b), the current results can be seen to be slightly higher than the numerical result from (Liu 2017), with a difference of around 1 dB, because of the sharp corner effect, which is also found in the rms comparison of $C_{l,rms}$ in Table 4.5.

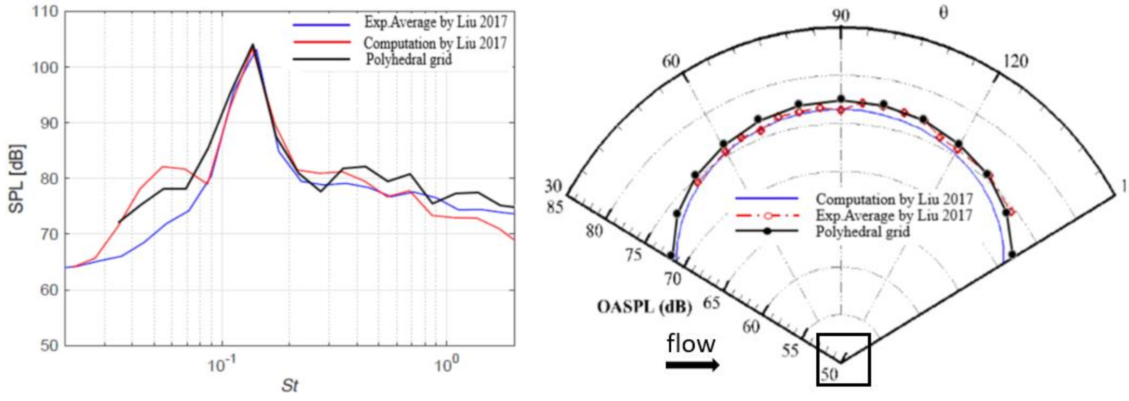

(a) 1/3 octave noise spectra at 90° (b) directivity

Figure 4.14 Comparison of the aerodynamic noise of square cylinder at Re=8.2×10^4.

4.2 Isolated train wheelset

Wheelsets are important in the aerodynamic noise generation of a train bogie because they are not completely shielded by the bogie cavity. The impingement of the flow produces large turbulence intensity and pressure fluctuation on the wheel surface. Therefore, before simulating the whole bogie, the application of the hybrid grid system is tested. The scale of the wheelset model is 1:10. In order to reduce the computational cost, only a half of the wheelset is modelled, and the shape of wheel is idealized to a disc with diameter of 92 mm and thickness of 12.7 mm. The diameter of the axle is 17.5 mm, and the distance from the inner wheel side surface to the mid-span of the axle is 67.7 mm. These parameters are chosen to correspond to the case studied numerically and experimentally by Zhu et al. (2014).

4.2.1 Computational setup

As in the simulations of the cylinders, the isolated wheelset case has also been calculated by DDES. The computational domain is shown in Figure 4.15; the coordinate origin is located at the intersection between axis of the axle and the symmetry plane. The walls around the wheelset, such as the top, bottom, axle mid-plane, and side surface, are set as symmetry boundaries, which have no friction and zero velocity perpendicular to the boundaries. The velocity of the upstream inlet flow is steady with a uniform value of 30 m/s, and the numerical viscosity $\tilde{v}$ is 10^{-4}. Zero gauge pressure is set at the outlet surface.

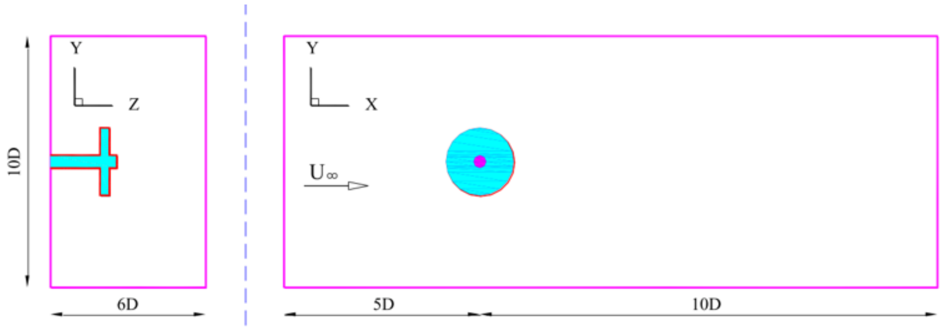

(a) Front view

(b) Side view

Figure 4.15 Sketch of the computational domain used for the isolated wheelset (*D* is the wheel diameter) (Zhu 2015)

The grid is shown in Figure 4.16. The boundary layer grid parameters are listed in Table 4.6 and are similar to those used by Zhu et al. (2014). A slice at the middle span of the wheel is shown in Figure 4.16(b). Two refinement boxes are set around the wheelset to refine the volume mesh. The maximum mesh size in the internal refinement box is 1 mm which is close to the maximum value in the circumferential direction and the value in the external refinement box is about 5 mm. The final number of cells is about 3.2 million, which is less than the 5.5 million used in the structured mesh of Zhu et al. (2014).

Table 4.6 The grid parameters of the wheel

Total number of cells	**Expansion Ratio**	$\triangle x/\triangle y$	$\triangle y\ (mm)$	$\triangle z/\triangle y$
3.2M	1.1	170	0.0064	130

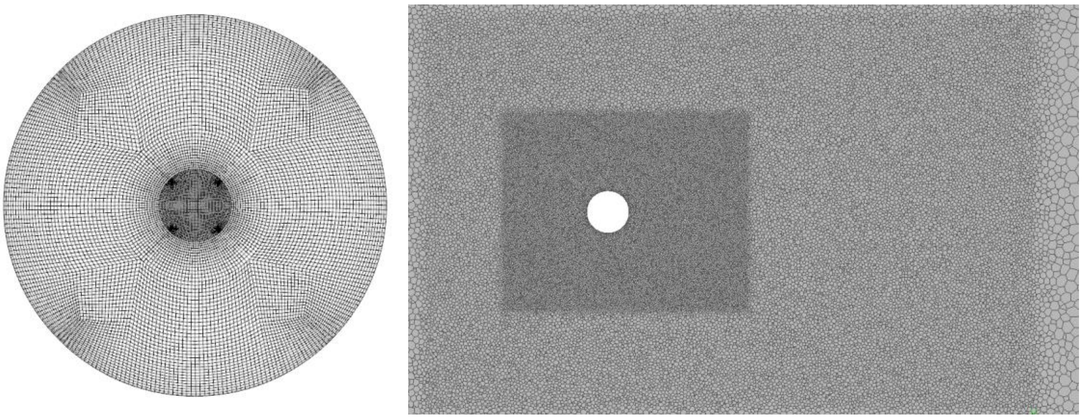

(a) wheel surface grid distribution

(b) volume refinement around the wheel

Figure 4.16 Wheel surface grid and volume slice of computational grid for DDES

In order to reduce the simulation time, steady simulations (RANS) are performed at the beginning and then the results from these are taken as the initial field for the unsteady simulations. In the simulations, a physical time step of 3×10^{-6} s is set, corresponding to a maximum *CFL* smaller than 3.5. The data for the post processing and noise calculation are collected after 0.4 s, with a total collection time of 0.55 s, which is about 180 passage times of the wheel diameter.

4.2.2 Aerodynamic results analysis

The results of the drag and lift force coefficients C_d , $C_{d_{,rms}}$, and $C_{l_{,rms}}$ are shown in Table 4.7. The value of C_d has about 3.3% difference with the one from Zhu et al. (2014). However, the rms values have greater differences than the mean value because they are more sensitive to the numerical parameters. This is especially true for $C_{d_{,rms}}$, which has values that are much smaller than $C_{l_{,rms}}$, and differs from the one from Zhu et al. (2014) by 50.3%.

The PSDs of the lift and drag force coefficients are presented in Figure 4.17 and plotted against the Strouhal number based on the diameter of the axle and the free stream velocity. The calculation of the PSD is based on Welch's method with a Hanning window. The width of the window is 0.125 s corresponding a frequency resolution of 8 Hz. Seven segments with an overlap of 50% are used. A large peak is apparent in the lift coefficient at *St* = 0.182, which is the same as the result from Zhu et al. (2014).

Table 4.7 Drag and lift force coefficients of isolated wheelset

Parameters	C_d	$C_{d,rms}$	$C_{l,rms}$
Simulated	0.966	0.0574	0.303
Zhu et al (2014)	0.935	0.0382	0.263

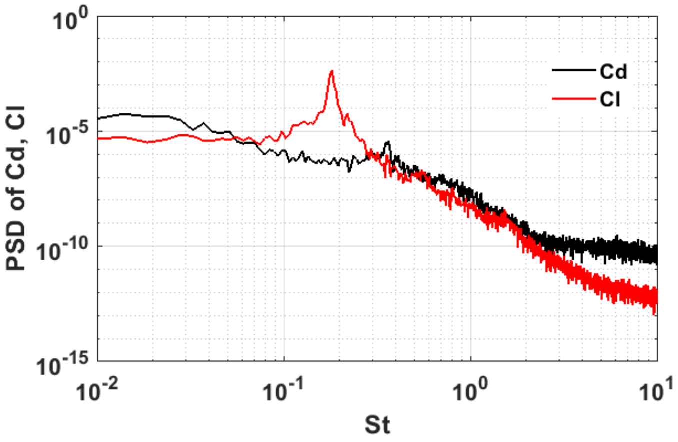

Figure 4.17 PSDs of lift and drag coefficients of the wheelset

Figure 4.18 visualizes the turbulence structures of the wheelset wake by plotting the iso-surfaces of the normalized Q criterion ($Q/[(U_0/D)^2]$, where Q is the second invariant of the velocity gradient tensor, U_0 is the freestream velocity and *D* is the wheel diameter) and they are coloured by the normalised velocity magnitude (U/U_0). The value of normalized Q criterion is set to 50 in Figure 4.18. The detailed flow structure of vortex shedding from the wheel axle and the wheel disc is captured by using the hybrid grid.

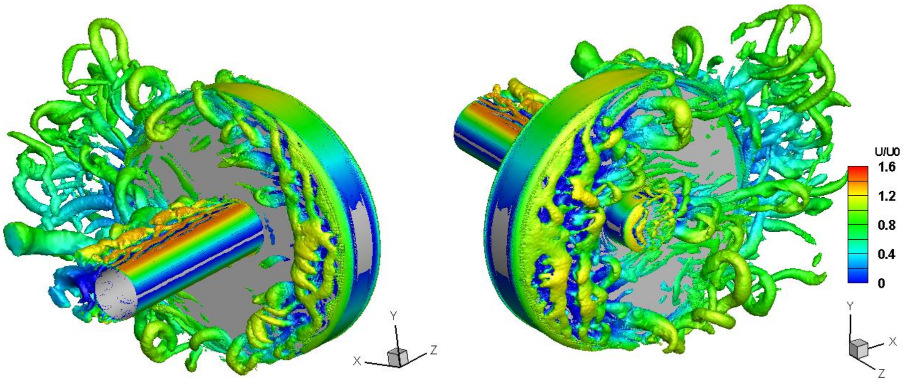

Figure 4.18 Iso-surfaces of the instantaneous normalized Q criterion

To investigate the noise source distribution on the wheelset surface, Equation (3.37) in section 3.2.1 is used to calculate the fluctuation of the pressure change rate $L_{\dot{p}}$, which is shown in Figure 4.19 in decibels. This indicates that the strong pressure fluctuations are mainly located at the rear part of the axle, the wheel side surfaces, and the axle end. The vortex shedding from the axle and the wheel front rim, as shown in Figure 4.18, is the main reason of the noise source generation.

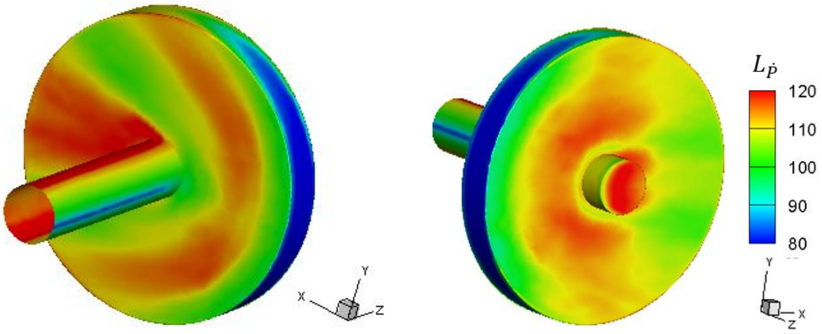

Figure 4.19 The distribution of the pressure fluctuation strength on the wheelset

4.2.3 Aeroacoustic results

Based on the unsteady pressure data on the wheelset surface, the far-field noise has been predicted by using the FW-H equation introduced in section 3.2.1. Since the Mach number based on the free stream velocity in this simulation is about 0.09, the quadrupole noise is not considered and only the dipole source on the wheel surface is calculated. The results are obtained at a top receiver and side receiver, which are located at (-18, 1375, 31.3) and (0, 185, 2211.3), in which the dimensions are in millimetres and the coordinates are as shown in Figure 4.15; more details can be found in Zhu et al. (2014). The pressure data is extracted at every time step and the sampling frequency of the unsteady pressure signal on the wheelset surface is 333 kHz. In the calculation of PSDs, which is based on Welch's method, the signal length is 0.5 s, and seven segments, with overlap of 50%, are used, resulting in a frequency resolution of 8 Hz.

In Figure 4.20, the current simulation results, which are calculated with the hybrid mesh, are compared with the simulated data (based on a structured grid) and experimental data from Zhu et al. (2014). The spectrum shapes are similar and the differences in the peak frequencies are all smaller than 3%. There is a large difference between the results at low frequency at the side receiver because it is affected by the background noise in the wind tunnel. As well as this, there are two further reasons for the deviations between the simulation results and the experimental data at the peaks. One reason is due to approximations introduced in the CFD model; for example, in the experiment, the behaviour of the vortex shedding from the axle differs near the rigid baffle plate, whereas in the simulation it is considered as a symmetry wall and the friction on the solid surface is also not considered. The axle forms a necklace vortex at the mounted end, which supress the regular vortex sheading there, because of the boundary layer on the rigid baffle plate (Okamoto and Yagita 1973; Fröhlich and Rodi 2004). This results in the experimental peak value at the top receiver, as shown in Figure 4.20(a), being smaller than the numerical ones. Another source of error is the free space radiation assumption used in the FW-H equation. The total sound pressure at the receivers is calculated by superposing the noise directly radiated from every element on the wheelset surface using the free space Green's function but the effect of the wheelset surface and the baffle plate on the radiation characteristics is not considered, which is believed to be the reason why the experimental values in Figure 4.20(b) greater than the numerical values in some frequencies.

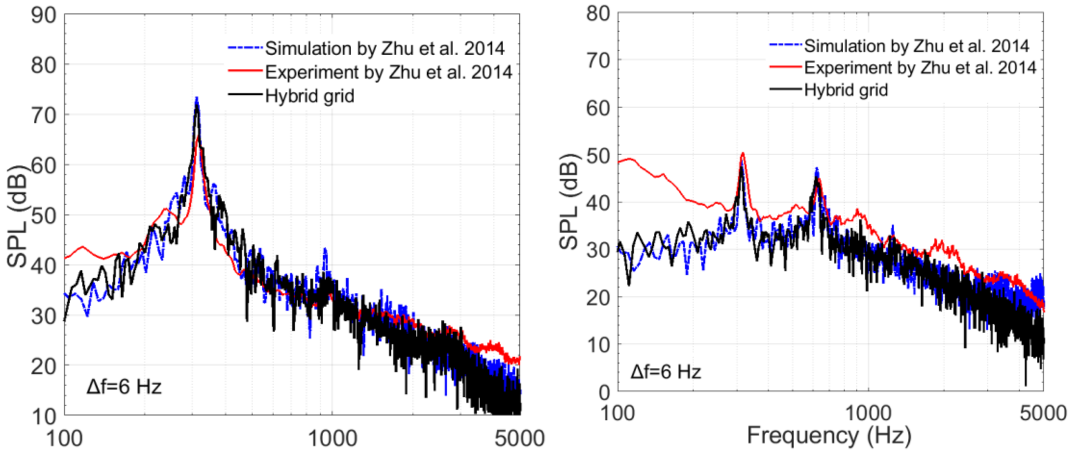

(a) top receiver (b) side receiver

Figure 4.20 Comparisons of the far-field noise spectra of an isolated wheelset between simulations and experiment from Zhu et al. (2014)

4.3 Summary

In this section, three benchmark cases are calculated. First, the concept of the hybrid grid system is tested by a circular and a square cylinder flow. The aerodynamic and aeroacoustic results agree well with the experimental data and the numerical results calculated by a structured grid. In addition, the aerodynamic noise of an isolated wheelset is calculated. The results are compared with the experimental and numerical data from the previous literature (Zhu et al. 2014) and give good agreement in the spectra shape and peak frequency, the difference between the peaks at the top receiver is reasonable. The strength of pressure fluctuations on the wheelset surface are also investigated. The results show that the vortex shedding from the axle and the wheel front rim is the main reason for the noise source generation. Thus, the DDES method, the noise calculation procedure and the generation procedure of the hybrid grid system will be applied in the subsequent simulations. In addition, the aspect ratio used for the three validation cases, as well as the structured grid blocks used for the wheelset, will be applied on the similar components of the bogie in the subsequent simulations.

Chapter 5 Aerodynamic and aeroacoustic simulation of a bogie in a simplified cavity

As reviewed in section 2.2, most previous numerical studies performed to investigate the flow field and aerodynamic noise of the train bogie focus on the general flow field or the influence from some part of the bogie's components. Further work is required to reveal the noise generation mechanism of the bogie with more components and features, but this faces two major obstacles: the first is to discretize a complex computational domain with a grid of high quality; the second is that the computational cost is very high.

In this chapter, the numerical methods which have been validated in Chapter 4 will be applied to investigate the noise generation mechanisms of a motor bogie. A grid generation procedure is developed to generate hybrid grids on models with different bogie geometry. Scaled models are used to limit the computational cost and the use of different grid densities for different bogie components is also explored. CFD simulations are performed to calculate the flow field around the bogie and to obtain the time-varying surface pressure signals of the bogie and the cavity. These simulations are conducted using the open source software package OpenFOAM 2.4.0. The Delayed Detached Eddy Simulation (DDES) method with Spalart–Allmaras (S-A) turbulence model is used. In the second step, the surface pressure data is used as the input for the Ffowcs Williams and Hawkings (FW-H) equations within ANSYS Fluent to calculate the far field noise.

5.1 Computational domain and meshing strategy

5.1.1 Computational domain and numerical setup

In reality, trains run on the tracks through air that is initially stationary relative to the ground. However, for the convenience of the CFD calculations, the train coordinates are chosen, in which the train is stationary, while the air and the ground move in the opposite direction to the train running direction. To simplify the computational model, in this chapter the effect from the train nose and the cowcatcher on the incoming flow is not considered and the rear car bodies are also neglected.

To limit the computational cost, the running speed of the train is taken as 10 m/s and the bogie model is considered at 1:12 scale, corresponding to a Reynolds number of 2.11×10^5 based on the scaled height of the train (0.316 m) in Chapter 6 or 1.91×10^5 based on the width (0.287 m), which is greater than the minimum Reynolds number (1.53×10^5) tested by Lauterbach et al.

(2012), based on the width (0.12 m) and the speed of the train. According to the review in section 2.1.2, there is only a weak dependence on the Reynolds number of the noise generated at the front bogie as long as its Reynolds number is in the self-similarity region (Lauterbach et al. 2012).

It should be pointed out that in the above scaled-down model, the flow speed and the model size are scaled down by a similar ratio and thereby, for a given Strouhal number, the frequency only changes by a small amount. The length of the bogie is about 2.6 m (between two axels) at full scale which corresponds to the wavelength at 130 Hz, so above 130 Hz it will not be compact at full scale. However, when the model size is reduced, the wavelength of concern remains the same while the size of the noise source is reduced to about 0.2 m, which corresponds to compact wavelength at 1500 Hz. Consequently, the compactness of the noise source is increased in the reduced-scale case. When the noise source is compact, its acoustic radiation is basically spherical and with constant phase across its wave front. The propagation of the acoustic wave is simple because the scattering of the solid boundaries and the effect of the flow field close to the noise source can be ignored. However, when the noise source is non-compact, the phases of the acoustic waves generated by different parts of the source are different, which may cancel or strengthen each other in the radiation field. In addition, the flow behaviour in the near field of the noise source and the mean flow close to the model will affect the propagation of the sound. For sound with same wavelength, its propagation is different when crossing the scaled model and full model. Therefore, in numerical and experimental research, when reducing the size of the noise source, attention should be paid to the ratio between the model size and the wavelength of concern, in case the compactness of the source is changed. In the current study, according to the literature review in Chapter 2, low frequencies are dominant in bogie noise and the noise propagation in the near field will not be considered in the following studies. Thus, the effect of the noise source compactness is considered to be secondary in the current study.

Figure 5.1 depicts the computational domain used for the case of the bogie in a cavity, which is simplified from a CRH train bogie cavity. The inlet section has length of $8D_w$, where D_w is the wheel diameter, 950 mm (full scale). To improve the stability of the simulation, a slip wall with no friction of length 1 D_w is applied on the vehicle after the inlet, which is shown by a dashed line in Figure 5.1, and the remaining length of 7 D_w is used to let the boundary layer to develop. The downstream length and total lateral section width are 7.68 D_w and 11.5 D_w respectively. The distance between the cavity bottom and the ground is about 0.49 D_w. To represent the distance of the wheels above the ground (track slab) when the train is running on the rails, there is a gap of 250 mm (0.33 D_w) between the bottom of the wheels and the ground; the rails are not included in the model.

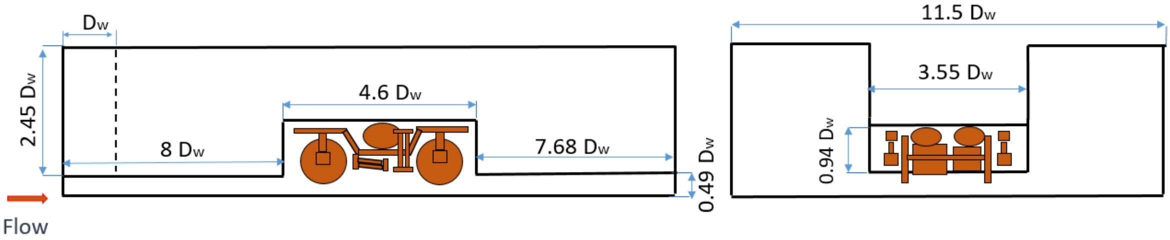

Figure 5.1 Sketch of the computational domain of the bogie in a simplified cavity, *Dw* is the diameter of the wheel (not to scale).

The simulation is started by running a steady RANS model, which is used to initiate the flow for the DDES simulations. Figure 5.2 illustrates the boundary condition settings used for both the steady RANS and DDES simulations. The effect of the ground friction on the flow has not been considered yet, so the boundary condition for the ground is set to free-slip. The side and top surfaces of the domain is set to symmetry walls, where no mass convection happens through the surface. The pressure outlet boundary condition is adopted with the gauge pressure set to zero. To ensure simulation stability and accuracy, the numerical schemes are the same as used in Chapter 4.

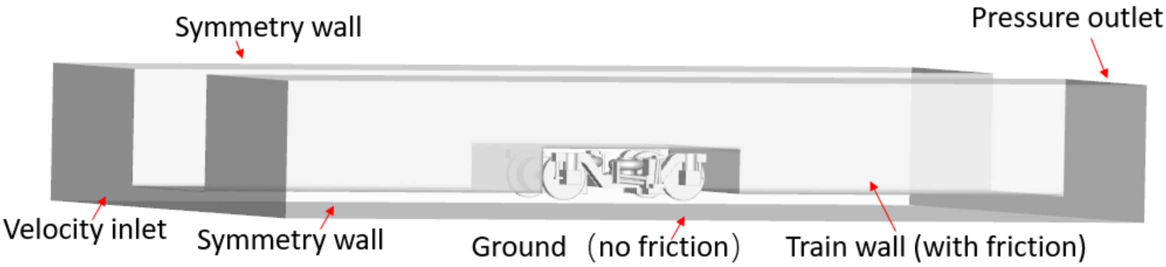

Figure 5.2 The boundary conditions for the computational model

5.1.2 Meshing strategy

Figure 5.3 shows the three-dimensional (3D) model of the bogie, in which all components are retained but with some small features simplified. The wheels are simplified to a disc, the flange and the smaller thickness in the wheel web region are neglected. Similar simplifications have been applied to the axles, motors and gear boxes, and the endplates of the side dampers. Some components below the bolster beam, such as the two lateral dampers and the traction block, are converted to a single block considering its blockage ratio. The components are indicated in Appendix A.

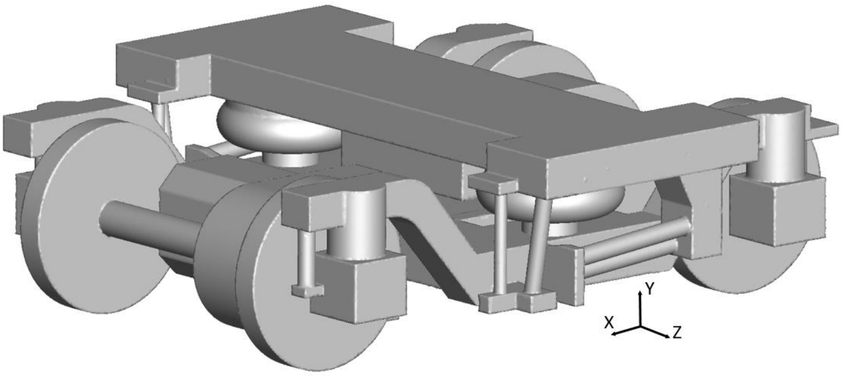

Figure 5.3 The 3D model of the bogie

Despite the above simplifications made to the bogie, the complexity of its geometry still makes the mesh generation extremely difficult. Generating a fully-structured mesh would cost much time while it would also be difficult to control the boundary layer mesh quality by using a fully-unstructured mesh generation strategy. Therefore, the hybrid mesh generation procedure presented in Figure 4.3 will be used. The hybrid mesh consists of structured hexahedral grids around the components, connected to tetrahedral unstructured grids, which are then converted to polyhedral grids.

When generating the hexahedral grid, the bogie is divided into five independent parts, as shown in Figure 5.4, according to their geometric characteristics. In order to generate structured grid, some blocks are built around the bogie surface by using ANSYS ICEM 19.1. The mesh resolution is defined by specifying the number of the grid nodes on every edge of the blocks. The most important criteria for the quality of the structured mesh are the orthogonality and skewness of the cells. Since the hexahedral mesh is generated in the blocks, by adjusting the position of the block nodes, the mesh quality can be improved manually.

The surface grid density of these five parts is specified to different values according to the local flow speed, which is estimated in the iteration of the grid dependence study. As a result, the grid density near the joints of the different parts will differ from each other. For example, the grid size on the frame surface, as shown in Figure 5.4(c), is greater than that on the dampers in Figure 5.4(d), which is refined because they have small components and immerse in the shear flow from upstream. A transition section of unstructured grid, as shown in Figure 5.5, is used to connect the two parts with different grid densities. By specifying the same height of the first boundary layer mesh and the expansion ratio, its grid distribution in the surface normal direction can be identical with the structured grids to be connected.

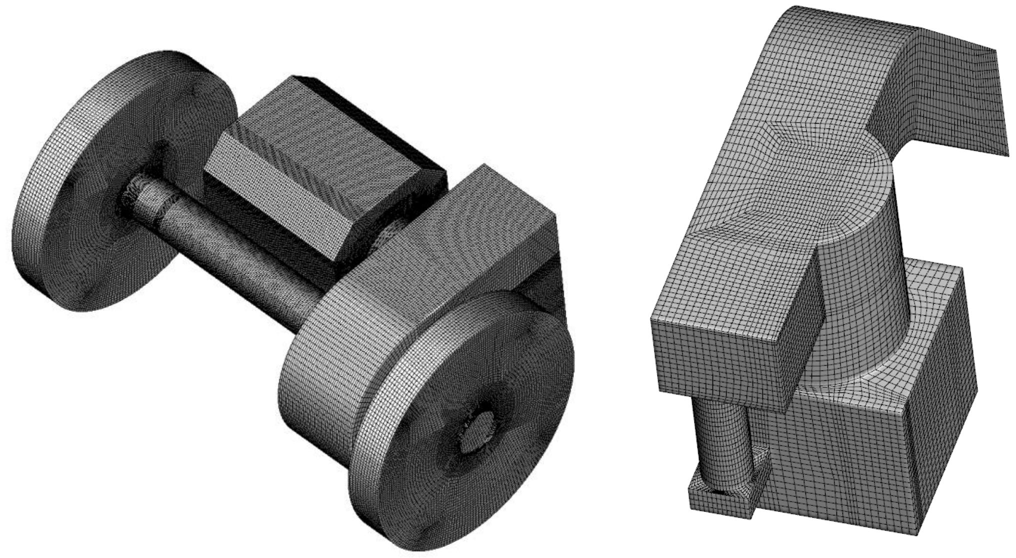

(a) wheelset (b) axle box

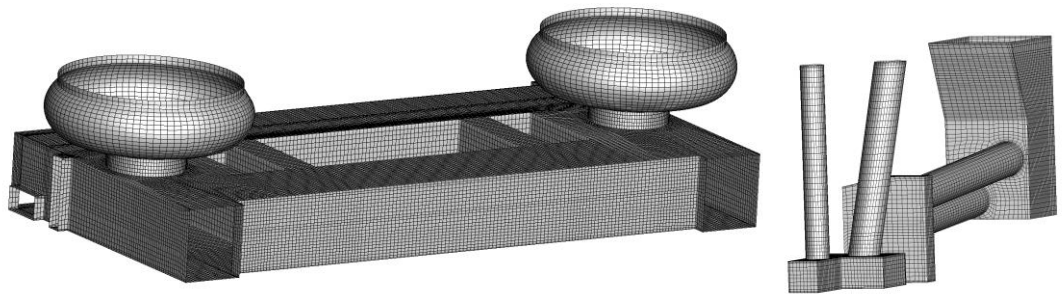

(c) frame components (d) side yaw dampers

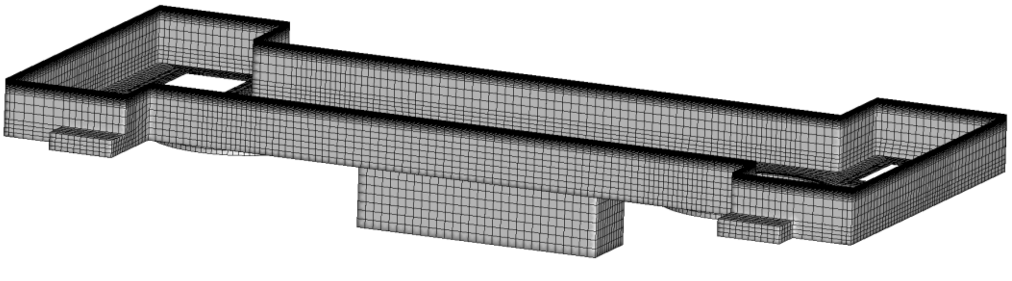

(e) bogie bolster beam

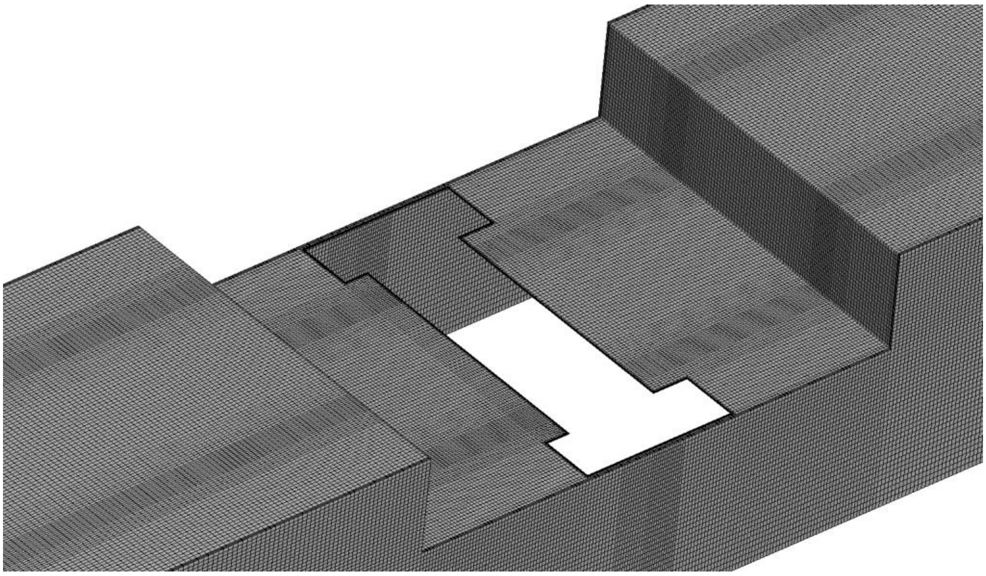

(f) bogie cavity

Figure 5.4 Surface mesh distribution of model components

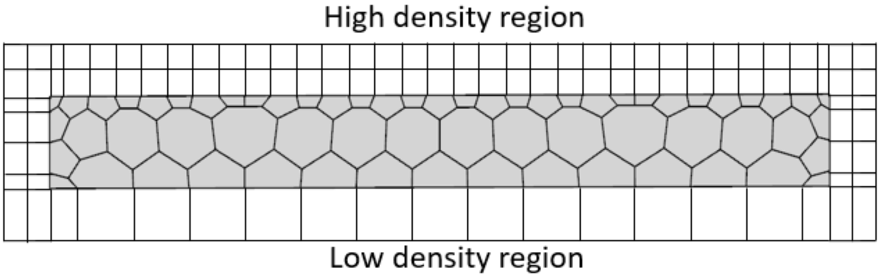

Figure 5.5 The joint surface mesh

Figure 5.6 shows the surface grid distribution of the complete bogie, which is assembled from the five independent parts shown in Figure 5.4.

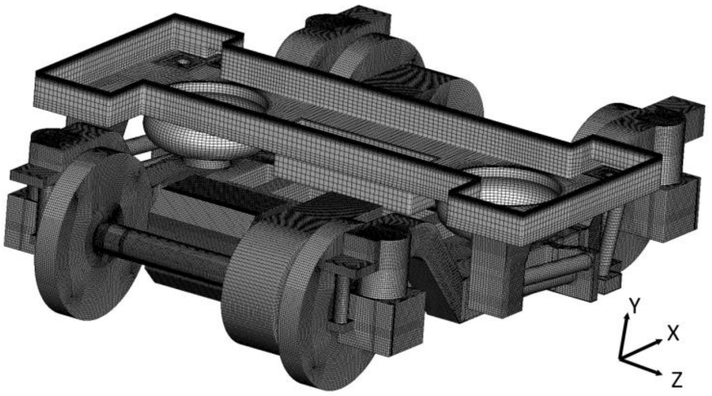

Figure 5.6 The grid distribution on the bogie surface

After generating the hexahedral grid, the remaining volume of the computational domain is filled by a tetrahedral grid. In order to improve the tetrahedral grid quality near the interface to the hexahedral grid, the grid density specified at the interface should be slightly greater than that of the structured grid on the interface. The volume grid near the cavity region is refined by adding a refinement box in the model. After connecting the tetrahedral grid with the hexahedral grid, the tetrahedral one is converted to polyhedral grid, which halved the number of the unstructured grid and helps to improve grid quality (Peric and Ferguson 2005).

Figure 5.7 shows three slices to illustrate the volume grid. Figure 5.8 shows the grid distribution on the slice Z0 and slice Y0. The grid has the highest density near the solid surfaces to get a high resolution in the boundary layer. A coarser structured grid is created between the boundary layer grid and the unstructured volume grid. In this way, not only can the grid quality near the boundary layer be improved, but also the flow near the boundary layer, which usually has a large velocity gradient, can be properly resolved without some negative effect from the transition of the grid type. The volume grid, as shown in Figure 5.8(b), shows that the grid density around the bogie is greater, as expected, than that in other areas.

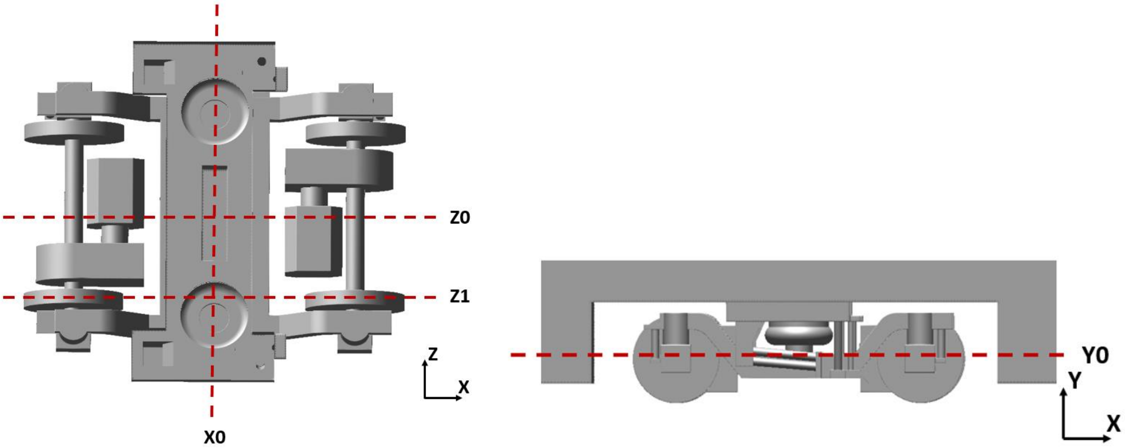

(a) lateral slice position (b) vertical slice position

Figure 5.7 The position illustration of the slices

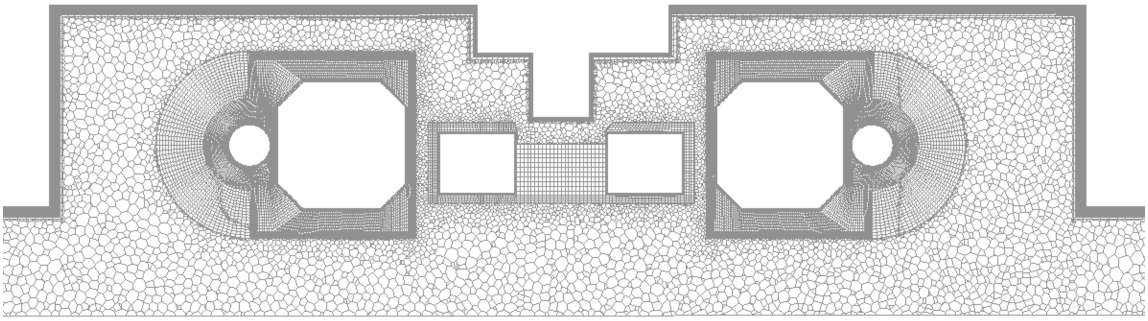

(a) slice of Z0

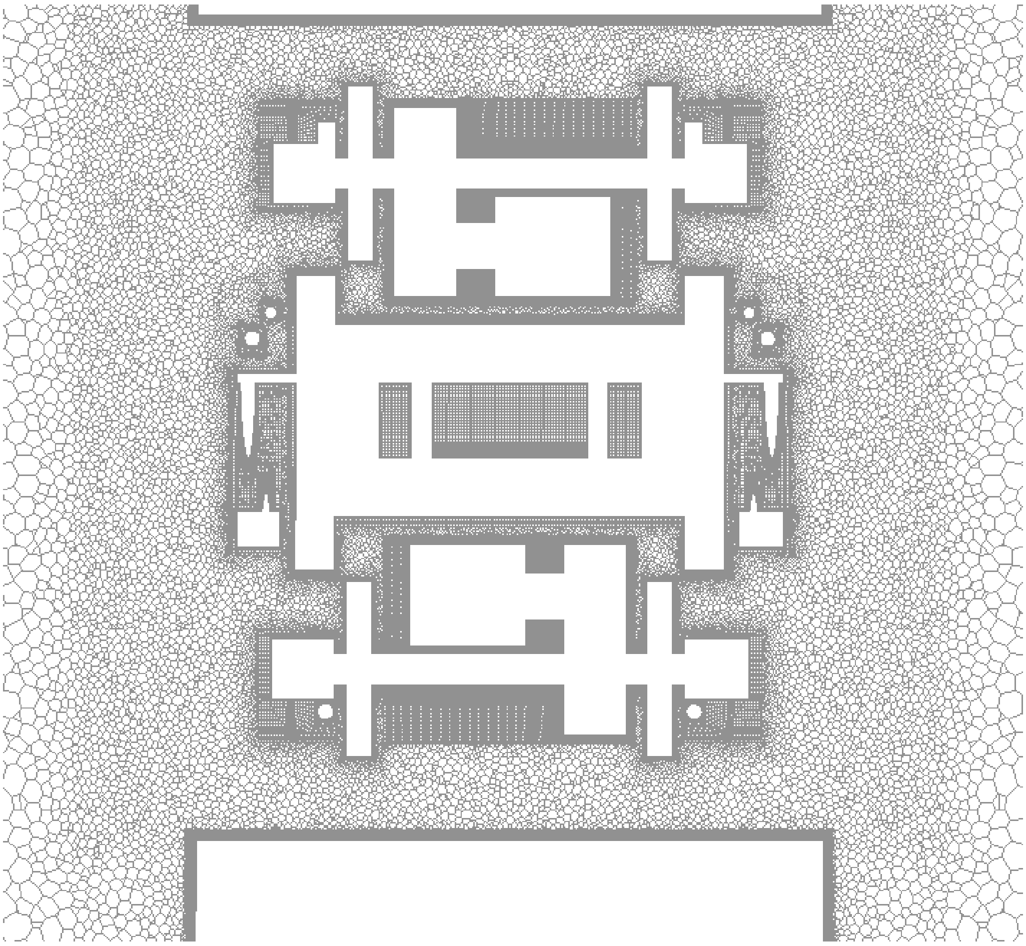

(b) slice of Y0

Figure 5.8 Mesh distribution on the slices

5.2 Grid and time step dependency study

Adequate grid density, especially for the grid in the boundary layer, and small enough time step are critical to obtain accurate aerodynamic results in CFD simulations. However, a finer grid and smaller time step usually means higher computational cost. Therefore, a good CFD simulation always requires a compromise between the simulation accuracy, which satisfies the simulation aims, and the computational cost which should be affordable. In this section, to choose an appropriate grid density and time step for the following simulation cases, the dependence on these parameters will be discussed.

5.2.1 Computational domain

In the present study, as shown in Figure 5.9, in order to reduce the complexity of the model, the bogie is simplified compared with the full model in Figure 5.3. The bolster, motors and gearboxes are removed. The end plates of the side dampers are simplified to independent plates. These simplifications make the bogie disconnected from the cavity, and consequently, their surface grid distributions could be specified independently. It is worth pointing out that, in reality, the simplified small features can generate small-scale vortices, which can contribute to the noise at high frequencies. However, this omitted sound energy from high frequencies should have minimum impact on the overall sound levels as the noise contribution from low frequencies is dominant for the bogie (Lauterbach et al. 2012; Latorre Iglesias et al. 2017; Zhu et al. 2018).

After the simplifications, the bogie model shown in Figure 5.9 is symmetric in the Z direction, allowing a half-width model to be used for steady simulations. The boundary conditions for the half-width model are the same with those in Figure 5.2 except for the middle plane, which is specified to be a symmetry boundary condition. For unsteady simulations, the velocity fluctuations in the normal direction of the symmetry plane will be neglected.

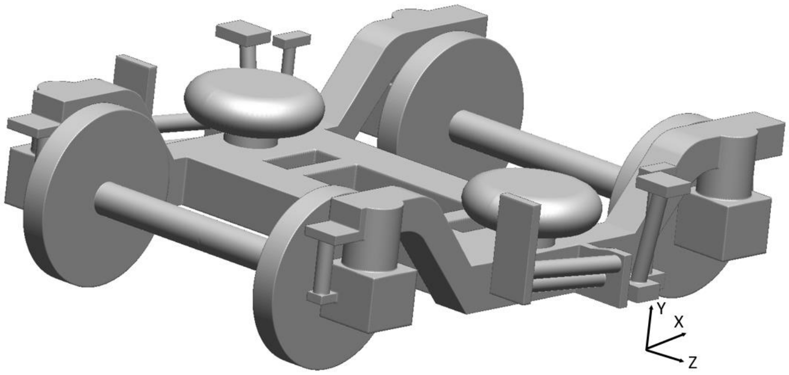

Figure 5.9 The 3D model of the simplified bogie without motors and gearboxes

5.2.2 Grid and time step parameters

For the purpose of grid sensitivity study, the two types of grid in the hybrid grid system, i.e. hexahedral and polyhedral, are refined by different strategies. Table 5.1 lists the grid information of four cases considered for the grid sensitivity study. The aspect ratio is defined as the ratio of the greatest side length of the first cell to its height, Δy. In the boundary layer region, the first cell height from the wall and the expansion ratio of 1.1 are kept constant and the grid sizes in the other two directions are refined. Figure 5.10 shows the contours of the y^+ value on the solid surface of case Medium1, which is also similar for other cases. As the S-A turbulence model is used in the simulation, the y^+ value is limited to be smaller than 1 on all solid walls of the four cases. For the cases Medium1 and Medium2, the maximum aspect ratios on all bogie components are less than 140, which has been shown to be sufficient in the circular cylinder simulation in Chapter 4. To test if the aspect ratio of the cavity grids is adequate, case Medium2 is created by changing only the cavity grid size compared with case Medium1. As intensive turbulent flow is expected in the region near the bogie, three refinement boxes, as shown in Figure 5.11, are used to increase the volume grid resolution when generating the tetrahedral grid. Refinement box1, the cell size of which is greater than Refinement box2, is used to refine the whole bogie region, while each Refinement box 2 is used to refine the area near the wheels. The grid sizes of the structured grid are changed by the ratio of 1.4 and those in the boxes are refined by the ratio of 1.35, which results in the total number of cells changing by a ratio of 2 between the fine, Medium1 and coarse cases. After connecting the tetrahedral mesh with the hexahedral mesh, the tetrahedral one is converted to polyhedral mesh and its number of cells is halved.

Table 5.1 Summary of the grid information

Components	Parts	Fine	Medium1	Medium2	Coarse
		Max aspect ratio			
Drive system	Wheelset	56	80		112
Bearing component	Axle box	48	65		90
	Front damper	80	110		150
Frame component	Frame	90	125		180
	Air springs	55	80		112
Side dampers	Vertical damper	80	112		160
	Lateral damper	90	128		176
Cavity		105	148	200	210
Refinement box 1 (1/12 scaled, mm)		2.5	3.43	3.43	4.7
Refinement box 2 (1/12 scaled, mm)		2.0	2.74	2.74	3.75
Expansion ratio		1.1			
Total number of cells (million)		18.1	9.6	8.1	4.8
CFL		<5			

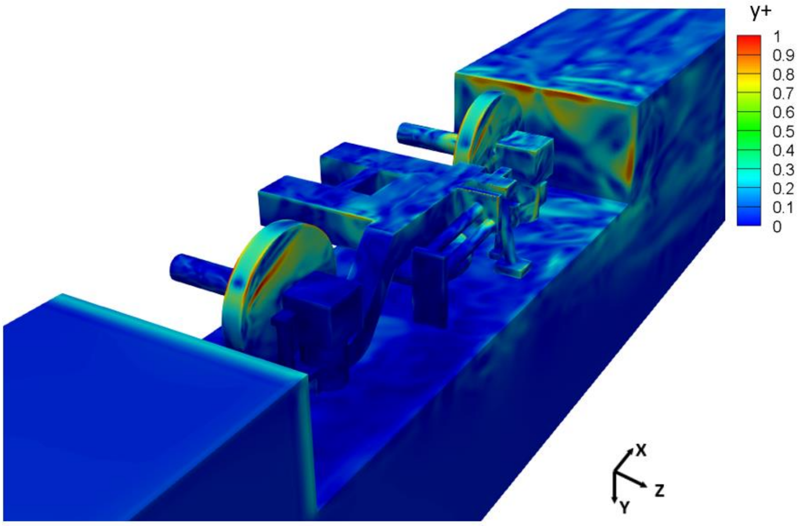

Figure 5.10 The distribution of the y^+ value on the surface of the model for case Medium1

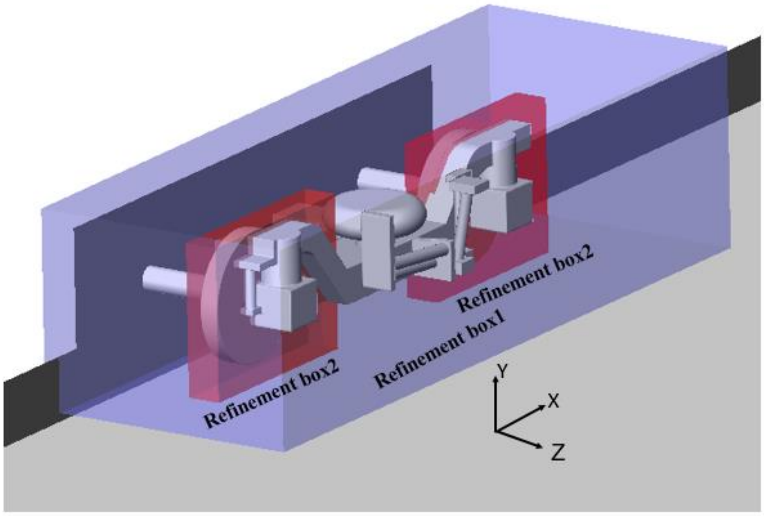

Figure 5.11 The refinement boxes in the bogie model

In order to minimize the influence of the time step size, all four cases are performed with the maximum value of *CFL* smaller than 5. After the grid size study, the chosen case will be used to evaluate the effect of the time step.

The maximum *CFL* value can be reduced by choosing a smaller time step, but the computational cost will undoubtedly be increased. In the simulations, it is found that the maximum *CFL* is produced by the polyhedral grid near the interface, which is located at the joint of the wheel and its axle. It is not feasible to increase the grid size any more. Therefore, the time step size of the simulation is limited by the grid. Although there is no hard requirement on the maximum value of *CFL* because the implicit time scheme and PIMPLE authorism are used, it is still necessary to assess the effect of using different maximum *CFL* values. Thus, four cases (CFL2.5, CFL3.5, CFL5, and CFL7) based on case Medium1 with different maximum *CFL* values are calculated. The physical time step size for case CFL5 is around 2×10^{-5} s and it changes by the ratio of 1.4 in the other three cases.

5.2.3 Influence of grid size

Before performing the unsteady simulation by DDES, a RANS simulation is carried out to initialize the flow field of each model. The force coefficients of the model are recorded during the subsequent DDES simulations. Figure 5.12 shows the time history of the drag force coefficient C_d and lift force coefficient C_l of the case Medium1, which are defined by the equation (4.6) and (4.7). The force is sum of the one of cavity and the one of bogie, the reference area is the cross-section area of the car body.

The simulation is run for 120 non-dimensional time units ($t^*=tU_\infty/L$) based on the cavity length *L* and freestream velocity U_∞. The data sampling begins from t^*=15.

In order to judge if the simulation has achieved the state of statistical convergence, the whole data sampling segment is divided into three parts with part having 50% overlap with its adjacent one. Table 5.2 summarizes the statistical results of the drag and lift coefficients from the three overlapping time windows. It is shown that the differences of rms and mean values calculated from the three segments are within 5% compared with those calculated from the whole segment. The similar comparisons are also carried out for the force coefficient of the bogie and the cavity. Therefore, it can be concluded that the total force coefficient has achieved statistical convergence.

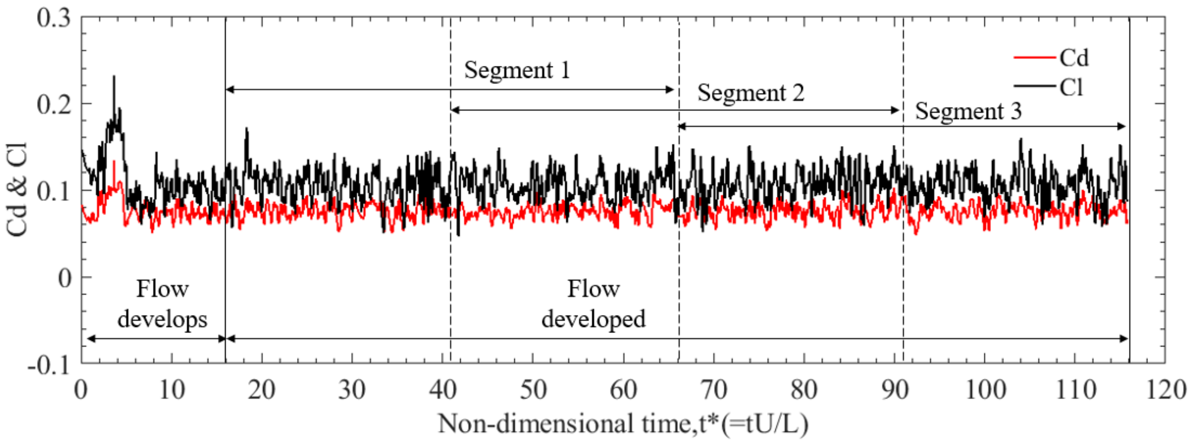

Figure 5.12 Time history of C_d and C_l of the case Medium1

Table 5.2 Summary of the total force coefficients of different segments

	C_d	C_l	Difference (%)		$C_{d,rms}$	$C_{l,rms}$	Difference (%)	
Whole segment	0.0753	0.1058	-	-	0.00872	0.0173	-	-
Segment 1	0.0753	0.1056	0.017	-0.16	0.00836	0.0172	-4.10	-0.78
Segment 2	0.0755	0.1059	0.26	0.077	0.00859	0.0168	-1.49	-3.17
Segment 3	0.0752	0.1060	-0.017	0.16	0.00906	0.0174	3.92	0.75

5.2.3.1 Aerodynamic results

The velocity parameters are collected from *t**=15 to *t**= 116. Figure 5.13 shows the mean contours of the streamwise velocity and the streamlines of the four cases at slice Z1 (defined in Figure 5.7). It can be noticed that the contours are similar with each other as are the flow direction and the positions of the vortex. This implies that the changes of the grid density have only a small impact on the general flow circulation and the development of the flow inside and outside the cavity.

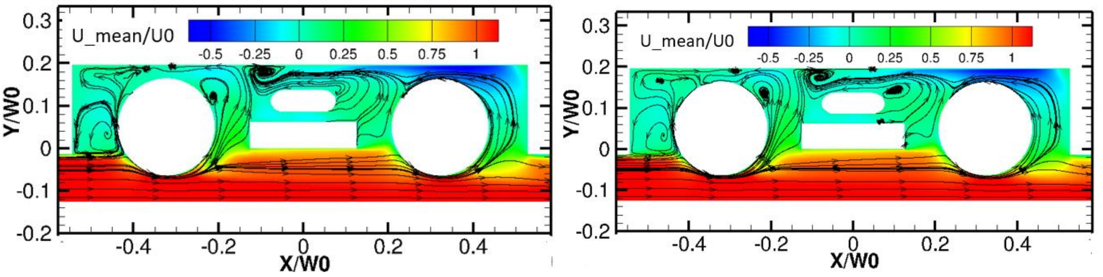

(a) case Fine

(b) case Medium1

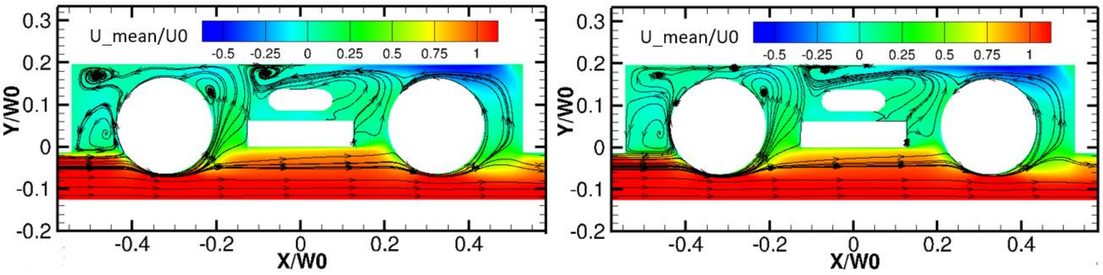

(c) case Medium2

(d) case Coarse

Figure 5.13 The mean streamwise velocity contour and streamlines of four cases at slice Z1

Table 5.3 and Table 5.4 presents the mean values and rms values of the force coefficients for the bogie and the cavity. The results for the fine case are taken as the reference values. In Table 5.3, the mean values of drag coefficient of for the cases Medium1 and Medium2 are around 5% smaller than that of the fine case. The relative differences for the mean lift coefficient are considerably greater than those of the mean drag coefficient, but these values can be disregarded as the mean values of the lift coefficients are close to zero. For the rms values, the differences are generally greater than those of the mean values because rms values are much more sensitive to the simulation parameters, such as the grid resolution, grid distribution and the time step. The rms values of the Medium1 and Medium2 cases are within 10% of the value for the fine case. Since the bogie is shielded by the cavity, the mean and rms values of its force coefficients are both smaller than those of the cavity in Table 5.4. The mean values of the Medium1 and Medium2 cases are within about ±5% of the fine case and the rms value differences are within ±10%. However, the differences for the coarse case in Table 5.4 are not so large as they are in Table 5.3. As expected from the statistical results of the force coefficients, the grid parameters of the cases Medium1 and Medium2 are more approparaiate than those of the coarse case.

Table 5.3 Summary of bogie force coefficients of different cases

Bogie	C_d	C_l	Difference (%)		$C_{d,rms}$	$C_{l,rms}$	Difference (%)	
Fine	0.0139	-0.00186	-	-	0.00489	0.00638	-	-
Medium1	0.0133	-0.00158	-4.3	-15.1	0.00452	0.00586	-7.6	-8.2
Medium2	0.0132	-0.00204	-5.0	9.7	0.00452	0.00605	-7.6	-5.2
Coarse	0.0111	-0.00050	-20.1	-73.1	0.00405	0.00528	-17.2	-17.2

Table 5.4 Summary of cavity force coefficients of different cases

Cavity	C_d	C_l	Difference (%)		$C_{d,rms}$	$C_{l,rms}$	Difference (%)	
Fine	0.0634	0.113	-	-	0.0108	0.0168	-	-
Medium1	0.0620	0.107	-2.2	-5.3	0.0101	0.0178	-6.5	6.0
Medium2	0.0665	0.109	4.9	-3.5	0.0104	0.0182	-3.7	8.3
Coarse	0.0678	0.110	6.9	-2.7	0.0103	0.0173	-4.6	3.0

Various monitors have been set on the bogie and cavity surface to sample the local pressure time histories, as shown in Figure 5.14. Two groups of monitors are located on the bottom surface of the wheels with 10 monitors in each group, which are distributed from upstream to downstream at an interval 9°. Five monitors are set on the cavity rear wall and numbered from outside to inside of the cavity, with a spacing of around 409 mm in full scale.

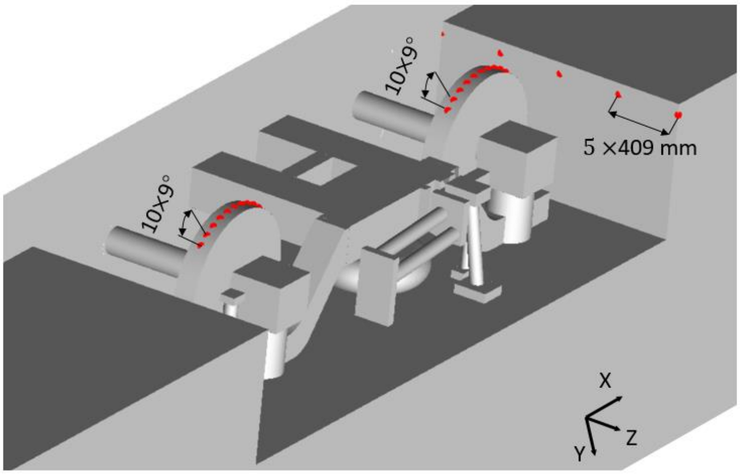

Figure 5.14 Positions of the monitors

Figure 5.15 and Figure 5.16 display the profiles of the mean and rms pressure at the monitors on the bottom of the wheels. For monitors 1 to 7, there is no noticeable difference in the mean and rms values between the various cases. However, the differences begin to increase after the 7th monitor because the flow separation, which is very sensitive to the grid density, occurs near this position. The profiles for the cases Medium1 and Medium2 are both closer to the fine case than the coarse one is. As shown in Figure 5.15(a), the maximum difference in the mean pressure between the medium cases and the fine case is approximately 10% at the 11th monitor. For the rms value profiles in Figure 5.16(b), the maximum difference between case fine and case Medium1 is around 20% and also appears at the 11th monitor.

Figure 5.17 shows the mean and rms values of the pressure at the monitors on the rear surface of the cavity. In Figure 5.17(a), the time averaged pressure for the case Medium1 is closest to that of the fine case and the maximum difference (13%) appears at the second monitor. The results for the case Medium2 have a greater difference from that of fine case and are quite close to coarse one because of their similar aspect ratios. As can be seen from Figure 5.17(b), the rms pressures from the different cases are much more similar than was found for the time-averaged pressure in Figure 5.17 (a). The largest difference is about 10% and appears at the fifth monitor. The differences of the rms values will be reflected in the radiated noise levels of the bogie. This will be discussed in the noise comparison section.

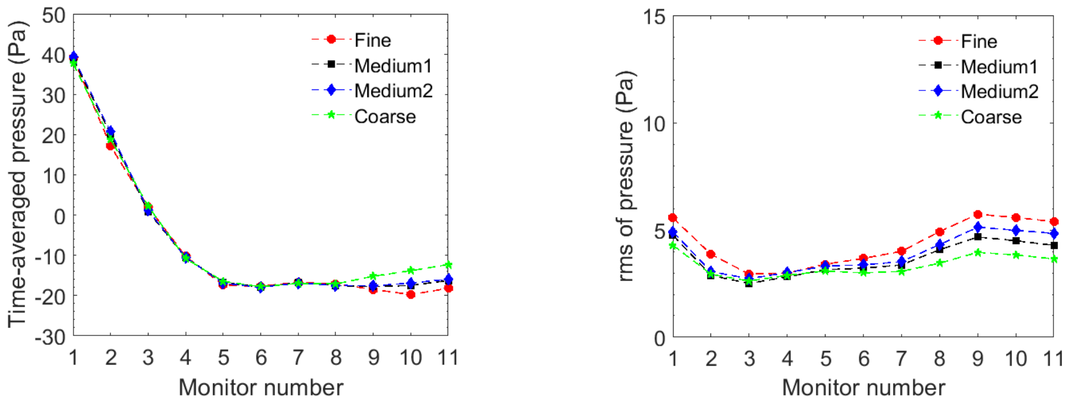

(a) time–averaged pressure (b) rms value of pressure

Figure 5.15 Mean and rms values of the pressure at the monitors on the bottom of the front wheel with different grid densities

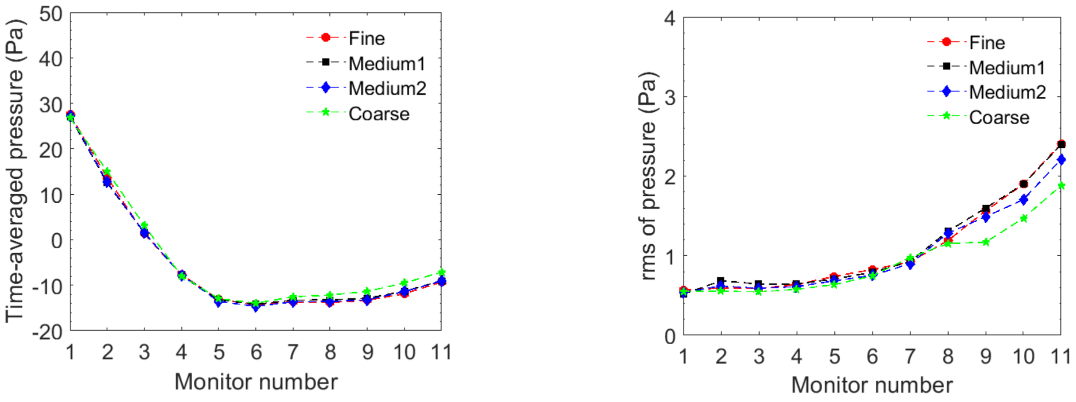

(a) time–averaged pressure (b) rms value of pressure

Figure 5.16 Mean and rms values of the pressure at the monitors on the bottom of the rear wheel with different grid densities

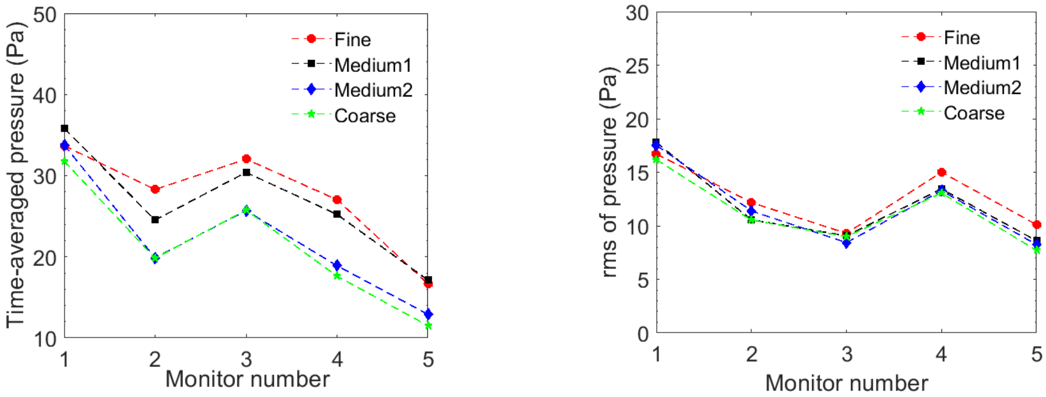

(a) time–averaged pressure (b) rms value of pressure

Figure 5.17 Mean and rms values of the pressure at the monitors on the rear side of the cavity with different grid densities

5.2.3.2 Aeroacoustic results

The pressure signals on the solid walls of the four cases are collected from t*=15. The data sampling frequency is around 20 kHz, which corresponds to a maximum spectral frequency of 10 kHz.

The collected time-dependent surface pressure is used to calculate the far-field noise by using the FW-H equation. After determining the sound pressure level (SPL) from the simulation model at a reduced scale, the SPLs and the frequencies are scaled up to the full scale situation:

$$\Delta SPL = 10\log_{10}\left[\frac{\left(\frac{D_1}{D_2}\right)^2\left(\frac{U_1}{U_2}\right)^6}{\left(\frac{r_1}{r_2}\right)^2}\right] \tag{5.1}$$

$$\frac{f_1}{f_2} = \frac{U_1}{U_2} * \frac{D_2}{D_1} \tag{5.2}$$

where f_1/f_2 is the frequency ratio, D_1/D_2 is the geometry ratio, U_1/U_2 is the velocity ratio and r_1/r_2 is the receiver distance ratio. Subscript 1 denotes the full scale situation, and 2 denotes the scaled model. As stated above, the running speed is reduced to 10m/s, which is about 1/11th of the original one (400 km/h), and the bogie model is also scaled down to 1/12th. The distance of the receiver will be kept the same in the subsequent simulations. Therefore, when scale the calculated noise of the model back, ΔSPL (84.1 dB) will be added. The frequency ratio is close to 1 according to Equation (5.2), which implies the calculated frequency is very close to the one of the full scale model with full speed. A series of receivers are set around the bogie as shown in Figure 5.18. The angle interval is 10° and the radius to the centre of the bogie is 20 m, which is greater than the longest sound wavelength of interest (17.25m at 20 Hz) and satisfies the acoustic far field requirement.

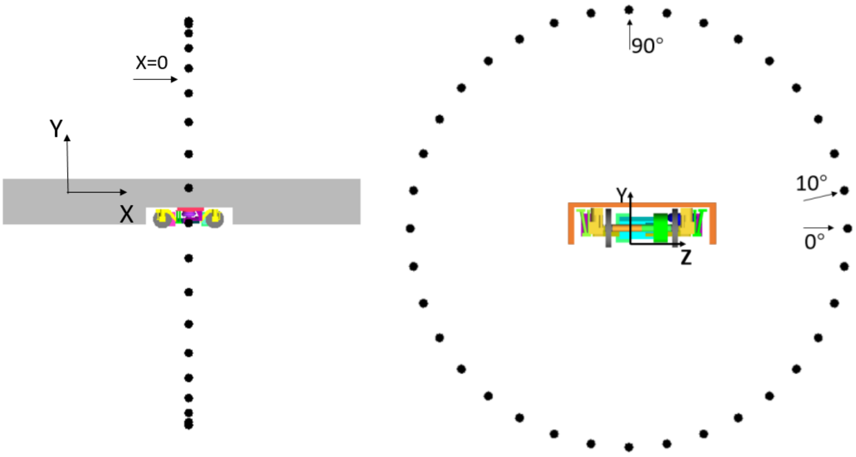

(a) left view (b) front view

Figure 5.18 Sketch of the receiver locations

For the receiver at 0°, the radiated noise spectra of the four cases in full scale with different grid density are plotted in Figure 5.19. The shapes of the spectra are similar, which means the four cases have similar distributions of sound power in the frequency domain. The main difference appears in the frequency range of about 60 Hz to 400 Hz with a maximum difference of around 7 dB between the fine and coarse cases. The SPLs difference between the medium cases and fine case is smaller than 2 dB in all frequencies except for the range of about 100 Hz to 400 Hz, where the maximum difference of 3 dB appears at 200 Hz. Therefore, the spectra of Medium1 and Medium2 cases are closer to that of the fine case than the coarse case is.

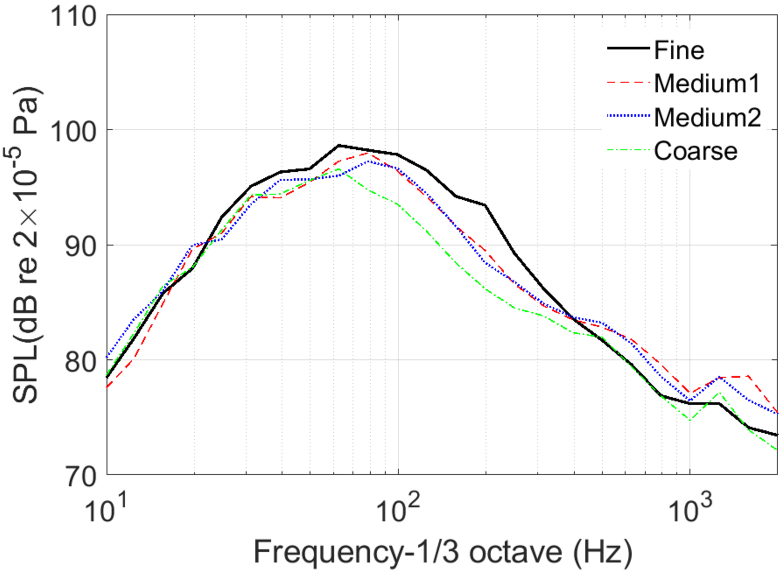

Figure 5.19 Noise spectra (1/3 octave) of cases with different grid density at the receiver 0^0.

The directivities of the bogie and the cavity obtained from the models with different grid density are presented in Figure 5.20. The noise levels of the two medium cases are almost the same as each other and they are both closer to those of the fine case than those of the coarse one. Compared with the results of the fine case, all the results of the other three cases are under predicted. The maximum difference of 3 dB, which appears at the vertical direction, is found in the comparison of the bogie noise levels of the fine and coarse cases. For the comparison of noise levels of the cavity, the maximum difference is about 2 dB.

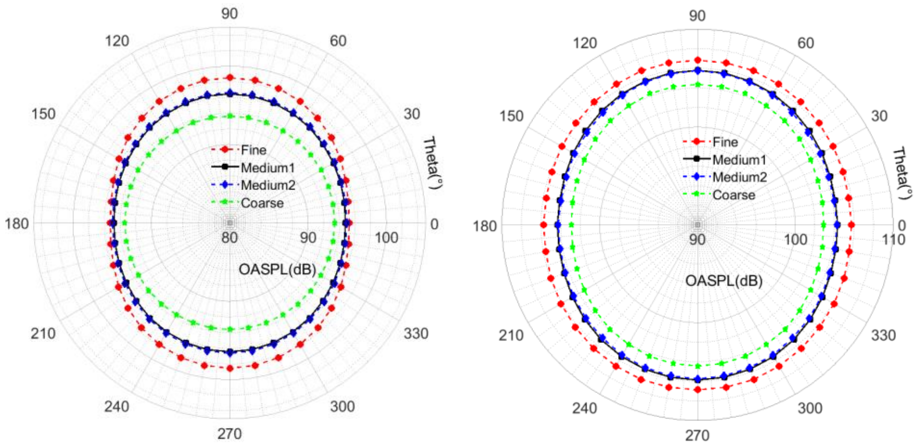

(a) bogie (b) cavity

Figure 5.20 Noise directivity of the cases with different grid density

In conclusion, from the above analysis, the aerodynamic and aeroacoustic results of the medium cases are both found to be sufficiently close to those of the fine case. Therefore, the grid size of medium cases will be adopted in the next simulations. The simulation of time step dependency study will be carried out by using the model Medium1.

5.2.4 Influence of time step size

5.2.4.1 Aerodynamic results

Table 5.5 and Table 5.6 list the statistical results of the force coefficients of the bogie and cavity obtained with different time steps. Case CFL2.5 is considered as the reference. For the results of the cavity, cases CFL3.5, CFL5, and CFL7 are close to case CFL2.5. However, for the results of the bogie, a big difference is found for the mean values of the case CFL7. Compared with the results of the cavity, the results of the bogie are more sensitive to the time steps. It is inferred that the grid cell size around the bogie is smaller and the flow speed around the bogie is higher, especially at the bottom of the bogie, which results in the *CFL* number in that region being greater than that near the cavity.

Table 5.5 Summary of cavity force coefficients of different time steps

Cavity	C_d	C_l	Difference (%)		$C_{d,rms}$	$C_{l,rms}$	Difference (%)	
CFL2.5	0.0628	0.107	-	-	0.0101	0.0179	-	-
CFL3.5	0.0624	0.107	-0.8	-0.0	0.0112	0.0182	11.0	1.8
CFL5	0.0623	0.107	-0.9	0.0	0.0096	0.0173	-4.6	-3.1
CFL7	0.0615	0.108	-2.2	1.3	0.0093	0.0158	-8.1	-11.7

Table 5.6 Summary of bogie force coefficients of different time steps

Bogie	C_d	C_l	Difference (%)		$C_{d,rms}$	$C_{l,rms}$	Difference (%)	
CFL2.5	0.0134	-0.00167	-	-	0.00471	0.00602	-	-
CFL3.5	0.0133	-0.00170	-0.5	2.2	0.00491	0.00615	4.3	2.0
CFL5	0.0130	-0.00156	-3.3	-6.8	0.00439	0.00594	-6.8	-1.4
CFL7	0.0151	-0.00255	12.6	52.7	0.00452	0.00602	-4.0	-0.1

The mean and rms values of the pressure at the monitors with different time steps are plotted in Figure 5.21 to Figure 5.23. The differences of the mean pressure on the monitors of the four cases are within 2%. However, significant differences of rms value, with a maximum value of around 30%, have been found for the case CFL7 in Figure 5.21(b) and Figure 5.22(b). Therefore, the time step of case CFL7 is not appropriate for the next simulation.

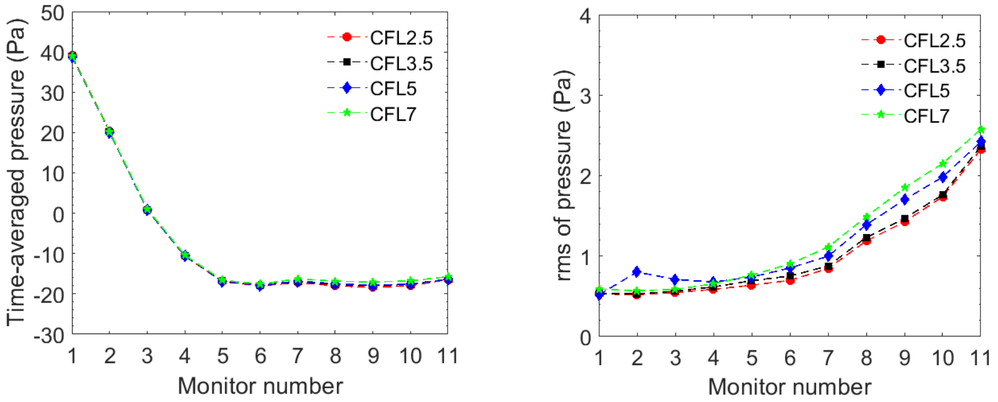

(a) time–averaged pressure

(b) rms value of pressure

Figure 5.21 The comparison of mean and rms values of the monitors on the bottom of the front wheel with different time steps

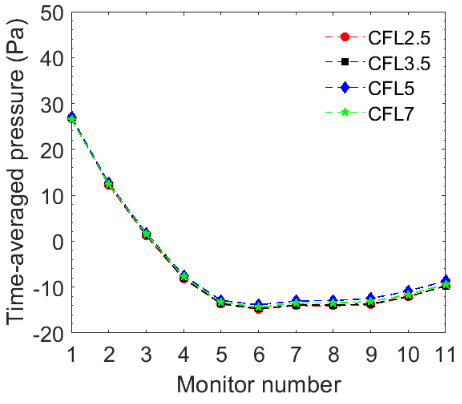

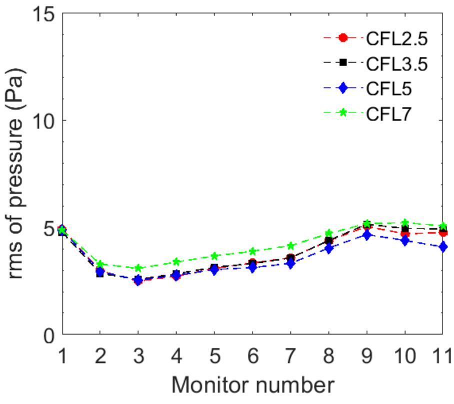

(a) time–averaged pressure (b) rms value of pressure

Figure 5.22 The comparison of mean and rms values of the monitors on the bottom of the rear wheel with different time steps

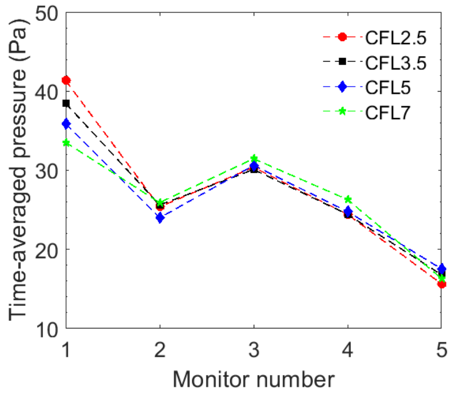

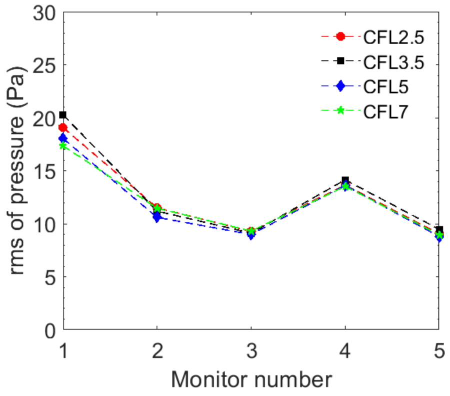

(a) time–averaged pressure (b) rms value of pressure

Figure 5.23 The comparison of mean and rms values of the monitors on the rear side of the cavity with different time steps

5.2.4.2 Aeroacoustic results

Figure 5.24 shows the noise directivity obtained from the cases with different time steps. The maximum difference of the noise levels of the bogie is less than 1 dB, as shown in Figure 5.24(a), and no appreciable difference is found in the noise directivity of the cavity in Figure 5.24(b). Although the time steps of all cases except CFL7 are acceptable, considering the balance of calculation accuracy and computational cost, the time step of Case CFL5 is chosen in the following calculations.

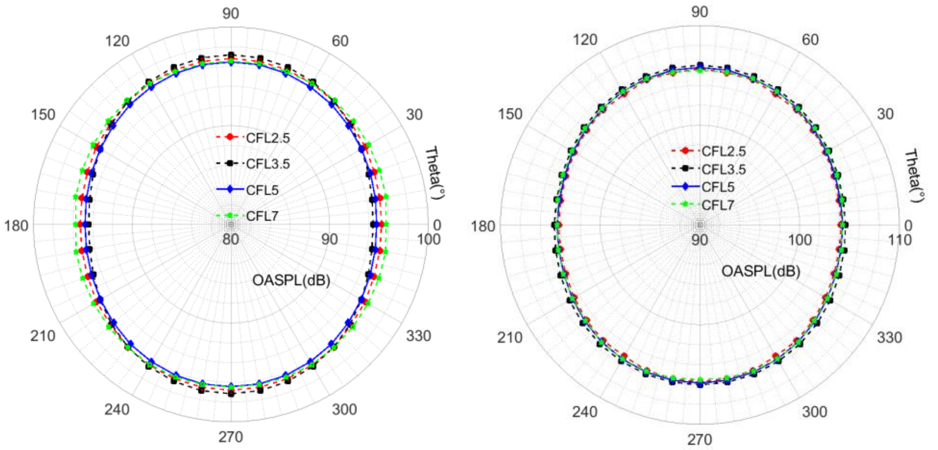

(a) bogie (b) cavity

Figure 5.24 Noise directivity of the cases with different time steps

5.2.5 Summary of grid and time step dependency study

In conclusion, according to the results of the grid sensitivity study, the grid densities of the cases Medium1 and Medium2 are both acceptable, the difference between them being in the cavity wall mesh. In the following simulations, the grid density of the bogies will be the same as that of the medium cases. For the cavities, the aspect ratio will vary between them according to the models with or without the bolster. In the time step study, it has been found that case CFL3.5 and CFL5 are both comparable to case CFL2.5. Considering the computational cost, the time step of the case CFL5 is more appropriate and will be used in the following simulations.

5.3 Simulation of a bogie in a simplified cavity

Having established suitable grid and time step parameters, in this section results are shown for the aerodynamic and aeroacoustic behaviour of the bogie in the simplified cavity.

5.3.1 Grid parameters

As discussed in section 5.2, the grid parameters of cases Medium1 and Medium2 are applied to the simulation model shown in Figure 5.3. Compared with the half-width model used in the grid dependence study, the geometry of the simulation model in Figure 5.3 is closer to the real bogie. Specifically, the bogie is connected with the cavity by the bolster beam, the geometry of the dampers represents better the actual bogie, and there are motors and gear boxes attached to the front and rear wheelsets. In Table 5.7, for the components which have the identical geometry with those of the half-width model, their grid parameters are kept the same, while for those with different geometry, such as the side dampers, the maximum aspect ratio does not exceed the one listed in Table 5.1. When choosing the grid parameters of the motors and gear boxes, the aspect ratios of the frame of case Medium1 in Table 5.1 and the square cylinder in section 4.1 are taken into consideration. Two refinement boxes as tested in section 5.2 are used to refine the local grid in the current simulation. The size of the refinement boxes is the same with the ones of case Medium1 in Table 5.1.

Table 5.7 The grid parameters of the model

Components	Aspect ratio	Components	Aspect ratio
Wheelset	80	Frame	125
Motor	56	Bolster beam	155
Gear box	91	Air springs	80
Axle box	65	Vertical damper	112
Front damper	110	Lateral damper	128
Cavity	148	Axle	65
Refinement box 1		3.43 mm (1/12 scaled)	
Refinement box 2		2.74 mm (1/12 scaled)	

As listed in Table 5.8, the final total number of cells is about 23.8 million, after the number in the unstructured grid is halved by converting it from a tetrahedral grid to a polyhedral one.

Table 5.8 The number of cells of the model

Number of cells	Before converting	After converting
Structured grid	15.3 M	15.3 M
Unstructured grid	16.4 M	8.5 M
Total grid	31.7 M	23.8 M

5.3.2 Aerodynamic results

Before running the DDES simulation, a RANS simulation is carried out to initialize the flow field. The time histories of the force coefficients, which are shown in Figure 5.25, are recorded from the beginning of the DDES simulation. The force coefficients are plotted against a non-dimensional time $t^* = tU_\infty /L$, where t is the physical time, U is the free stream velocity and L is the cavity length. The total simulation time corresponds to about 160 flow-through times of the cavity length (36 domain flow-through times). Flow parameter sampling begins after 20 flow-through times and the length of the sampling period is regarded as sufficient after the statistical stability of the force coefficients is achieved, as discussed in section 5.2.3. The computational wall-time is approximately 1120 hours with 512 processors on the Iridis4 cluster at University of Southampton.

Table 5.9 lists the statistical results of the force coefficients of the cavity, the bogie and their sum, which are averaged from t^* = 20 to 160. Rms values of the cavity are all greater than those of the bogie, which suggests that the noise generated by the cavity will be higher.

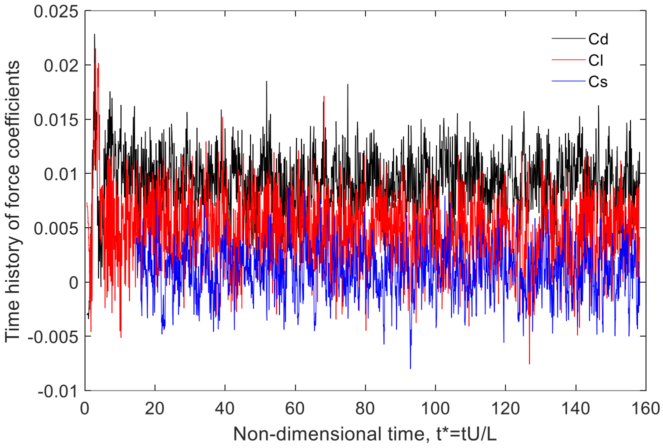

Figure 5.25 Time history of force coefficients, C_d: drag force coefficient, C_l: lift force coefficient, and C_s: side force coefficient

Table 5.9 Summary of force coefficients

	C_d	C_l	C_s	$C_{d,rms}$	$C_{l,rms}$	$C_{s,rms}$
Bogie	0.00913	0.00466	0.00107	0.00210	0.00260	0.00191
Cavity	0.0622	0.111	-0.000695	0.00452	0.00947	0.00880
Total	0.07135	0.1156	0.000378	0.00402	0.0102	0.00949

Figure 5.26 shows contours of the mean streamwise velocity superposed with mean streamlines. It can be seen that flow enters the cavity mainly from the bottom of the bogie and the flow inside the bogie cavity has a much lower speed and slowly recirculates from the rear part to the front part through the top of the cavity. The flow in the regions close to the border of the cavity, such as the bottom and two sides of the bogie, is accelerated by the free stream due to the influence of the viscosity, which makes its speed higher than that of the flow at the inside of the cavity.

Figure 5.27 shows contours of the instantaneous vorticity magnitude on three slices through the bogie region (see Figure 5.7). The shear flow detached from the bogie cavity leading edge, which is also found in the simulation of Zhu et al. (2018), impinges on some lower parts of the bogie and the trailing edge of the cavity. However, the shear layer does not bend upwards into the cavity after detaching from upstream cavity edge, as shown in Zhu et al. (2018), but travels downstream and interacts with some components, such as the bottom of the bogie and the side dampers. This difference with the results of Zhu et al. (2018) is due to the presence of more components in the cavity in the more detailed model. The interaction disperses the detached shear layer in the downstream direction and some of it impinges on the rear surface of the cavity. Morris (2011) points out that, for a shallow opening cavity, the detached shear layer leads to unsteady pressure oscillations on the cavity surface, which is the origin of the dipole noise source. This also applies for the bogie and cavity model, for which the regions impinged by the detached shear become potential noise sources due to the pressure fluctuation on them.

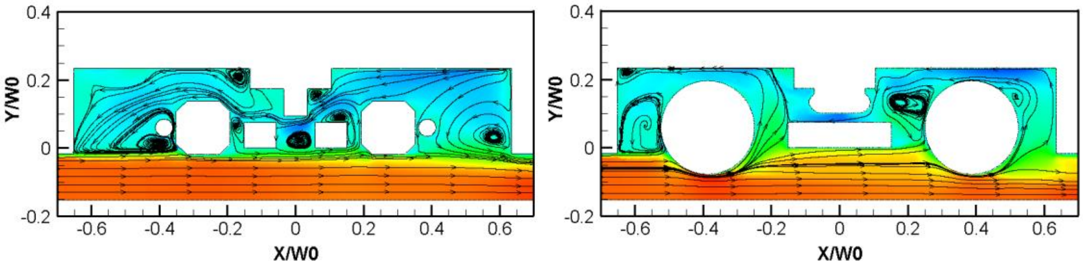

(a) Z0

(b) Z1

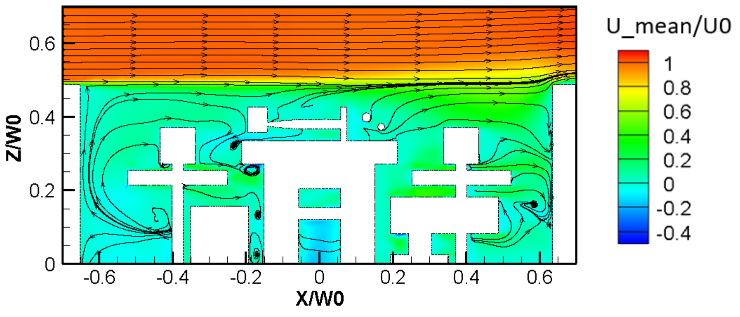

(c) Y0 (half-width)

Figure 5.26 Time-averaged streamwise velocity contours together with mean streamlines, W_0 is the width of the cavity.

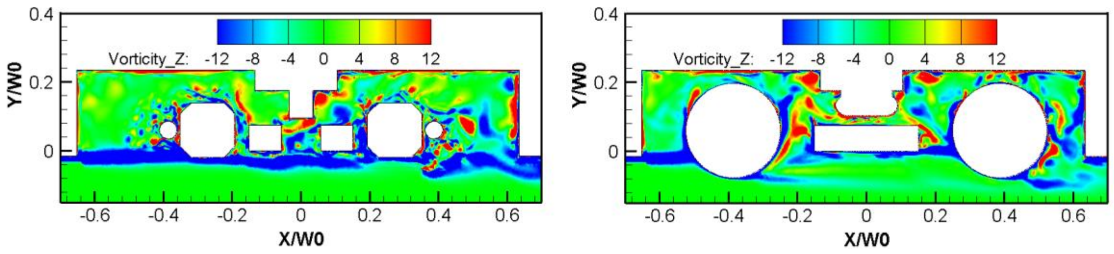

(a) Z0

(b) Z1

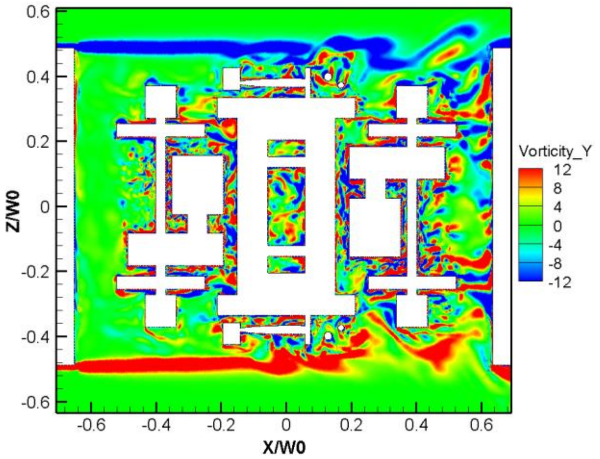

(c) Y0

Figure 5.27 Contours of instantaneous vorticity field, W_0 is the width of the cavity.

According to the analysis in Chapter 3, the far-field noise level has a positive correlation with the rms value of dp/dt on the solid walls. Therefore, variable dp/dt can be used to indicate a dipole noise source and the level of its fluctuation, as defined in Equation (3.37), can be used to measure the intensity of the pressure fluctuation. During the simulation, the pressure signal on the surface elements of the solid walls (there are about 1.12×10^6 of them) is collected over a total data sampling time of around 5 s. The PSD of every surface element is computed based on Welch's method with a Hanning window. There are 25 segments with 50% overlap and the segment length is 0.4 s, giving a frequency resolution of 2.5 Hz. In section 5.2.3.2, Figure 5.19 shows the noise contribution from low frequencies is dominant. Thus, the intensity of the fluctuation of dp/dt integrated from 20 to 1600 Hz on the cavity and bogie surfaces is calculated and presented in Figure 5.28.

Figure 5.28(a) shows the pressure fluctuation distribution on the whole model surface. Generally, it is stronger on the bottom walls, especially at the rear part. This is consistent with the experimental results from Sawamura et al. (2018), who also found the strongest pressure fluctuation is located at the rear part of the bogie.

As shown in Figure 5.27, the flow is initially detached from the cavity leading edge, and forms a detached shear layer, which is unstable and will disperse and accelerate the flow around it in the streamwise direction due to the effect of viscosity. Then, this detached shear layer will impinge on the front part of the bogie and forms a wake flow with highly turbulent intensity, which is, as shown in Figure 5.26, convected by the high-speed flow in the downstream direction. This highly turbulent and non-uniform wake will then impinge on the rear components of the bogie and produce a strong pressure fluctuation at the rear part, as shown in Figure 5.28(b). Figure 5.28(c) shows there is a strong pressure fluctuation region on the cavity surface, especially at the corners of the rear surface and the edges of the top surface. The first cause of the strong pressure fluctuation is the detached shear layer from the upstream cavity edge, as shown in Figure 5.27, and the second one is the invaded wake flow from upstream. As shown in Figure 5.26(a), the wake from upstream cannot continue to be convected in the downstream direction because of the cavity rear wall, which makes some of the wake invade the cavity, and the strong pressure fluctuation region will extend to the upper part of the bogie and the cavity as shown in Figure 5.28(b) and (c). The overall level of the pressure change rate $L_{\dot{p}\_total}$, as defined by Equation (3.38), on the bogie surface is 2.3 dB stronger than that on the cavity surface. However, when calculating $L_{\dot{p}\_total}$, the phase information is not considered. Therefore, the far field noise level of the bogie is not necessarily greater than that of the cavity.

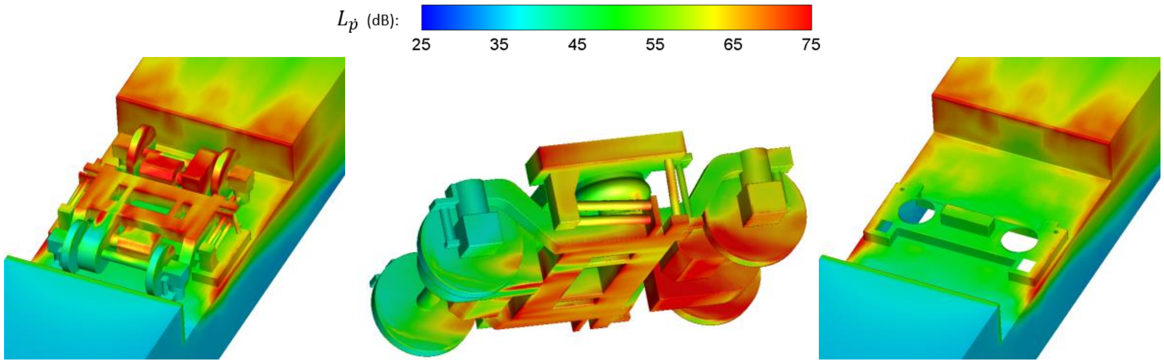

$L_{\dot{p}\_total}$ =60.8 dB $L_{\dot{p}\_total}$ =58.6 dB $L_{\dot{p}\_total}$ =56.9 dB

(a) whole model(bottom view) (b) bogie (c) cavity(bottom view)

Figure 5.28 Surface contours of the pressure rate of change dp/dt on the model components integrated from 20 to 1600 Hz

The experimental results of Sawamura et al. (2018) show the noise source distribution is different in different frequency ranges. To investigate this, the level of the fluctuation of dp/dt on the cavity surface is integrated over three different frequency bands, 20-200 Hz, 200-400 Hz and 400-600 Hz, as shown in Figure 5.29. Figure 5.29(a), the range of 20-200 Hz, has the highest value of $L_{\dot{p}\_total}$, 55.8 dB, compared with those in Figure 5.29(b) and Figure 5.29(c). The pressure fluctuation distribution shown in Figure 5.29(c) is similar with that shown in Figure 5.28(b) and is located mainly at the rear corners and side rims. In Figure 5.30, the pressure fluctuation distribution in the range of 20-200 Hz is further divided into three segments and the results show that the pressure fluctuation power in the range of 60-120 Hz contributes the most and the pressure fluctuation near the cavity edge is stronger than other areas. This can be attributed to the impingement by the detached shear layer in Figure 5.27. Therefore, one of the design concepts to reduce the aerodynamic bogie noise of the cavity should be to prevent the impingement from the shear layer.

Figure 5.31 and Figure 5.32 show the pressure fluctuation distribution of the bogie in different frequency bands. Although $L_{\dot{p}\_total}$ has the highest value in the frequency range 20-200 Hz, the pressure fluctuation strength of the higher frequency ranges, 200-400 Hz and 400-600Hz, is as strong on the bottom surface as that in the lower frequency band. It is believed that the wake flow detached from the upstream components of the bogie, as shown in Figure 5.27, is the main cause of the pressure fluctuation on the downstream components of the bogie (Zhu et al. 2018). This is in contrast with the pressure fluctuations on the cavity which are mainly produced by the shear flow detached from the upstream rims of the cavity and the recycling flow inside the cavity. Compared with the detached shear flow or the recycling flow inside the cavity, the wake flow has smaller eddies and thus has a wider frequency range of velocity fluctuation, which is believed to produce the pressure fluctuation on the components surfaces. For the pressure fluctuation distributed at the upper front part of the cavity shown in Figure 5.29 and the bogie shown in Figure 5.31, it is very small in the range 200-600 Hz. The pressure fluctuation in those areas is mainly produced by the recycling flow inside the cavity, which has a much lower speed than the flow outside the cavity and the eddies are larger than those in the lower downstream region.

It can be concluded that the overall level of the pressure fluctuation has greatest value in the low frequency band (20-200 Hz) both for the bogie and cavity. This is consistent with the experimental studies from Sawamura et al. (2018) and Latorre Iglesias et al. (2017), which indicate that the noise energy is concentrated in the low frequency region.

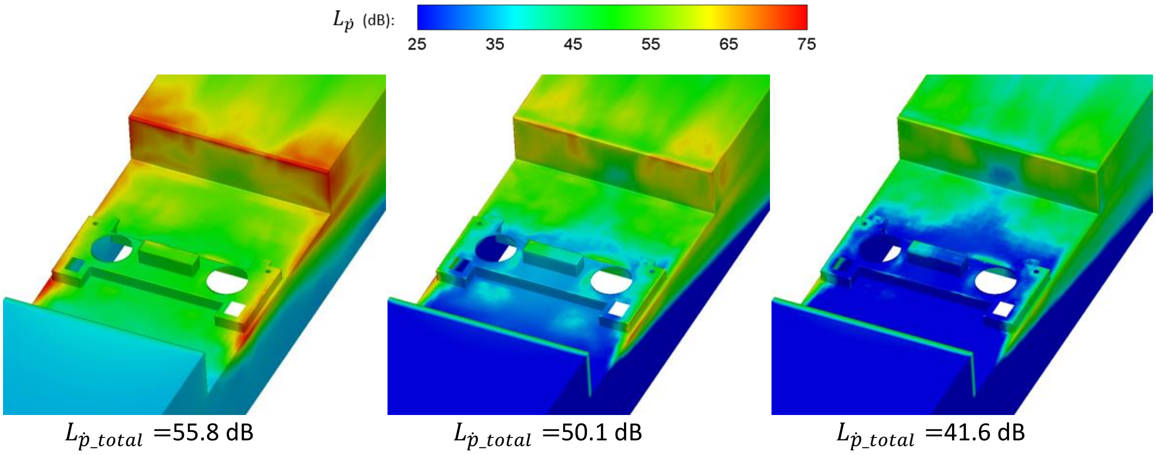

(a) 20-200 Hz (b) 200-400 Hz (c) 400-600 Hz

Figure 5.29 Surface contours of the pressure rate of change dp/dt on the cavity integrated from 20 to 600 Hz (bottom view)

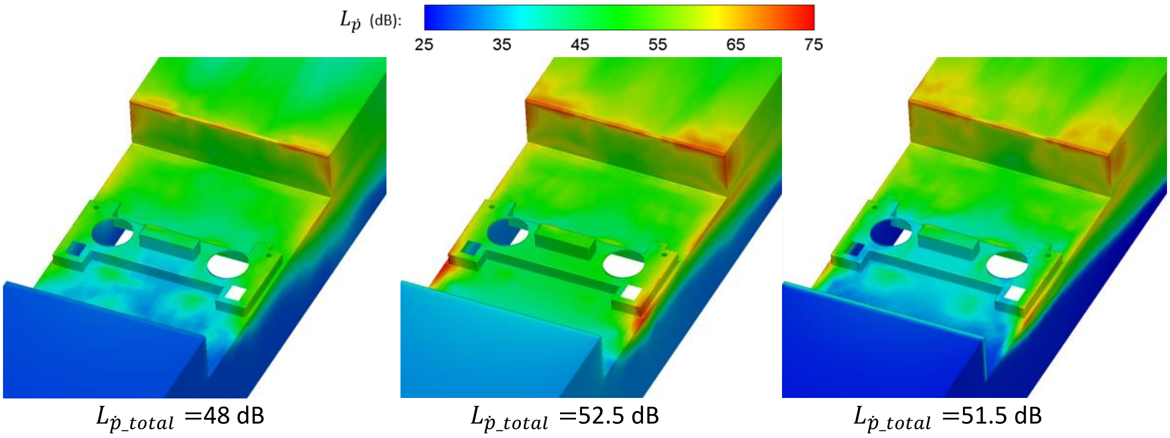

(a) 20-60 Hz (b) 60-120 Hz (c) 120-200 Hz

Figure 5.30 Surface contours of the pressure rate of change dp/dt on the cavity integrated from 20 to 200 Hz (bottom view)

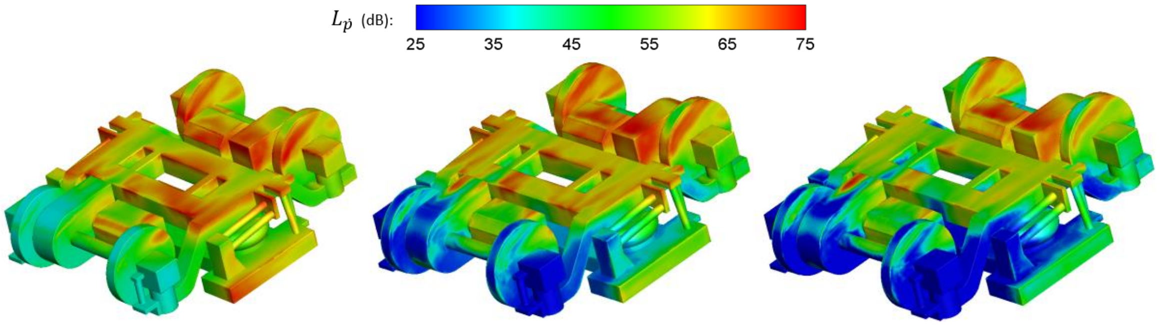

$L_{\dot{p}\_total}$ =55.4 dB $L_{\dot{p}\_total}$ =54 dB $L_{\dot{p}\_total}$ =51.1 dB

(a) 20-200 Hz (b) 200-400 Hz (c) 400-600 Hz

Figure 5.31 Surface contours of the pressure rate of change dp/dt on the bogie integrated from 20 to 600 Hz (bottom view)

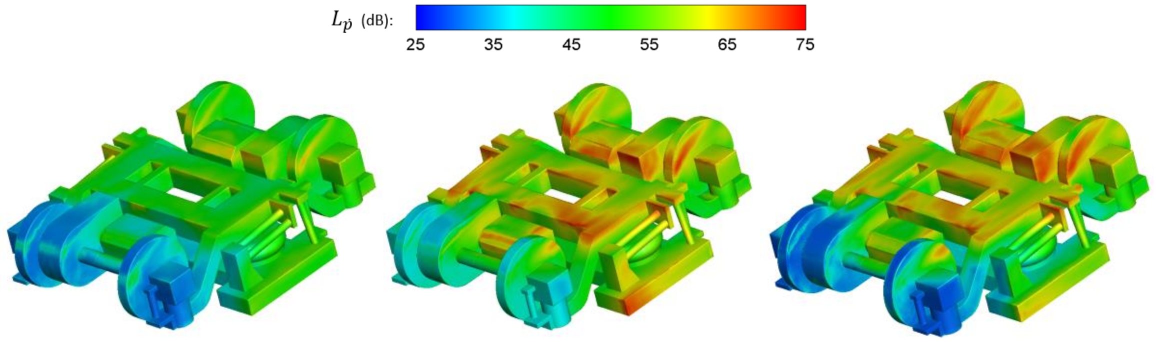

$L_{\dot{p}\_total}$ =44 dB $L_{\dot{p}\_total}$ =52.2 dB $L_{\dot{p}\_total}$ =51.8 dB

(a)20-60 Hz (b) 60-120 Hz (c) 120-200 Hz

Figure 5.32 Surface contours of the pressure rate of change dp/dt on the bogie integrated from 20 to 200 Hz (bottom view)

5.3.3 Aeroacoustic results

The pressure data on the solid surface is collected from 20 to 160 flow-through times of the cavity. the bolster is included as part of the cavity in the noise calculation. The data sampling rate is around 20 kHz, leading to a maximum spectral frequency of 10 kHz. The collected pressure fluctuation then is taken as the input to the FW-H equation to calculate the aerodynamic noise. The 36 receivers in Figure 5.18 are used to investigate the directivity in free space. After the calculation, the noise is converted to full scale by using Equations (5.1) and (5.2).

Figure 5.33 shows the noise spectra of the cavity and bogie at the 0° receiver in Figure 5.18. The noise generated by the cavity is much greater than that from the bogie. For both the cavity and the bogie, the noise spectrum has higher values at low frequencies, which is consistent with the pressure fluctuation analysis in section 5.3.2 and the experimental research from Lauterbach et al. (2012) and Latorre Iglesias et al. (2017). The generation of the noise at low frequency is related to the large-scale flow phenomena in the flow field, such as the flow circulation, flow flapping and the vortex at the rear part of the cavity, as shown in Figure 5.26 and Figure 5.27. In addition, a small peak on the cavity spectra and two on the bogie spectra are found. The first one is at about 78 Hz and the second one is at about 100 Hz. According to the pressure fluctuation strength shown in Figure 5.30(b) and Figure 5.32(b), which the peaks are in the integral frequency range, the area with strong pressure fluctuation is contacting with the detached shear layer from upstream. Thus, it can be inferred that the peaks in the noise spectra are related to the detached shear layer from upstream.

Figure 5.34 shows the far field directivity of the noise generated by the cavity, the bogie and the main components, assuming free field propagation. The composition of the components can be found in Appendix A. The noise generated by the cavity is considerably greater than that generated by the bogie. Yamazaki et al. (2019) and Latorre Iglesias et al. (2017) also found a similar conclusion, although, in their experiments, it was assumed the flow conditions were not affected by introducing the bogie parts in the cavity.

The overall sound pressure level (OASPL) of the cavity is approximately omnidirectional, whereas the bogie has a typical dipole directivity shape. The OASPL values of the bogie are greater in the vertical direction than in the horizontal direction. In reality, the rear corners of the cavity are usually modified to reduce the drag and noise, which will make the relative noise contribution from the cavity less significant. Although the directivity is shown based on free space calculations, in reality, the car body and the ground will reflect the sound, modifying this directivity considerably.

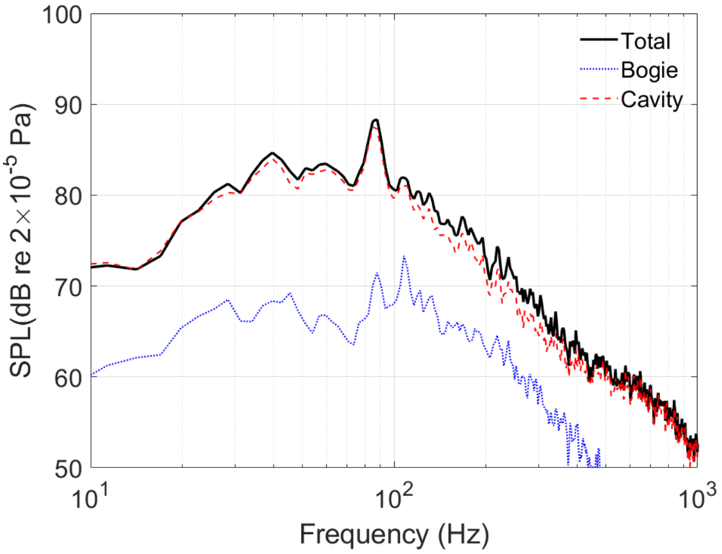

Figure 5.33 Noise spectra of the model at the receiver at 0°

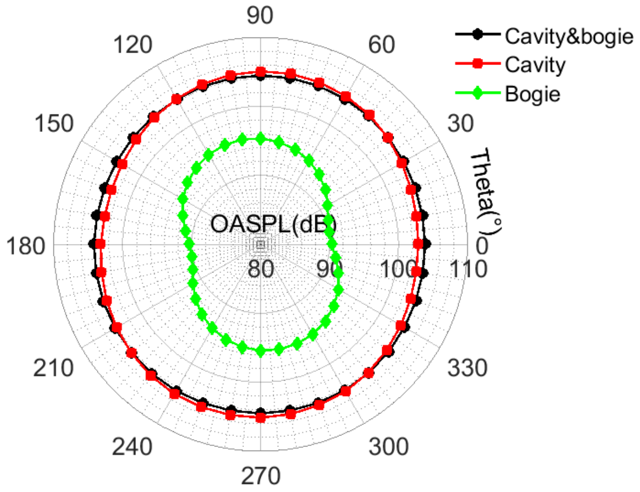

Figure 5.34 The far-field noise directivity of the model

For the noise from the bogie, Figure 5.35 gives the noise spectra of different components at the top and side receivers and the frequencies are not scaled to full model by Equations (5.2). The contribution from the bogie is divided into the upstream dynamic components (leading wheelset, gearbox, motor and axle boxes), downstream dynamic components (equivalent components for the trailing wheelset) and bogie frame components. The composition of the components can be found in Appendix A. It is found that the downstream components emit more noise than the upstream ones at all frequencies. It is believed that the impingement from the upstream wake, which has higher turbulence intensity and more eddies with different sizes, produces higher pressure fluctuation on the downstream components as shown in Figure 5.31 and Figure 5.32. Another point should be pointed out is that, according to the pressure fluctuation strength in Figure 5.31, it is distributed in a wider frequency range on the downstream components than on other components, whereas the shape of its noise spectrum seems to be similar with that of other components, which has higher value at low frequency and starts to decline above 100 Hz. Another point should be noticed is that the spectra of the component have peaks at about 78 Hz and 100 Hz. To identify the source of these peaks, the pressure fluctuation strength, which is calculated by equation (3.37), integrated from 75 to 85 Hz and 95 to 105 Hz is shown in Figure 5.36. It can be noted that the area with high pressure fluctuation strength is the location where the shear layer impinges as shown in Figure 5.27. To further investigate the spectra of the pressure fluctuation, two points, Point1 and Point2, are set as shown in Figure 5.36(b). The spectra of *Cp(t)* are shown in Figure 5.37 and there are two significant peaks, whose frequencies are also 78 Hz and 100 Hz. In the shear layer detached from upstream of the cavity rim, the vortices shed periodically and are bought to downstream as the shear layer propagates with the convection(Lauterbach et al. 2012). Therefore, the components at the downstream will be impinged by the vortices and generate periodic pressure fluctuations on their surface and peaks in their noise spectra.

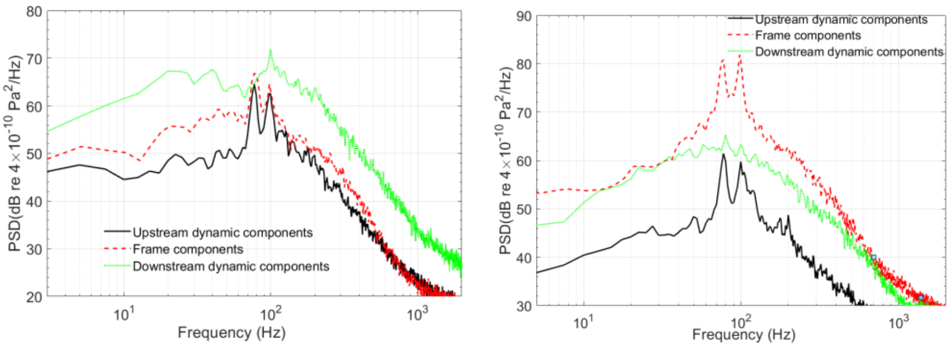

(a) 0 °

(b) 90°

Figure 5.35 Noise spectra of the bogie components (frequencies not scaled)

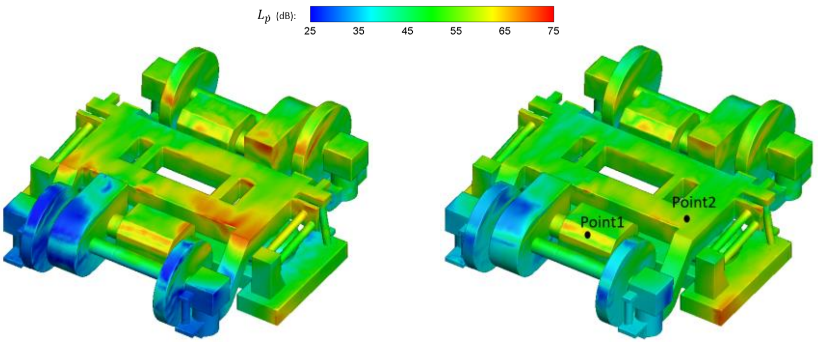

(a) 75-85 Hz

(b) 95-105 Hz

Figure 5.36 Surface contours of the pressure rate of change dp/dt on the bogie integrated around the peak frequencies in Figure 5.35. (bottom view)

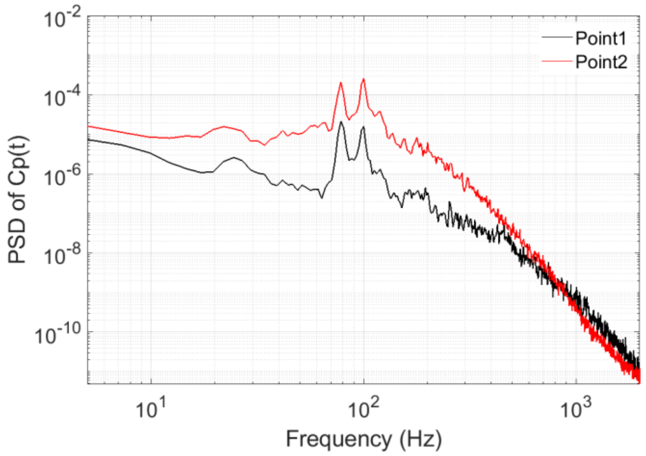

Figure 5.37 PSD of *Cp*(*t*) of Point1 and Point2 in Figure 5.36 (b)

Figure 5.38 shows the directivity of the frame components, and the front and rear dynamic components. These directivities have different shapes. The frame components have greater OASPL in the vertical direction (as seen in Figure 5.35) while the other components have a greater one in the horizontal direction. In Figure 5.28, the bottom of the frame has high pressure fluctuation, which is the main reason for the frame components having large noise radiation in the vertical direction. Compared with the upstream dynamic components, the downstream ones have higher noise levels because of the impingement from the upstream wake, as illustrated in Figure 5.27.

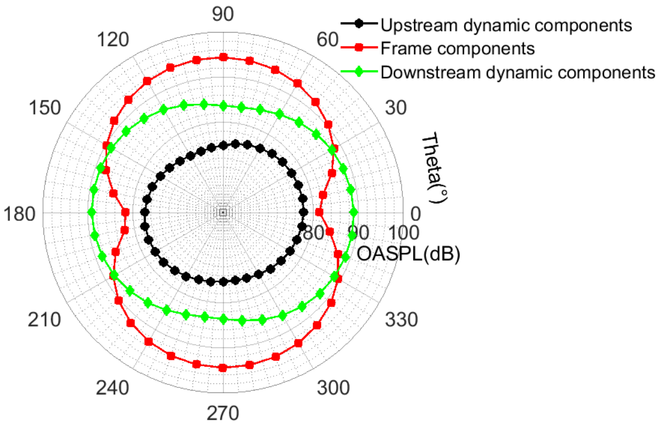

Figure 5.38 The far field noise directivity of the bogie components

To compare the noise contributions of the various bogie components, Figure 5.39 shows their overall noise levels in the side and top direction. In Figure 5.39(a), in the lateral direction, the noise levels of the wheelsets are the highest within both the upstream and downstream dynamic systems, which is consistent with the experimental research from Yamazaki et al. (2019). In addition, their noise levels at the side receiver are both higher than those at the top receiver. Figure 5.31 and Figure 5.32 show the pressure fluctuation distributed on the side surfaces of the wheels is comparable with that distributed on the tyre surface. However, the area of the side surface is greater and makes the sound pressure in the lateral direction greater than that in the upward direction. In Figure 5.39(b), the noise level of the frame is much higher than that of other components, which can be also attributed to the greater area of the frame bottom surface. Therefore, from the explanation of Figure 5.39, it can be concluded that the noise level of a component in a certain direction is dependent on the pressure fluctuation strength and the projected area of the components in that direction.

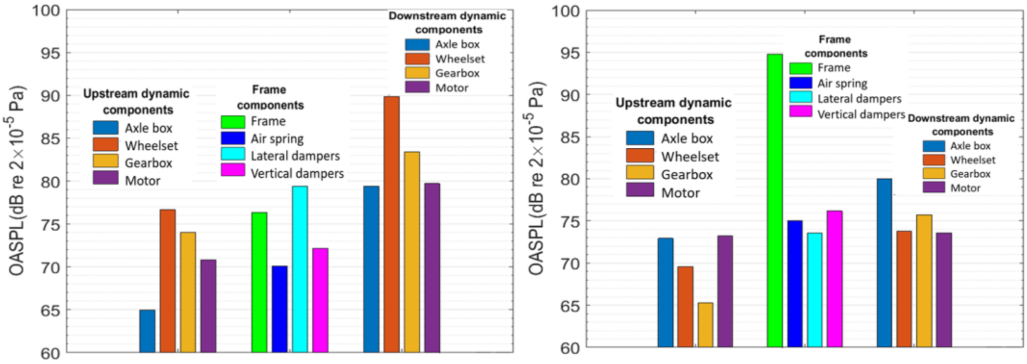

(a) 0°

(b) 90°

Figure 5.39 Noise levels of different bogie components at side and top receivers

5.4 Summary

In this chapter, the aerodynamic noise of a bogie in a simplified cavity is investigated. The discretization of the complex bogie has been a great challenge for a long time in the numerical simulation research (Sima et al. 2008; Meskine et al. 2013; Zhu et al. 2016). In order to address this challenge, a hybrid grid system is proposed, which is hexahedral grid near the solid surface and polyhedral grid in the rest of the volume. The quality of the grid in the boundary layer can be guaranteed by adjusting the block nodes in the hexahedral grid generation. The unstructured grid, which is initially tetrahedral and then converted to a polyhedral one, can fill the rest of the volume rapidly because of its flexibility. The conversion between tetrahedral grid and polyhedral grid can not only reduce the number of cells but also increase the grid quality. Moreover, the unstructured grid density can be controlled by adding some refinement boxes at the necessary locations. Therefore, by adopting the proposed hybrid grid system, both the grid quality and quantity can be controlled in an acceptable range.

To conduct the grid dependence study, a simplified half-width model of the bogie and cavity is used. Four cases with different grid density have been investigated and the aerodynamic and aeroacoustic results are compared. The result shows the grid densities of case Medium1 and case Medium2 are both acceptable, which means they can be used as the basis for the grid density used in the following simulations; the term 'Medium' means that the aspect ratio and the size of the refinement boxes are between those of case Fine and case Coarse and the difference between Medium1 and Medium2 is in the meshing of the cavity walls. The effect of different time steps is also evaluated. The result shows the time steps of both case CFL3.5 (maximum $CFL<3.5$) and case CFL5 (maximum $CFL<5$) are acceptable. Considering the computational cost, the one of case CFL5 is finally chosen.

After establishing the hybrid grid system, it is applied to a simulation of the aerodynamic noise of a full bogie in a simplified cavity. First of all, the flow field is calculated. The aerodynamic results show the shear layer detached from the upstream cavity rims and the turbulent wake at the downstream of the front components are both possible causes of the aerodynamic noise of the bogie. The components, which are immersed in the wake or the detached shear layer, are the potential noise source regions; this is confirmed by the subsequent pressure fluctuation identification based on the level of the pressure gradient dp/dt. The results of these calculations show the rear part of the bogie and the rear corners of the cavity have high pressure fluctuation strength. In the analysis of the distribution of the pressure fluctuation energy in the frequency domain, it is found that, for the cavity, the pressure fluctuation energy is concentrated in the range 20-200 Hz. For the bogie, it is distributed over a wider range of frequencies, from 20-600 Hz, especially for the components at the rear part of the bogie, such as the downstream gear box and motor. The wake from upstream, which contains small eddies, is believed to be the reason why the rear part of the bogie has a wider distribution of the pressure fluctuation energy.

The characteristics of the far field noise directivity and spectra of the bogie and cavity have also been investigated. The noise level generated by the cavity is considerably greater than that generated by the bogie. The spectra of the cavity and the bogie have no aeolian tone and they have much higher levels at low frequencies. These conclusions are consistent with the experimental results of Yamazaki et al. (2019) and Latorre Iglesias et al. (2017). In the comparison of the noise of different bogie components, it has been found that the components at the rear part of the bogie have higher noise levels, which is also shown by the pressure fluctuation identification.

In next chapter, simulations of a bogie under a leading vehicle of a high-speed train, which is a more realistic and complex model, will be presented. It is known that the incoming flow of the bogie region will be affected by the train nose and especially the cowcatcher. It is necessary to assess the noise from the leading bogie and its influencing factors. The hybrid grid system developed in this chapter will be used in the following simulations.

Chapter 6 Aerodynamic and aeroacoustic simulations of a bogie under a leading vehicle

As reviewed in Chapter 2, the aerodynamic noise becomes the dominant contributor to the overall noise when the train speed exceeds about 300 km/h (Thompson et al. 2015). Of the various aerodynamic noise sources, the bogies are very important noise sources (Thompson et al. 2015; Zhu et al. 2018; Liu et al. 2021). Compared with the model shown in Figure 5.1, flow around the motor bogie under the leading vehicle is more complicated. The geometry at the front of the train, such as the train nose and the cowcatcher, make the incoming flow highly turbulent, while many parts of the bogie are shielded from the incoming flow by them. Some experiments in wind tunnels have been carried out to investigate the characteristics of the bogie aerodynamic noise (Lauterbach et al. 2012; Latorre Iglesias et al. 2017). However, although numerical methods are very helpful in revealing noise generation mechanisms, they have rarely been used to study the bogie and the whole train noise, except for some simplified bogie models and models with insufficient or not well defined mesh quality, due to the extremely complex geometry (Zhu 2015). In this Chapter, a careful balance will be made between the model simplification, computational cost and grid quality. Simulations in this Chapter also aim to reveal the mechanisms of generation of the bogie aerodynamic noise.

In this Chapter, to facilitate feasible simulations, a scaled model is used. The hybrid computational grid validated in Chapter 4 and applied in Chapter 5 will be further developed for the simulations of a bogie under a leading vehicle and used to perform DDES calculations.

6.1 Grid system and numerical setup

In the current simulations, the computational domain, shown in Figure 6.1, is designed with the focus on the bottom region of the leading car, including the cowcatcher and the bogie region. The bogie model used is the same as that given in section 5.1 and shown in Figure 5.3. As reviewed in Chapter 2, the bogie region, especially for the leading bogie, is responsible for significant low-frequency noise, which is critical for the neighbouring urban areas because of its high transmission into buildings (Minelli et al. 2020). To simulate the aerodynamic noise generated by the flow over structural elements, there are stringent requirements for the grid density, especially in the boundary layer. Considering the computational cost, in the current numerical domain, the car body has been shortened, and only the leading car of the CRH train model will be simulated. The slipstream, wake, flow features between the car body gaps and flow features related to the consecutive bogie cavities are neglected.

Figure 6.1 shows dimensions of the computational domain, defined in terms of the height of the train H_0, which is about 3.795 m. To avoid the influence from the domain boundaries, including the upstream velocity inlet boundary and the symmetry boundaries at the top and two sides, they are set at a distance of around $10H_0$ away from the car body. As for the outlet boundary, because the rear part of the car body is truncated, the outlet plane, at which a zero-pressure outlet boundary condition is specified, is located at about $5.6H_0$ away from the train nose. In addition, the ground is 250 mm (full scale) to the bottom of the wheels and specified as a moving wall to reproduce the conditions beneath a moving train.

As discussed inChapter 5, to reduce the computational cost, the model size is reduced to 1/12 and the air speed is also reduced to 1/11 (10m/s). This gives a Reynolds number of 2.11×10^5 based on the scaled height of the train (0.316 m) or 1.91×10^5 based on the scaled width (0.287 m), which is greater than the minimum tested Reynolds number (1.53×10^5, based on the width of the train) in the study from Lauterbach et al. (2012).

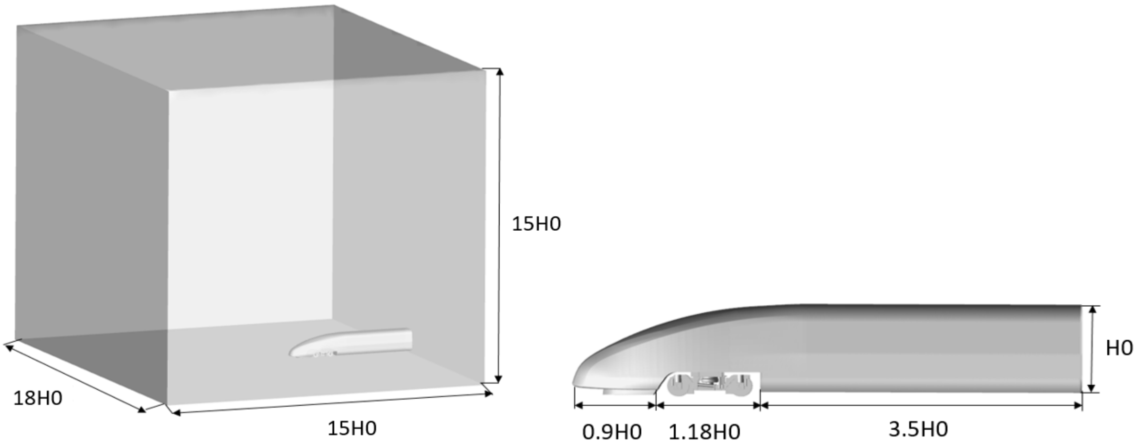

(a) the full computational domain (b) the side view of the model

Figure 6.1 Computational domain dimensions

The hybrid grid system used in Chapter 5 is adopted. The bogie geometry shown in Figure 6.1 is identical with the one used in section 5.3 and thus the structured grid parameters of the bogie given in Table 5.7 will be used in the current grid system. The simplified cavity in Chapter 5 is replaced by the car body with a more complex geometry. Therefore, a new grid dependence study will be conducted in section 6.2. Figure 6.2 gives the generation blocks used for the hexahedral grid of the car body. The boundary layer grid is divided into some small blocks according to the topology of the car body geometry. By adjusting the nodes of the blocks, the quality of the hexahedral grid can be improved.

Particular attention is paid to the grid refinement at the train nose and the bogie cavity regions. Three refinement boxes have been used as sketched in Figure 6.3. Refinement box1 wrapping the whole car body has the greatest grid size, while refinement box3 covering the cowcatcher and bogie cavity region, which are the focus of these simulations, has the finest grid.

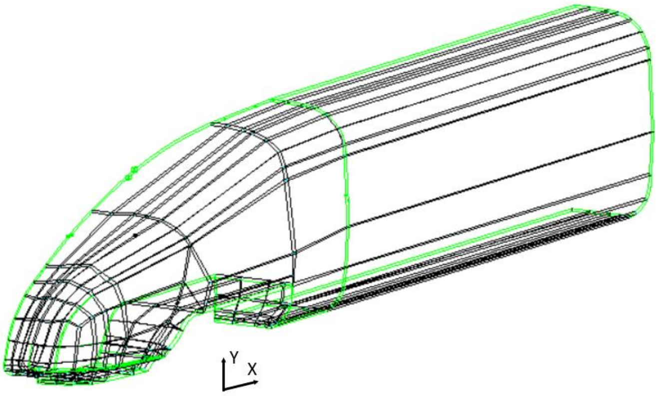

Figure 6.2 Grid blocks of the car body (half-width)

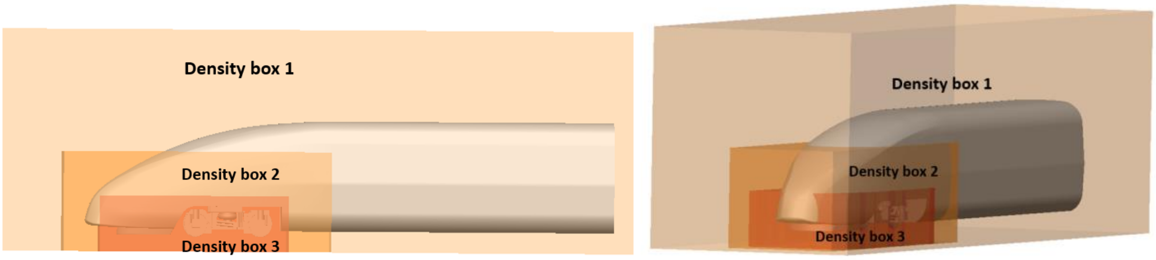

(a) side view (b) oblique view

Figure 6.3 Sketch of the refinement boxes used in the model

Figure 6.4 shows the structured mesh on the model surface. For the bogie, its geometry and the distribution of the structured mesh are all the same as described in section 5.1.2. In addition, the grid parameters of the structured mesh are the same as those listed in Table 5.7. When generating the structured mesh of the car body, to get a good connection with the unstructured grid, the ratio of the edges of the surface cells should not exceed 3. As shown in Figure 6.4(b), the grid size of the train nose and the cowcatcher is refined compared with that of the rear part of the car body as those locations are targeted regions. The minimum 'Equiangle skewness' of the grid of 0.4 has been achieved and the minimum Determinate is 0.7. The definition of the 'Equiangle skewness' and Determinate can be found in ICEM (2019).

The grid distribution inside the bogie is illustrated in Figure 6.5 by three slices identified in Figure 5.7. As shown in Figure 6.5(a) and(b), in some areas, there is some transitional hexahedral volume grid between the hexahedral boundary layer grid and the polyhedral grid. This configuration is beneficial to the grid quality near the interfaces and avoids the possible effects on the flow bought by the grid transition at the interface; these interfaces are usually close to the solid boundary where the flow is changing with a large gradient. In other areas, where there is no space for the structured volume grid, such as the wheel surface which is close to the axle box in Figure 6.5(b) and the cavity roof in Figure 6.5(c), the structured boundary layer grid is directly connected to the polyhedral volume grid. The height of the outermost structured cell, which is close to the interface, is critical as it affects the orthogonality of the polyhedral grid near the interface. Therefore, there should not be a big disparity between the volumes of the hexahedral grid and the polyhedral grid near the interface and thus, there has to be enough hexahedral boundary grid layers to render the grid transition moderate.

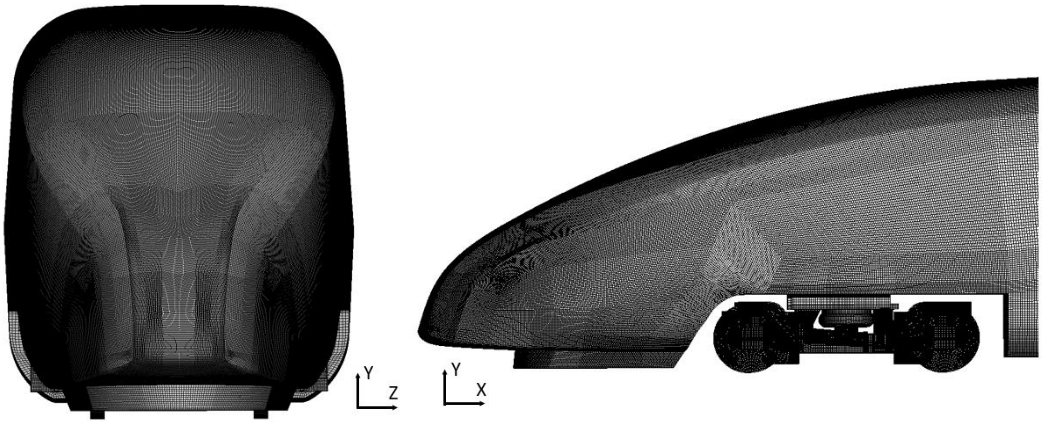

(a) front view (b) side view

Figure 6.4 Grid distribution on the surface of the car body

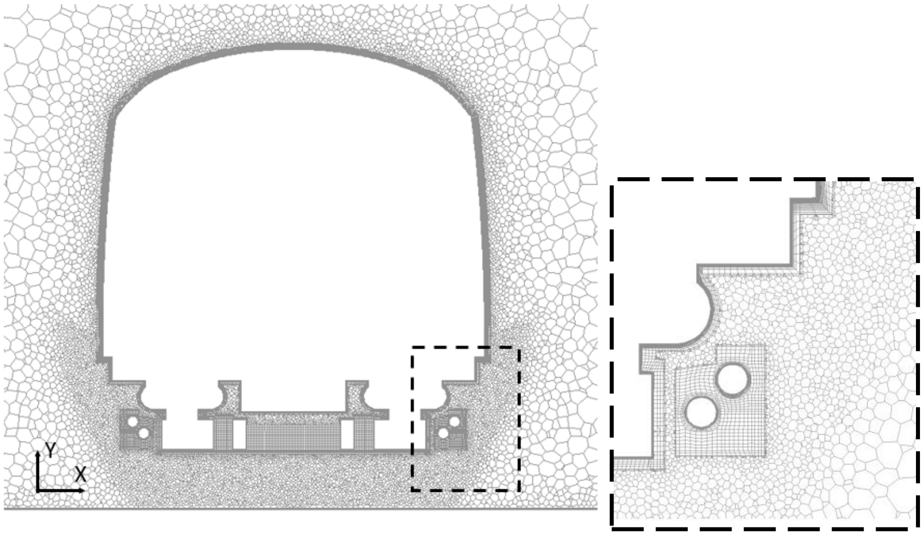

(a) slice X0 and local enlarged view

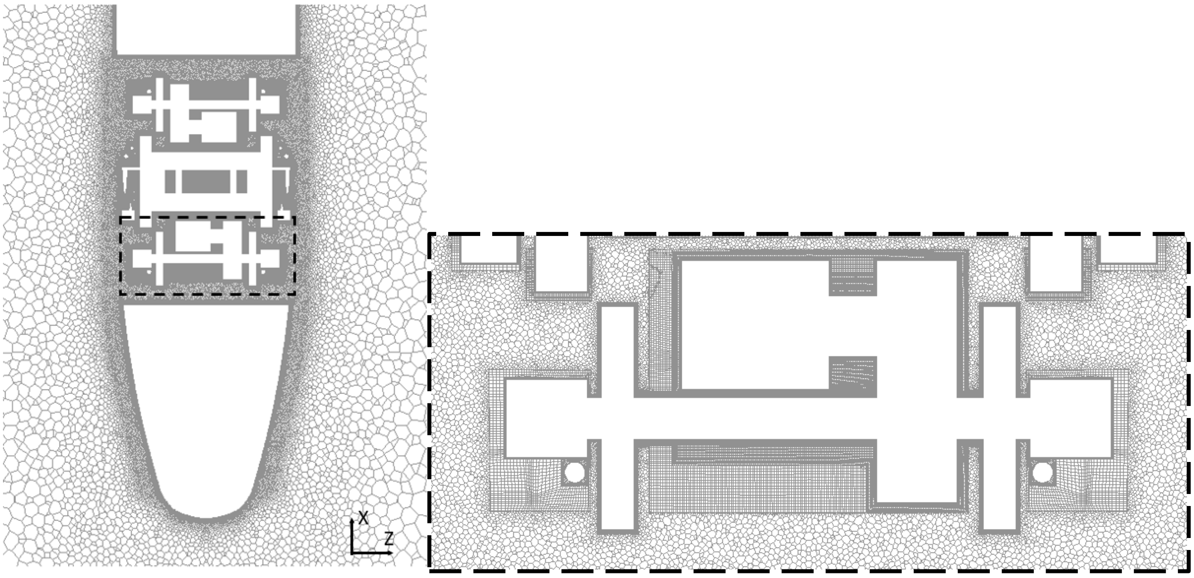

(b) slice Y0 and local enlarged view

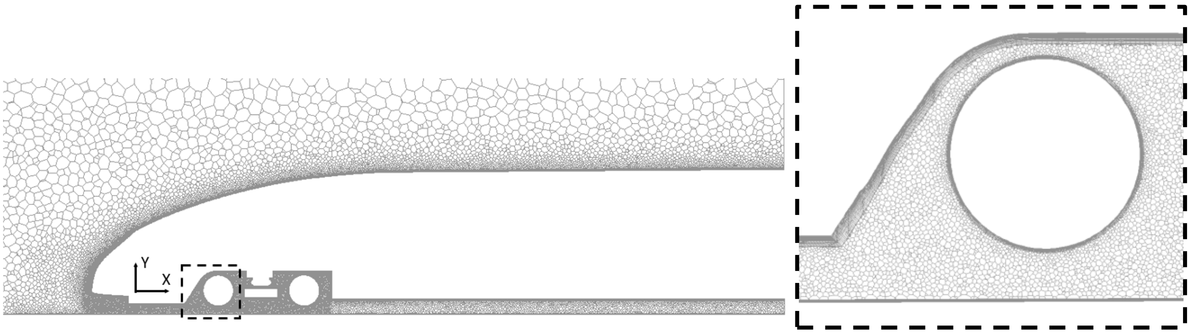

(c) slice Z1 and local enlarged view

Figure 6.5 Mesh distribution on slices identified in Figure 5.7

Before the unsteady simulation, a RANS calculation is carried out to initialize the flow. The implicit iteration PIMPLE algorithm is used, as in Chapter 5. The physical time step is 2×10^{-5} s, which guarantees a *CFL* smaller than 5. The numerical schemes for the temporal scheme, the divergence term and convection term are the same as those discussed in section 5.1.1.

6.2 Grid dependence study of leading car

A half-width model of the leading car, as visualized in Figure 6.6(a), which has no bogie in the cavity, is used to conduct the grid dependence study. The hexahedral boundary layer grid is generated from the blocks shown in Figure 6.2. Table 6.1 describes the main parameters of the cases of considered in the grid dependence study. The hexahedral grid is refined only along the spanwise and streamwise directions and not in the wall normal direction, where the first grid layer is chosen to guarantee a value of y^+ smaller than 1 and the expansion ratio is 1.1. The size refinement ratio of the tetrahedral cell is around 1.4 and the refinement boxes, visualized in Figure 6.3, are refined by 1.3. Compared with the baseline case, the cowcatcher and train nose areas are refined for the ‘front-fine’ case, while for the ‘volume-fine’ case the volume boxes are refined. When calculating those cases, the *CFL* is always maintained well below 5, as discussed in Chapter 5.

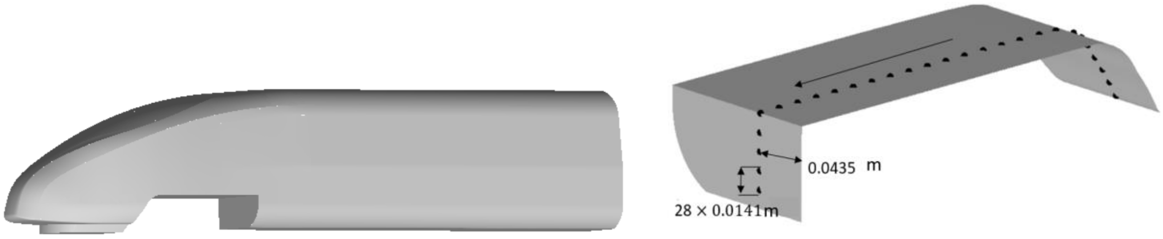

(a) half-width car body model (b) monitors on the cavity roof (1/12 scaled)

Figure 6.6 3D model used for grid dependence study and pressure monitors on the cavity roof

Table 6.1 Grid parameters of the grid dependence study cases of the car body

	Aspect ratio			Density (mm)			Number of cells (million)	
Case name	Cowcatcher	Cavity	Nose	Box1	Box2	Box3	Hex-grid	total grid
Fine	110	140	85	1.5	7.5	22.5	8.2	15.5
Front-fine	112	164	95	2.0	10.0	30.0	5.4	10.1
Volume-fine	152	220	115	1.5	7.5	22.5	4.3	9.9
Baseline	152	220	115	2.0	10.0	30.0	4.3	8.4
Coarse	235	333	175	2.67	13.3	40.0	2.1	3.9

Table 6.2 compares the mean and rms values of the drag and lift coefficients. The prediction of the mean values lies within 5% of the fine case for all cases, except for the coarse case. For the rms value, which is much more sensitive to changes in the grid than the mean value, there are greater differences of up to 25% for the ‘front-fine’ case because of the grid is not uniformly refined. However, for the baseline and ‘volume-fine’ cases, the difference is within 15% and their parameters should be given priority in the discretization of the full-width model.

Table 6.2 Summary of the car body force coefficients of different cases

	C_d	C_l	Difference (%)		$C_{d,rms}$	$C_{l,rms}$	Difference (%)	
Fine	0.136	-0.132	-	-	0.0124	0.0209	-	-
Baseline	0.139	-0.129	2.3	-2.0	0.0140	0.0218	13.4	4.3
Front-fine	0.140	-0.130	3.4	-1.3	0.0154	0.0227	24.8	8.5
Volume-fine	0.139	-0.130	2.0	-1.1	0.0135	0.0214	8.8	2.2
Coarse	0.151	-0.133	11.3	1.1	0.0148	0.0245	19.5	17.1

As shown in Figure 6.6(b), 23 pressure monitors are set on the cavity roof and 5 on the rear wall of the cavity. The monitors are uniformly distributed by an interval of 0.0141m at 1/12 scale and numbered from upstream to downstream. Figure 6.7 shows the time-averaged and rms values of the monitored pressure. For the time-averaged values, a good agreement is found between all cases. However, for the rms value, from points 12 to 18, a maximum difference of 20% is found between the fine case and the other cases, and there is a maximum difference of 15% between the case ‘front-fine’ and fine case after point 18.

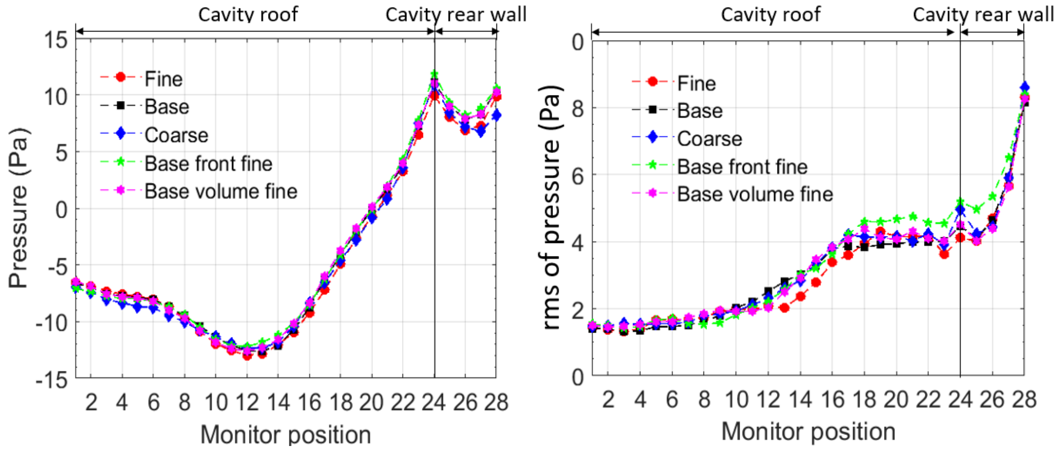

(a) time-averaged value (b) rms value

Figure 6.7 Mean and rms pressure at the monitors on the roof and rear of the car body cavity

Figure 6.8 shows contours of the time-averaged streamwise velocity and the location of the cavity recirculation vortex on the symmetry plane. The shear flow detached from the cowcatcher is accelerated because of the small gap between the cowcatcher and the ground. This flow feature will be critical for bogie noise generation. The comparison shown in Figure 6.8 shows that the jet flow under the cowcatcher is consistently predicted in all simulations, giving consistent locations of the vortex core.

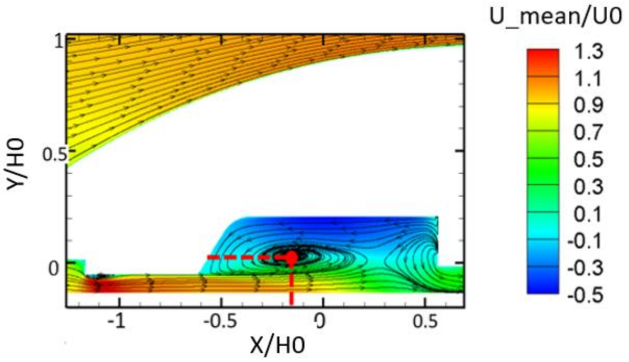

(a) case Fine

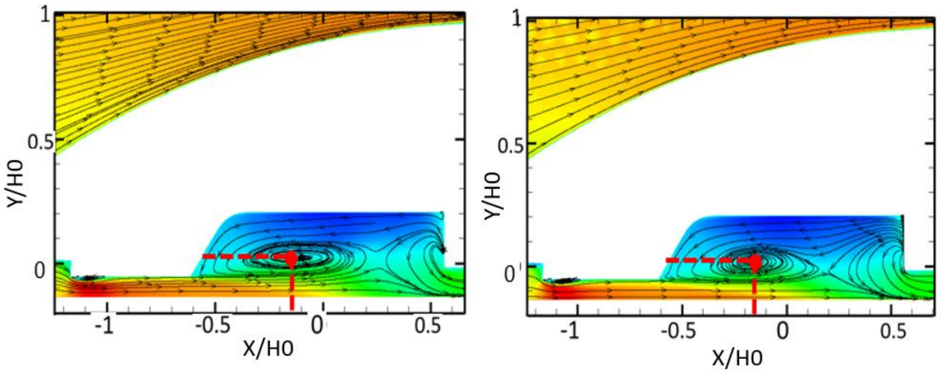

(a) case medium (b) case Coarse

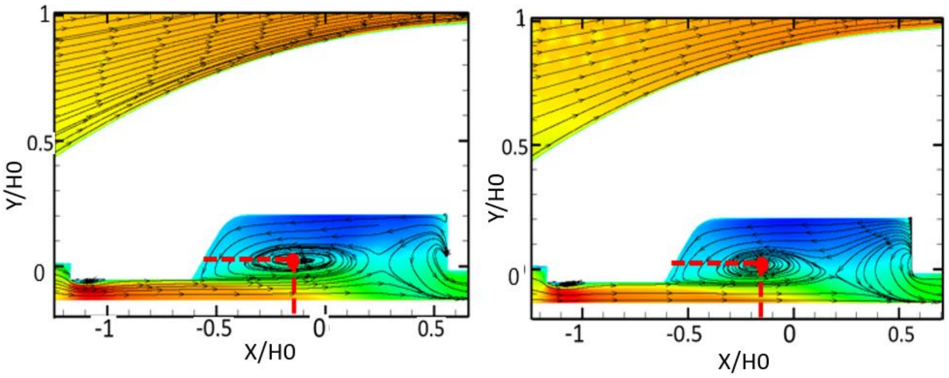

(a) case Front-fine (b) case Volume-fine

Figure 6.8 The average streamwise velocity and the location of the recirculation vortex inside the cavity, H_0 is the height of the car body as shown in Figure 6.1

Figure 6.9(a) shows the far field noise directivity of the five cases, which is computed at the receivers depicted in Figure 5.18. Although the directivity patterns are similar, radiated pressure in the comparison cases, especially for the coarse case, are over-predicted compared with the fine case. A good agreement is found for the other three cases; the maximum difference between them and the fine case is only about 1 dB. Figure 6.9(b) shows the noise spectra at the top receiver. The noise spectra at the top receiver are shown in Figure 6.9(b). The spectrum the of the coarse case has some significant deviations, with over-predicted values in the region 20 Hz to 40 Hz and above 400 Hz.

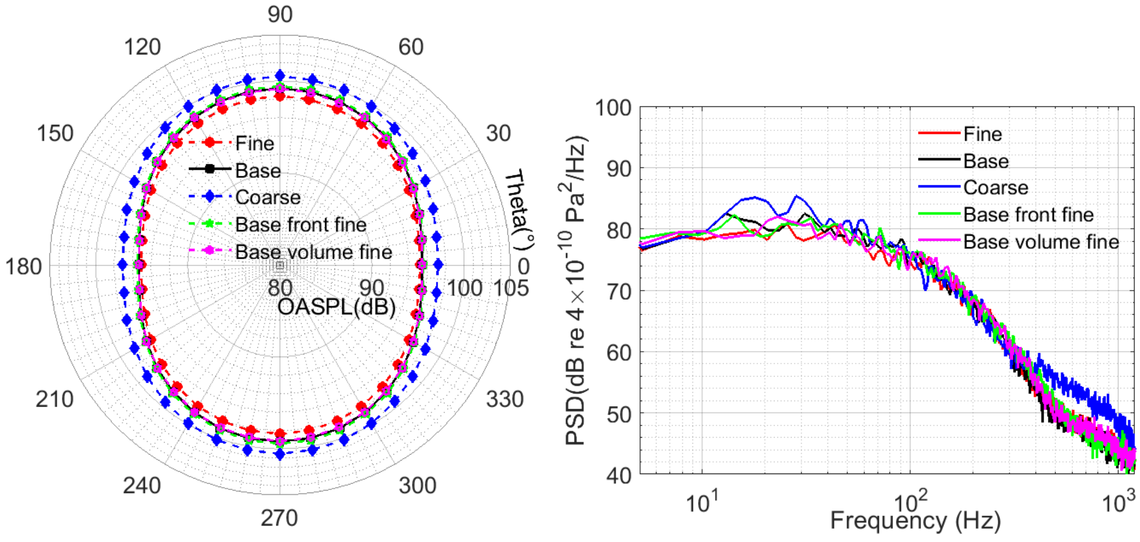

(a) far field directivity (b) noise spectra at top receiver

Figure 6.9 Noise comparison of the car body cases with different grid density

In conclusion, according to the comparison results, the coarse mesh over-predicts both the rms values of the force coefficients and the noise levels. For the case 'front-fine', although there is an over-prediction of the drag coefficient, it is still acceptable because the noise is well predicted. Therefore, the grid parameters for cases baseline, 'front-fine', and 'volume fine' are all considered to be acceptable. Those parameters will be used, together with the structured grid generation approach used around the bogie, as discussed in Chapter 5, in the following simulations on the full-width model with the bogie present in the cavity.

6.3 Aerodynamic results

Following the grid dependence study of the leading vehicle, the grid density of the baseline case is chosen. To improve the grid quality in the connection with the bogie grid, some local variations in grid density are applied to the car body between the ones of the cases 'front-fine' and 'volume-fine'. The same hexahedral grid density is used for the bogie as listed in Table 5.7. The total number of cells in the model is about 36.4 million. The total simulation time is around 4.3 s corresponding to 25 flow-through times of the length of the car body in the model. The data collection is started when the simulation becomes statistically steady, which takes about 0.6 s, and it is stopped after the collected force coefficients achieve statistical convergence as discussed in section 5.2.3. The computational wall-time is approximately 650 hours with 640 processors on the Iridis5 cluster at the University of Southampton.

6.3.1 Summary of force coefficients

Table 6.3 summarizes the mean and rms values. As in equations (4.6) and (4.7), the forces are normalized by $\frac{1}{2}\rho U_0^2 A$, where ρ is the mean air density, 1.225 $\mathrm{kg/m^3}$. U_0 is the free stream velocity and A is the area of the cross-section of the rear car body. It is noted that the absolute mean values of C_d and C_l of the car body are much greater than those of the bogie, the rms values about twice those of the bogie. This is because the car body has a larger area and moreover most parts of the bogie are shielded by the cavity, and thus, the high-speed flow cannot directly impinge on them. Compared with the absolute values of the mean drag force coefficient C_d and the lift force coefficient C_l, the values of the side force coefficient C_s are much smaller. However, the fluctuation in the side force is comparable with those of other two forces, which indicates that although most of the geometry of the model, especially for the car body, is symmetric, there still are lateral oscillations caused by the flow instability, such as the separation, detachment or impingement.

Table 6.3 Summary of force coefficients

	C_d	C_l	C_s	$C_{d,rms}$	$C_{l,rms}$	$C_{s,rms}$
Bogie	0.00351	-0.00662	0.000598	0.00264	0.00286	0.00316
Car body	0.110	-0.118	-0.00077	0.00555	0.00688	0.00547
Total	0.113	-0.125	-0.00017	0.00480	0.00749	0.00647

The PSD of the force coefficients of the car body and the bogie are presented in Figure 6.10. The calculation is based on Welch's method with a Hanning window. The width of the window is about 0.4 s corresponding a frequency resolution of 2.5 Hz and the segment overlap is 50%. No appreciable peak is identified in the spectra, which implies there is no large regular vortex shedding in the flow field. The spectra drop for frequencies above about 100 Hz so that the values at low frequency are greater than those at high frequency, which indicates that the large scale flow patterns, such as the big vortex and the low frequency flapping and impingement, are playing a major role in the flow field. Thus, greater dipole noise can be expected at these low frequencies.

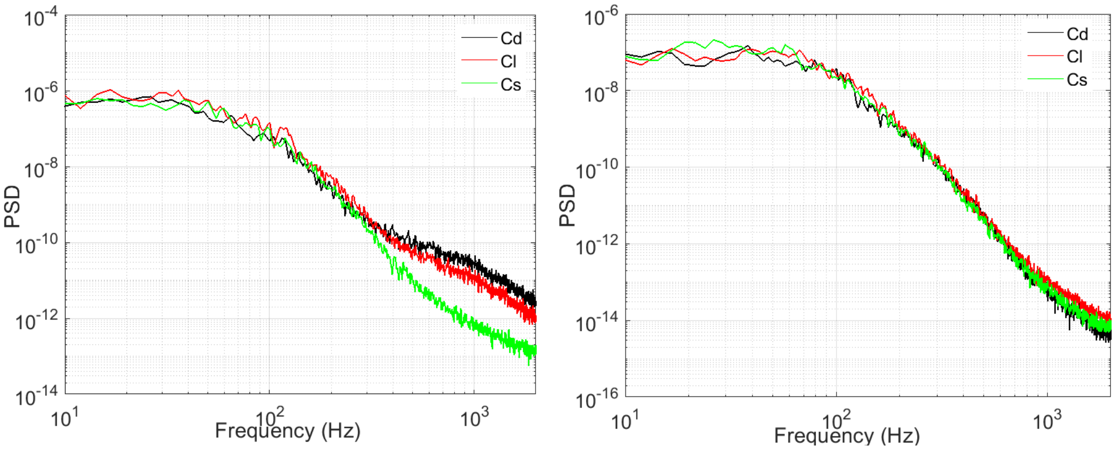

(a) leading car body

(b) bogie

Figure 6.10 PSDs of force coefficients of the model with the model frequency.

6.3.2 Analysis of flow field

Figure 6.11 depicts the time-averaged streamlines around the leading car. In Figure 6.11(a), the flow at the bottom is very complex. The incoming flow is divided by the front face of the cowcatcher, as indicated by the red arrows. Part of the flow separates at the front edge and other parts flow to the two sides of the cowcatcher. The stream separating at the front edge of the cowcatcher flows to the bottom of the bogie and is expected to impose great influence on the flow field there. In Figure 6.11(b), it can be noted that the flow at the side of the cavity consists of two parts. One is from the streamlines divided by the train nose, some of which enters the cavity and forms the vortices at the rear cavity as indicated by the blue arrows in Figure 6.11(c). The other part is formed from that split by the front face of the cowcatcher, which forms the vortices at the front of the cavity, as indicated by the red arrows in Figure 6.11(c).

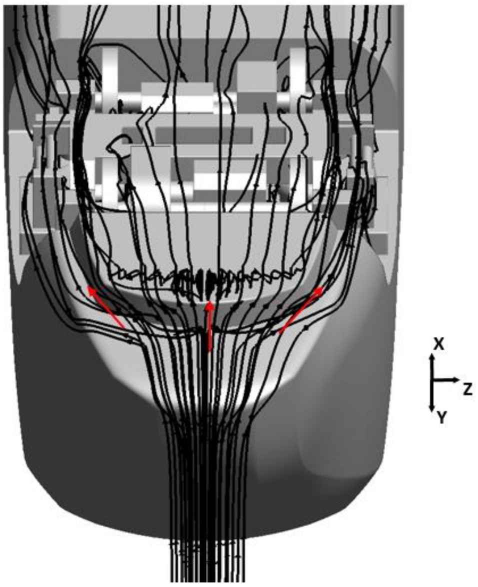

(a) streamlines at the bottom

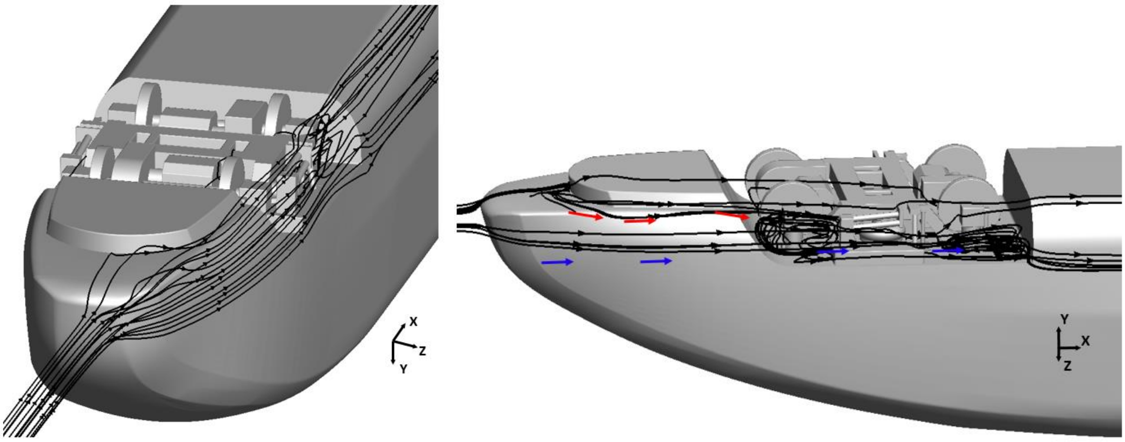

(b) streamlines at side surface

(c) streamlines of vortex in the cavity

Figure 6.11 Time-averaged 3D streamlines for flow over the leading car.

Figure 6.12 depicts the normalized time-averaged streamwise velocity field and streamlines on the slices defined in Figure 5.7. It can be seen from Figure 6.12(a), the horizontal slice at the height of the centre of the axles, that the flow is divided by the train nose and the flow speed ratio at the front edge of the cavity increases to 1.1 because of the curvature of the train nose. The shear layer formed at the train nose surface detaches from the front edge of the cavity. Some low pressure cores, as shown by the pressure coefficient in Figure 6.13(a), are identified as shear vortices (Minelli et al. 2020). These vortices are produced by the Kelvin-Helmholtz instability of the shear layer, which can also be found in some separated shear layers from bluff bodies (Brun et al. 2008). Thereafter, the detached shear layer accelerates the flow close to the two sides of the cavity because of the role of viscosity and will disperse when flowing in the downstream direction. This is the reason why the flow speed at the two sides of the cavity is greater than that in the middle area. Some large vortices are formed, especially at the rear part of the cavity, during this momentum transmission from the outside to the inside of the cavity. In Figure 6.12(b) and(c), vertical slices at the bogie centre and at the wheel position, it is noted that the incoming flow is accelerated by about 25% through the bottom of the cowcatcher because of the reduced gap between the cowcatcher and the ground. Moreover, as shown in Figure 6.13(b), there is a separation zone formed directly after the front edge of the cowcatcher. The blockage due to the separation zone increases the flow velocity underneath the cowcatcher further. Subsequently, when the flow leaves the cowcatcher and enters the cavity, the flow is suddenly expanded and slows down, especially towards the rear part of the cavity. Compared with the two sides of the cavity, there is more flow entrainment into the cavity through the bottom, as shown in Figure 6.12(b) and (c). Inside the cavity, the flow recirculates from the rear part to the front part around the cavity roof at a much lower speed.

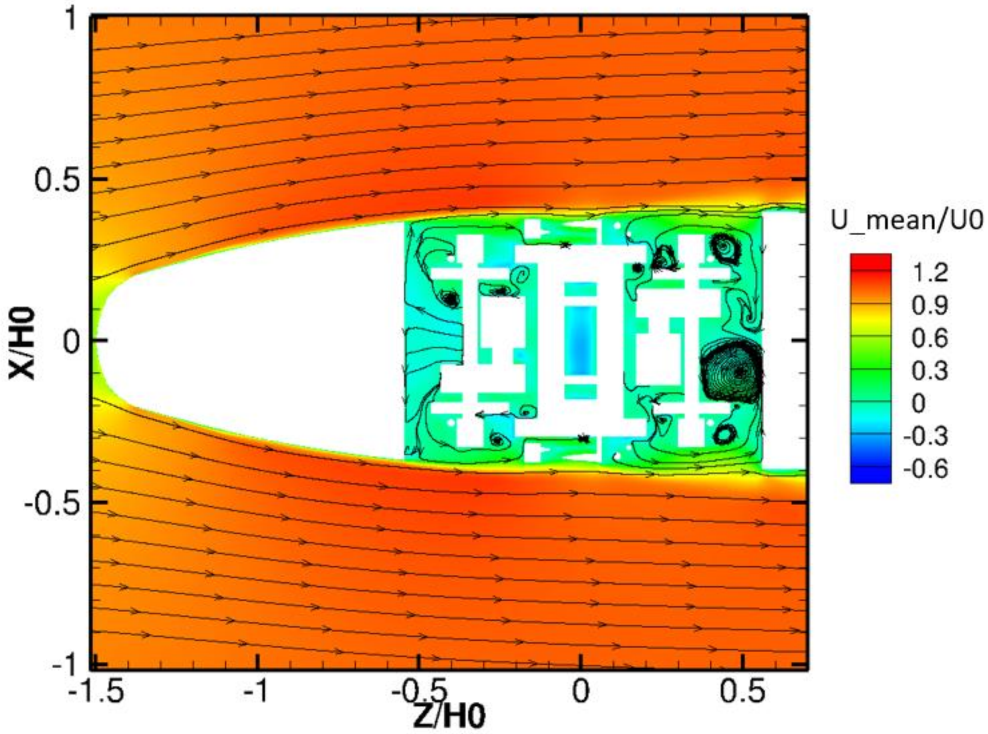

(a) Y0

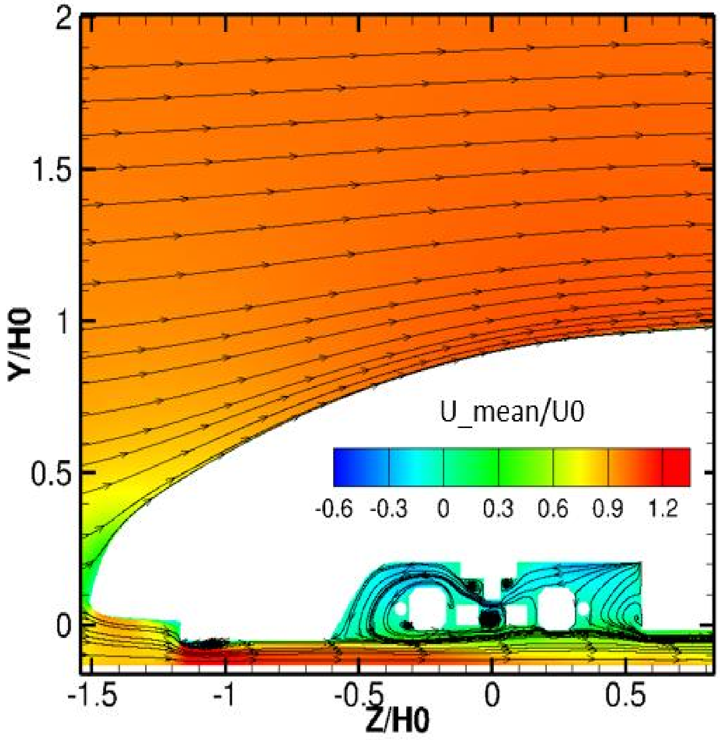

(b) Z0

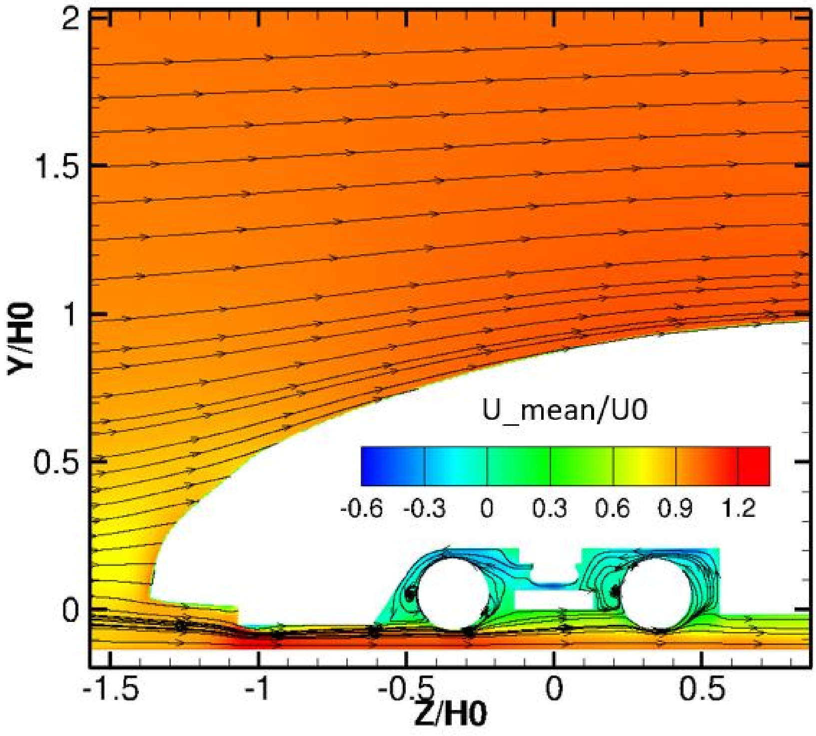

(c) Z1

Figure 6.12 The average streamwise velocity contour and the streamline on slices defined in Figure 5.7, H_0 is the height of the car body as shown in Figure 6.1

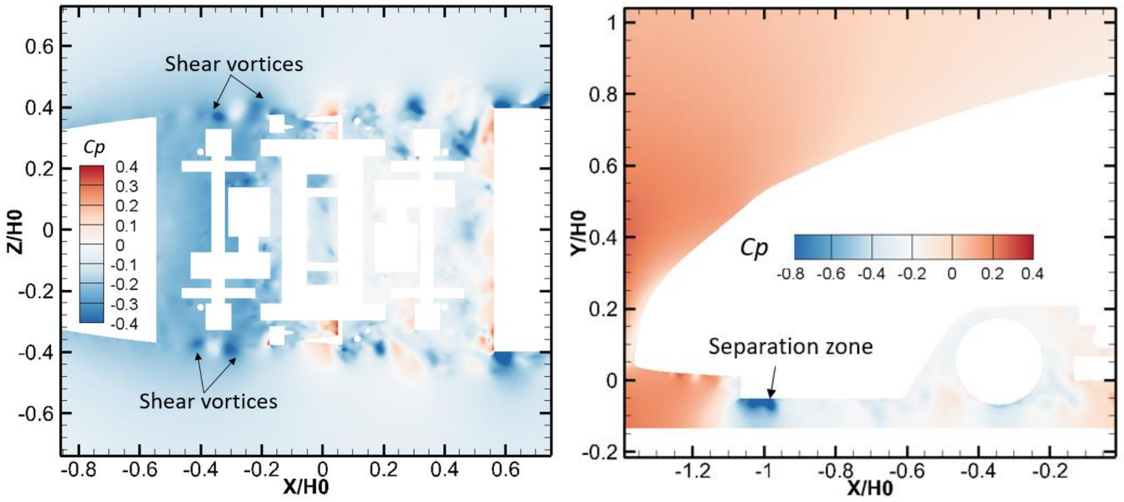

(a) Y0

(b) Z1

Figure 6.13 Instantaneous field of pressure coefficient C_p on slices Y0 and Z1 defined in Figure 5.7, H_0 is the height of the car body as shown in Figure 6.1

Figure 6.14 visualizes the instantaneous flow structure, represented by the iso-surfaces of the normalized second invariant of the velocity gradient (Q criterion) at a value of 12, which is based on $Q/(U_0/H_0)^2$, where U_0 is the free stream velocity and H_0 is the height of the car body. The iso-surfaces are coloured by the normalized streamwise velocity U/U_0. Figure 6.14(a) shows the vortices, which originate from the front area of the cowcatcher, at the bottom of the model. As shown in Figure 6.11(a), one part of the incoming flow towards the cowcatcher separates at its front edges and generates a highly turbulent wake, the other part of the incoming flow is divided by the circular arc of the cowcatcher and separates near the end of the arc and the generated wake is detached from the front edge of the cavity, as shown in Figure 6.14(b). The bogie components are immersed in the highly turbulent wake and face more complex incoming flow than that of the simulated model in the simplified cavity in section 5.3. In addition, it is noted that, compared with the flow developed around the bogie, the vortices dissipate rapidly after the rear of the bogie cavity. It is believed that, considered together with the results shown in Figure 6.12, the rear side wall impedes the further development of the wake, some of it impinges on the wall and deforms largely, and subsequently, enters the cavity (Zhu et al. 2016). This turbulent flow invasion may cause high pressure fluctuations on the upper part of the cavity and the bogie.

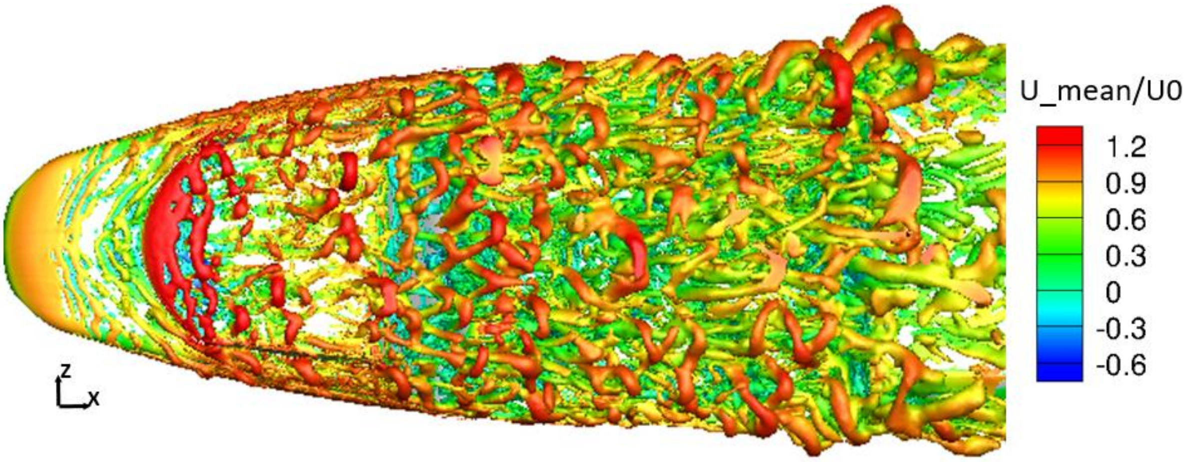

(a) bottom view

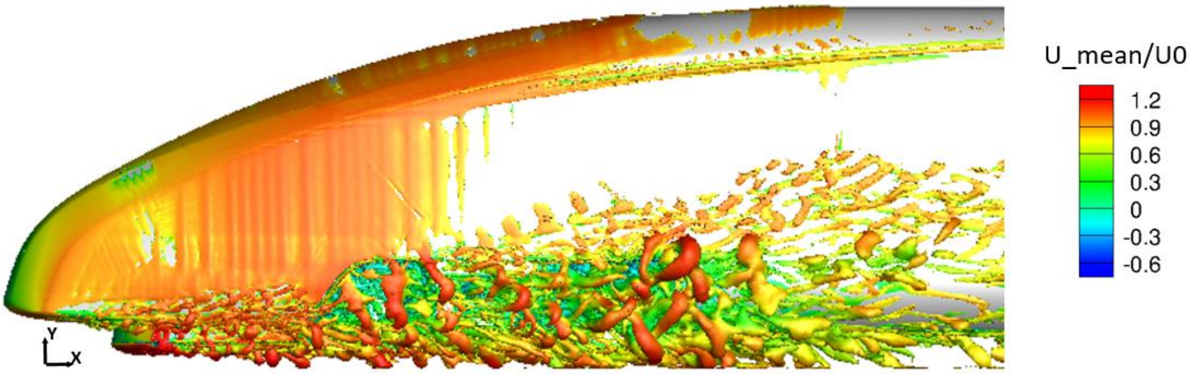

(b) side view

Figure 6.14 Instantaneous flow structures represented by the normalised second invariant of the velocity gradient $Q/(U_0/H_0)^2$, coloured by the ratio of the time-averaged streamwise velocity to the free stream velocity.

Figure 6.15 shows the instantaneous vorticity field on the different slices. It can be seen from Figure 6.15(a) and(b) that the wake separated from the cowcatcher has strong vorticity. It travels downstream and impinges on the lower part of the front components of the bogie, including the front motors, wheels and the bottom of the frame. This impingement increases the turbulence intensity of the wake flow and disperses it in a wider direction. As a result, more of the rear bogie components are immersed in the turbulent wake and the pressure oscillation on them is the origin of the main dipole source. A similar phenomenon can be noticed in the horizontal slice, as shown in Figure 6.15(c). The detached shear layer at the sides interacts with the side dampers and the axle boxes, which makes its turbulent wake have a wider influence region. This is the main reason why it can be observed that the rear part of the cavity has a greater vorticity flow than that at the front part.

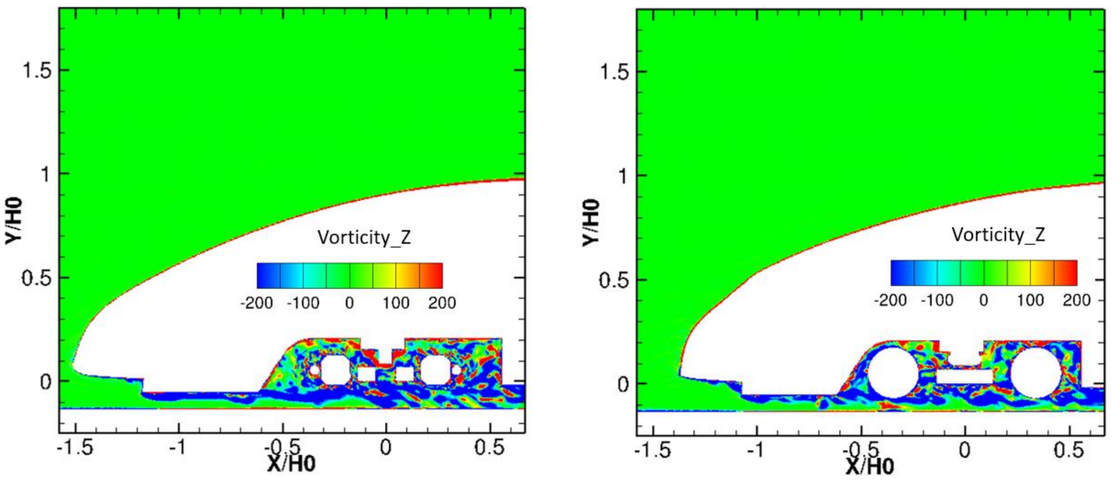

(a) Z0

(b) Z1

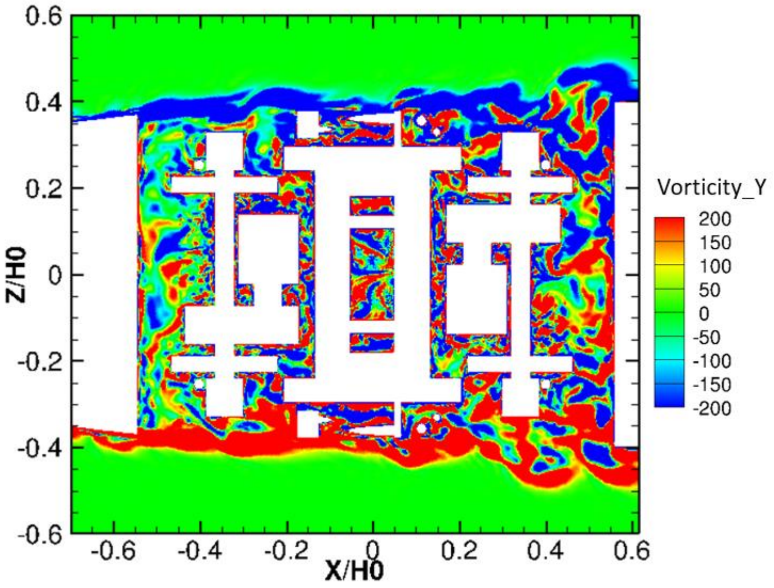

(c) Y0

Figure 6.15 Contours of instantaneous vorticity field on slices defined in Figure 5.7, H_0 is the height of the car body as shown in Figure 6.1

From the discussion above, it can be pointed out that the detached shear layer from the two sides of the cavity and the wake flow formed at the bottom of the cowcatcher are critical to the local flow around the bogie region and also, it can be expected, to the generation of pressure fluctuations there. Nevertheless, it is worth mentioning that, in reality, there are rails located directly below the wheels, and thus, the local flow behaviour around the bottom of the wheels will be slightly different.

6.3.3 Analysis of noise source

The flow field around the bogie is complex as displayed above; the resulting pressure oscillations on the solid boundaries become the source of the radiated dipole noise. The mechanism of the generation of the dipole noise source is the presence of the solid boundaries, which creates or augments noisy flow features such as unsteady separation and vortex shedding (Wang et al. 2005) or impingement. To identify the regions with strong noise sources, Figure 6.16 displays the level of the pressure rate of change dp/dt, which is integrated from 20 Hz to 1600 Hz by equation (3.37), and the overall level of this quantity $L_{\dot{p}\_total}$, which is calculated by equation (3.38). It can be observed that the bottom of the model, including the cowcatcher and the bottom of the bogie components, forms very strong pressure fluctuations. The reason is, as shown in Figure 6.14(a) and Figure 6.15(a) and(b), that this area has a very strong interaction with the highly turbulent wake separated from the front edge of the cowcatcher. It is noted that, compared with the pressure fluctuation distribution on the bogie in the simplified cavity, as shown in Figure 5.28(b), stronger pressure fluctuations are observed on the bogie surfaces, especially for the front components. Although the bottom of the cowcatcher is at a lower height than that of the bottom of all bogie components apart from the wheels, it seems the bottom components are not benefiting from this shielding. This is due to the sudden flow expansion behind the cowcatcher, which makes the jet under the cowcatcher expand when entering the bogie region and consequently, the turbulent wake is brought into the cavity. Another area with strong pressure fluctuations is the area around the side components, such as the lateral dampers, the vertical dampers, and the side parts of the bolster. This area is mainly affected by the shear layer detached from the two side edges of the cavity, as shown in Figure 6.15(c). The lateral dampers, which directly face the detached shear layer, are almost all covered by a strong pressure fluctuation distribution. Moreover, the rear wall of the cavity also has a strong pressure fluctuation distribution. As discussed above, the presence of the rear wall of the cavity has a great influence on the pressure fluctuation distribution on the bogie and the cavity. On the one hand, it impedes the further development of the turbulent wake towards downstream and strong pressure fluctuation on the wall is produced by the impingement from the wake; on the other hand, the impeded wake flow forms vortices in the rear part of the cavity, as shown in Figure 6.12(a), and consequently, the rear part of the bogie has a greater area covered by strong pressure fluctuations.

Based on this analysis, the wake flow at the bottom, the detached shear flow at the two sides, and the presence of the rear wall of the cavity are the most important factors that affect the generation of the noise. In the noise reduction study in Chapter 8, some measures will be developed to reduce the noise level based on these observations.

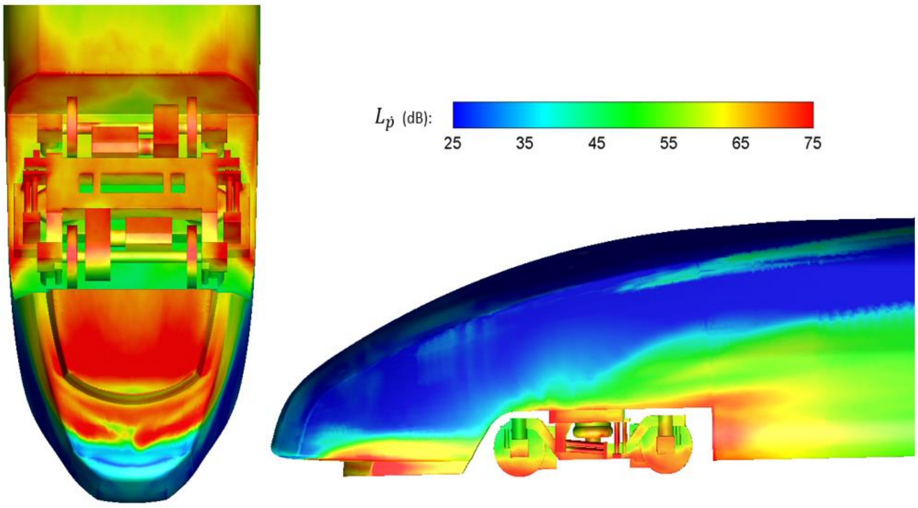

(a) bottom of the model (b) side of the model

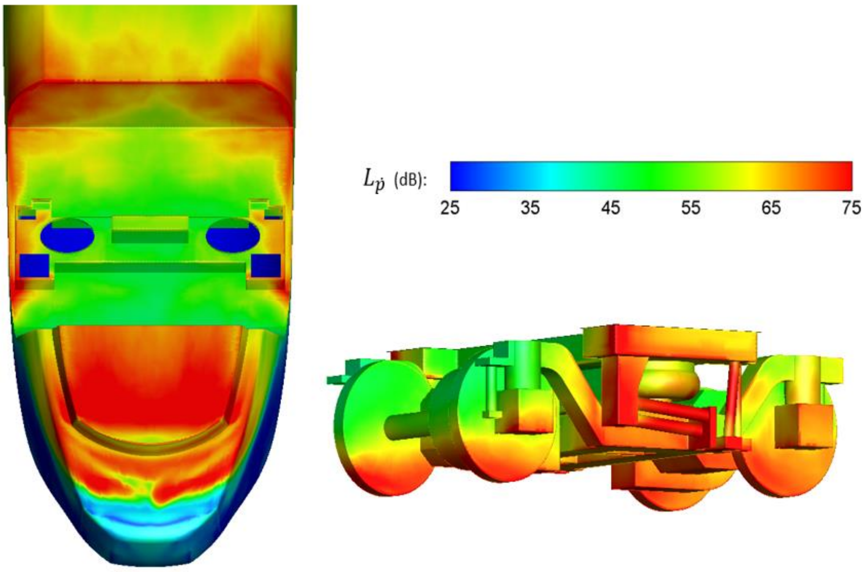

$L_{\dot{p}\_total}$ =62.5 dB $L_{\dot{p}\_total}$ =60.5 dB

(c) bottom of the car body (d) side of the bogie

Figure 6.16 Surface contours of the pressure rate of change dp/dt on the bogie components integrated from 20 to 1600 Hz

Figure 6.17 to Figure 6.20 show the level of the pressure fluctuation distribution on the car body and the bogie, integrated over different frequency bands. In Figure 6.17 and Figure 6.18, the pressure fluctuation on the bottom of the cowcatcher and the rear wall of the cavity is seen to be significant. Compared with the rear wall of the cavity, the pressure fluctuation on the bottom of the cowcatcher has energy in a wider frequency range, which is from 60 Hz to 600 Hz. This is because the turbulent wake that separates from the front edge of the cowcatcher, as shown in Figure 6.14(a) and Figure 6.15(a) and(b), has a wide range of scales of vortices, which produce pressure fluctuations by flapping on the bottom of the cowcatcher. Conversely, the pressure fluctuation distribution on the rear wall of the cavity is generated by the wake of the unstable detached shear layer, as shown in Figure 6.14(b) and Figure 6.15(c), and the large scale vortices at the rear part of the cavity, as shown in Figure 6.12, produced by the impeded bottom wake flow. Therefore, for the rear wall of the cavity, the pressure fluctuation is only strong in the frequency range 60-200 Hz and mainly contributes the noise at low frequencies. $L_{\dot{p}\_total}$ of the car body shows it has the highest overall level, 58.5 dB, in the frequency range 20-200 Hz although the one in the range 200-400 Hz is very similar, at 58.3 dB. Of the power in the low frequency range, Figure 6.18 shows overall level in the range 120-200 Hz has the highest value, 55.9 dB.

For those bogie components that are immersed in the turbulent wake flow, such as the gear boxes, the motors, the wheels and the side dampers, the source strength contains contributions over a wider frequency range, whereas the upper parts of the bogie only contribute to noise at low frequencies. The overall level from the frequency range 20-200 Hz is the highest, 57.8 dB and, more specifically, the highest contribution is 54.7 dB from 120-200 Hz.

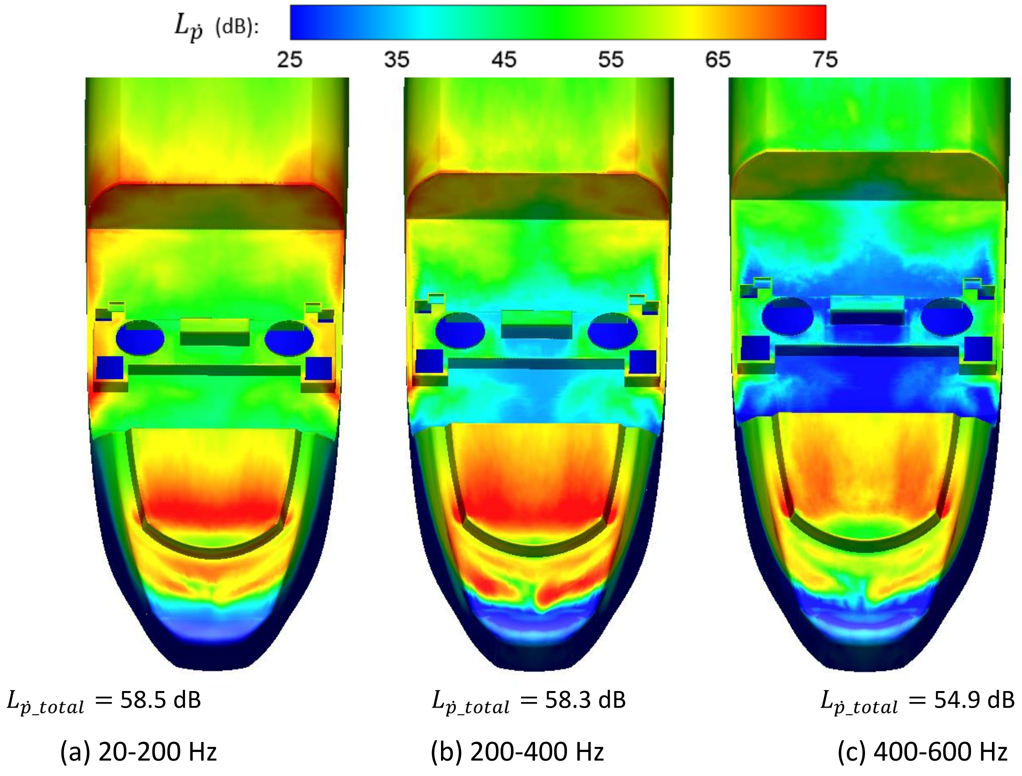

(a) 20-200 Hz (b) 200-400 Hz (c) 400-600 Hz

Figure 6.17 Surface contours of the pressure rate of change dp/dt on the car body integrated from 20 to 600 Hz (bottom view)

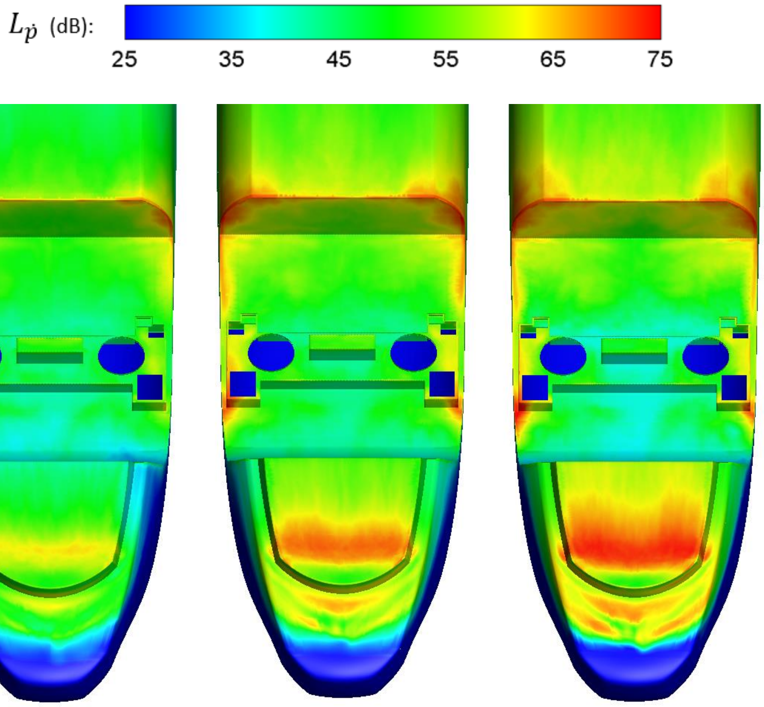

$L_{\dot{p}\_total} = 48.7$ dB
(a) 20-60 Hz

$L_{\dot{p}\_total} = 53.9$ dB
(b) 60-120 Hz

$L_{\dot{p}\_total} = 55.9$ dB
(c) 120-200 Hz

Figure 6.18 Surface contours of the pressure rate of change dp/dt on the car body integrated from 20 to 200 Hz (bottom view)

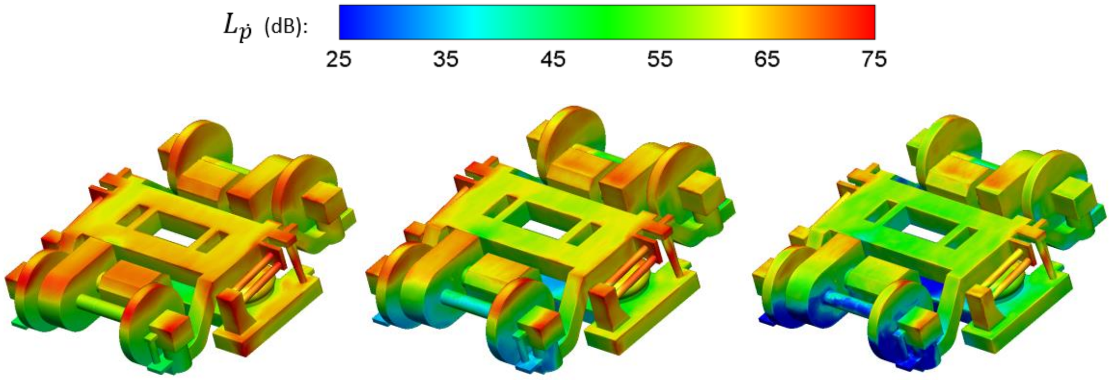

$L_{\dot{p}\_total} = 57.8$ dB
(a) 20-200 Hz

$L_{\dot{p}\_total} = 55.6$ dB
(b) 200-400 Hz

$L_{\dot{p}\_total} = 51.2$ dB
(c) 400-600 Hz

Figure 6.19 Surface contours of the pressure rate of change dp/dt on the bogie integrated from 20 to 600 Hz (bottom view)

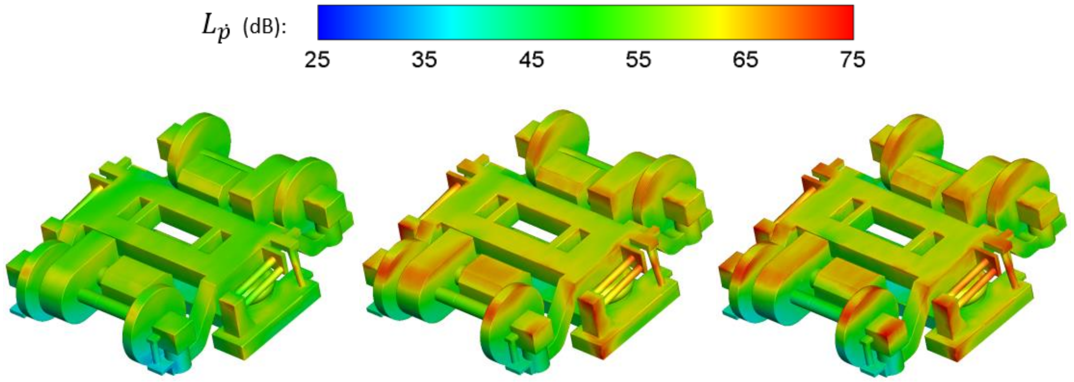

$L_{\dot{p}\_total} = 48.1$ dB $L_{\dot{p}\_total} = 54$ dB $L_{\dot{p}\_total} = 54.7$ dB

(a) 20-60 Hz (b) 60-120 Hz (c) 120-200 Hz

Figure 6.20 Surface contours of the pressure rate of change dp/dt on the bogie integrated from 20 to 200 Hz (bottom view)

6.4 Aeroacoustic results

The collection of the pressure fluctuation on the model surface starts from 0.6 s, with a total sampling time of about 3.7 s, corresponding to 21 flow-through times of the length of the car body model. The collected pressure fluctuation is taken as the input to the FW-H equation to predict the far field noise, assuming free space propagation. To investigate the noise directivity at the plane normal to the streamwise direction, receivers are specified on a circle, as illustrated in Figure 5.19. Besides that, 26 receivers as shown in Figure 6.21 are set to investigate the noise at the side of the model. These side receivers are located at 20 m away from the bogie centre and at the same level as the 0° receiver in Figure 5.18 . After getting the noise levels and spectra, they are converted to full scale and full speed by using equation (5.1) and (5.2). It should be pointed out that the small differences in source-receiver distance will lead to level differences of less than 0.3 dB (the furthest receiver is 20.8 m from the source, 20log10(20.8/20) = 0.3 dB) due to geometrical attenuation and the convective amplification, which has an effect around ±3dB at two of the furthest receivers from the source, is also not considered.

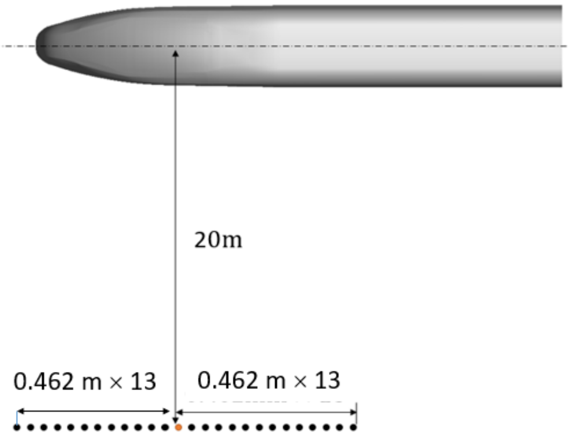

Figure 6.21 Sketch of the location of the side receivers

6.4.1 Sound pressure levels

Figure 6.22 shows the 1/3 octave noise spectra of the bogie, the car body and their combined spectrum at the side receiver (0°) shown in Figure 5.18. The PSD is first calculated based on Welch's method using a Hanning window with a 50% overlap for each segment to get a smooth spectrum. The length of each segment is about 0.4 s, resulting in a frequency resolution of 2.5 Hz. Then, the noise spectra in narrow band are converted to 1/3 octave bands. No discrete peaks are found in the spectra and, thus, they are broadband. The noise spectrum of the car body is greater than that of the bogie at all frequencies. Moreover, it is noted that the noise levels around 100 Hz have greater values than those of other frequency regions. A similar conclusion can be found in the experiment conducted by Lauterbach et al. (2010).

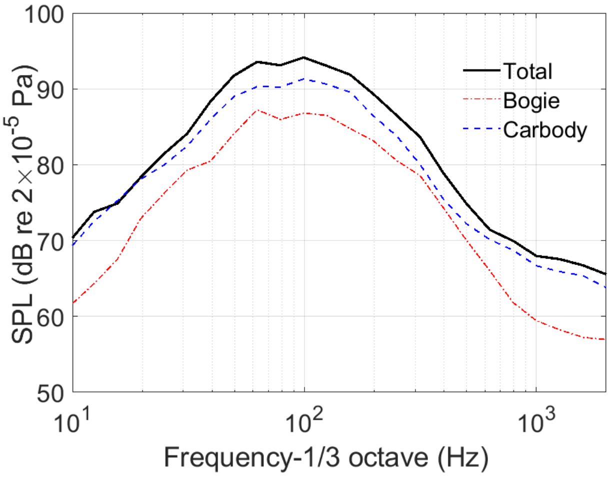

Figure 6.22 Noise spectra (1/3 octave) of the model at the receiver at 0°

Figure 6.23 shows the overall noise levels of the car body, the bogie and the total at the side receivers and on the circle of receivers. Generally, it is noted that the noise levels generated by the car body are greater than those generated by the bogie, with a difference of about 5 dB at the side receivers. The reason is because most of the bogie is shielded from the incoming flow by the cavity and the flow speed inside the cavity is much lower than that outside, as shown in Figure 6.12. In Figure 6.23 (a), the values of the noise levels at the side of the model have a maximum difference between them of less than 1 dB. Also, in Figure 6.23(b), the noise directivities are almost omnidirectional. The noise directivity of the bogie in the simplified cavity, showed earlier in Figure 5.34 had a typical dipole pattern, with larger values in the vertical direction. By contrast, in Figure 6.23(b), it has slightly greater values in the lateral direction. It is believed the greater pressure fluctuation strength on the upstream wheels and the side surface of the end plates of the lateral damper, as shown in Figure 6.16(d), is the reason for the difference.

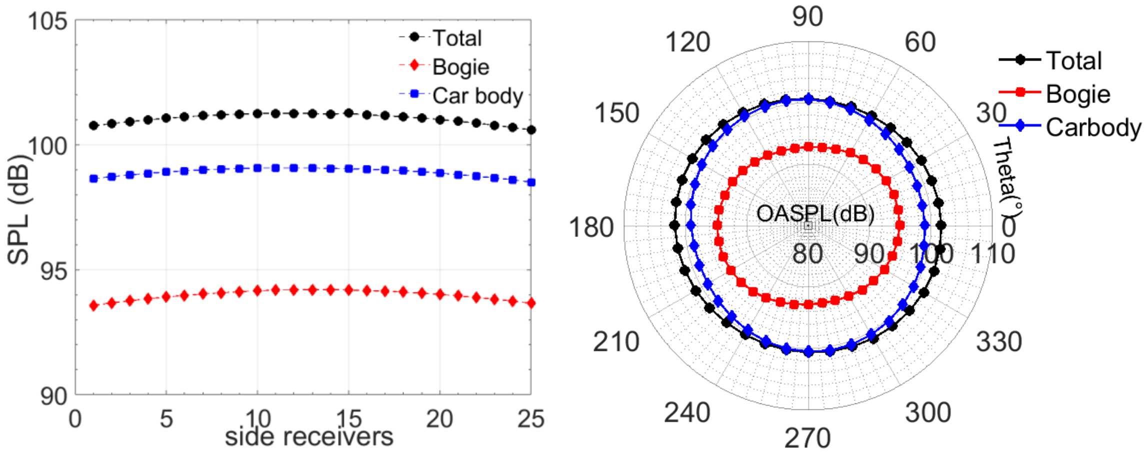

(a) side noise levels

(b) noise directivity

Figure 6.23 The far field noise directivity and side noise level

The noise directivities of the upstream dynamic system, frame system and downstream dynamic system, the parts of which are depicted in Appendix A, are shown in Figure 6.24. The upstream and downstream dynamic systems have greater noise levels in the lateral direction and their values are much closer than those in Figure 5.38 for the simplified cavity. The reason is the incoming flow from upstream, which is separated from the front edge of the cowcatcher, has higher turbulence than that detached from the front rim of the simplified cavity. In addition, as shown in Figure 6.15(a) and(b), the wake becomes unstable after developing for some distance in the streamwise direction and is flapping in the vertical direction and, consequently, it can affect a greater area on the upstream dynamic system. It is also noticed that the upstream and downstream wheelsets have the greatest values in the lateral noise levels of the dynamic systems and the wheels are inferred to be the main contribution area according to the pressure fluctuation distribution shown in Figure 6.16(d). The noise directivity of the frame system has the greater values in the vertical direction in Figure 6.24. Figure 6.25(c) shows that, of these components, the frame surface contributes the most in the vertical direction. The pressure fluctuation on the bottom surface of the frame is produced by the flapping of the wake from upstream. In the lateral direction, the lateral dampers have more contribution and the detached shear layer shown in Figure 6.15(c) is the cause of the pressure fluctuation.

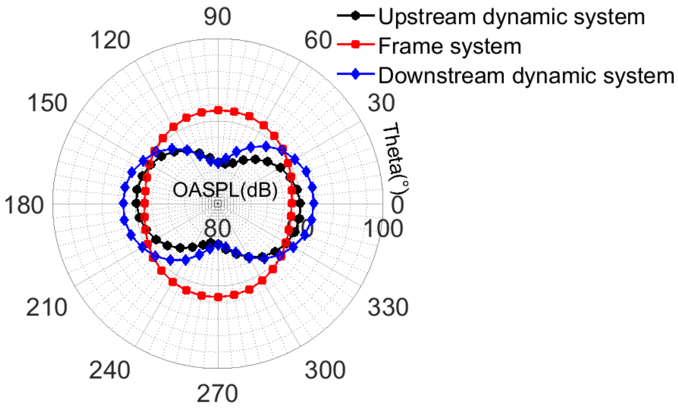

Figure 6.24 The far field noise directivity of different components system

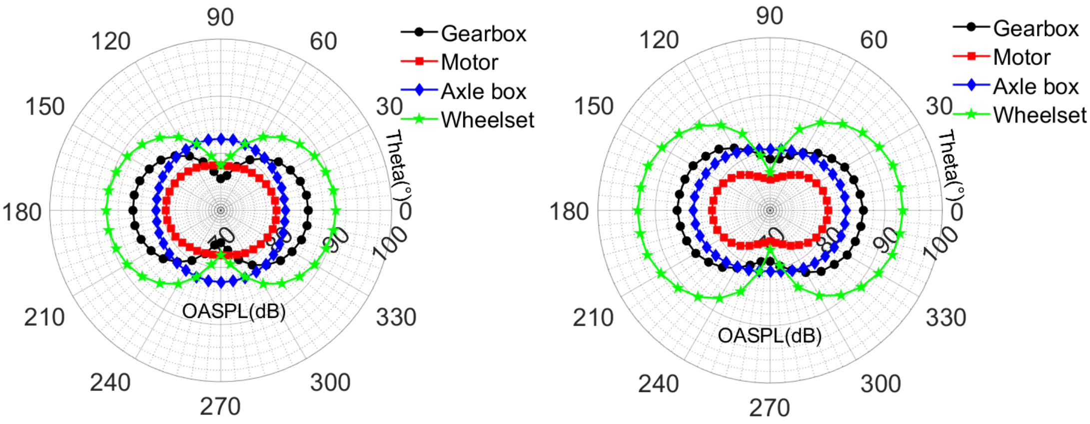

(a) upstream dynamic system (b) downstream dynamic system

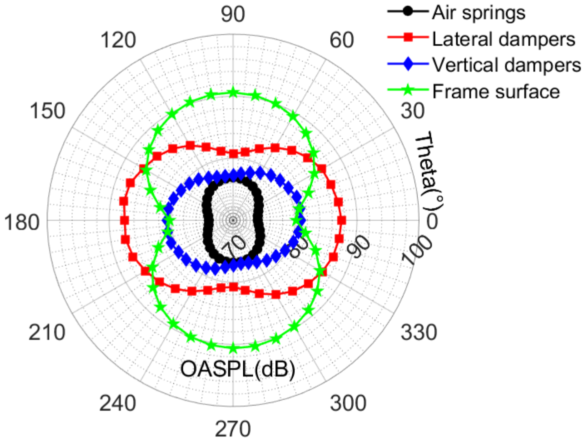

(c) frame system

Figure 6.25 The far field noise directivity of the bogie components

Figure 6.26 summarizes and compares the overall noise levels of every bogie component at the side receiver (0°) and the vertical receiver (90°). At the side receiver, the upstream and downstream wheelsets contribute the most. The lateral side dampers have the largest contribution from among the frame components, contributing a similar noise level to the gearboxes. At the vertical receiver, contributions from the frame surface and the axle boxes are significant, both of which have strong noise sources at their bottom surfaces.

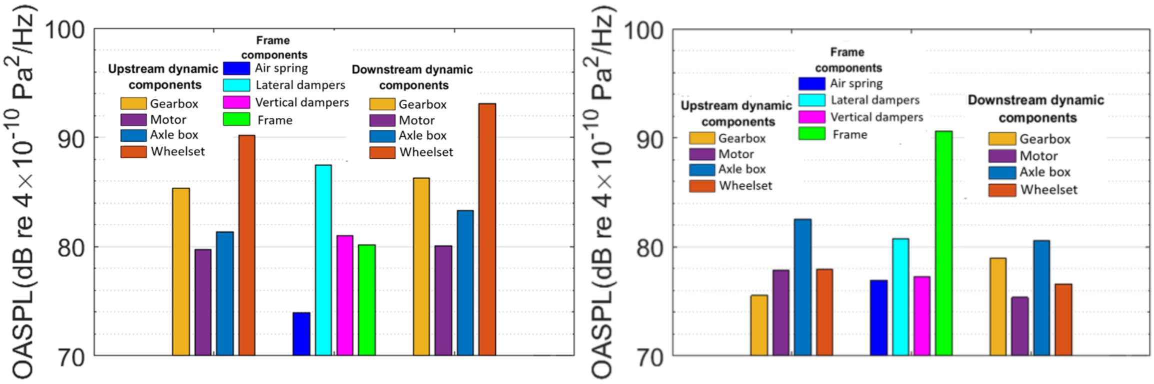

(a) 0 degree

(b) 90 degree

Figure 6.26 Noise levels of bogie components at side and horizontal receiver

6.4.2 Sound power levels

The sound pressure levels have been calculated using a free space assumption. In reality, the car body will shield the sound in the upwards direction and both the car body and the ground will reflect the sound. Nevertheless, the overall sound power of the various sources is expected not to be strongly affected by this limitation in the model.

To understand better the noise contribution from different components and identify the key areas for noise reduction, the sound power level (SWL) emitted by different components is investigated. A sphere with radius 20 m is defined, encircling the model, which is almost uniformly divided into 486 segments. The central point of each segment is taken as a receiver. The SWL is obtained by integrating over all the segments:

$$SWL = 10\log_{10}\left(\oint_S \frac{p_{rms}^2}{\rho c_0} ds\right) / W_{ref} \tag{6.1}$$

where p_{rms} is the rms of acoustic pressure, ρ is the density, c_0 is sound speed, S is the surface of the sphere and ds is the area of each segment, W_{ref} is the reference sound power, 10^{-12} W. This equation is based on the assumption that, sufficiently far from the source, the intensity normal to the sphere can be approximated by $p_{rms}^2/\rho c$.

Figure 6.27 shows the distribution of sound power among the model components. The composition of the components can be found in Appendix A. In Figure 6.27(a), it is noted that the sound power generated by the cavity walls is the highest one and the ground is the next highest. According to the pressure fluctuation distribution shown in Figure 6.16, the rear part of the cavity is the key area that contributes the highest sound power. In addition, the sound power generated by the ground is due to the jet flow at the bottom of the cowcatcher, as shown in Figure 6.12(b) and (c). The sound power emitted by the whole bogie is very similar to that produced by the train nose. Although, there are strong pressure fluctuation regions on the cowcatcher and the car body, as shown in Figure 6.16, their contribution to the sound power is the smaller because the total areas of the regions with high source levels are small.

For the bogie, the sound power contributions of the various components are shown in Figure 6.27(b). The downstream wheelset, the upstream wheelset, the frame and the lateral dampers contribute significantly to the sound power. These four components, as shown in Figure 6.15, are either directly immersed in the highly turbulent wake from upstream, such as the wheelsets and the lateral damper, or have a large surface area interacting with the wake, such as the bottom surface of the frame. The gearboxes and axle boxes, from both the upstream and downstream dynamic systems, have a medium contribution because they are shielded by the cavity but their bottom surfaces are flapped by the wake and generate strong pressure fluctuations, as shown in Figure 6.16, Figure 6.19 and Figure 6.20. The rest of the components, such as the motors, air springs and vertical dampers, are either almost completely shielded by the cavity or upstream components or have a smaller area.

From the analysis above, it can be concluded that the most important regions for the sound power reduction of the whole model are the rear parts, especially the rear wall of the cavity and the ground beneath the cowcatcher and the bogie. The sound pressure generated by ground has a large value in the vertical direction but a very small value in the horizontal direction. In free space, it is therefore not important for the receivers at the side of the bogie, but in terms of sound power it can become important. As for the sound power by the bogie, the components in direct contact with the highly turbulent wake separated from upstream and the shear layer detached from the front edge of the cavity are the most important ones. Noise reduction methods related to these areas will be developed in Chapter 8.

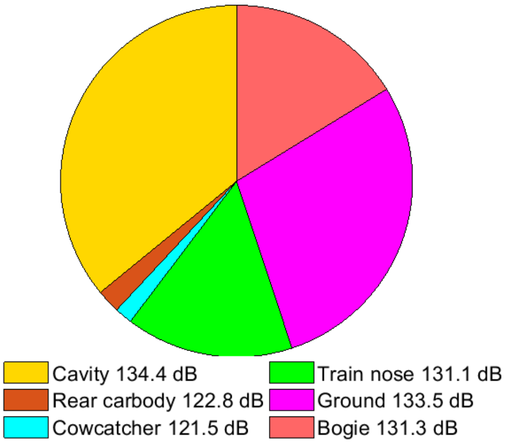

(a) car body components and bogie

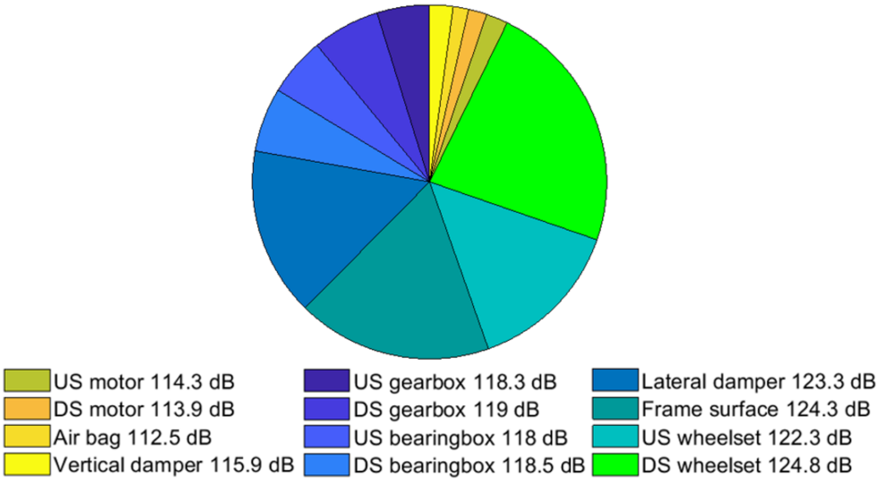

(b) bogie components

Figure 6.27 Proportion of sound power emitted by different components

6.5 Summary

In this chapter, the aerodynamics and aeroacoustics of the bogie under the leading vehicle is simulated. The generation procedure of the hybrid grid system developed in Chapter 5 has been applied to discretise the model in this Chapter. At first, a grid dependence study for the isolated car body is conducted. Five cases are simulated and the results of different grid density for the hexahedral grid near the solid surface and the refinement boxes with different grid densities are compared. From the comparison of the time-averaged value and rms value of the force coefficients, it is concluded that the grid parameters of baseline and 'volume-fine' cases are both acceptable. Then the pressure values at a set of monitors, which are set at the roof of the cavity, are compared. This also shows that the results of the baseline and 'volume-fine' cases are better than coarse and 'front-fine' cases. To compare the internal flow near the bottom region, the core position of the vortex in the cavity is compared. No large difference is found between the different grid densities in the comparison. Finally, the noise directivity and spectra are compared. Compared with the results of fine case, the coarse case is over-predicted by about 3 dB and the other cases are also over-predicted but by less than 1 dB. Therefore, the grid parameters of these three cases are all acceptable when discretizing the car body model. The grid parameters for the bogie are based on those in Table 5.7 derived in Chapter 5.

From the analysis of the aerodynamic force coefficients, it can be pointed out that the bogie contributes much smaller mean forces and smaller force fluctuations than the car body. The PSDs of the force coefficients show that the spectra are dominated by low frequencies, which implies the large scale flow patterns are more effective in the flow field. In the identification of the locations with strong pressure fluctuations, areas that are in direct contact with the highly turbulent wake and detached shear layer have strong pressure fluctuations; this includes the bottom of the cowcatcher and the bogie, the cavity rear wall, and the side dampers. This conclusion clearly indicates that the wake flow separated from the front edge of the cowcatcher and the detached shear layer at the two sides of the cavity are critical to the generation of noise.

After the calculation of the unsteady flow field, the collected pressure fluctuations on the model surfaces are taken as the input to the FW-H equation. The noise generated by the bogie is about 5 dB lower than that from the car body. The reason is that most of the bogie is shielded from the incoming flow by the cavity. The different bogie components have different contributions to the noise levels at the lateral and vertical directions. The upstream and downstream wheelsets have the greatest bogie noise contributions in the lateral direction, while the frame surface has the greatest one in the vertical direction. From this result, it can be concluded that the contribution from a component in a certain direction is determined by both the pressure fluctuation strength and the projected area of the surface in that direction. In the comparison of the sound power contributions from different components, it is found that the cavity and the ground emit the greatest sound power and that from the bogie is 2-3 dB smaller than these two components and comparable with the train nose. For the bogie the wheelsets, the lateral damper and the frame surface make the largest contributions to the sound power.

According to the analysis above, it is not hard to conclude that, for noise reduction, the highly turbulent wake flow separated from the front edge of the cowcatcher and the detached shear layer at the two sides of the cavity are the two critical flow patterns. In addition, the rear part of the cavity and the ground are key regions on which strong pressure fluctuations should be reduced. Therefore, in Chapter 8 noise reduction measures, including disturbing the flow patterns or absorbing the pressure fluctuation on the key regions, will be explored and developed based on the analysis above.

Chapter 7 The effect of side components on the aerodynamic noise generation

The chapter studies the aerodynamic noise from side components of the bogie under a leading car, including the axle boxes, the lateral dampers and vertical dampers. As seen in Chapter 6, on the one hand, the detached shear layer from upstream directly impinges on these side components, as shown in Figure 6.15, thereby generating strong pressure fluctuations on their surfaces, as shown in Figure 6.16; on the other hand, the wake behind them will directly impinge on the rear wall of the cavity, which also generates a strong pressure fluctuation on it, as shown in Figure 6.16. In reality, the relative distance between the side components and the side surface of the coach can vary because of the combination of different car bodies and bogies, which are designed to satisfy the compliance with different loading gauges and track gauges.

In this Chapter, the numerical method developed in the previous Chapter will be adopted to investigate the characteristics of the aerodynamic noise generated in situations with different relative distances between the side components and the side surface of the car body. Four cases with different positions of side components are simulated and their aerodynamic results, such as the force coefficients, flow features and pressure fluctuation distribution, and aeroacoustic results, such as the noise directivities and the sound power levels of different components, will be discussed.

7.1 Computational setup of bogie models with different side component positions

Figure 7.1 depicts the four cases with different relative positions between the side components and the side surface of the car body. In reality, the width of the car body is usually the varying parameter because of different loading gauges. However, in order to keep the shape of the train nose unchanged, in the model the axle of the bogie is extended, similar to the experiments by Latorre Iglesias et al. (2017). The shaft of case m100 is shortened by 100 mm (full scale) compared with the standard case; this represents the case of a narrower track gauge and standard car body width. Compared with standard case, more of the components are shielded by the cavity. In the Cases 200 and 400 the wheels are moved further apart by 200 mm and 400 mm on each side, representing also cases with a smaller loading gauge and standard bogie. With the shaft extension, more bogie components will protrude out of the side of the cavity and an increase can be expected in the speed of the flow impinging on those components.

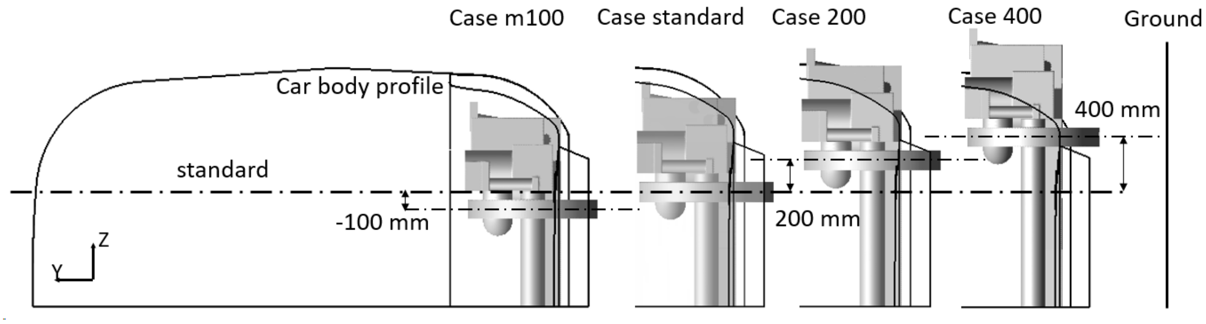

Figure 7.1 Sketch showing the relative positions of the bogie components with respect to the car body for the different wheel axis extensions: -100, 0, 200 and 400 mm (at full scale). End view with vertical direction towards the left of the figure

To reduce the computational cost, the motors and gearboxes of the bogie are omitted. In addition, the half-width car body model used in section 6.2 and the bogie shown in Figure 5.9 are adopted. Figure 7.2 gives the grid distribution on the model surface. The grid parameters of the car body are identical with those of the baseline case in section 6.2 and the grid parameters of the bogie are the same with those of Case Medium1 in section 5.2. The total number of cells of the four cases considered here are very similar, at around 13.9 million.

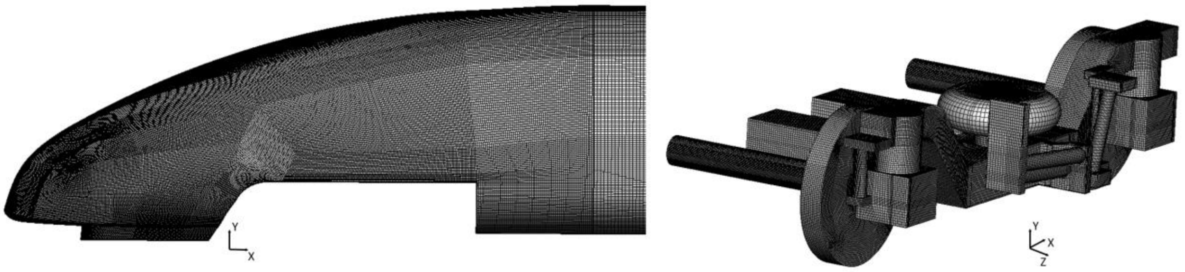

(a) surface mesh on leading car body (b) surface mesh on simplified bogie

Figure 7.2 Grid distribution on the surface of the model

The dimensions of the computational domain are the same as those shown in Figure 6.1 but with only half the width. The boundary conditions are also the same as those used in section 6.2.

A RANS calculation is carried out to initialize the flow field before the unsteady simulation. For the DDES simulations the implicit iteration PIMPLE algorithm is used, as in Chapter 5 and Chapter 6. A physical time step of 2.2×10^{-5} s is chosen to guarantee the *CFL* number remains smaller than 5. The numerical schemes for the temporal scheme, the divergence term and convection term are the same as the ones used in section 5.1.1.

7.2 Aerodynamic results

In order to understand and compare the flow fields of the cases with different side component positions, the simulation results are presented in terms of the time-averaged streamwise velocity contour and streamlines, the instantaneous normalized vorticity field and the pressure fluctuation on the model surfaces. Figure 7.3 displays the streamwise velocity field together with two-dimensional streamlines on an XZ-plane at *y* = 200.9 mm (full scale), as defined in Figure 5.7, for the four cases. Figure 7.4 shows the corresponding instantaneous vorticity fields. For Case m100 and the standard case, the side components are well shielded by the cavity, and thus, as shown in Figure 7.4(a) and (b), and they only face the detached shear layer from upstream and the lower-speed flow accelerated by it. In addition, both Figure 7.4(a) and (b) show the side rim area of the cavity rear surface is also swamped or even impinged by the detached shear layer from upstream. However, for Case 200 and Case 400, as the shaft extension increases, some parts of the side components protrude out of the cavity and even intrude into the free stream. The protruding side components, especially for Case 400, already exceed the detached shear layer region and will directly face the impingement from the high-speed incoming flow. These protruding side components create a low-speed flow zone behind them, which makes the side rim area of the cavity rear wall remain away from the high-speed flow, as shown in Figure 7.3(c) and (d). In Figure 7.4(d), the exposed upstream axle box interrupts the detached shear layer from upstream but also generates separated flow at its rim. However, the turbulent wake of this separated flow seems to stay away from the side rim area of the cavity rear wall and the pressure fluctuation there will also be different from other cases.

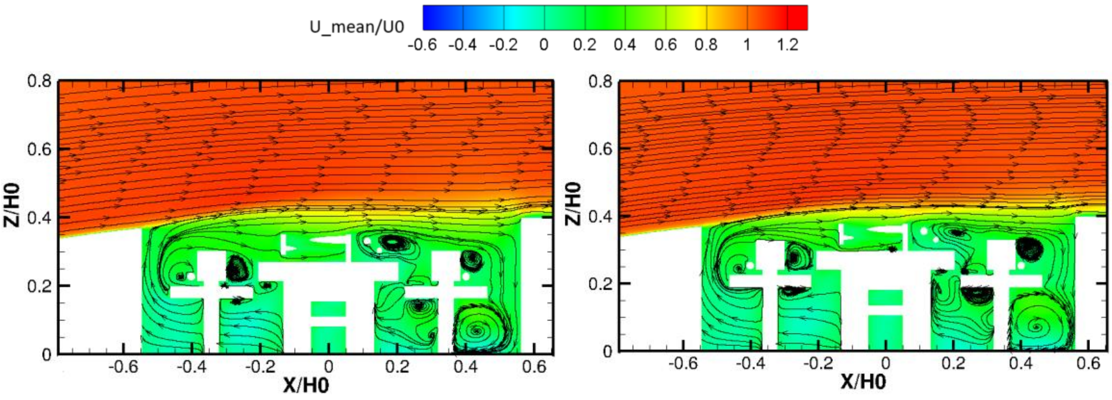

(a) case m100

(b) case standard

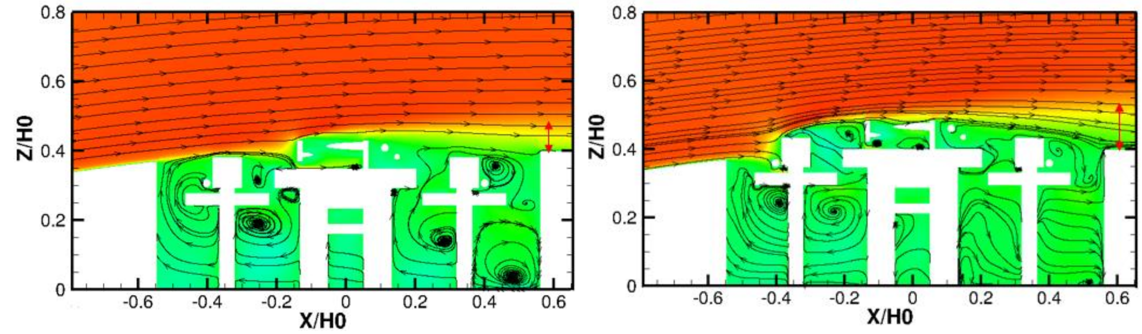

(c) case 200

(d) case 400

Figure 7.3 The average streamwise velocity contour and streamlines of the four cases, H_0 is the height of the car body as shown in Figure 6.1

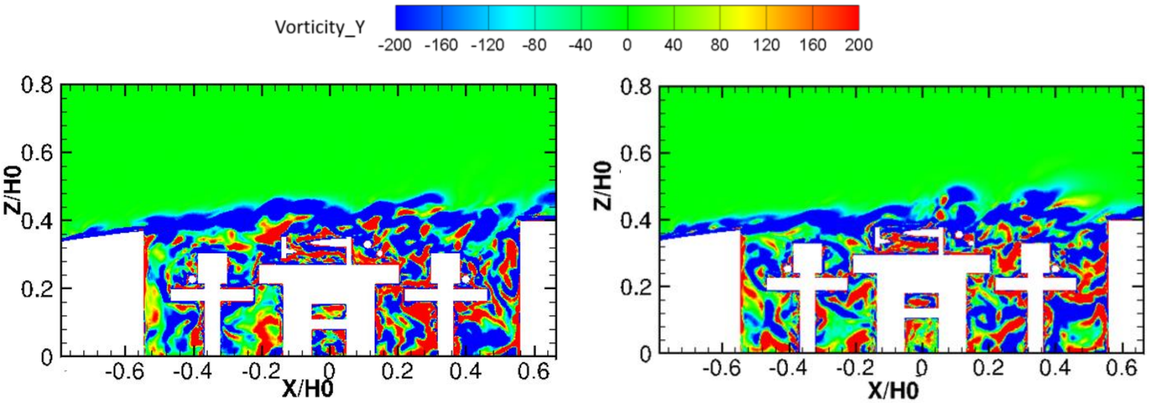

(a) case m100

(b) case standard

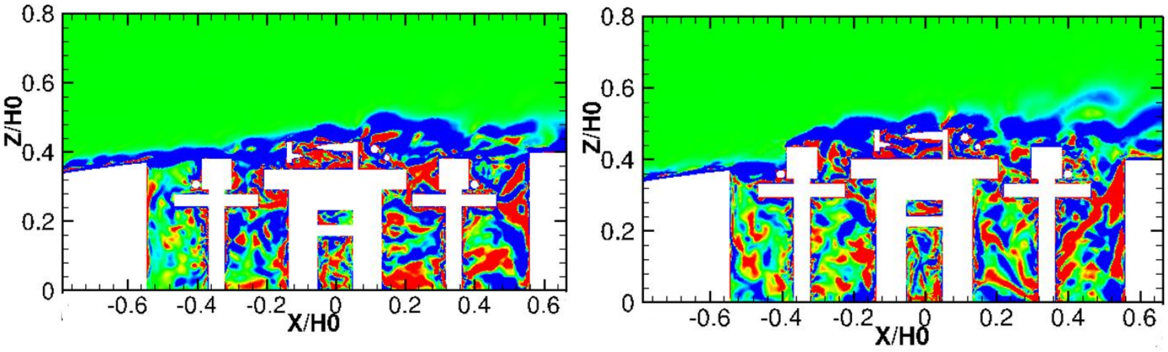

(a) case 200

(b) case 400

Figure 7.4 Contours of instantaneous vorticity fields of four cases, H_0 is the height of the car body as shown in Figure 6.1

Figure 7.5 shows the mean and rms values of the drag (C_d), lift (C_l) and side (C_s) force coefficients from the bogie, car body and the whole model. Equations (4.6) and (4.7) are used to calculate each of the force coefficients. All cases are run for 0.6 s, corresponding to about 16 times flow-through times of the cavity length, to allow the flow field to stabilize before collecting the time histories of the forces. The data are then collected at each time step and the collected time histories of the total forces are divided into three segments, which have 50% overlap between them. It is ensured that the difference between the mean and rms values of each segment is smaller than 5%. The data collection time varies for different cases (from 4.5 to 5.2 s) to ensure that their sampling periods are all sufficient.

Figure 7.5(a) shows that the mean drag coefficient $\overline{C_d}$ of the bogie monotonically increases from a negative value to a positive value. As shown in Figure 7.1, for Case m100, the bogie is completely shielded by the cavity except for the bottom parts of the wheels. However, as shown in Figure 7.3(a) most of the components, which are shielded by the cavity, are affected by the flow circulation inside the bogie cavity, which is believed to make the drag value become negative. As more of the bogie protrudes from the cavity, more components are exposed to the incoming flow, thereby making the mean drag of the bogie increase. Meanwhile, the drag of the car body reduces as the extension of the shaft increases. This is due to the fact that, as shown in Figure 7.3(c) and (d), some parts of the rear surface of the cavity, which are originally impinged by the high-speed wake flow from upstream, are shielded by the protruded side components of the bogie. For Case 400, although, the exposed side components of the bogie reduce the drag of the car body, they also bring a greater increase of the drag to the bogie. Consequently, the mean value of the total drag coefficient is greatest in this case. For the rms value of the drag $C_{d_{rms}}$, as shown in Figure 7.5(b), the values for the bogie have only small variation, while the ones for the car body as well as the total drag reduce significantly from the standard case to Case 400.

In Figure 7.5(c), the mean value of the lift of the bogie is much smaller than that of the car body and the values increase from negative to positive as the exposed parts of the side components increase. There is only a small difference between the values of the total lift in Figure 7.5(c) and the total side force in Figure 7.5(e), which implies that the protruded side components have little effect on the mean value of the lift or side force of the model. The rms values of the total lift in Figure 7.5(d) and total side force in Figure 7.5(f) decrease significantly from Case m100 to Case 400. It is believed that the protruded parts of the side components interrupt the high-speed wake from upstream and reduce the force fluctuations on the car body considerably.

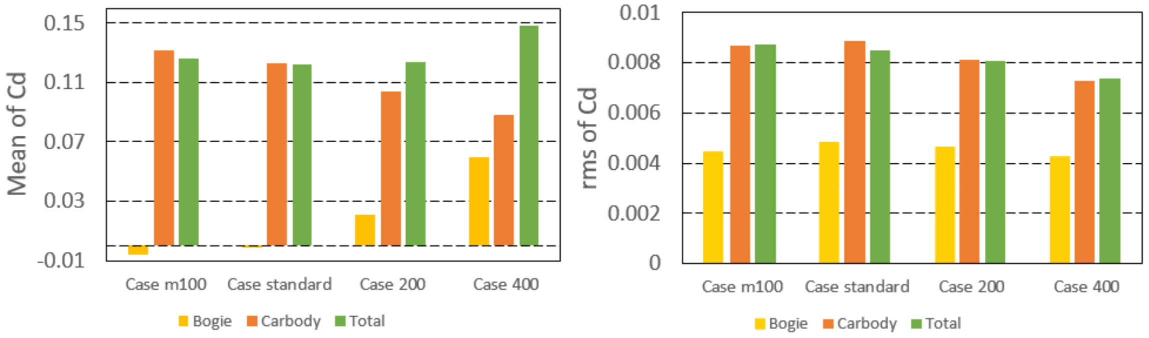

(a) mean value of drag $\overline{C_d}$ (b)rms value of drag $C_{d_{rms}}$

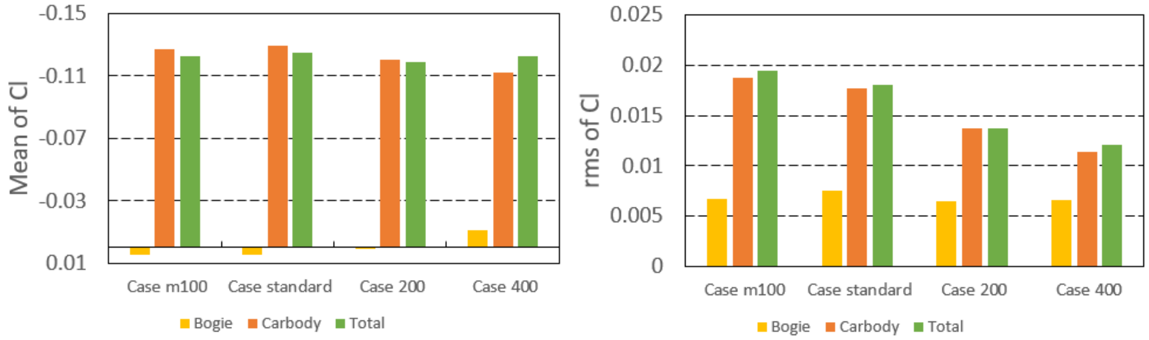

(c) mean value of lift $\overline{C_l}$ (d) rms value of lift $C_{l_{rms}}$

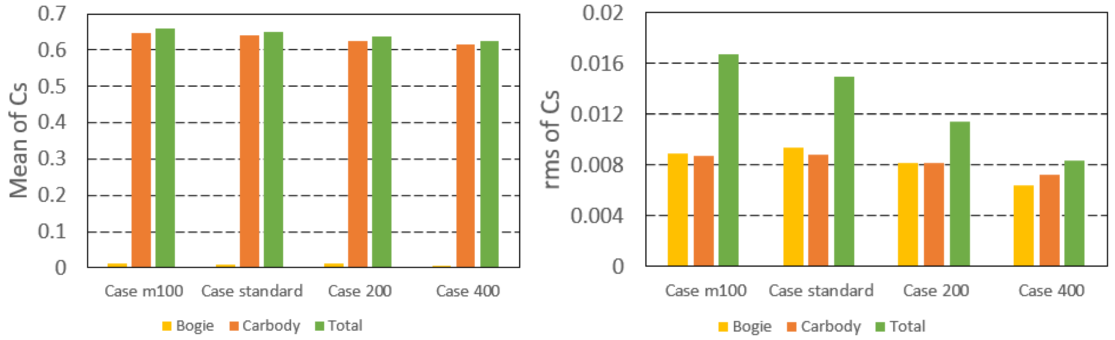

(e) mean value of side force $\overline{C_s}$ (f) rms value of side force $C_{s_{rms}}$

Figure 7.5 Force coefficients for different side component positions

The PSDs of C_d, C_l, and C_s are shown in Figure 7.6. The calculation is based on Welch's method with a Hanning window with 50% overlap between 19 segments. The width of the window is about 0.4 s corresponding a frequency resolution of 2.5 Hz. Figure 7.6(a) shows the three force coefficients for the bogie, Figure 7.6(b) shows them for the car body and Figure 7.6(c) shows the total.

For the spectra of the bogie force coefficients, as shown in Figure 7.6(a), all three spectra for Case 400 have greater values, compared with the other three cases, for frequencies 100 Hz to 2000 Hz and smaller values below 100 Hz. This is produced by the flow pattern in which the high-speed incoming flow directly impinges on the protruding components and separates at some of their edges. Compared with the flapping or impingement by the detached shear layer from upstream, the flow separation on the side components produces smaller vortices, which have a smaller length scale. For the spectra of the force coefficients of the car body, as shown in Figure 7.6(b), it seems that Case 400 has smaller values at frequencies below 100 Hz and as well as frequencies greater than 300 Hz, especially for the drag spectra. In the flow field, shown in Figure 7.3(c) and Figure 7.3(d), the protruding components prevent the rear region of the cavity from being impinged or flapped by the detached shear layer from upstream. The spectra of the total force coefficients in Figure 7.6(c) have a similar trend with the ones of the car body because the force contribution from the car body is dominant.

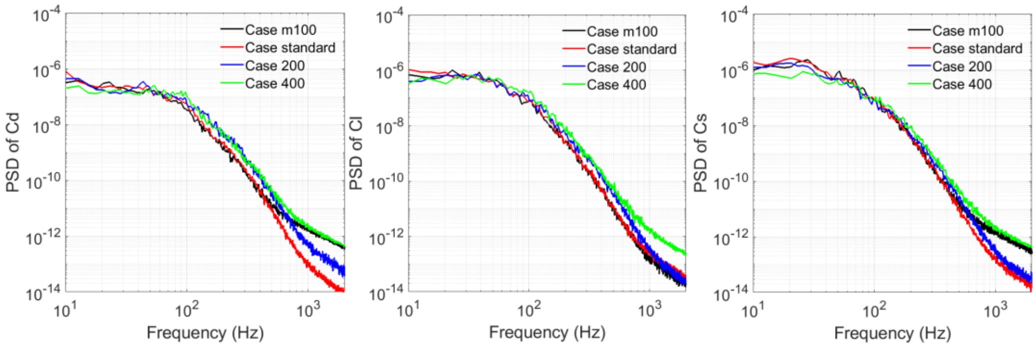

(a) spectra of the bogie force coefficients

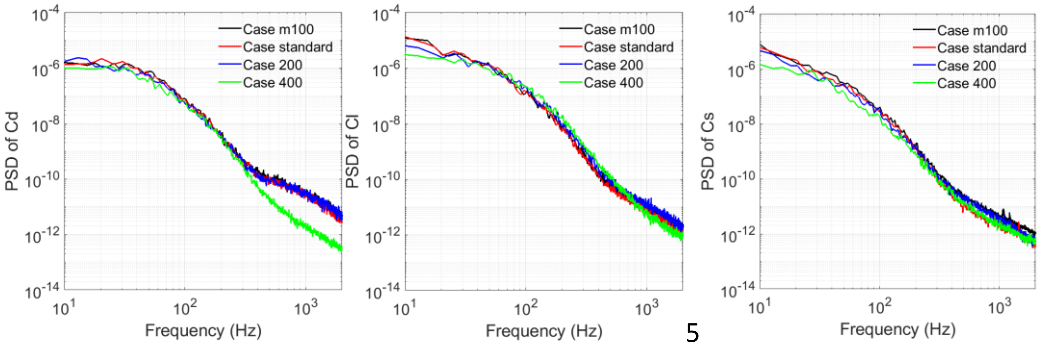

(b) spectra of the car body force coefficients

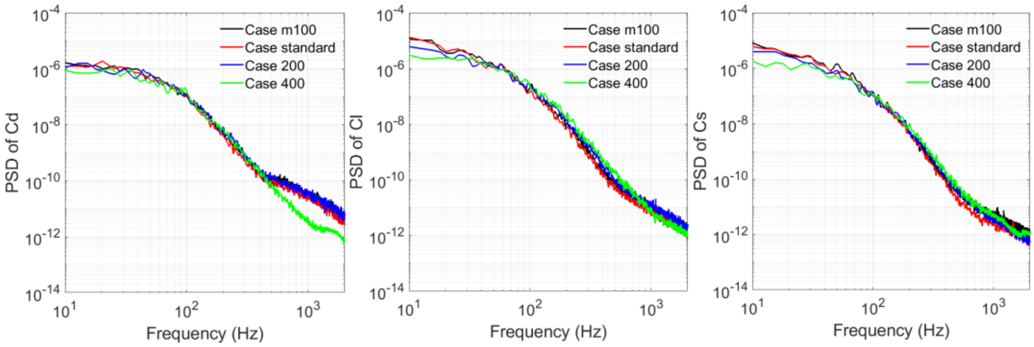

(c) spectra of the total force coefficients

Figure 7.6 PSD of force coefficients for different side component positions

To explore the origin of the difference in the force coefficients, seen in Figure 7.5, the pressure fluctuation $C_{p_{rms}}$, defined by equation (4.12), on the model surface is shown in Figure 7.7. It can be noted that the distribution of $C_{p_{rms}}$ on the front components of the car body, including the train nose and cowcatcher, and the middle components of the bogie, including the wheels and frame, are similar in the various models. Significant differences appear on the side dampers and the side rim area of the cavity rear wall. For Case 400, as discussed in relation to Figure 7.3 and Figure 7.4, as the side components are moved out into the flow the pressure fluctuation on them increases due to the flow impingement and separation, whereas they shield the side rim area of the cavity rear wall, which reduces the pressure fluctuation near there. This is further evidence of why the drag of the car body reduces and that of the bogie increases as the extension of the shaft is increased in Figure 7.5(a) and differences are seen in the force coefficient spectra in Figure 7.6(a) and (b).

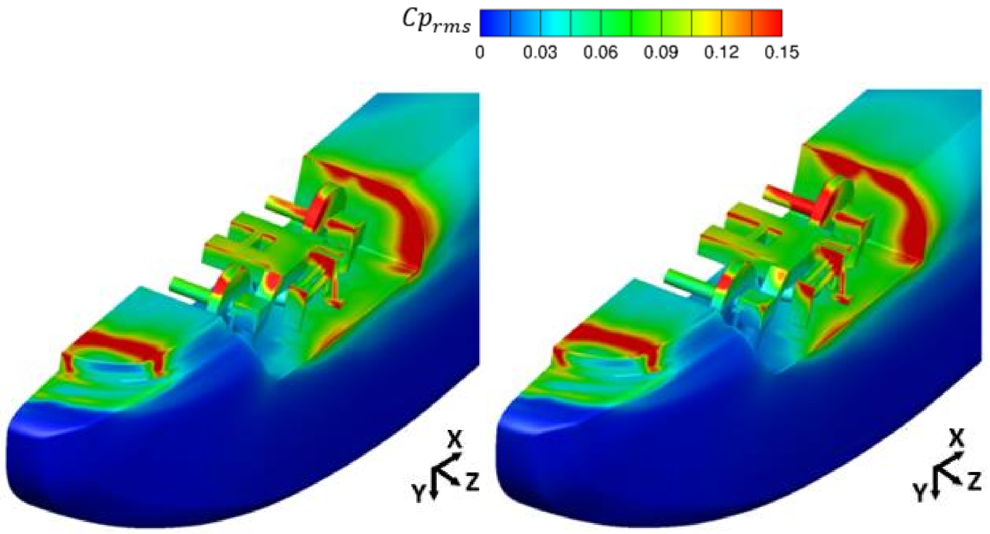

(a) case m100

(b) case standard

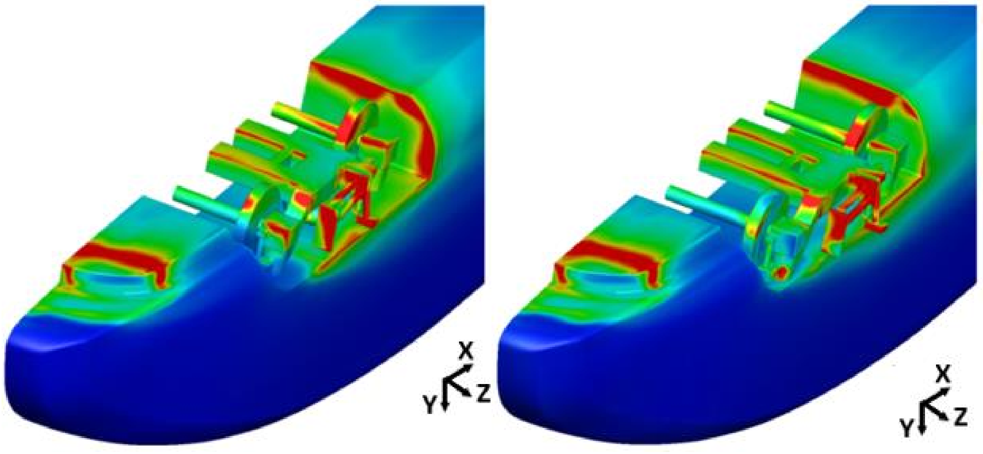

(c) case 200

(d) case 400

Figure 7.7 Contours of surface pressure flucutation $C_{p_{rms}}$ of four cases

To investigate how the pressure fluctuation near the side rim area of the cavity rear wall changes, a pressure measurement point is set, as shown in Figure 7.8. Figure 7.9 gives the instantaneous pressure coefficient $C_p(t)$ and PSDs at the monitor point of the standard case and Case 400. Figure 7.9(a) shows, for Case 400, not only that the mean pressure coefficient reduces from 0.421 to -0.101, but its rms value is also reduced to one fifth. This indicates that both the mean speed and the turbulence intensity of the flow being stagnated on the surface in Case 400 are lower than those in the standard case. The spectra in Figure 7.9(b) show that the pressure fluctuation at the monitor point of Case 400 is lower than that in the standard case at all frequencies, especially below 100 Hz and greater than 1000 Hz. Although the side rim area of the cavity rear wall in Case 400 is shielded by the protruding side components, it is still impinged by the wake flow separated from them. Nevertheless, the reduced rms value shows the intensity of the impingement becomes much smaller than that produced by the detached shear layer from upstream in the standard case.

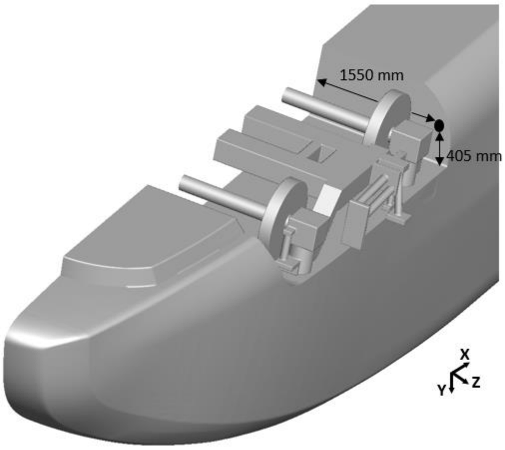

Figure 7.8 Pressure measurement point at the rear surface of the cavity

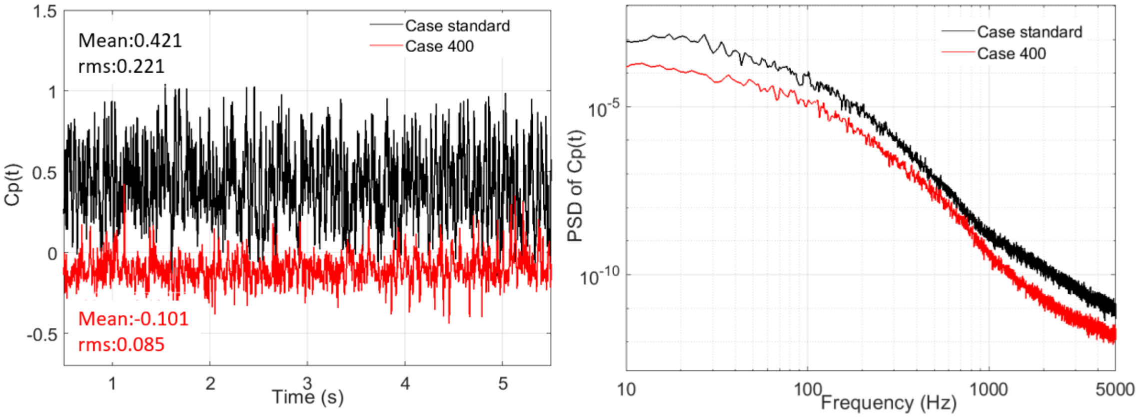

(a) time history of the pressure coefficient $C_p(t)$ (b) spectra of $C_p(t)$

Figure 7.9 The comparison of the pressure coefficient signals of the measurement point of Case standard and Case 400

Figure 7.10 shows the levels of the pressure change rate $L_{\dot{p}}$, which can be used to indicate the intensity of dipole noise sources and is calculated by Equation (3.37). The frequency range is integrated from 20 to 1600 Hz. The main difference between the distributions is seen on the side components and the side part of the rear region of the cavity. When the side components protrude out of the cavity, the pressure fluctuation strength on them increases because of the impingement from the incoming flow, as shown in Figure 7.3. For Case 400 in Figure 7.10(d), the pressure fluctuation near the side region of the rear cavity wall is reduced by the shielding from the protruding side components. More specifically, as shown in Figure 7.9, the vorticity of the wake flow separated from the side components and impinging on the rear cavity wall is much weaker than that of the detached shear layer in other cases. In addition, as shown in Figure 7.3(d), the turbulent wake stays away from the rear arc corner of the cavity, which prevents it from flapping on the side surface of the rear part of the car body.

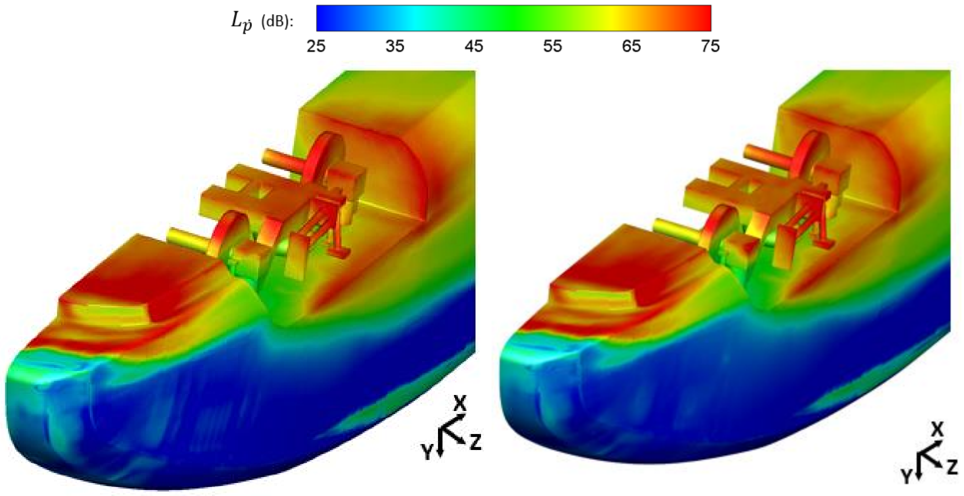

(a) case m100

(b) case standard

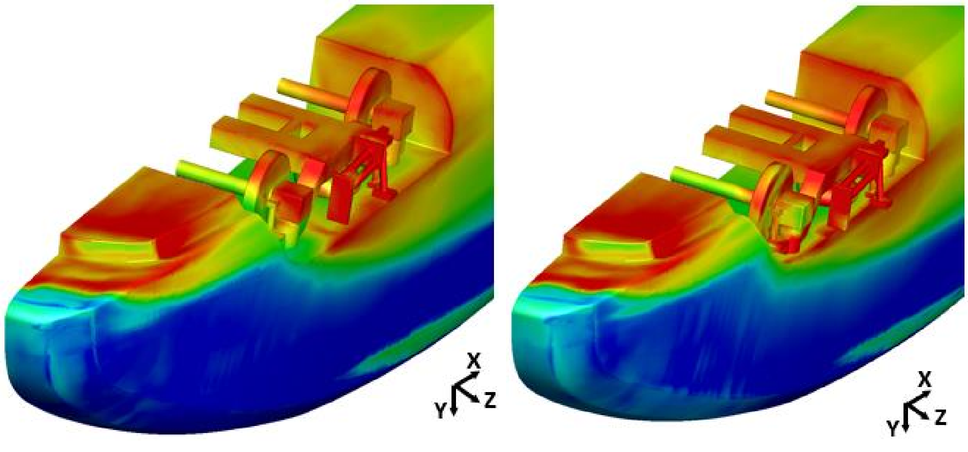

(c) case 200

(d) case 400

Figure 7.10 Surface contours of the pressure rate of change dp/dt

7.3 Aeroacoustic results

The sampled time histories of the pressure fluctuation on the models' surface are taken as the input of the FW-H equation. The calculated noise levels are converted to the full scale and full speed by using Equation (5.1) and the final values are the superposed results of a receiver and its image in the symmetry plane because half-width models are used in the calculation.

7.3.1 Results comparison of half-width and full-width models

In order to reduce the computational cost, a half-width model, as shown in Figure 7.2, is used in the simulation. Some components, such as the bolster, the gearboxes and motors are omitted and some components are simplified, such as the side dampers and the air spring. These omissions and simplifications will alter the blockage ratio of the bogie and the front area of the components and inevitably bring some different characteristics compared with the results of the full-width model in Figure 6.4. To assess this, Figure 7.11 shows a comparison of the directivities of different components of the current standard case and the case simulated in Chapter 6. Due to the omission of the gear boxes and motors, there will be more turbulent air circulating around the wheels and the axle boxes. Therefore, the pressure fluctuation on the wheelsets, which are the main contributor to the noise of the dynamic system in the horizontal direction as shown in Figure 6.25(a) and (b), will increase. Consequently, the noise levels in the horizontal direction of the half-width model in Figure 7.11(a) and (b) are greater than those of the full-width model. Meanwhile, the noise levels of the half-width model in the vertical direction are evidently smaller than their values in the horizontal direction. Figure 7.11(c) compares the directivities of the frame system, which includes the side dampers, the air springs and the frame. Compared with the results of the full-width model, the directivity of the half-width model has greater values in the horizontal direction and smaller ones in the vertical direction. According to Figure 6.25(c), the lateral dampers are the main contributor in the horizontal direction and the frame surface contributes most in the vertical direction. In Figure 7.11(c), the difference in the vertical direction is produced by the omission of the upstream gearbox and motor, which makes the turbulent wake directly flap the bottom of the frame. In addition, the difference in the horizontal direction is caused by the simplification of the end plate of the lateral damper, which makes the projected area in the horizontal direction smaller. Figure 7.11(d) and (e) shows the comparison of the directivities of the bogie and car body. In the horizontal direction, the difference between the results of the half-width model and the full-width model is about 2.5 dB and is more significant than that in the vertical direction. The car body of the half-width model has much smaller SPLs in the horizontal direction because the bolster, which belongs to the cavity when calculate the noise of the car body as shown in Appendix A, is omitted in the calculation.

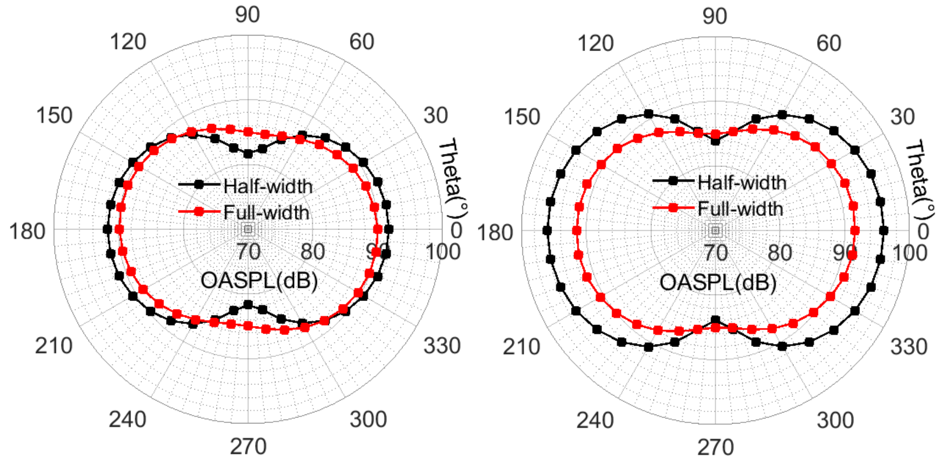

(a) upstream dynamic system

(b) downstream dynamic system

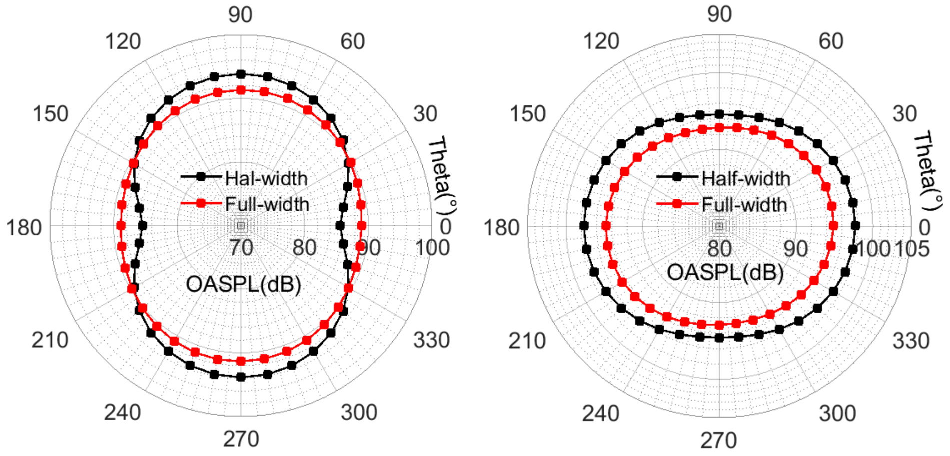

(c) frame system

(d) bogie

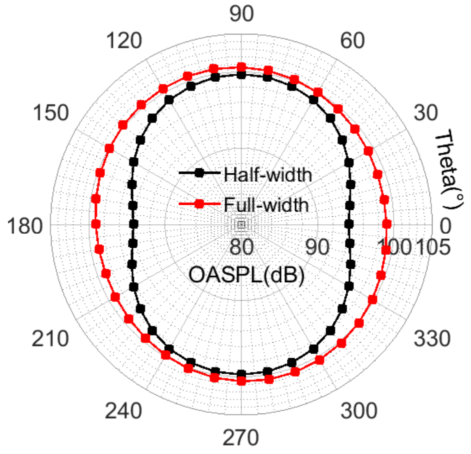

(e) car body

Figure 7.11 Noise directivity comparison of different components

The SWLs of the two models are also calculated by using Equation (6.1). A sphere with a radius of 20 m, centred at the same point as previously, is divided into 486 segments. The centre points of each segment are taken as the receivers.

Figure 7.12 shows the overall SWLs of the components of the half-width model and full-width model. Generally, the difference between them is very small. All the components of the full-width model generate slightly greater SWLs than those of the half-width model except for downstream dynamic system. The smaller blockage ratio of the half-width model is believed to be the reason.

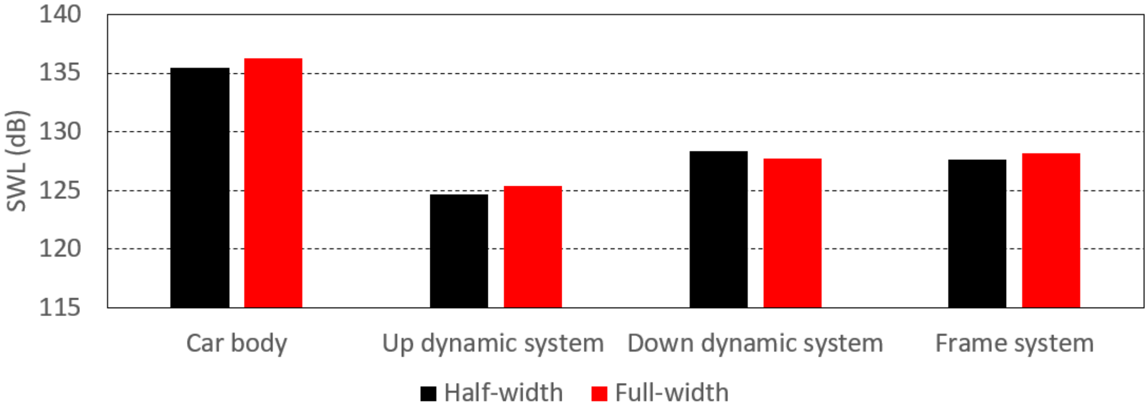

Figure 7.12 Sound power levels comparison of different components

7.3.2 Results comparison of four cases

The sound pressure spectra at the side receiver are shown in Figure 7.13. In Figure 7.13(a), as the extension of the shaft is increased, the SPLs reduce at frequencies below 150 Hz, and increase at frequencies above this. This shows consistency with the comparison of the PSDs of the force coefficients in Figure 7.6(a). It is believed that the flapping of the detached shear layer from the front side rim of the cavity has a greater contribution to the bogie force at low frequencies, whereas the impingement from the free stream contributes more at the higher frequencies. Therefore, when the protrusion of the side components increases, the effect of the detached shear layer is weakened because of the position of the side components, while the impingement of the free stream begins to play a bigger role. The noise spectra of the car body in Figure 7.13(b) follow a similar trend. The lower SPLs at low frequencies for Cases 200 and 400 are caused by the shielding of the protruded side components of the bogie, which prevents the detached shear layer from flapping on the rear area of the cavity. The increased SPLs at the high frequencies are produced by the wake from the protruded side components.

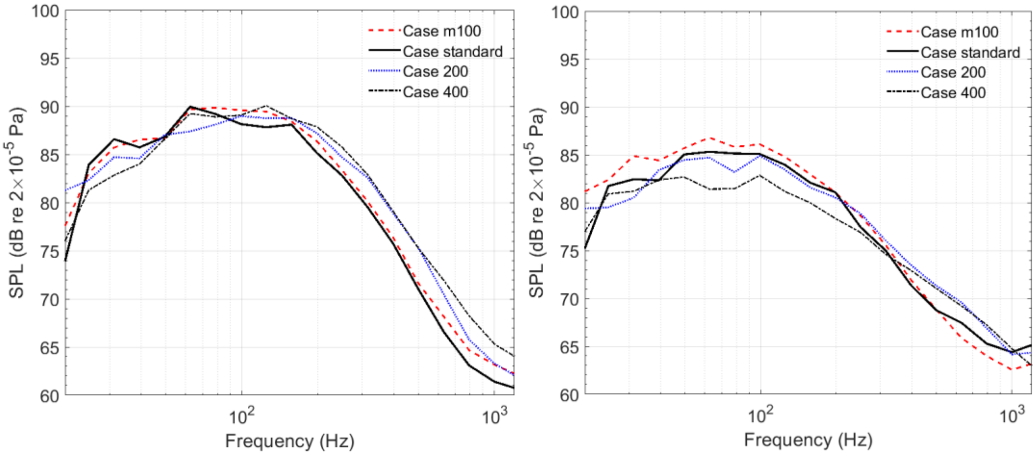

(a) bogie

(b) car body

Figure 7.13 Noise spectra (1/3 octave) of four cases at the side receiver (0°)

The receivers illustrated in Figure 5.18 are used to calculate the noise directivities, which are shown in Figure 7.14. For the directivities of the bogie, shown in Figure 7.14(a), there is no appreciable difference between Case m100 and the standard case, whereas Case 200 and Case 400 have greater values in the vertical direction. For the directivities of the car body, shown in Figure 7.14(b), the most significant difference between the four cases appears in the horizontal direction and the maximum difference is about 4 dB between Case m100 and Case 400. As the protrusion of the side components increases, the SPLs in the horizontal direction increase monotonically. The reason is mainly attributed to the shielding from the protruding side components, which reduces the pressure fluctuation on the arc corner near the rear surface of the cavity as shown in Figure 7.7(c) and (d).

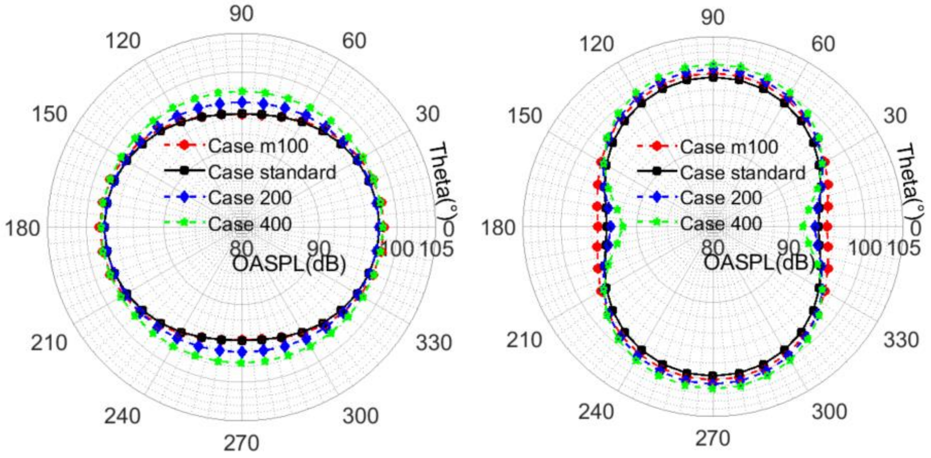

(a) bogie

(b) car body

Figure 7.14 Noise directivities of four cases

Figure 7.15 shows the overall noise levels at the receivers illustrated in Figure 6.21. For the bogie, the maximum difference between them is less than 1 dB, while, for the car body, the maximum difference is about 2.5 dB. Case 400 has the smallest value because the protruding side components reduce the flapping of the detached shear layer on the rear car body, which is believed to be the main region that generates the SPL differences in the horizontal direction. In addition, this reduction in the SPL from the car body makes the total SPL of Case 400 the smallest, as shown in Figure 7.15(c). The main reason is that the rear part of the car body, which is flapped by the detached shear layer or the turbulent wake from upstream, has a considerable effect on the noise levels in the horizontal direction. When the bogie is well shielded by the cavity, some of the detached shear layer can directly flap on the rear car body, whereas when the bogie protrudes out of the cavity, only some turbulent wake from the side components can flap on it.

In Figure 7.15, the trend of the bogie noise levels, which increase when the bogie protrudes out of the cavity, is consistent with the experimental data from Latorre Iglesias et al. (2017). However, the total noise levels show a different trend compared with the experiments. It is believed the reason is that the noise contribution from the cavity to the total noise levels in the current numerical simulation is greater than that in the experiments from Latorre Iglesias et al. (2017), where the cavity corners were rounded to mitigate the cavity noise.

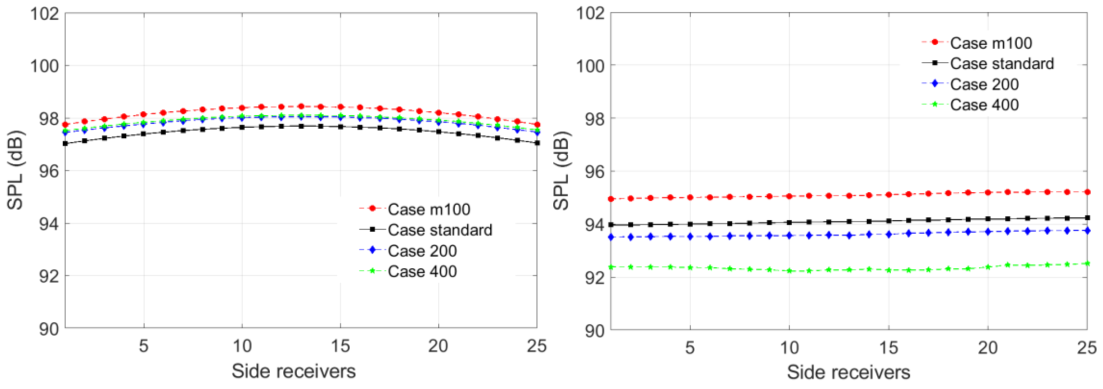

(a) bogie

(b) car body

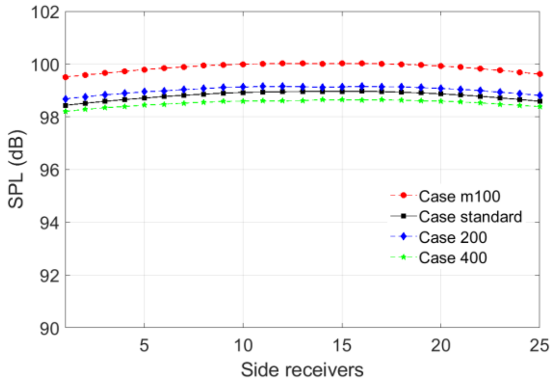

(c) total

Figure 7.15 Noise levels of four cases at the side receivers

Figure 7.16 displays the side view of the noise level contour on the sphere, which encloses the model with radius 20 m. The maximum values of all four cases appear in the direction above and slightly behind the bogie (and below and slightly ahead of it). The maximum values increase monotonically from Case standard to Case 400. As the side components protrude further, the noise levels close to the streamwise direction also increase.

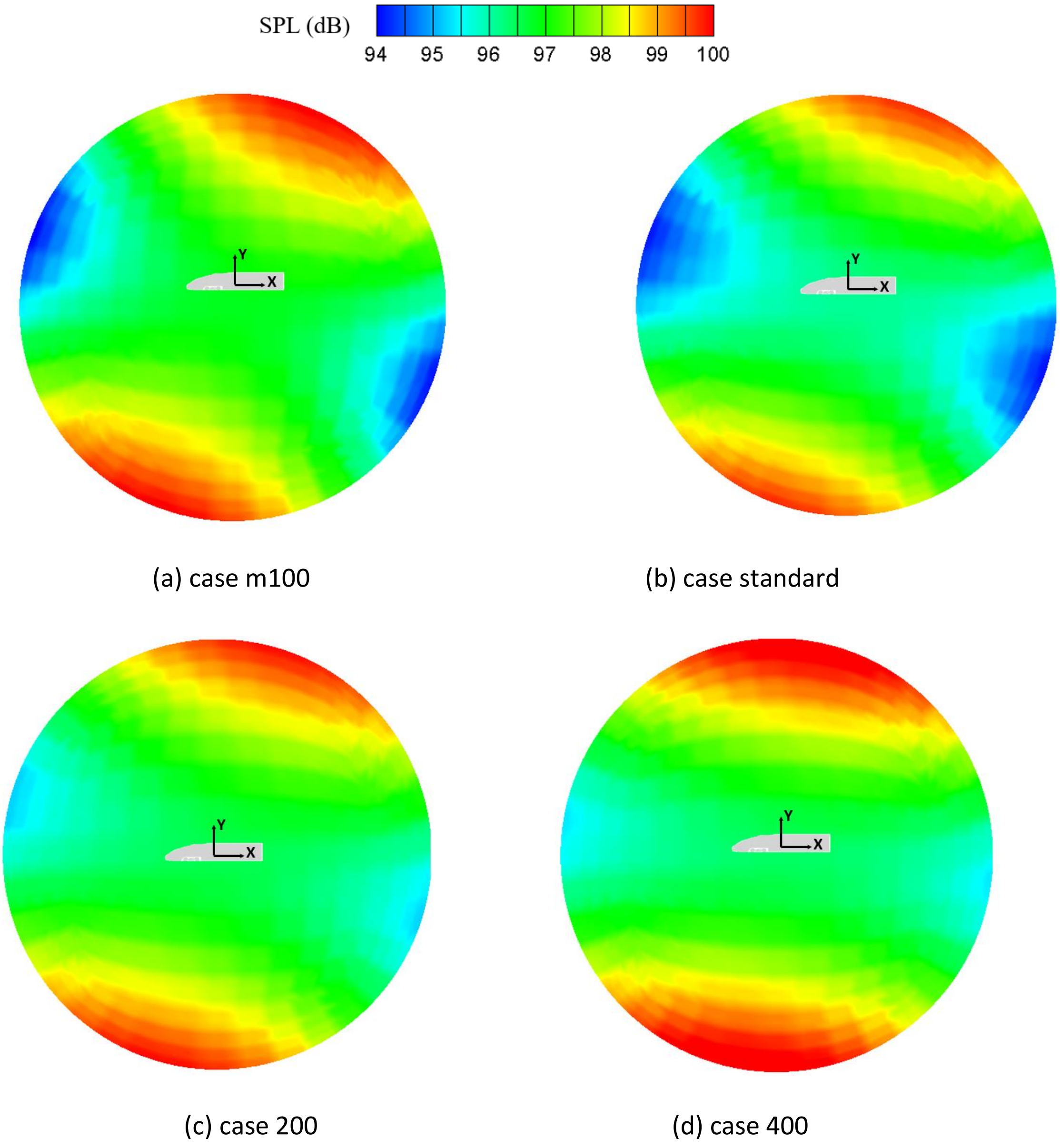

(a) case m100 (b) case standard

(c) case 200 (d) case 400

Figure 7.16 Noise level contours of four cases on the sphere surface (side view)

To compare the sound power emission of four cases, Figure 7.17 shows the SWLs of the components of the four cases. For the results of the car body, the upstream dynamic system and the downstream dynamic system, the difference between the various cases is smaller than 1 dB and the change is non-monotonic. However, the results of the frame system, which contains the side dampers, the air spring, and the frame surface, increase monotonically as the protrusion of the bogie increases. However, the sound power generated by the car body is much higher than the other components, which makes the difference between the total SWLs of four cases very small.

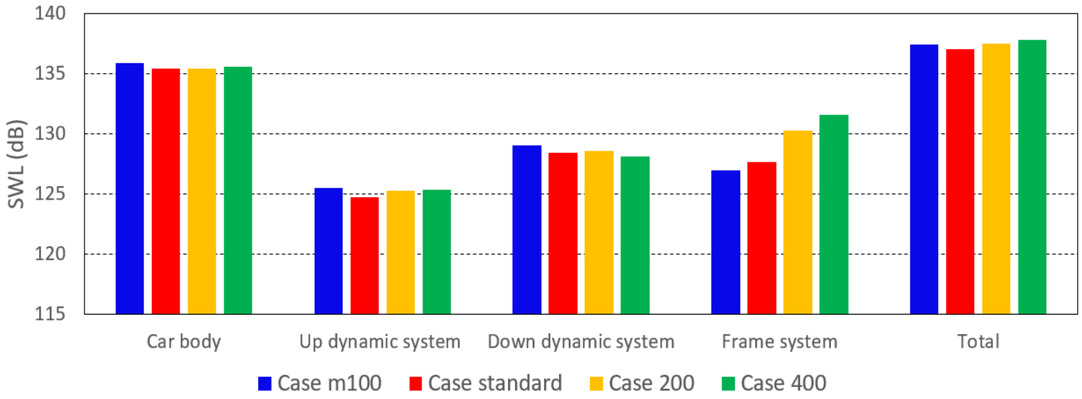

Figure 7.17 Sound power levels of different components from the four cases

7.4 Summary

In this Chapter, in order to simulate the effect of the loading gauge on the aerodynamics and aeroacoustics of the train, a half-width model, which has a smaller number of cells than the full model, is used. The motor bogie from section 5.2 is used but with the gear boxes and motors omitted, and the car body model from section 6.2 is adopted. In the simulation, to simulate the different relative positions between the bogie and the car body, which are caused by different loading gauges in reality, the bogie is extended in the lateral direction while the car body is kept unchanged. Four cases, called Case m100, Case standard, Case 200 and Case 400, are calculated.

The flow field results show that as the protrusion of the side components increases, the rear part of the cavity is shielded by the side components of the bogie. The detached shear layer from the front rim of the cavity, which can directly flap on the rear part of the cavity in Case m100 and the standard case, is disrupted by the protruded side components in Case 200 and Case 400. The protruding side components then directly face the high-speed flow from upstream and generate turbulent wake flow at its downstream. Meanwhile, instead of the detached shear layer, the turbulent wake impinges on the rear cavity and the car body. These are the main differences between the flow phenomena of the four cases and they are the origins of the difference of the pressure fluctuations and aerodynamic noise.

The pressure fluctuations on the side components increase when the components protrude further into the flow. However, they are reduced at the rear wall of the cavity, especially at the arc corner near the rear surface. According to the PSDs of a monitor located on the rear wall of the cavity, the fluctuation has a greater reduction at lower frequencies, as the flapping of the detached shear layer has a low-frequency characteristic. In the comparison of the force coefficients, it is found that the mean value of the drag coefficient is the highest in Case 400 whereas the mean values of the lift and side force coefficients of the four cases are very similar. The rms values of the force coefficients reduce monotonically as the protrusion of the bogie components increases. The changes of the flow field at the rear part of the cavity are regarded as the main reason. Before comparing the aerodynamic noise generated by the four cases, the difference between the noise generated by the half-width model and the full-width model is investigated. It is found that the noise from the bogie of the half-width model is greater although the gearboxes and the motors are omitted. The reason is that the half-width bogie has a smaller blockage ratio and thereby, more air can enter and stay in the cavity, which generates larger pressure fluctuations on the bogie components. For the car body, the half-width model has a much smaller sound pressure level in the horizontal direction because of the omission of the bolster. There is no large difference between the sound power levels of the components.

In the comparison of the noise directivities of the four cases, it is found that as the protrusion of the side components is increased, the noise levels of the bogie in the vertical direction also significantly increase while the noise levels of the car body in the horizontal direction reduce. The changes of the flow field described above are believed to be the reason. The comparison of the noise spectra at the side receiver shows that, as the extension of the shaft increases, the SPLs reduce at low frequencies, while they have the opposite trend at higher frequencies. This occurs because the protrusion of the bogie suppresses the effect from the detached shear layer, which is a low-frequency characteristic, whereas the wake of the side components, which replaces the detached shear layer, contributes more at the high frequencies. The comparison of the noise levels of the side receivers shows Case 400 does not have greater values despite the protrusion of the side components, but in contrast, Case m100 has the greatest ones. This result is different from the results of Latorre Iglesias et al. (2017) in which the noise contribution of the cavity was suppressed by rounding of the cavity edges. On the other hand, this reveals that the detached shear layer has a greater effect on the noise levels in the horizontal direction than the turbulent wake from the protruded side components. Finally, the sound power levels of the four cases are compared. Apart from the frame system, no large differences are found in other components. The SWL of the frame components increases monotonically as they are extended into the flow. However, the difference in the total SWLs of the four cases is not significant because the proportion of the sound power generated by the frame system is small.

According to the analysis above, it can be concluded that the protruded side components bring some flow field changes to the side components themselves and the rear part of the cavity. However, these changes only result in a significant effect on the aerodynamic noise at the side receivers and have a very small effect on the total sound power level.

Chapter 8 Aerodynamic noise reduction measures

After analysing the results from Chapter 5 and Chapter 6, it is realised that the bogie cavity, particularly its rear wall, is emitting the greatest proportion of the sound power from the bogie region. Therefore, the cavity is very important in achieving noise reduction for the bogie region.

The length to height ratio (L/H) of the bogie cavity is around 5, which belongs to the ‘open’ cavity category (Plentovich et al. 1993). In open cavity flow, the shear layer detaches from the leading edge of the cavity and then spreads downstream carrying Kelvin-Helmholtz vortices, which are generated due to the velocity difference between the free stream and cavity zone, and eventually impinges on the rear cavity wall. Izawa et al. (2011) concluded that the vortex–edge impingement at the rear wall produces strong pressure fluctuations, which becomes the primary noise source on the cavity surface, as also found in Figure 5.28 and Figure 6.16. A part of the acoustic wave travels upstream and interacts with the detached shear layer. When the instability timescale of the detached shear layer is close to the acoustic travel time between the front and rear cavity walls, acoustic resonance occurs (Rossiter 1964; Morris 2011). One of the most important topics in the study of the instability of open cavity flow is supressing its acoustic-flow resonance.

There are extensive studies on the noise reduction of open cavities, from active control methods (Cattafesta et al. 2003; Cattafesta III et al. 2008) to passive control ones (Saddington et al. 2016; Demir et al. 2021). Compared with active control methods (Yoo and Lee 2007; Cattafesta III et al. 2008), passive ones are simpler and do not need additional energy to achieve effective control. As mentioned above, the rear wall of the cavity plays an important role in the noise and resonance generation and thus, the most direct and effective way of noise mitigation is to modify its geometry (Saddington et al. 2016; Kim et al. 2020; Kim et al. 2020; Martin et al. 2022). Another effective method is to install devices to disturb the generation of the shear layer at the front edge of the cavity, including rods (Arunajatesan et al. 2002; Comte et al. 2008), spoilers (Knowles et al. 2010; Zhao et al. 2019), and vortex generators (Mary and Lê 2005; Abdelmwgoud and Mohany 2021). Recent experiments (Showkat Ali et al. 2018) show that destroying the spanwise coherence of a shear layer can also reduce the noise. Li et al. (2020) used a porous material installed on a cavity floor to break the vortex structure in the shear layer, which weakens the vortex–edge impingement and thereby acoustic feedback and resonance are attenuated. Lamp and Chokani (1997) used a small jet placed within the front wall of cavity to disturb the detached shear layer and their results show that the size of the vortex structures in the shear layer is reduced and the amplitude of the oscillations in the cavity was successfully supressed. Zhuang et al. (2006) and Arunajatesan et al. (2009) applied several discrete microjets distributed in the spanwise direction of the cavity leading edge to reduce the cavity noise. The spanwise coherence of the shear layer is also broken up and thus the pressure flucutations at the rear cavity wall are reduced. Compared with other passive mitigation methods,e.g. rods, vortex generaters and porous material, the jet flow has advantages of low self-noise and self-weight and easy maintanence.

The analysis of Chapter 6 indicates that high noise intensity components are located at the bottom of the bogie, the side of the bogie, and the rear part of the bogie cavity including the rear wall and the rear rim areas. The intense pressure fluctuation is produced by the impingement of flow from the upstream detached shear layer and the highly turbulent wake on those components. Therefore, flow control measures, which can disturb the shear layer and push it away from the components, are expected to have potential to reduce the aerodynamic noise of the model.

As reviewed above and in section 2.3, jet injection, applied perpendicular to the main streamwise direction, can introduce transverse momentum into the main stream and create a low speed zone downstream of the injection location. Thus, it has potential to disturb the development of the shear layer around the bogie cavity and it is worthwhile to try the concept proposed by Oerlemans and De Bruin (2009) on the leading car model.

8.1 Feasibility study of noise reduction by jet injection

8.1.1 2D calculation to assess the jet inlet effect

To simulate a jet introduced in cross flow, the mesh and the velocity profile near the outlet of the jet nozzle are very important, which directly affect the trajectory of the jet flow (Dai et al. 1994; Zhao et al. 2018). Therefore, a very fine mesh is needed to discretise the zone of the nozzle outlet and a realistic velocity profile is also required at the jet inlet. However, the current study focuses on a conceptual design of the jet flow, which is expected to push the shear layer away from the model components to reduce the dipole noise generation. The detailed flow field near the outlet of the jet nozzle is not the main focus. The outlet of the nozzle will be directly imposed on the car body surface and only the momentum flux injected by the jet will be treated as the variable of concern. Thus, before applying the jet on the car body, it is necessary to assess the effect of different numerical treatments of the jet inlet. In addition, the effect of a single jet and a dual jet will also be studied.

Figure 8.1 shows the computational domain for simulation of a single jet in crossflow. The simulation results will be compared with the experimental data from Zhao et al. (2018). The width of the jet, w_j, is 10 mm and its length is $3w_j$. The main stream inlet has a height *H* of 75 mm. The distance between the jet upstream surface and the main stream inlet is $18.5w_j$. The downstream surface of the jet is $40w_j$ away from the domain outlet. The height of the domain is $4H$. 2D RANS simulations, which require relatively low computational cost, are used in this study. The bottom surface of the domain and the jet surfaces are set as non-slip walls. The other boundaries except for the flow inlet surface are set to ''opening outlet'' in OpenFOAM, which allows flow circulation at the outlet boundaries. A uniform velocity inlet boundary condition is set at the main stream surface, with velocity 40 m/s. For the jet inlet, a velocity profile similar to Dai et al. (1994) is imposed on the inlet, which is expressed as:

$$\frac{u_j(\mathrm{x}_p)}{u_{jMax}} = 1 - (\frac{x_p}{0.5w_j})^8 \tag{8.1}$$

where x_p is the distance to centre of the inlet, u_j is the local inlet speed, u_{jMax} is the maximum magnitude of the jet speed. The injected momentum flux ratio of the jet is defined as

$$R_j = \frac{\bar{u}_j A_j}{U_\infty A_m} \tag{8.2}$$

where $\bar{u}_j$ is the mean speed of the jet, A_j is the area of the jet inlet, U_∞ is the velocity of the main stream and A_m is the area of the inlet of the main stream. A series of monitors are set at the locations from P1 to P4, as shown in Figure 8.1, to record the calculate velocity, which will be used to compare with those from Zhao et al. (2018).

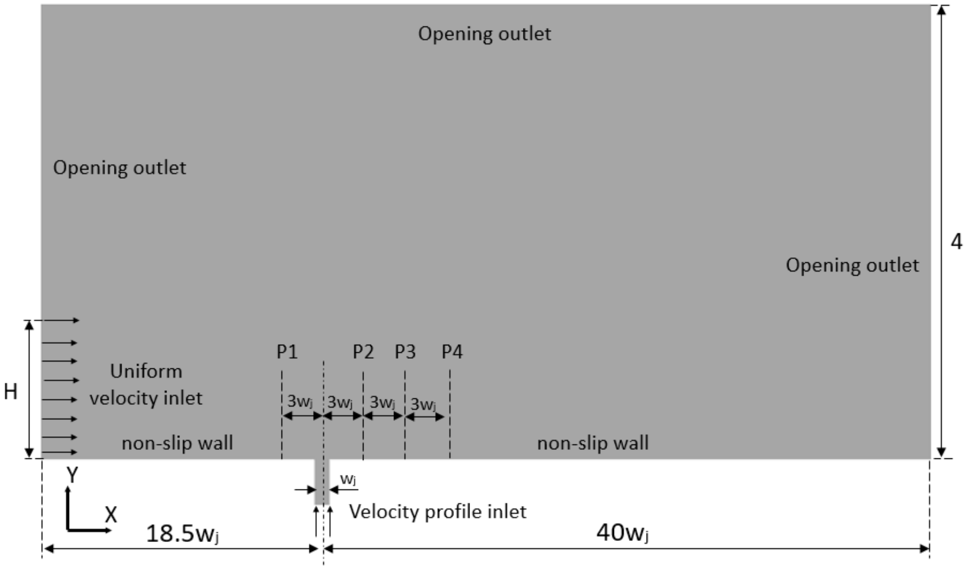

Figure 8.1 Computational domain of the model

In order to study the effect of the different treatments of the jet nozzle outlet, two cases are designed as shown in Figure 8.2. In case a, the mesh near the outlet area is created in the software pointwise4.1

with high quality. By contrast, to reduce the difficulties in mesh generation and make it easier to apply the jet on the car body model, in case b, the jet nozzle is not considered and instead of the inlet profile given by equation (8.1), only a mean velocity is directly imposed on the grid elements on the boundary. These have an area that is the same as that of the jet nozzle in case a, to ensure the momentum flux injected in case a is the same as that in case b. To carry out a grid dependence study, simulations are run with three different meshes for case a, which are called fine, medium and coarse. The first height of the boundary layer grid is set to 0.005 mm to guarantee the value of y^+ remains smaller than 1. The first grid height and the expansion ratio (1.1) remain the same in the three cases. The aspect ratios near the corner of the nozzle outlet are set to 100, 200 and 400.

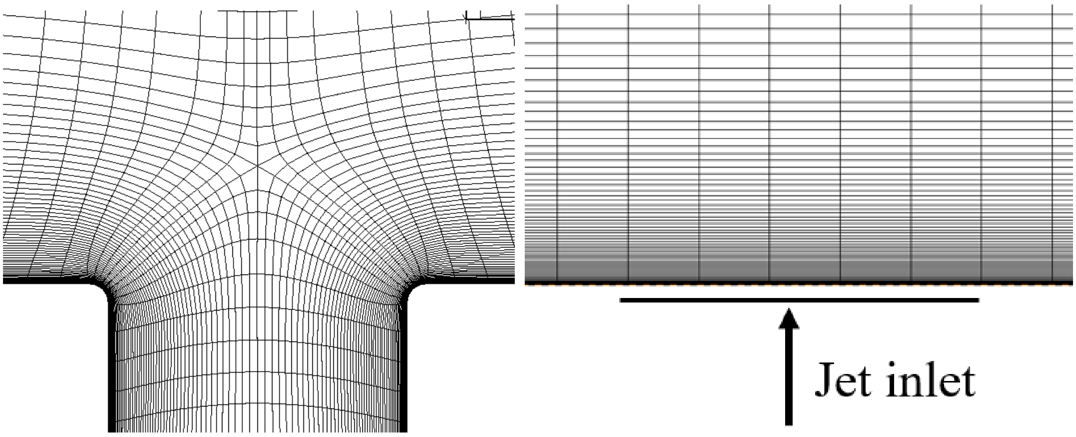

(a) case a (b) case b

Figure 8.2 Grid distribution near the jet inlet section of two cases

Figure 8.3 shows results of the grid dependence study in terms of the velocity profile at locations P1 to P4, as shown in Figure 8.1. x_P is the streamwise distance between the measured location (x_P) and the centre of the jet nozzle. y is the height above the bottom of the domain. It can be seen that the results of case fine are closest to the experimental data and followed by the medium ones. The difference between the results of the fine and medium cases is small and thus, the grid parameters of the medium case will be used in the following calculations. For the case without jet nozzle (case b), the velocity profile is slightly different from the other cases, which will have a limited effect on the trajectory height of the jet flow.

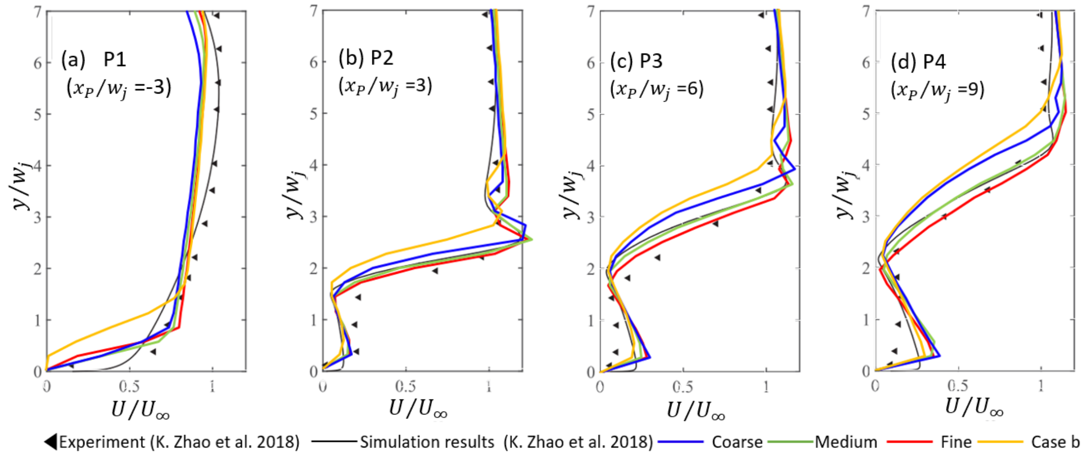

Figure 8.3 Grid dependence study for velocity profiles at the measurement locations from P1 to P4 as shown in Figure 8.1.

Figure 8.4 illustrates the velocity contour and centreline trajectory (streamline from the centre of the jet inlet) of cases with different jet configurations. It can be noticed that, for all cases, the main stream is pushed up because of the vertical momentum flux injected by the jets. The pushed-up main stream reattaches further downstream and there is a shielding zone created between the reattachment point and the jet. The mean velocity in the shielding zone is much smaller than that of the main stream. Therefore, objects in the shielding zone will generate much less dipole noise than ones directly exposed to the main stream.

Figure 8.4(a) shows the velocity contour and centreline trajectory for case a in Figure 8.2 (a) and case b in Figure 8.4(b). The black dashed-dotted line in Figure 8.4(b) represents the centreline trajectory of the single jet case with jet nozzle, as shown in Figure 8.4(a). The vertical red dashed line in Figure 8.4(a) and (b) represents the estimated location of the maximum height of the shielding zone, which can be used to assess the expected noise reduction by the jet. The higher the shielding zone is, the greater the noise reduction can be expected (Zhao et al. 2018). For the single jet in Figure 8.4(a), the height of the shielding zone is about 0.05 m. Compared with the case with nozzle, the height of the case without a nozzle in Figure 8.4(b) is about 10% higher.

It has been proven that the trajectory of a single jet can be elevated by dual jet (Ziegler and Woller 1973; Yu et al. 2006; Zhao et al. 2017; Zhao et al. 2018). Therefore, dual jet cases are also calculated, as shown in Figure 8.4(c) and (d). The second jet nozzle has the same geometry as the first one and is located at $4.5w_j$ downstream. For the dual jet in Figure 8.4 (c), the height of the shielding zone is about 0.1 m, which is twice of the height created by the single jet. For the dual jet case in Figure 8.4(d), the height of the shielding zone increases by about 30%.

It can be pointed out that although, the velocity profile at the outlet of the jet has some effect on the height of the shielding zone, the shape of the flow field is similar. Therefore, in the next section, considering the difficulty of the meshing and computational cost, a uniform velocity profile will be directly imposed on the solid surface. The effect of the detailed geometry parameters of the jet nozzle will not be considered and only the injected momentum flux ratio and the distribution of the jet in the spanwise direction will be studied.

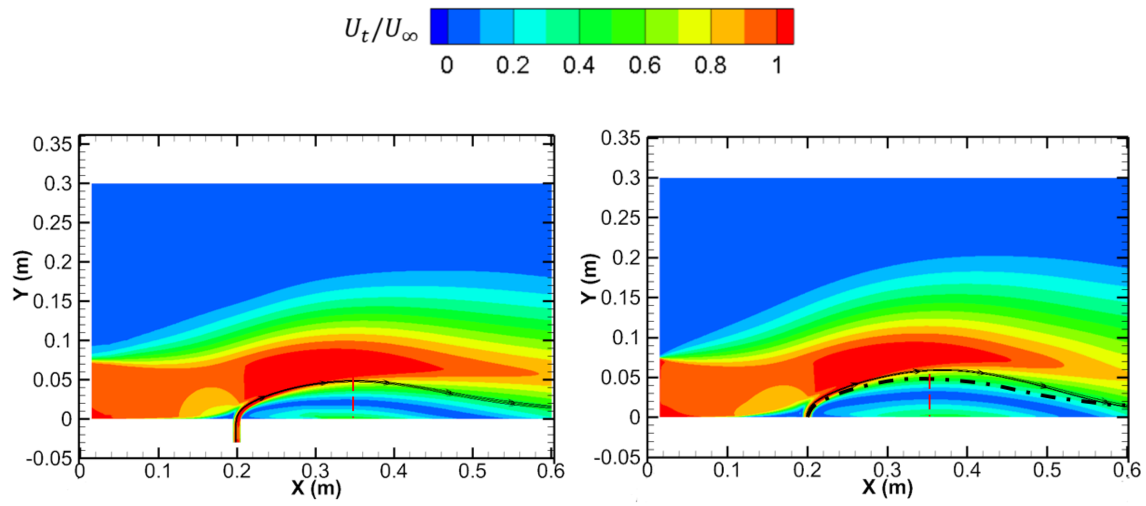

(a) single jet

(b) single jet without nozzle

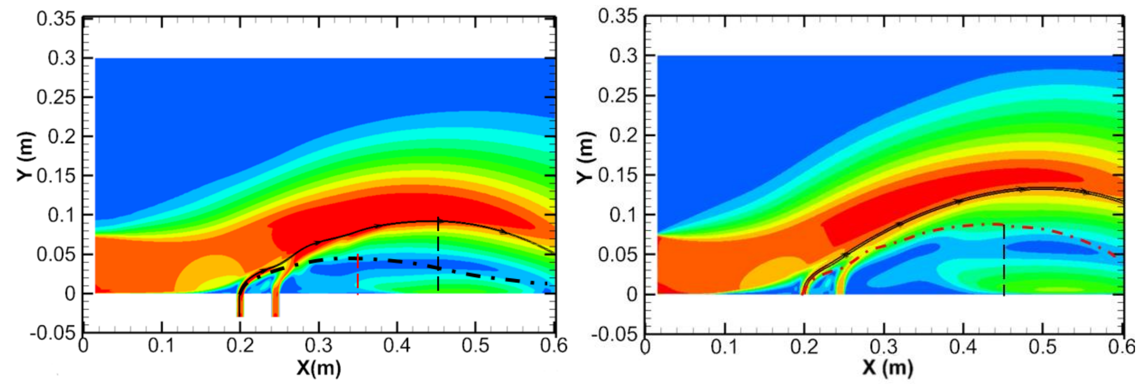

(c) dual jet

(d) dual jet without nozzle

Figure 8.4 The comparison of the velocity contour and centreline trajectory from CFD cases of different jet configurations, U_t is the total velocity.

8.1.2 Testing cases of jet applied on the half-width model

The analysis of section 8.1.1 shows the momentum normal to the main stream, which is provided by the jet, can disturb the main stream and create a shielding zone behind it. According to the results of Chapter 6, the aerodynamic noise generated by the bogie and its cavity is closely related to the detached shear layer from the upstream cavity edges. Figure 6.16 shows the components close to the shear layer have stronger pressure fluctuations than other components inside the cavity. Therefore, increasing the distance between the detached shear layer and the components will reduce the generation of the pressure fluctuations. Figure 8.5 shows the schematic installation location of the jet at the front rims of the bogie cavity. The jet slots will be added in the regions shaded black in Figure 8.6, and are expected to provide a momentum perpendicular to the solid walls to push the shear layer away from model components. The air of the jet is collected in the area shaded green, which is located on the front surface of the cowcatcher.

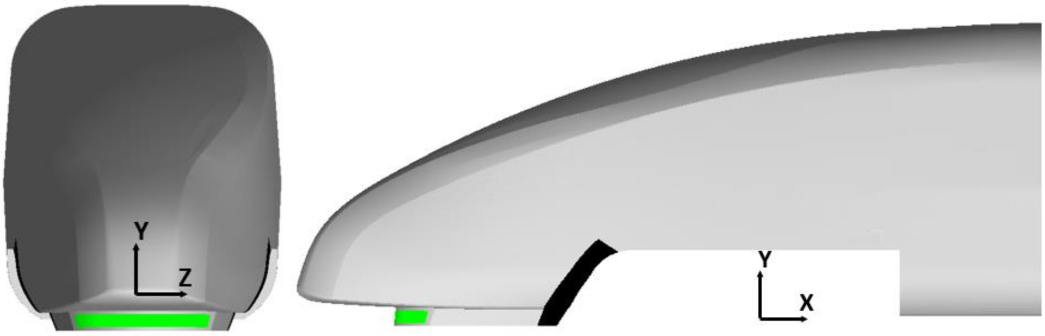

(a) front view (b) side view

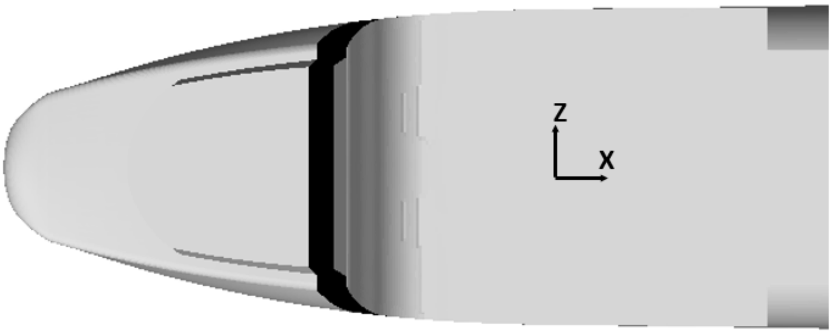

(c) bottom view

Figure 8.5 The schematic jet section located on the car body

Three types of jet slot are compared, as shown in Figure 8.6. These are a single straight jet slot, a single row of staggered jet slots and dual rows of staggered jet slots. The staggered jets can reduce the effect of the cuts through the car body on the structural strength. In addition, it may provide some cancellation of the possible jet flow impingement effects on the rear components, which are correlated with the position of the jet, in the frequency domain. According to the results of section 8.1.1, the shielding height of the dual jets is greater than that of single jet. Thus, the dual staggered jet in Figure 8.6(c) is expected to produce a greater noise reduction. The momentum flux of the single straight jet and single staggered jet is the same and the one of the dual staggered jet is double that.

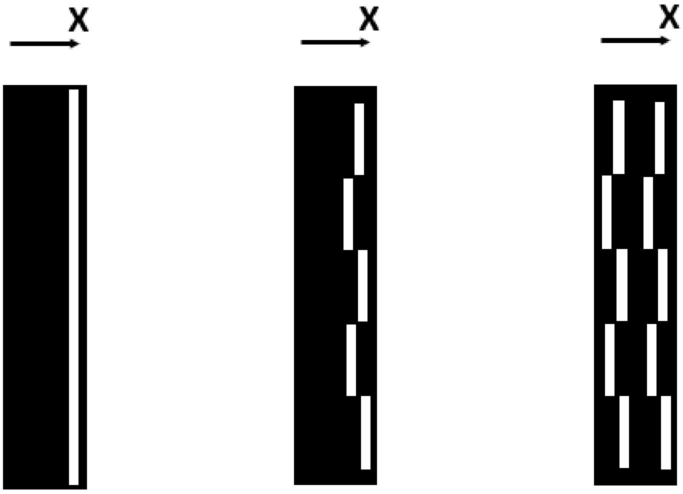

(a) single straight jet (b) single staggered jet (c) dual staggered jet

Figure 8.6 The conceptual design of three types of jet slot

In order to reduce the computational cost, the half-width model of the car body and bogie used in Chapter 7 is adopted to test the noise reduction by the jet. The boundary conditions of the model are the same as those used in Chapter 7. The boundary conditions of the jet inlet are directly imposed on the model surface as considered in section 8.1.1. For simplicity, and to prevent excessive noise generated by the jet itself, the jet speed $\bar{u}_j$ is set equal to the main stream speed U_∞ (10 m/s). However, it should be pointed out that in reality, in incompressible flow, $\bar{u}_j$ is determined by the pressure difference and pressure loss between the inlet of the air collection nozzle and the jet nozzle. Ideally, if there is no pressure loss, as long as the pressure difference equals the dynamic pressure ($\frac{1}{2}\rho U_\infty{}^2$) then it can maintain a jet flow with speed of U_∞. However, pressure loss may occur in the connection channel, between the air collection nozzle at the front face of the cowcatcher and the jet slot due to its geometry. Therefore, in reality, to get a jet speed of U_∞, a pressure difference greater than $\frac{1}{2}\rho U_\infty{}^2$ is required. As shown in Figure 7.8(a), the value of C_p at the front surface of the cowcatcher is close to 1 because the air flow is stagnated by the surface, while in Figure 7.8(b), the local value of C_p at the outlet positions is close to -0.2, thereby the pressure difference is nearly 1.1 to 1.2 times $\frac{1}{2}\rho U_\infty{}^2$. Therefore, as long as the connection channel is carefully designed, sufficient pressure difference can be guaranteed and thereby the jet speed can achieve U_∞ without a requirement for additional power. On the other hand, the pressure difference may vary with position, which may produce different jet speeds. This is not considered here, a uniform jet speed being specified for simplicity.

Equation (8.2) is used to calculate the momentum flux ratio R_j of the jet flow. The area of the single jet is about $4.98 \times 10^{-4}\ \mathrm{m}^2$ in the scaled half-width model. The reference area A_m , which is the cross-section area of the gap between the cowcatcher bottom and the ground, is about 0.0022 m^2. Therefore, the R_j of a single jet is about 0.225, which is doubled to 0.45 for the dual jet. The area of the nozzle for the air collection of a single jet at the front face of the cowcatcher is designed to be about $6.4 \times 10^{-4}\ \mathrm{m}^2$, which is about 20% greater than the area of a single jet slot. The mean velocity (around 8m/s) of the air collection nozzle, which is equal to the injected momentum flux divided by the nozzle area, is directly imposed on the collection surface.

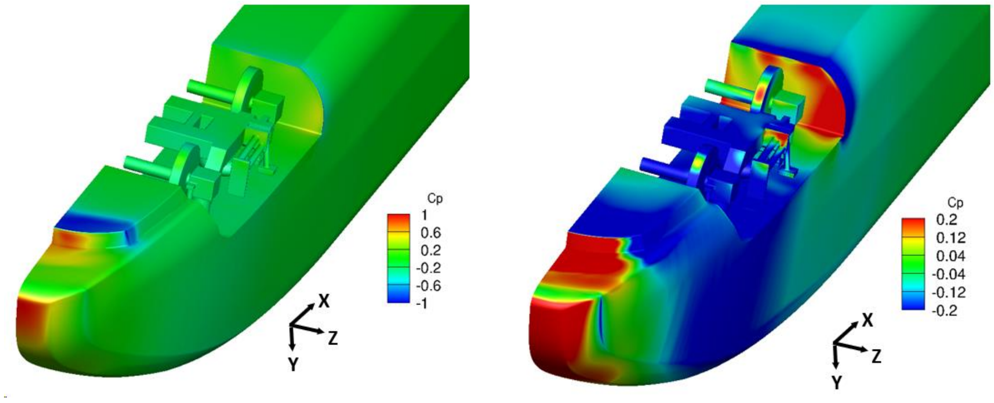

(a) range from -1 to 1 (b) range from -0.1 to 0.1

Figure 8.7 Surface pressure coefficient C_p by Equation (4.11) plotted with different scales

Due to the high velocity of the jet inlet imposed at the solid surface, where the size of the boundary layer mesh is very small, the *CFL* becomes around 14 with the same mean time step 2×10^{-5} s as previously. In order to reduce the iteration time of the calculation, the data sampling time length of the three cases is about 1.2 s, which is only one third of the data sampling length of the standard case in Chapter 7. The sampling frequency of the surface pressure data is around 16.7 kHz, corresponding to a maximum spectral frequency of 8.33 kHz.

The sampled surface pressure is used to calculate the level of the fluctuation of dp/dt, which is shown in Figure 8.8. It can be noted that, in Figure 8.8(b), the pressure fluctuation intensities at the bottom of the frame, the rear wheelset, the side dampers, and the rear surface area of the cavity are significantly reduced compared with the standard case in Figure 8.8(a). However, it seems the jet has little effect on the upstream components, such as the train nose and the bottom of the cowcatcher. Compared with the model in Figure 8.8(b), in Figure 8.8(c) the air collection nozzle is introduced and the distribution of the jet becomes staggered. The pressure fluctuation strength at the bottom of the cowcatcher is reduced because a part of the high-speed air, which normally impinges on the front face of the cowcatcher and separates at its front rim, as it does in Figure 8.8(a) and (b), is sucked away by the air collection nozzle. Consequently, less turbulent air sweeps over the bottom of the cowcatcher. However, the pressure fluctuation distributions on the bogie and cavity in Figure 8.8(c) show no noticeable difference compared with Figure 8.8(b). Figure 8.8(d) shows the distribution of the pressure fluctuation strength with the dual staggered jet. Compared with Figure 8.8(c), the air collection is increased and consequently, the pressure fluctuation strength at the bottom of the cowcatcher is further reduced. As discussed in section 8.1.1, the dual jets inject greater momentum into the main stream, which is pushed further away from the downstream components. The pressure fluctuation strength on the bottom components, especially the frame and the axle box, and the rear surface of the cavity is reduced more than that of the model in Figure 8.8(c).

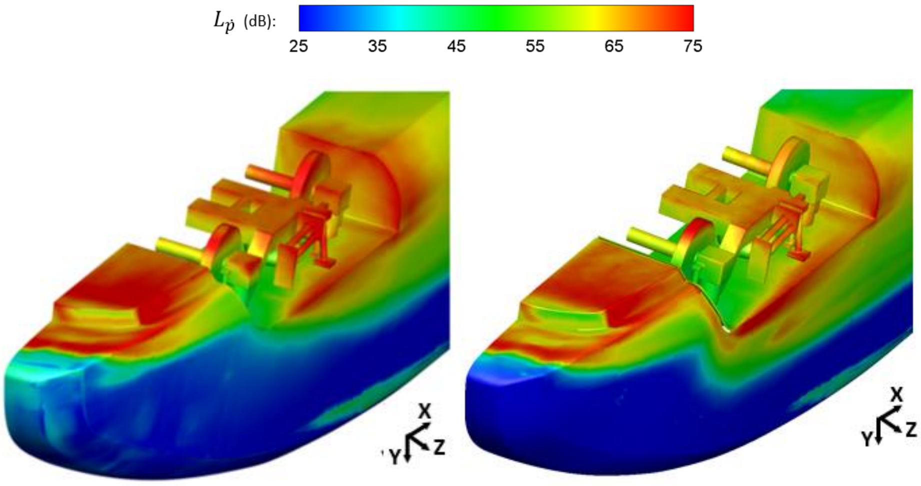

(a) original model (standard case)

(b) single straight jet

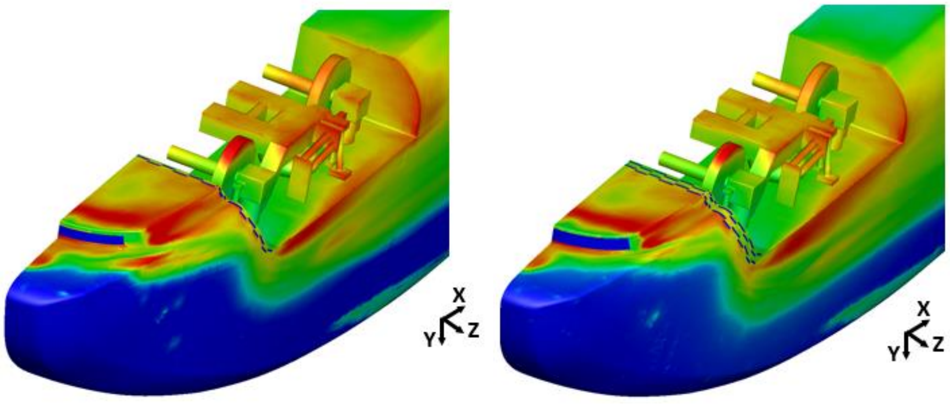

(c) single staggered jet

(d) dual staggered jet

Figure 8.8 Surface contours of the level of dp/dt.

The sound power levels of the three cases are calculated by the Equation (6.1) and compared with the reference case in Figure 8.9. For the bogie, the dual staggered jet reduces the sound power by the largest amount, which is 3.9 dB. However, it seems the single staggered jet reduces it by 0.5 dB less than the single straight jet. For the cavity, the sound power reduction by the single and dual staggered jets is almost the same, at 3.7 dB, but both are greater than the reduction by the single straight jet. For the total sound power, the dual jet reduces the sound power generated by 3.8 dB compared with the original model.

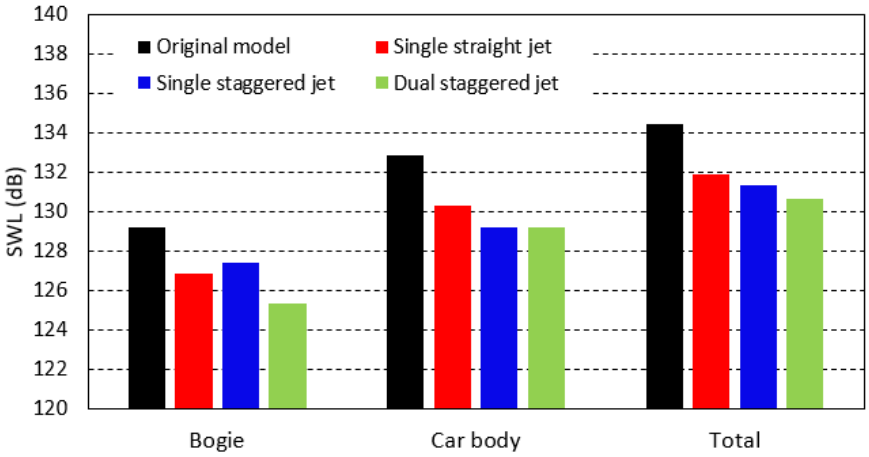

Figure 8.9 Comparison of sound power level of different cases

Comparison of the noise reduction results by the three different strategies shows that the sound power is reduced most by the dual staggered jet. The air collection nozzle located at the front face of the cowcatcher also has a positive effect on the noise reduction. Therefore, in the next section, the geometry parameters of the dual staggered jet slot and the air collection nozzle will be applied to the full-width model.

8.1.3 Noise emitted by jet vs noise emitted by train model

Before applying the jet to the car body model, it is necessary to compare the noise emitted from the car body model with that from the jet itself, in case the noise of the jet is so large that it exceeds the potential noise reduction of the train model. The experimental data from Oerlemans and De Bruin (2009) are used to estimate the noise of the preliminarily designed jet.

There are two kinds of components responsible for the noise of a blowing jet. The first one is a high-frequency mixing noise component, which can be scaled by the 8th power of the jet speed; the other one is a low-frequency blowing slot edge (lip) noise, which scales with the 5th power of the jet speed. Oerlemans and De Bruin (2009) propose scaling laws for the noise level and frequency for high aspect ratio nozzles:

$$SPL_{norm} = \mathrm{SPL} + 20\log_{10}(r) - 10\varepsilon\log_{10}(V_j) - 20\log_{10}(h^{\gamma}w^{1-\gamma}) + 50\log_{10}(1 - M_c\cos\theta) + 98.72 \tag{8.3}$$

$$f_{norm} = \log_{10}\left(fh^{\gamma}w^{1-\gamma}(1 - M_c\cos\theta)/V_j\right) \tag{8.4}$$

where the subscript *norm* means the normalized value, ε is speed exponent, γ is the geometry factor which can be varied in analysis of the experimental results, h and w are the length and width of the slot, M_c is the convective Mach number. Munro and Ahuja (2003) conducted experiments of jet noise with speeds higher than 150 m/s ($M > 0.4$) and the spectra collapse well under the speed exponent of 8. The jet speeds in the experiments conducted by Oerlemans and De Bruin (2009) are below 140 m/s ($M < 0.4$) and the spectra collapse using the speed exponent of 5. Therefore, the edge noise component can be attributed to lower jet speeds ($M < 0.4$), whereas the mixing noise component can be attributed to higher jet speeds ($M > 0.4$). Because the full speed of the train is taken as 400 km/h (111 m/s, M=0.32), which is assumed equal to the jet speed, the jet noise is dominated by the edge noise and the appropriate speed exponent is 5. According to the experimental results from Oerlemans and De Bruin (2009), a geometry factor γ of 0.75 is appropriate. In Equations (8.3) and (8.4), the term $(1 - M_c\cos\theta)$ represents the directivity effect, which is relatively small compared with other terms, such as the speed and geometry terms. Thus, when estimating the noise of the jet, which will be applied to the full-width train model, the directivity effect will not be considered.

Table 8.1 lists the parameters of the jet slot in the experiment from Oerlemans and De Bruin (2009) and the single straight jet considered in section 8.1.2. The length of the targeted jet slot is 2.4 m, which is twice the length of the jet slot at the cowcatcher bottom and similar to the total length of the ones at the side of the car body (2.3 m). Figure 8.10 shows 1/3 octave sound pressure spectra at the side receiver. The black solid line is the noise spectrum of a full-width model converted from the standard half-width one in Chapter 7, and the red solid line is the noise spectrum of the model with single straight jet calculated in section 8.1.2. When estimating the total jet noise, which is the blue dashed line in Figure 8.10, the jets at the bottom and the side of the car body are assumed to be incoherent sources. It can be noted that although the jet noise near 1000 Hz is greater than that of the case with the single straight jet, the total noise level will not be largely affected as this is dominated by lower frequency components. Therefore, the noise reduction by the jet is large enough to compensate for the additional noise created by the jet itself.

Table 8.1 Scaling parameters of the jet

Model parameters	*w* (m)	*h* (m)	*r* (m)	V_j (m/s)
Experimental jet	0.011	0.436	0.8	113
Targeted jet	0.0266	2.4	20	111

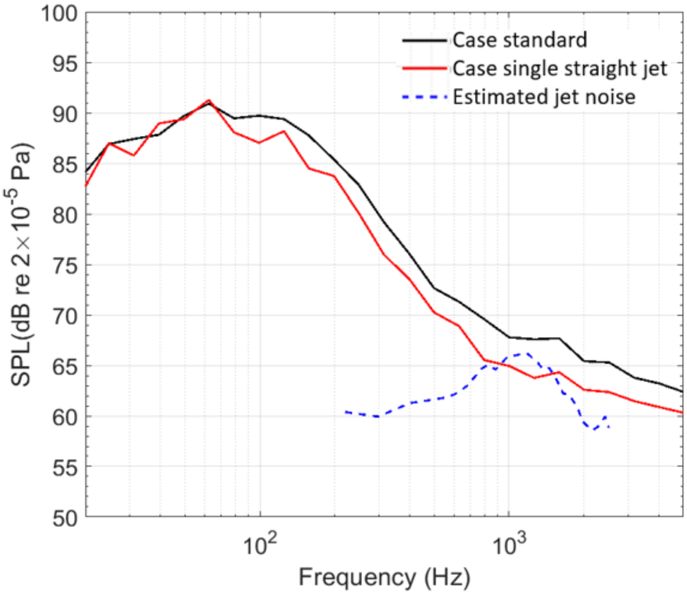

Figure 8.10 Comparison of noise spectra from jet and train models at side receiver 0°

8.2 Application of jet flow on full width model

After the test calculations, the parameters of the dual staggered jet, as shown in Figure 8.5 and Figure 8.6(c), are chosen to be applied on the full-width model depicted in Chapter 6. The grid parameters and the numerical settings, including the boundary conditions, time steps and numerical schemes are all the same as those of the full-width model in Chapter 6.

The total simulation time is about 4.4 s, the non-dimensional time t^* is about 26. The data collection is from 0.6 s to 4.4 s, corresponding to 22 flow-through times of the length of the car body model. The computational wall-time is approximately 700 hours with 640 processors on the Iridis5 cluster at the University of Southampton.

8.2.1 Aerodynamics comparison

Table 8.2 compares the force coefficients of the components of the model with the application of the jet and without it. The components listed, the motors, the gearboxes, side dampers and the cavity surface, are the ones affected by the shear layer, as shown in Figure 6.15, and their geometry can be found in Appendix A. The rms values for the upstream motor and gearbox are all reduced, $C_{d,rms}$ by

26%, $C_{l,rms}$ by 6%, and $C_{s,rms}$ by 51%. Compared with the upstream motor and gearbox, the force fluctuations of the downstream one has a smaller difference. For the side dampers $C_{d,rms}$ and $C_{s,rms}$ are reduced by around 50% by the jet flow but the reduction of $C_{l,rms}$ is only 6%. The reduction of the force fluctuations of the cavity is about 21% for $C_{d,rms}$ and 9% for $C_{l,rms}$. The mean total drag coefficient C_d is slightly reduced after the application of the jet. However, the mean total lift coefficient C_l increases by about 15%. The rms value of drag $C_{d,rms}$ reduces by about 19%, whereas $C_{l,rms}$ and $C_{s,rms}$ are nearly doubled. This difference is mainly from the car body, which is swept by the mixed flow of the jet and the detached shear layer at the rear part of the car body.

Table 8.2 Summary of force coefficients of the components with jet and without jet

Comp. with jet	C_d	C_l	C_s	$C_{d,rms}$	$C_{l,rms}$	$C_{s,rms}$
Up_motor_gear	-0.0037	0.00079	0.000616	0.0016	0.0014	0.0012
down_motor_gear	0.00218	-0.00271	0.00143	0.00151	0.00141	0.00151
Side dampers	0.00341	-0.00041	-0.000338	0.000796	0.000415	0.000716
Cavity	0.062	-0.09	-	0.00523	0.00601	-
Bogie	0.00351	-0.00662	0.000598	0.00264	0.00286	0.00316
Car body	0.110	-0.118	-0.00077	0.00555	0.00688	0.00547
Total	0.113	-0.125	-0.00017	0.00480	0.00749	0.00647
Comp. without jet	C_d	C_l	C_s	$C_{d,rms}$	$C_{l,rms}$	$C_{s,rms}$
Up_motor_gear	-0.00442	0.00123	0.000169	0.00127	0.00132	0.000792
down_motor_gear	-0.00285	0.000704	0.0021	0.00152	0.0014	0.00148
Side dampers	-0.00168	-0.00188	-0.000114	0.0005	0.000394	0.00055
Cavity	0.0951	-0.228	-	0.00432	0.00551	-
Bogie	-0.0364	-0.0124	0.000741	0.00242	0.00323	0.00298
Car body	0.146	-0.131	0.000406	0.00443	0.0124	0.0138
Total	0.110	-0.144	0.00115	0.00389	0.0136	0.0143

The PSDs of the force coefficients of the car body and the bogie are presented in Figure 8.11. The calculation method is the same as that used in section 6.3. It can be noticed that when the frequencies are greater than 30 or 40 Hz, the PSDs of the model with the jet are all lower than those of the model without jet, but they increase at very low frequencies. This implies that the momentum injected by the jet flow has a positive effect on the force fluctuations at all frequencies except for the very low ones (<30 Hz). Thus, the increases of the rms value of C_l and C_s in Table 8.2 are from the very low frequencies.

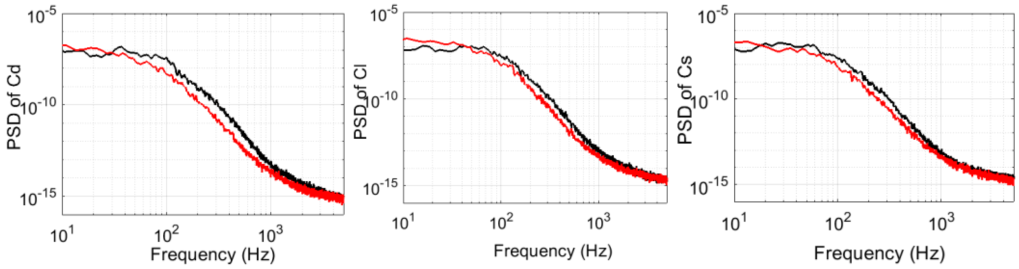

(a) bogie

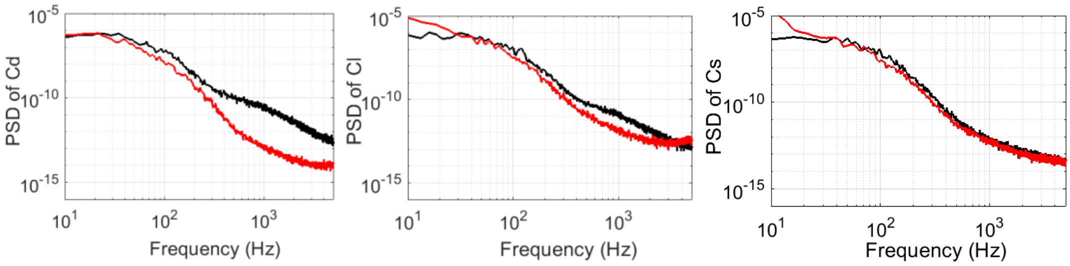

(b) car body

Figure 8.11 Comparison of PSD of force coefficients, the black line is the model without jet, the red line is the model with jet

Figure 8.12 shows the mean flow field around the jet slots at the side and bottom of the train. The direction of the jet flow is perpendicular to the train surface. The jet flow, which has a speed that is the same as the main stream, is inserted into the main stream through the boundary layer near the solid surface. At the root of the jets, it creates a blockage effect that changes the direction of the boundary layer flow. The detached shear layer is pushed away from the cavity region by the jet momentum. Figure 8.13 illustrates the changes of the trajectory of the detached shear layer. In Figure 8.13(a) and (b), the black line is the trajectory of the shear layer detached from the side of the train. It can be noted that the main stream is pushed away from the cavity, which makes the side dampers and the corners of the cavity stay away from the high-speed stream. A similar effect is also made by the jet at the bottom. The main stream is pushed away from the bottom of the cavity towards the ground. According to the analysis in section 6.3, the detached shear layer has a great influence on the pressure fluctuation generation of the downstream components. Therefore, since the detached shear layer is pushed away from the components, a reduction in the pressure fluctuation on them can be expected.

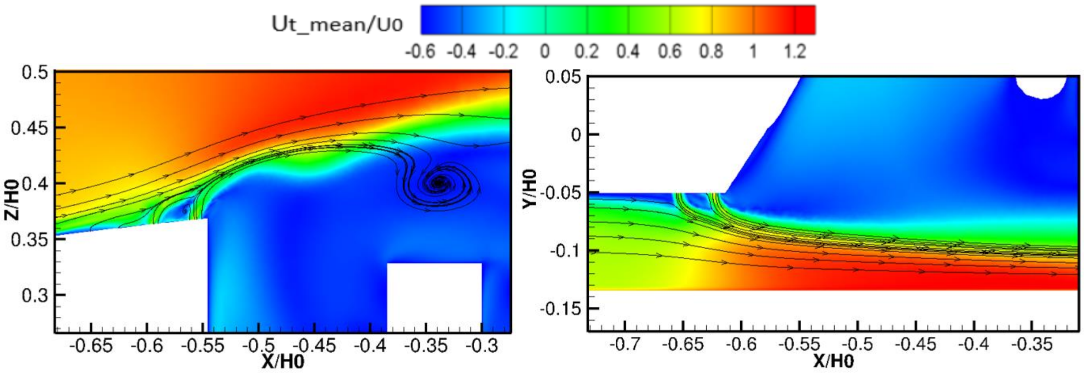

(a) side jet (b) bottom jet

Figure 8.12 Mean velocity field and streamlines near the jet nozzle

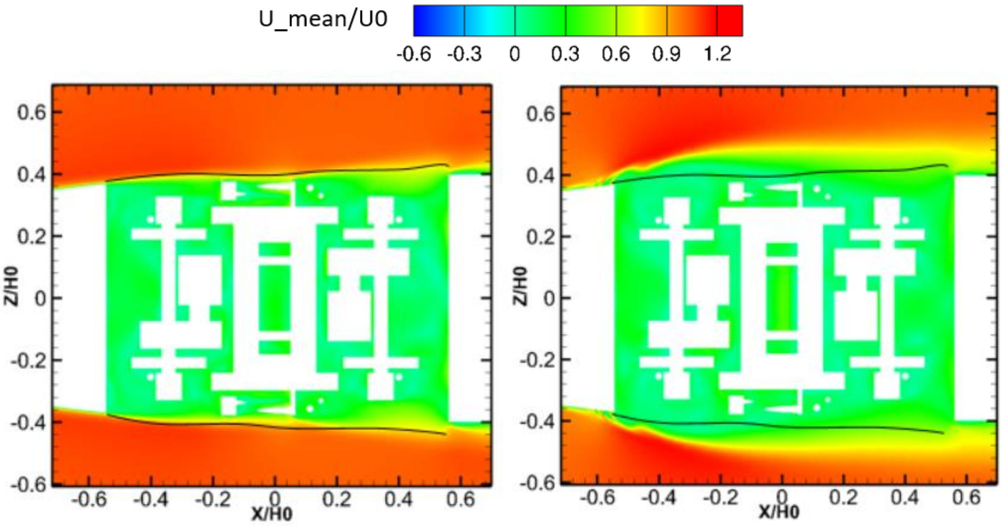

(a) slice Y0 of original model (b) slice Y0 of jet-installed model

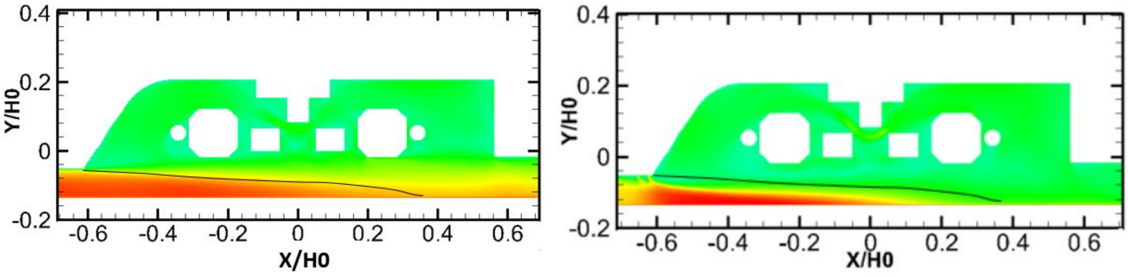

(c) slice Z0 of original model (d) slice Z0 of jet-installed model

Figure 8.13 Streamwise velocity field comparison of original model and jet-installed model

In Figure 8.14, the levels of the pressure change rate $L_{\dot{p}}$, which is defined by Equation (3.37), on the models are compared. The pressure fluctuations on the components, such as the bogie bottom and cavity bottom, as shown in Figure 8.14(a), are significantly reduced. Figure 8.14(b) compares the pressure fluctuation on the car body. The pressure fluctuation at the bottom of the train nose and cowcatcher is reduced because of the air collection nozzle at the front face of the cowcatcher. For the rear surface of the bogie cavity, the flow impingement produced the highly turbulent wake from upstream is the main reason for the pressure fluctuation generation. The jet pushes away the shear layer, as shown in Figure 8.13, and consequently reduces the pressure fluctuation on the rear surface of the cavity. For the cavity roof, the pressure fluctuation at the two sides is also reduced by the side jet but there is no significant reduction in the middle. In Figure 8.14(c) and (d), it can be noted that the pressure fluctuation on the side components of the bogie including the side dampers and the side of the wheels and axle boxes are reduced. However, the pressure fluctuation near the side rim of the bogie cavity increases because of the wake of the jet flow. For the pressure fluctuation on the moving ground, as shown in Figure 8.14 (e), it is reduced at the front part because of the air collection nozzle at the cowcatcher, whereas it is increased by the bottom jet which pushes the turbulent stream towards the ground as shown in Figure 8.13(d).

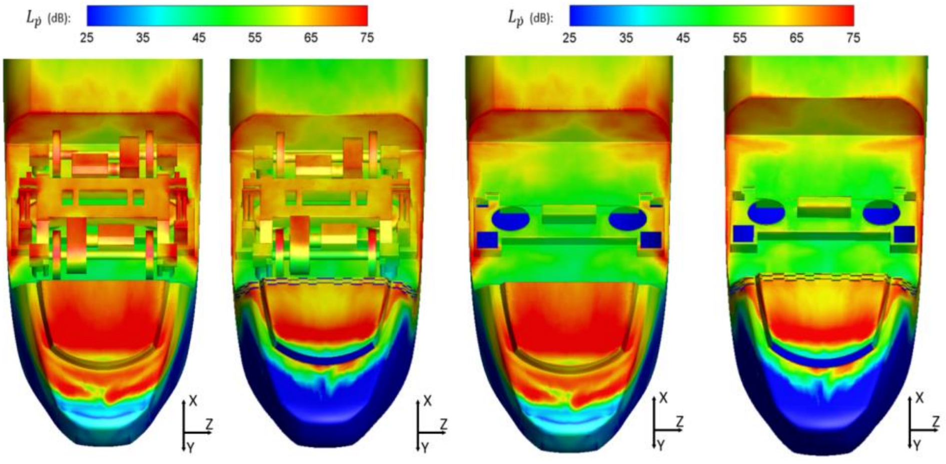

(a) bottom of whole models

(b) bottom of car bodies

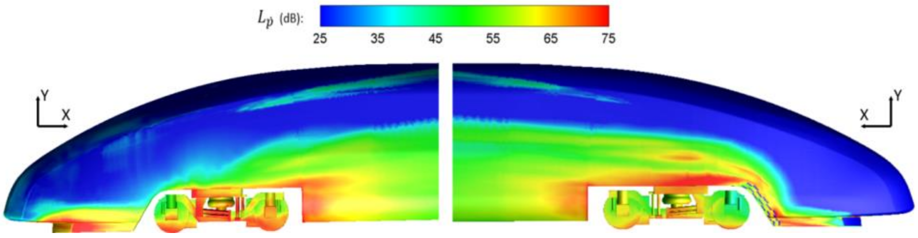

(c) side of whole models

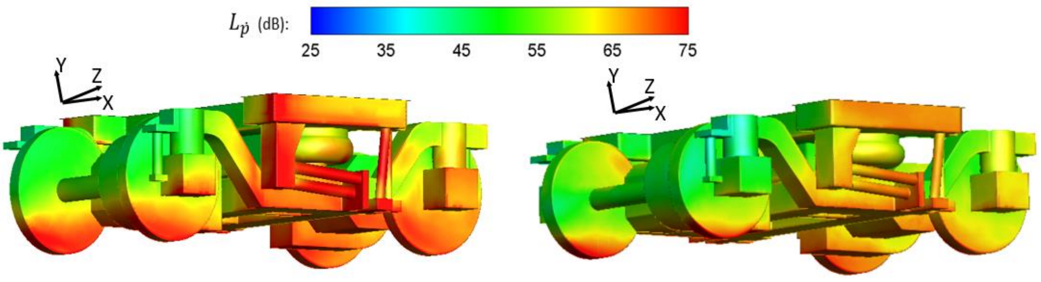

(d) side of bogies

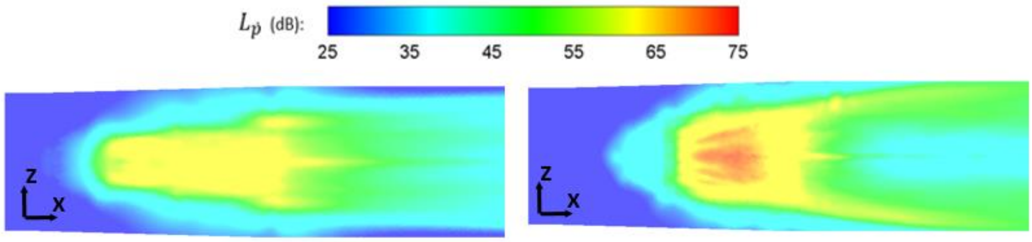

(e) ground

Figure 8.14 Comparison of surface contours of $L_{\dot{p}}$ integrated from 20 to 1600 Hz. The left one is from the original model, the right one is from the jet-installed model.

8.2.2 Aerodynamic noise comparison

The collected pressure data on the solid surface, with sampling length of around 22 flow-throughs of the car body model, is used to calculate the far field noise by the FW-H equation. The sampling frequency is the same as that illustrated in section 6.4. Figure 8.15 shows the noise spectra of the two models at the side receiver. For the spectra of the car body, shown in Figure 8.15(a), it can be noted that the noise levels of model with jet are smaller than those of the original model from 30 to 2000 Hz at full scale. In Figure 8.15(b), for the bogie spectra, the range is 30 to 800 Hz. However, the noise levels at very low frequencies, from about 5 Hz to 25 Hz, are increased after the application of the jet. In section 8.2.1, this increase at very low frequencies is also found in the spectra of C_l and C_s. This implies that the side jet strengthens the very low frequency fluctuation in the lateral direction and the bottom jet does that in the vertical direction. However, the upper limit of the frequency of this increase is very close to 20 Hz, which is at the lower limit of the normal range of human hearing. Therefore, the increased noise levels at the very low frequencies (< 20Hz) are not considered in the SPL calculation.

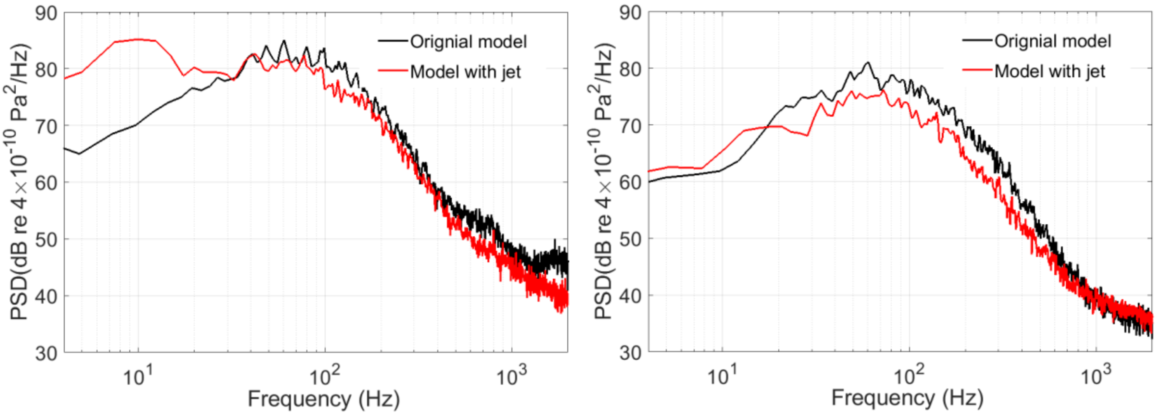

(a) car body

(b) bogie

Figure 8.15 Comparison of noise spectra of the side receiver at 0°

Figure 8.16 compares the overall SPLs, which are integrated from 20-2000Hz, of these two models at the side receivers shown in Figure 6.21. In Figure 8.16(a), the noise reduction of the car body is about 2 dB at all receivers. The maximum reduction of the bogie in Figure 8.16(b) is about 3.5 dB and the minimum is about 3 dB. Figure 8.17 compares the directivities of the models. The directivities of the model with the jet installed are omnidirectional. The noise levels are all reduced in all directions for both of the car body and the bogie. The maximum noise reduction of the car body is about 2 dB at the receivers of 150° and 330° and 3 dB for the bogie at two of the side receivers.

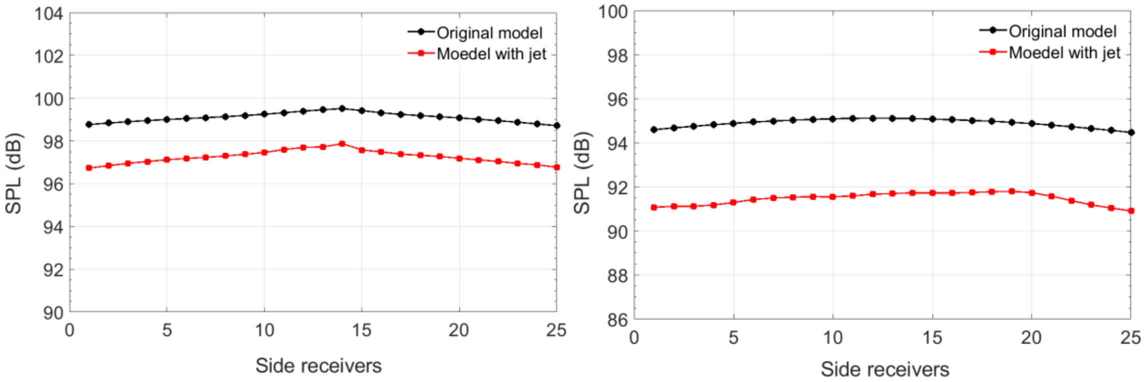

(a) car body

(b) bogie

Figure 8.16 Comparison of SPLs at the side receivers

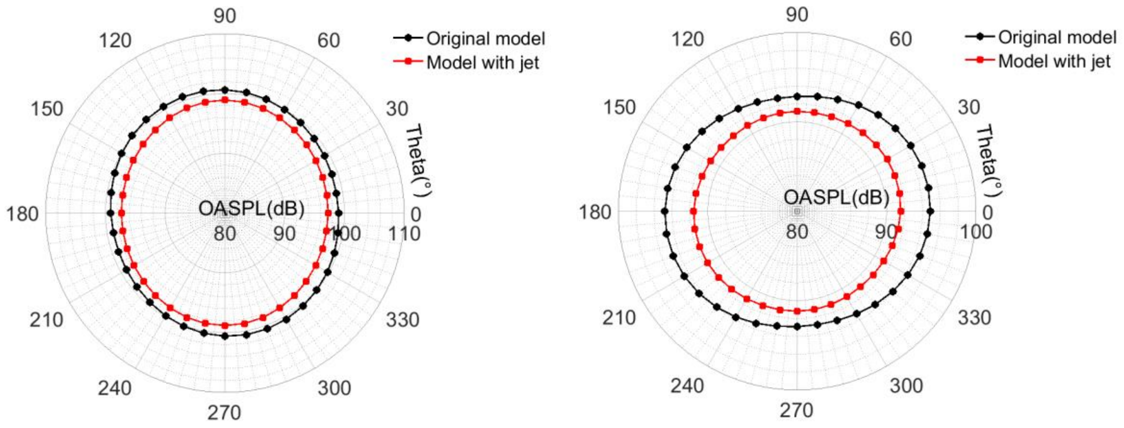

(a) car body (b) bogie

Figure 8.17 Comparison of the directivity

The overall sound power (20-2000Hz) emitted by the car body, the bogie and their total are compared in Figure 8.18. The calculation method of the SWL of the model with jet is the same as the one illustrated in section 6.4. The sound power reduction for the car body is 3.2 dB and the one for the bogie is 4.5 dB. The total noise is reduced by 3.5 dB. To investigate the sound power reduction of each component, Figure 8.19 compares their SWLs. All of the SWLs of the model with the jet installed are reduced, except for that of rear part of the car body, which increases by about 1 dB. It is believed that the turbulence of the wake from upstream is increased, which is one of the detrimental effects brought by the jet flow, and then, the intensity of the pressure fluctuation rises. In addition, the reduction of the noise from the ground is only 1.4 dB, which is smaller than those of other components. As shown in Figure 8.14(e), although the pressure fluctuation on the area of the ground under the cowcatcher is reduced because part of the air is sucked by the air collection nozzle at the front face of the cowcatcher, the air under the bogie is pushed down to the ground by the jet at the bottom of the cowcatcher, which increases the pressure fluctuation strength from that area. Therefore, the overall percentage of the sound power reduction is not as high as those of other components.

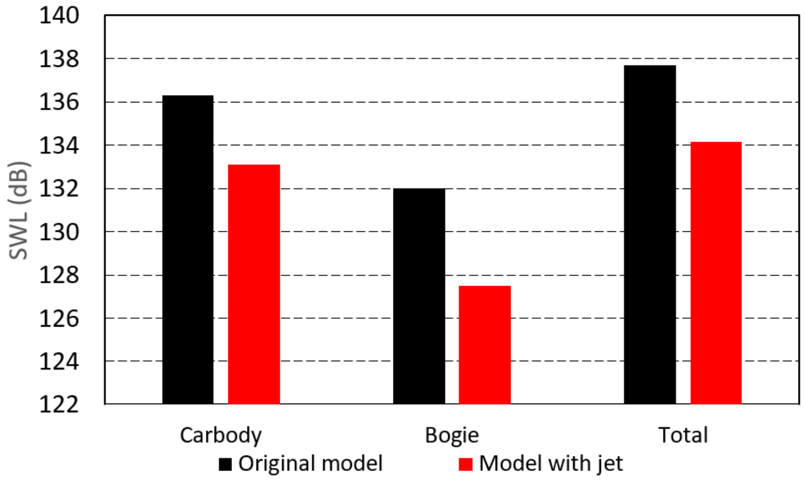

Figure 8.18 Comparison of the SWLs of the car body, the bogie and their total

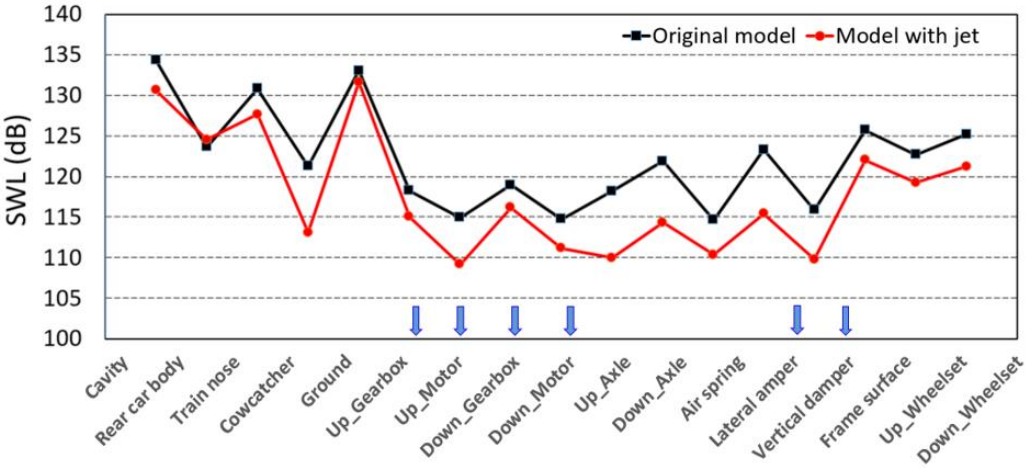

Figure 8.19 Comparison of the SWLs of different components: the components indicated by the blue arrows are directly exposed to the shear layer

8.3 Summary

In this Chapter, a noise reduction measure based on introducing a secondary jet is explored. The possible noise emitted by the jet is compared with that generated by the bogie and the car body. The result shows the potential jet noise is much smaller than that of the simulated model. The effect of the velocity profile at the jet outlet on the jet trajectory is assessed as well as a comparison of the single jet with a dual jet. The uniform velocity profile at the outlet slightly increases the shielding height of the single jet and significantly increases that of the dual jet. The shielding height of a dual jet is about twice of that of a single jet, which implies that the dual jet has a potential that can be used to improve the noise reduction effect. In order to test the effect of different jet slots, three kinds of strategies of the jet slots are tested by using the half-width model from Chapter 7. The air collection nozzle is also considered in the simulations. The results show that compared with the single straight jet and the single staggered jet, the dual staggered jet is able to achieve a greater reduction in the sound power generated by both the car body and the bogie. In addition, the air collection nozzle at the front face of the cowcatcher has a positive effect on the noise reduction of the bottom of the cowcatcher and the ground surface below it.

In the following simulation, the configuration parameters of the dual staggered jet and the air collection nozzle are applied to the full-width model from Chapter 6. The aerodynamic results show that the detached shear layer, which is close to the outside components of the bogie and its cavity, is pushed away from the bogie region. Therefore, the noise intensity on the bottom and side components of the bogie and the rear surface of the cavity is significantly reduced. Besides that, the pressure fluctuation at the bottom of the cowcatcher is also reduced because of the suction of the air flow by the air collection nozzle. The comparison of the noise spectra at the side receiver shows the noise levels are reduced by the jet at almost all frequencies in the range 30-2000 Hz but are increased at very low frequencies. The SPLs on the side receivers and circular receiver grid are all reduced. The maximum reduction in the SPL value is about 3.5 dB for the bogie and 2 dB for the car body. Finally, the SWLs of those two models are also compared. The total SWL is reduced by 3.5 dB which means the sound power of the original model is reduced by about half. For the components of the model, the SWLs of almost every component are reduced except for the one of the rear part of the car body, which is affected by the turbulent wake from upstream strengthened by the jet flow.

Chapter 9 Feasibility of using decomposed CFD models

In previous chapters, many simplifications are made to reduce the computational cost of the simulations, such as reducing the scale of the geometry, ignoring some small features of the bogie, and using the half-width model. Nevertheless, those simulations are still time-consuming, both in generating the mesh and in solving the Navier-Stokes equations. It is desirable to investigate flow around different geometries, as studied in Chapter 7, especially the downstream components of the bogie and cavity, to improve the aerodynamic and aeroacoustic performance of the train (Shuanbao et al. 2014; Munoz-Paniagua and García 2020). To do this, it is reasonable to consider the incident flow from upstream as unchanged. This allows the local flow around those components to be studied without performing simulations of the whole train, which are much more time-consuming. To reduce the computational cost, the current work proposes a novel CFD simulation method to calculate a decomposed zone from a high-speed train model, where machine learning is used to generate the incoming flow. The method includes the decomposition and discretization of the large model, the generation of the boundary condition data including the turbulence recycling and usage, and the boundary data storage.

9.1 Model decomposition method

9.1.1 Method and validation model description

To reduce the computational cost of a model with a complex geometry, eliminating excess structures to reduce the grid number is a direct and effective way. Only the area of concern is modelled and the effects due to other structures are considered in boundary conditions. Figure 9.1 shows the procedure of the proposed decomposition method. In the first step, the model is decomposed according to its geometrical characteristics. Then the flow field properties at the boundaries of the studied zone, which may be reused, are collected. In the last step, the decomposed model containing different component geometries is calculated using the boundary conditions that are reproduced from data obtained in the second step.

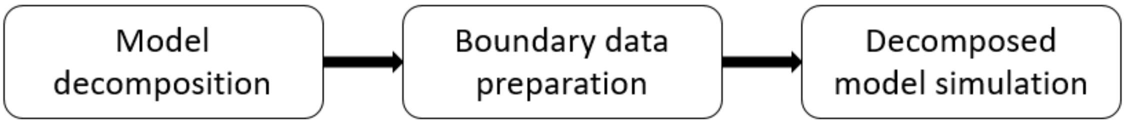

Figure 9.1 Procedure of the decomposition method

A simple model as shown in Figure 9.2 is used to illustrate and test the decomposition method. Figure 9.2(a) is the complete model for two tandem square cylinders. The model is three-dimensional, the spanwise length is 3*D* (*D* is the side length of the square cylinder). The whole domain can be divided into two parts, as indicated by the red dashed line. The first part is used to generate inflow data for simulations of flow around the second cylinder using a decomposed model as shown in Figure 9.2(b). Therefore, the wake flow from the turbulence generation zone is the boundary condition of the downstream decomposed zone.

The side lengths (*D*) of the upstream and downstream square cylinders are both 7.5 mm and the incoming flow velocity is 1 m/s, which gives Re of 500 based on the incoming flow velocity and cylinder width. The geometry of the downstream cylinder can be arbitrary, but, in the current simulation, a square cylinder with the same geometry as the upstream one is chosen. A large separation distance between the two cylinders of 28*D* is chosen to eliminate the interaction from the downstream cylinder on the upstream one. Therefore, to produce a turbulent inflow for the decomposed model in Figure 9.2(b), a model as shown in Figure 9.2(c) can be used and the wake flow at the red dash line will be collected. When the geometry of the downstream cylinder changes, the flow properties near its stagnation face will be inevitably affected. Therefore, the data sampling surface should not be too close to the downstream cylinder. In order to investigate the effect of the position of the data sampling surface, three values of L_s (L_{s1}=10 *D*, L_{s2}=16 *D*, and L_{s3}=22 *D*) will be tested.

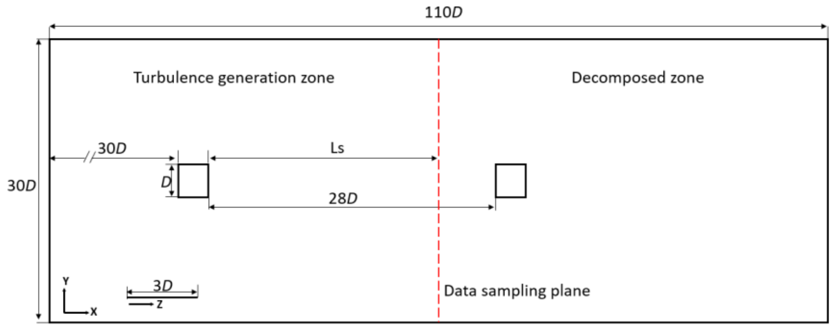

(a) complete model

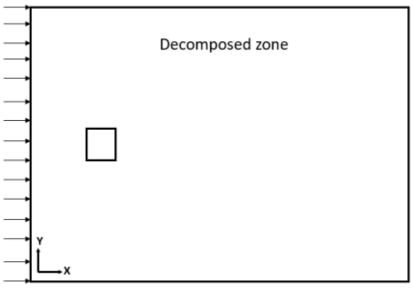

(b) decomposed model

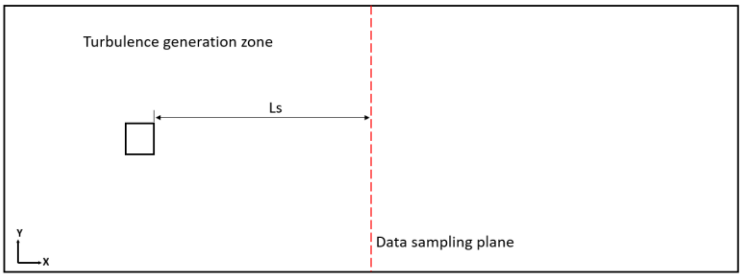

(c) model for the boundary data sampling

Figure 9.2 Schematic models for the validation of the decomposition method

9.1.2 Computational parameters

The mesh distribution of the complete model is shown in Figure 9.3. The height of the first grid layer on the cylinder surface is 1×10^{-4} m, which guarantees the maximum y^+ on the cylinder surface, which appear at the front corners of the cylinder, is smaller than 2. The maximum aspect ratio at the square sides is 3.5, which is much smaller than the aspect ratios tested in section 4.1 and adequate for the simulation with a *Re* of 500; in the spanwise direction the maximum aspect ratio is 12. The grid expansion ratio is 1.05 around the cylinders. The grid parameters near the cylinders of the decomposed case and data sampling case are all the same. The total numbers of cells are listed in Table 9.1. Compared with the complete model, the grid size of the decomposed model is reduced by more than 50%, which is expected to result in a significant reduction of computational cost.

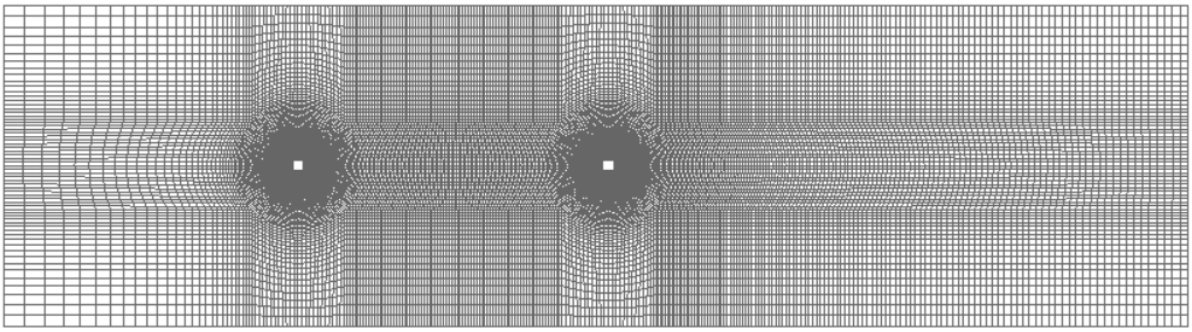

Figure 9.3 Grid distribution of the complete model

Table 9.1 The total number of cells of the three models

Case	Complete model	Decomposed model (L_{s2})	Data sampling model
Total number of cells	0.55 M	0.263 M	0.393 M

The boundary conditions for the complete model, the data sampling models as well as the decomposed model (except for the inlet ones) are the same as those listed in Table 4.1. Table 9.2 lists the inlet boundary conditions of the decomposed model. The boundary condition function

‘Time varying mapped fixed value’ in OpenFOAM 2.4.0 is used to provide the inlet data, which are collected in the simulation of the model shown in Figure 9.2(c), for numerical viscosity $\tilde{v}$ and velocity *U*; a developed boundary condition ‘Time varying mapped fixed gradient’ is used for the sub-grid viscosity *nusgs.* For the inlet boundary condition of pressure *p*, a zero-gradient boundary condition is used, which ignores the pressure change in the streamwise direction.

Table 9.2 The inlet boundary conditions of the decomposed model

Boundary	Inlet of decomposed model
nusgs	Time varying mapped fixed gradient
$\tilde{v}$	Time varying mapped fixed value
U	Time varying mapped fixed value
P	zero gradient

The physical time step of the simulations is 1.1×10^{-4} s, which ensures the maximum *CFL* number in the simulations is smaller than 1.5. The numerical schemes and convergence parameters are all the same as discussed in section 4.1.2.

The simulation results are very sensitive to the fluctuation of the mass flux at the inlet surface (Kim et al. 2013), especially for the pressure field near the inlet section of the decomposed model. Therefore, a mass flux corrector is embedded into the ‘time varying mapped fixed value’ boundary condition function in OpenFOAM 2.4.0. The corrector $f(t)$ is calculated as follows:

$$f(t) = \frac{\overline{Flux}}{Flux(t)} \tag{9.1}$$

where $\overline{Flux}$ is the prescribed mass flux value of the inlet, which can be calculated from the time-averaged velocity normal to the inlet plane. $Flux(t)$ is the mass flux of each time step, which is calculated as:

$$Flux(t) = \sum_{i=1}^{n} U_i(t) * A_i \tag{9.2}$$

where n is the number of cells on the inlet plane, $U_i(t)$ is the normal velocity on each cell, and A_i is the area of the cell. After calculating the mass corrector $f(t)$, it is applied to the three components of the velocity field, as $f(t) \times [u_i(t)\ \ v_i(t)\ w_i(t)]$.

9.1.3 Results analysis

9.1.3.1 Aerodynamic results

To collect the inflow data, the data sampling model in Figure 9.2(c) is simulated and the flow properties, such as the normal gradient of sub-grid viscosity *nusgs,* numerical viscosity $\tilde{v}$*,* and *U*, of every time step are collected. The physical simulation time step of the sampling model is 1.1 $\times 10^{-4}$ s, which is chosen to be the same with the ones of the complete model and the decomposed model and makes the maximum *CFL* smaller than 1.5. The data of every time step at the sampling surface is collected. Then it is used to reproduce the turbulence inflow data for the downstream domain. Figure 9.4 compares the original flow field from the data sampling model (left side) and the reproduced one for the decomposed model without the cylinder (right side) at different values of normalized time t^* (tU_∞ /D). A good qualitative agreement is found in the comparison of the instantaneous flow fields between the original and reproduced flow fields.

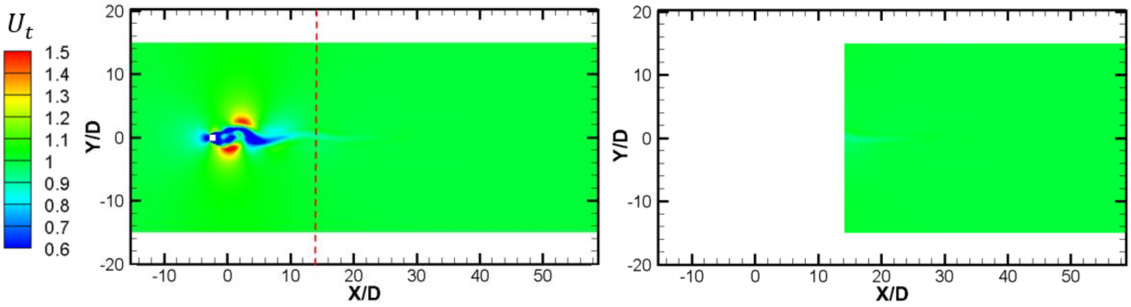

(a) t^*=35.2

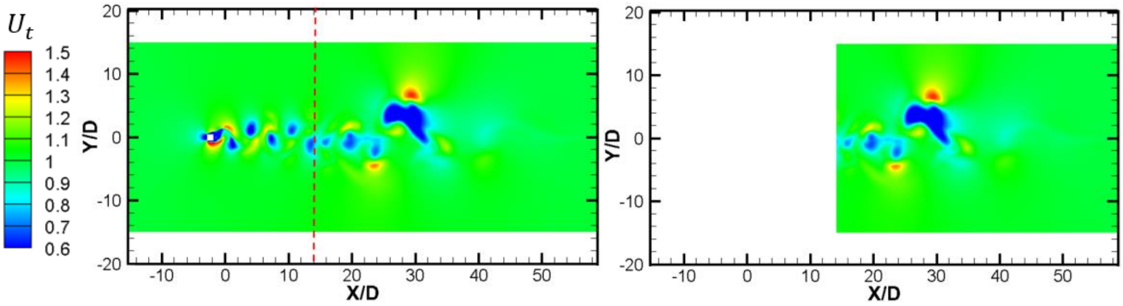

(b) t^*= 70.4

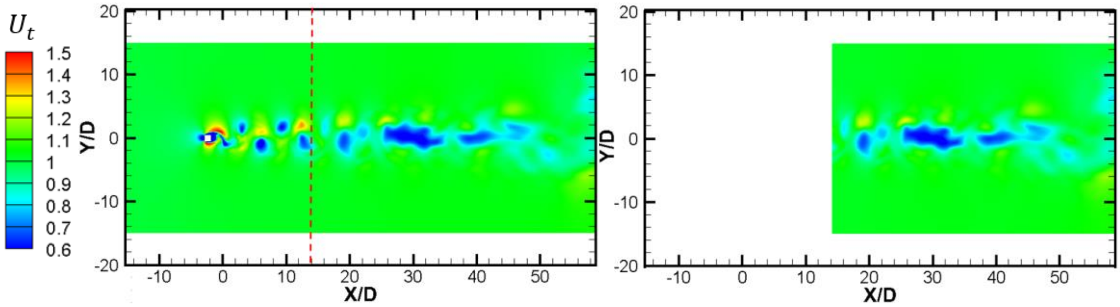

(c) t^*=105.6

Figure 9.4 The instantaneous velocity field of the data sampling model and the reproduced field at the same time instants.

Table 9.3 lists the computational time using 20 processors for every 100t^* of the complete model and the decomposed model. It is noticed that the computational time of the decomposed model is less than that of the complete model. However, as indicated in Table 9.1, the grid size of the complete model has been reduced about 50% by the decomposed model, but the computational time of the decomposed case L_{s2} is only reduced by around 30%. A possible reason is the 'Time varying mapped' boundary condition listed in Table 9.2 reads and interpolates the collected inflow data at the inlet surface of the decomposed model, and the Input/output process slows down the computation in OpenFOAM.

Table 9.3 The computational time (per 100t^* with 20 processors) of the complete and decomposed models

Case	Complete model	Decomposed model (L_{s2})	Time saved
Simulation time	241 Minutes	170 Minutes	29.6%

To compare the flow field qualitatively, 39 monitors are set in front of the downstream cylinder within the decomposed domain, as shown in Figure 9.5. The distance between the streamwise position of the monitors and the rear surface of the upstream cylinder is 24 D and the interval between the monitors is 0.5D.

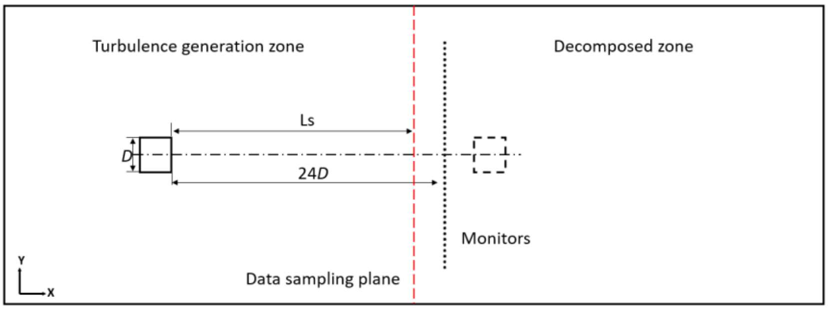

Figure 9.5 The position of the monitors

The data collected from t^*=700 to 1000 is used as the inflow data of the decomposed model and the statistical flow profiles, as shown in Figure 9.6, are compared. $\overline{U}_t/U_0$ is the velocity ratio, where $\overline{U}_t$ is the time-averaged total velocity, Tu is the tubulence intensity ($Tu = U_t'/\overline{U}_t$, with U_t the total velocity and U_t' is the rms of the turbulent velocity fluctuations). The profiles obtained with the decomposed model for the three positions of the data sampling planes, L_{s1}, L_{s2}, and L_{s3}, are compared. For the velocity ratio, as shown in Figure 9.6(a), the value of L_{s1} is about 5.5% smaller than that of the data sampling model; the difference between L_{s1} to L_{s3} is smaller than 3%. For the turbulence intensity, the difference between L_{s1} and the data sampling model is about 7% and the values of L_{s2} and L_{s3} are closer to the ones from the data sampling model. This is due to the fact that the velocity fluctuation is much stronger close to the upstream cylinder and there are more likely to be missing fluctuations between two sampling time steps and thus, the missing velocity fluctuations may have a stronger influence on the reproduced flow field. A similar conclusion was also found by Chawdhury and Morgenthal (2016), who propose to use the Vortex Particle Methods

(VPM) to reproduce the flow field. However, the curent method is still not as sensitive as the VPM used by Chawdhury and Morgenthal (2016) to the location of the sampling surface. Meanwhile, the position of the sampling surface should not be too close to the front surface of the downstream cylinder because the flow stagnation at the front surface of the downstream cylinder affects the flow properties in that region (Breuer 1998; Liu 2017). Therefore, the position of the data sampling plane is chosen as L_{s2} as a compromise.

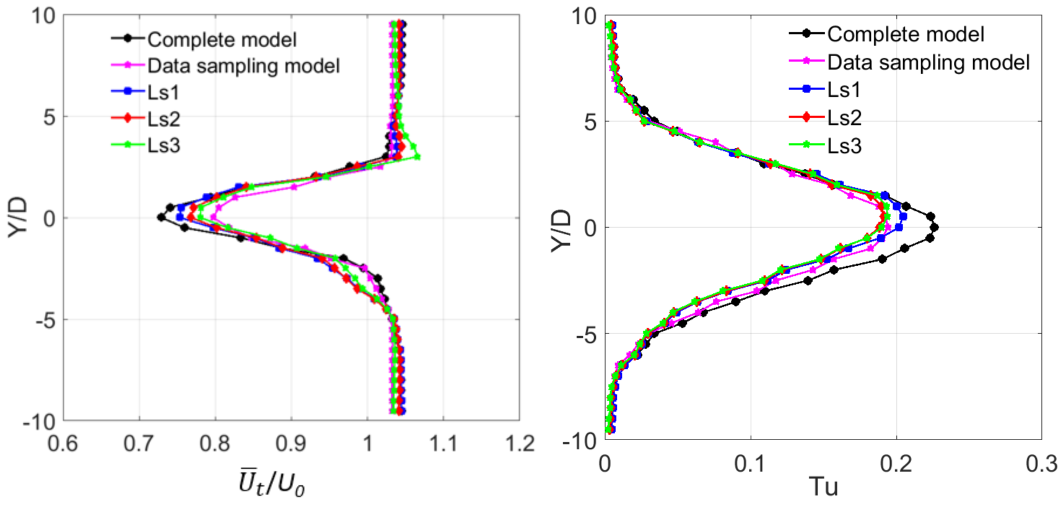

(a) $\overline{U}_t/U_0$ (b)*Tu*

Figure 9.6 The comparison of characteristic flow profiles

Figure 9.7 shows the instantaneous pressure coefficient $C_p(t)$ of the central monitor in Figure 9.5. In Figure 9.7(a), the time histories of the three models are similar. The mean absolute values of the complete model and L_{s2} are very small and their differences with the one of the data sampling model are believed to be due to the effect of the front stagnation point of the downstream cylinder, where the static pressure is successively increasing as the flow approaches the cylinder (Breuer 1998). The difference between the rms value of the L_{s2} and complete model is less than 10%, which is smaller than that between L_{s2} and the data sampling model. In Figure 9.7(b), the PSD of C_p from the three models is calculated based on Welch's method with a Hanning window. The segment length is 0.4 s, 11 segments with 50% overlap are used, corresponding to frequency resolution of 2.5 Hz. The shape of the spectra match well and the values also have a good agreement except for there is slightly difference found between the complete model with other two models at the frequency range of 50 to 100 Hz. Therefore, from the above analysis, it can be concluded that the reproduced flow field has reasonable velocity and pressure field.

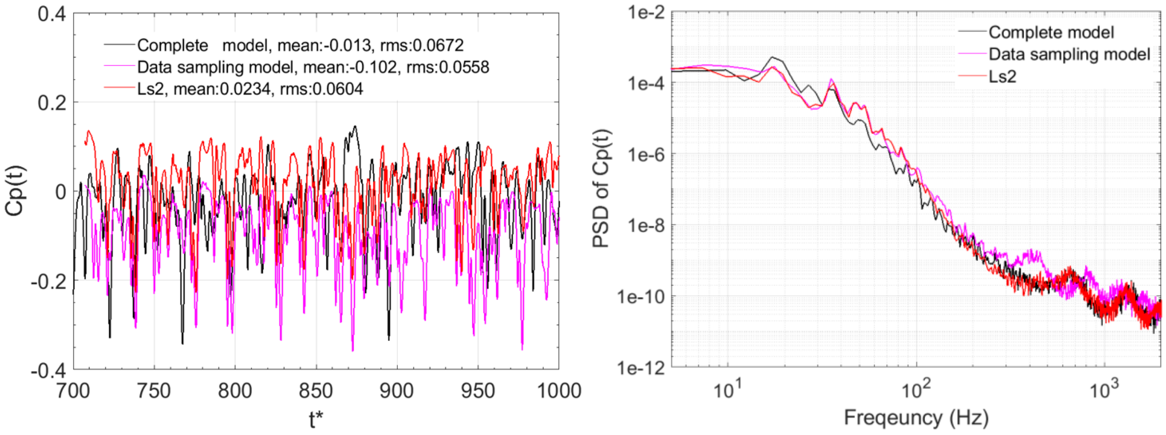

(a) time history (b) spectra

Figure 9.7 $C_p(t)$ at the monitor on the central line in Figure 9.5

Table 9.4 lists the parameters of the force coefficients of the downstream cylinder. The drag force of case L_{s2} is 12% greater than that calculated by the complete model. The flow field difference at the position of the data sampling plane of the complete model and the data sampling model is believed to be the reason. Compared with the difference in C_d, the difference in $C_{d,rms}$ and $C_{l,rms}$ of these two models are much smaller, only about 3%. Figure 9.8 compares the PSDs of C_d and C_l, which are calculated by the same method used for the spectra of C_p above. Good agreements are found in the spectra of both C_d and C_l.

Table 9.4 The flow parameters of the downstream cylinder

Case	C_d	$C_{d,rms}$	$C_{l,rms}$
Complete case	0.945	0.252	0.774
L_{s2}	1.084	0.244	0.750

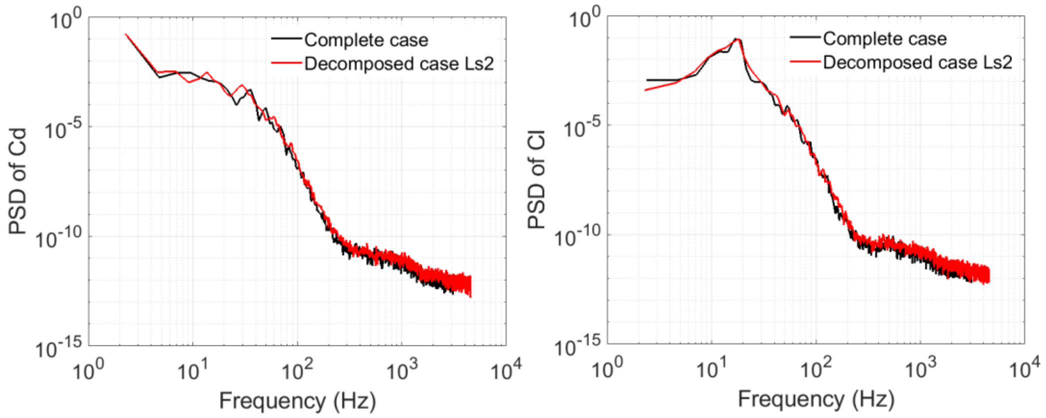

(a) PSD of C_d (b) PSD of C_l

Figure 9.8 Power spectral density of C_d and C_l

9.1.3.2 Aeroacoustic results

To investigate the noise generated by the downstream cylinder, 36 receivers are set uniformly on a circle with 5 m radius around the cylinder centre. The collected pressure on the cylinder surface is used as the input of the FW-H equation. Figure 9.9(a) shows the noise spectra at the top receiver calculated using the same Welch's method as described earlier. A good agreement between the complete and decomposed models is found, including the peaks at the vortex shedding frequency. Figure 9.9(b) shows the directivities which have the typical shape of the dipole noise source. The maximum difference is only about 1 dB at 50° and 230°. This is probably caused by the slightly asymmetric distribution of the flow profiles in Figure 9.6 due to the limited data sampling time. The good agreement of the noise results indicates that the decomposed model can well reproduce the pressure fluctuation on the cylinder surface.

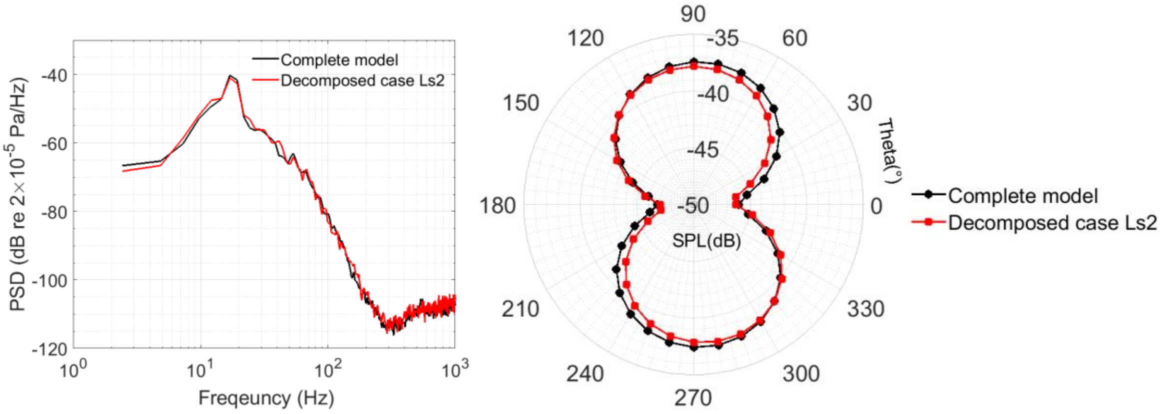

(a) spectra at top receiver (b) directivities

Figure 9.9 Comparison of the noise generated by the downstream cylinder

9.2 Boundary data storage and reusage

A problem with the decomposition method is the size of the collected inflow data from the sampling model could be very big, which makes the storage and reusage of the data very inconvenient. It is noticed that the contour of the variables, e.g. velocity components, and pressure field, in the previous chapters can be regarded as images. Therefore, the collected inflow data can be also regarded as a series of images that need to be stored.

Conventional data compression techniques can be used to transform the original data to compact forms by various algorithms, coding schemes and the recognition and utilization of patterns existing in the data (Huffman 1952; Ahmed et al. 1974; Ziv and Lempel 1977; Abedi et al. 2019). Such techniques involve analysing the data and capturing particular forms of regularities within the data. Consequently, they are not efficient when dealing with images with a broad range of features and the compression ratio varies according to the structure of the data (Kattan 2010). However, studies in recent years show that neural networks have great potential in image compression (Baldi 2012; Jayasankar et al. 2021). Thus, in this section a convolutional variational AutoEncoder (VAE) neural network based on the one proposed by (Laubscher and Rousseau 2020) will be applied to solve the problem of inflow data storage. The use of the reconstructed inflow data obtained by the VAE neural network will also be discussed.

9.2.1 VAE neural network

A basic unit of a neural network, as shown in Figure 9.10, is a perceptron, which is analogous to the biological neuron and was invented by Rosenblatt (1958). A single perceptron can be used to solve a problem such as linear binary classification. When the problem becomes more complex, for example, the nonlinear binary classification problem, it can only be solved by a network of perceptrons. As shown in Figure 9.10, such a neural network consists of an input layer, a hidden layer and an output layer. The adjective “deep” in deep machine learning refers to the use of multiple hidden layers in the neural network. The number of hidden layers usually depends on how complex the problem is. The coefficients W1 and W2, which represent the weights of the input signal given to a perceptron, are the main coefficients that need to be trained. The neural network in Figure 9.10 is the basis of the advanced machine learning programs.

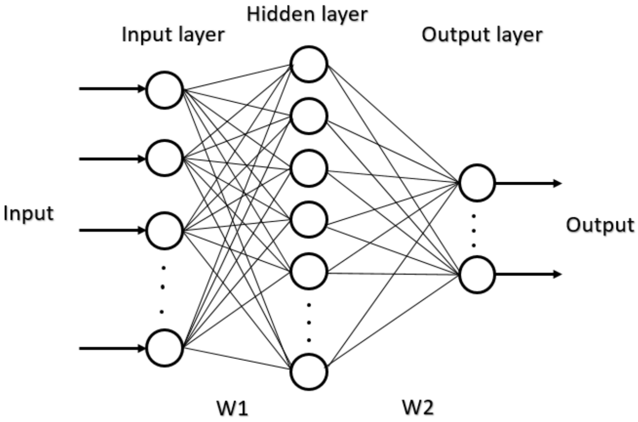

Figure 9.10 A neural network

In image processing, the input data of the neural network are the pixel values of an image that need to be processed. For image recognition or classification, the computer identifies the image by the specific coherence between a pixel and other pixels around it, which would require a large number of hidden nodes if the image has many features. As shown in Figure 9.10, the number of coefficients $W1$ equals the product of the number of inputs (pixels) and the number of hidden nodes. Therefore, using a conventional neural network to identify an image with some detailed features, many coefficients will need to be trained and, thus, the computational cost will be inevitably large. Considering this, a more efficient method, which is called a convolutional neural network was proposed by LeCun et al. (1989) and developed further by LeCun and Bengio (1995) and LeCun et al. (1998). This can identify an image by patterns or features instead of the specific coherence of the pixels. The aim of the convolution is to reduce the raw image to a form that is easier to process without losing its features (Albawi et al. 2017). Instead of directly importing the pixel values into the hidden layer, as shown in Figure 9.10, the raw image is convolved with a kernel of a specific size allowing the number of pixels to be reduced. The size and values of the kernel can be designed according to the features of the image. The kernel moves from left to right in the horizontal direction and from top to bottom in the vertical direction with a certain stride until the whole image is traversed. The values of the area in the original image are multiplied by the corresponding ones in the kernel and their sum is the pixel value of the convolved image. After the convolution, the size of the original image is reduced. There can be multiple convolutional layers and, moving from the first layer to the last layer, the features that can be captured change from low-level ones such as edges, colours and gradient orientation to high-level ones such as faces and legs (Zeiler and Fergus 2014). After a convolution layer, a pooling layer is usually used to extract further dominant features, and which can also reduce the computational cost. There are two types of pooling layer, the max pooling which outputs the maximum value from the portion of the image covered by the kernel and the average pooling which outputs its average value. The size of the image after the conversion layer and pooling layer is greatly reduced and can then be imported to a conventional neural network as shown in Figure 9.10. The number of parameters that need to be trained for the convolved image is much less than the original ones.

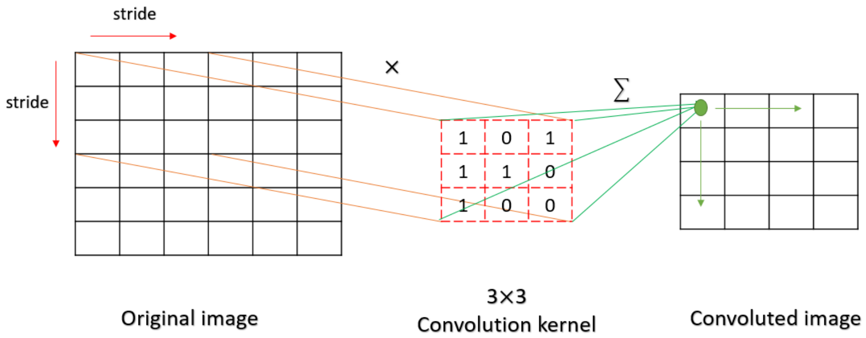

Figure 9.11 A schematic workflow of the convolutional layer

In machine learning, the AutoEncoder (AE), which can carry out unsupervised learning and was first introduced by Hinton and the PDP group (Rumelhart et al. 1985), is usually used for image compression and image interpolation (Baldi 2012). As shown in Figure 9.12, an AE consists of an encoder and a decoder. The encoder compresses the image with a high dimensionality into a latent space, which looks like a ‘’bottle neck’’ of the neural network in Figure 9.12, while the decoder does the opposite. Therefore, the number of nodes of the input layer is the same as that of the output layer. To ensure the latent space extracts all the features of the input data, the loss function, which is the mean squared error between the encoder input and the decoder output, should be small enough after training. When an AE is well trained, its latent vectors can be used to reproduce the original images together with the decoder, which makes the size of the data that needs to be stored become much smaller than that of the original images. As shown in Figure 9.13, the hand-written digits in MNIST data(Deng 2012) are converted to points in latent space. The cluster with points of the same colour represents one particular digit with different shapes. Inputting any point within a cluster to the decoder will generate a specific digit that the cluster belongs to. However, points in the regions that do not belong to any cluster in the latent space will generate "garbage" output, which may make the interpolation between different images fail in some situations.

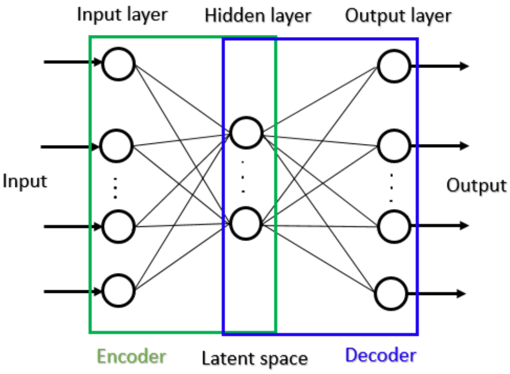

Figure 9.12 Neural network of AutoEncoder

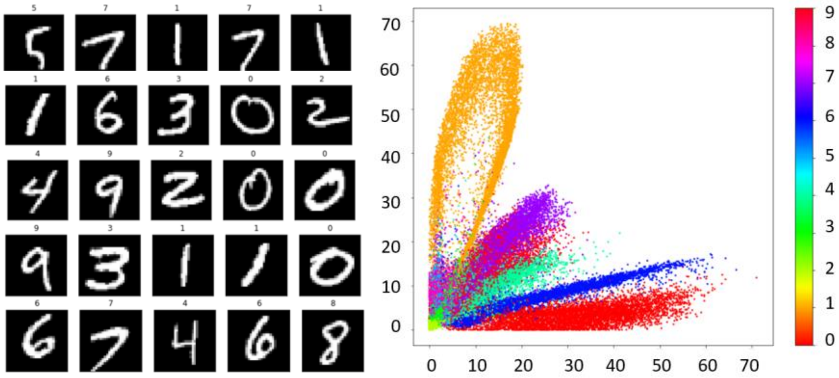

(a) hand-written digits (b) latent space

Figure 9.13 An example of hand-written digits and the latent space

To address the issue, Kingma and Welling (2013) introduced a Variational AutoEncoder (VAE) to provide the generative capability over the entire space. As shown in Figure 9.14, instead of outputting the latent vector, the encoder of VAE outputs the mean and the standard deviation of a pre-defined distribution, which is regularized to a normal distribution after training. In the latent space, the latent vector is then sampled from this distribution. The decoder works similarly to that of the AE. The loss function of the VAE is used to quantify the difference between the expected output and the real output by VAE. It contains two parts, one is the same as for the AE (reconstruction loss, the mean squared error between input and output), the other one is the Kullback-Leibler divergence (KL loss or similarity loss), which is a measure of divergence between the latent space distribution and a normal distribution (Kingma and Welling 2013; Doersch 2016). In the training, it is necessary to find a balance between these two losses. A small similarity loss ensures that there are no significant gaps between the boundaries of similar clusters, such as shown in Figure 9.13(b), while a small reconstruction loss ensures that the original images can be well reconstructed after compression. In this work, the focus is on the compression function of VAE, and thus, the reconstruction loss is primary to reduce.

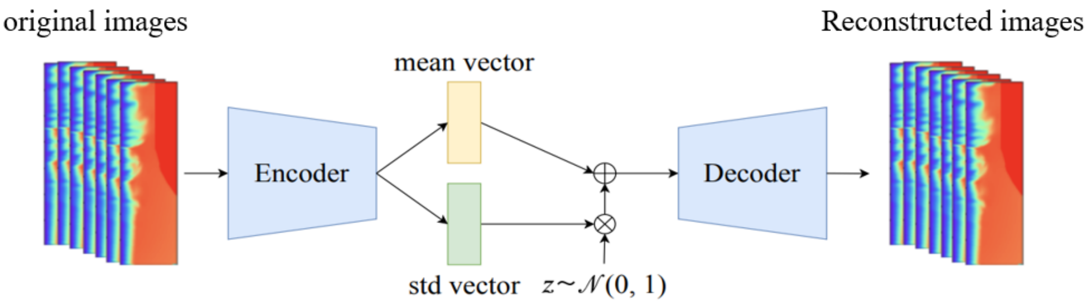

Figure 9.14 Schematic structure of VAE

In this work, a convolutional VAE neural network, as shown in Figure 9.15, will be used, which is based on the one used by Laubscher and Rousseau (2020). The convolutional VAE, which combines the convolutional neural network and conventional VAE, can extract and compress the features of images more efficiently than the conventional VAE, which does not contain the convolutional layers.

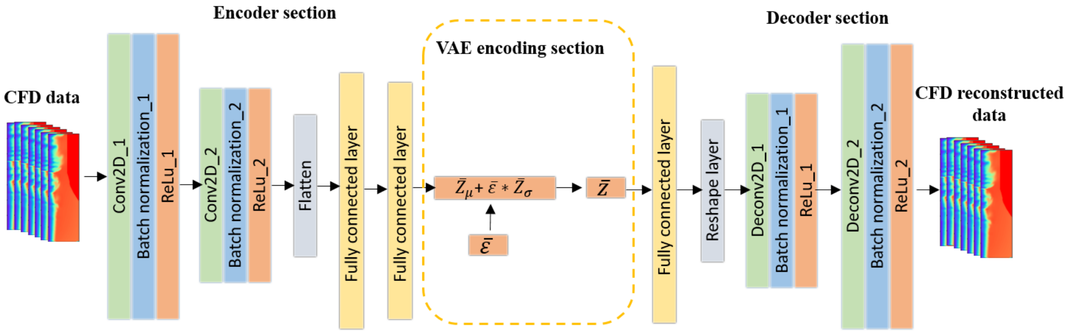

Figure 9.15 Schematic structure of the convolutional VAE

9.2.2 The inflow data storage by VAE

Figure 9.16 illustrates the details of the encoder and decoder sections of the convolutional VAE in Figure 9.15. The pixel size of a single input image is 64×24, which has a similar total number of pixels as the number of cells at the data sampling surface as shown in Figure 9.2. After importing the image, there are two convolutional layers both using a 3×3 kernel to compress the image into a smaller data batch. The stride of the convolutional layer is set to 2, which is based on the balance of the image features that can be captured and the parameters that need to be trained (O'Shea and Nash 2015). The output array from the convolutional layer is then connected with two fully connected layers, which build the connection between the pieces of the features extracted by the convolutional layers and map them into the final output (Yamashita et al. 2018). The dimensionality of the latent space is set to 200, which can be smaller but is chosen considering the validation of the application in section 9.3 below. Therefore, the input image is compressed into a vector with 200 elements. In the decoder section, two de-convolutional layers corresponding to the two in the encoder section are used to join the features. The pixel size of the output image of the decoder is the same as that of the input image.

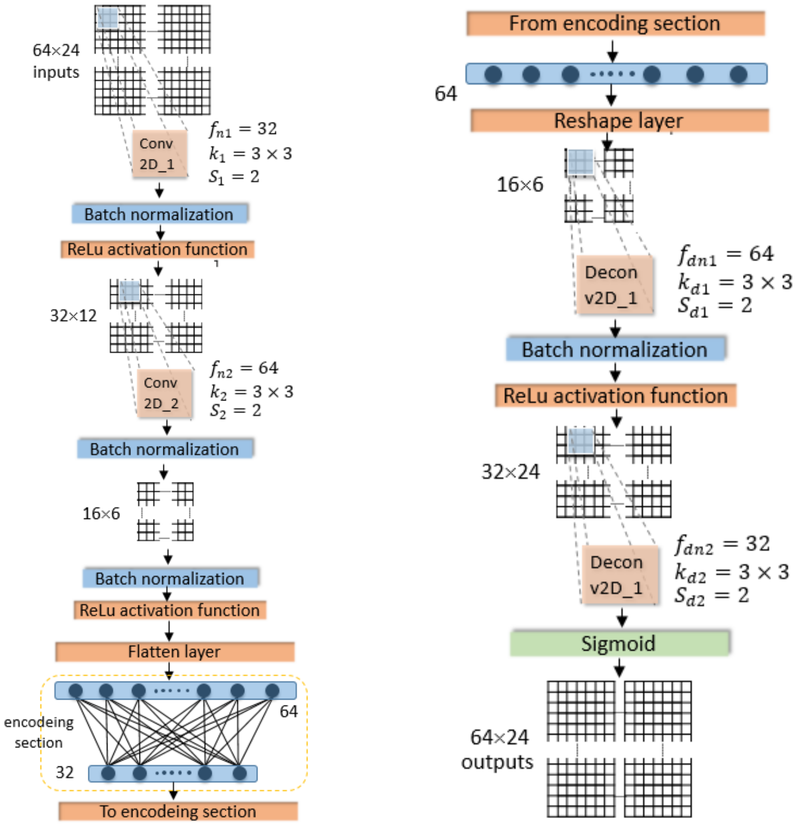

(a) encoder section (b) decoder section

Figure 9.16 Schematic diagram of the encoder and decoder section of the VAE

When calculating the data sampling CFD model shown in Figure 9.2(c), the flow parameters on the data sampling surface, three components of the gradient of *nusgs*, $\tilde{\nu}$, and *U(u, v and w)*, are collected at around 2.2×10^4 time steps. The size of the input layer of the neural network in Figure 9.16 is 64×24×7, which requires the same size of pixel array for the feeding images. Figure 9.17 shows an example of the data preparation for the input of the neural network. As shown in Figure 9.17(b), an interpolation grid is designed to convert the streamwise velocity to an image with 64×24 pixels as shown in Figure 9.17(c). The interpolation grid is refined at the middle, where there is higher gradient of the variables. The pixel values should vary in the range [0, 1]. They are therefore normalized as follows:

$$\emptyset_{pixel} = [\emptyset - \min(\emptyset)]/[\max(\emptyset) - \min(\emptyset)] \tag{9.3}$$

where $\emptyset$ is the collected variable, $\max(\emptyset)$ is the maximum value of the whole dataset, and $\min(\emptyset)$ is the minimum value of the whole dataset. The total array size of the input images, which are converted from the collected inlet data, is 21,672×64×24×7.

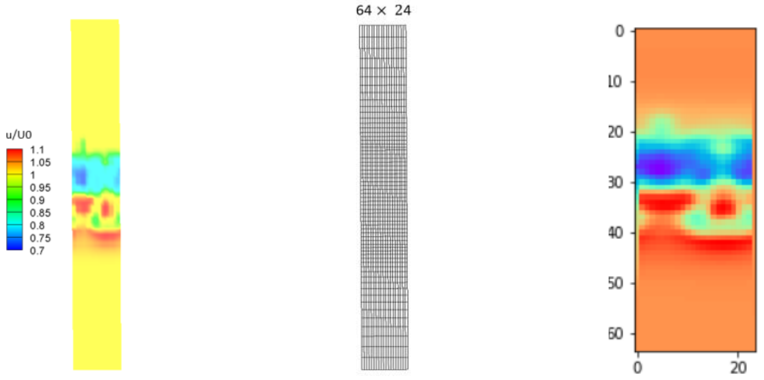

(a) contour of u (b) interpolation grid (c) image of u

Figure 9.17 The data preparation for the VAE neural network

After obtaining the image arrays for the training, they are fed to the neural network illustrated in Figure 9.15 to train it. The aim of training is to make the output images look like the feeding ones. In other words, it is to find the appropriate coefficients W1 and W2, as shown in Figure 9.10, to minimize the loss function. To minimize a loss function, Gradient Decent, which is an iterative first-order optimisation algorithm, is usually used in machine learning(Bottou 2010). The training of the neural network is carried out using the Google cloud GPU platform. The training is run in 200 steps until the change in the reconstruction error, which is defined as the mean squared error between the input and output images, becomes very small. The elapsed time of the training process is about 1.5 hours. Figure 9.18 shows an example comparing the original velocity images in *x*, *y* and *z* directions and the reproduced ones. It is hard to distinguish between the original images and the reconstructed ones by the naked eye. However, as shown in Figure 9.18(c), the difference of the pixel values, which is normalized by equation (9.3), is still appreciable. The main differences appear at the boundaries between the large and small values. As discussed in section 9.2.1, the reconstruction loss is one of the two origins of the loss function, the other one being the similarity loss. When training the neural network, it is necessary to achieve a balance between these two losses according to the goals of the neural network (Asperti and Trentin 2020). Although the weight of the KL loss was set to a very small value, 0.1%, it still has some effect on the reconstruction loss. Besides this, the exact value of the local minimum of the loss function cannot be achieved but can only be approximated when using the gradient descent method. This is another origin of the reconstruction loss.

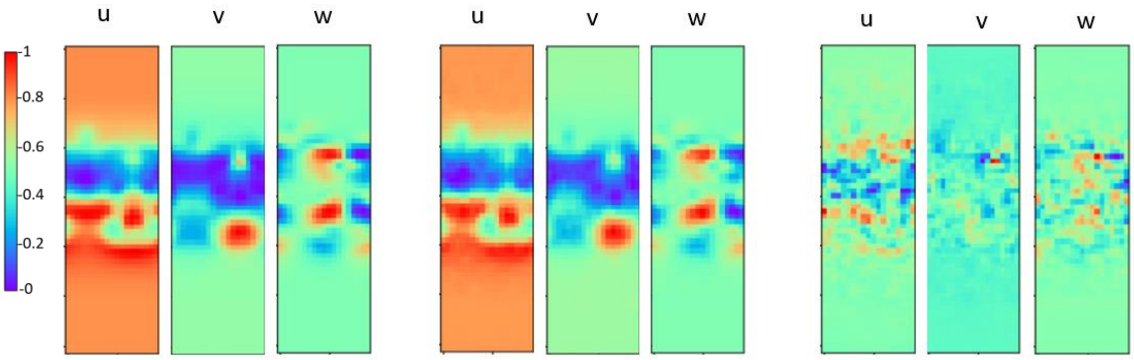

(a) original velocity (b) reconstructed velocity (c) normalized reconstruction error

Figure 9.18 An example of the images of the velocity components and the error, the colour is normalized by equation (9.3)

The original data is stored as '.mat' data in MATLAB v7.3, with a size of about 1.24 GB. The parameters of the VAE data are only 20 MB, which achieves a data compression ratio of 63.5. Therefore, the input data is greatly compressed by the VAE neural network. It should be pointed out that as the time length of the collected data increases, the number of parameters of the neural network will remain the same, which means that longer inflow data would achieve an even higher compression ratio. In addition, the size of the latent vector is not considered here because it is also changing with the length of the input data.

9.2.3 Reconstruction of the inflow data

Applying this to the decomposed CFD model as shown in Figure 9.2(b), the stored latent space and the trained VAE model is used to reproduce the inflow data obtained from the data sampling model shown in Figure 9.2(c). After that it is interpolated back to the grid elements on the inlet boundary of the decomposed model L_{s2} shown in Figure 9.2(b). The same computational parameters as used in section 9.1.2 are adopted. Figure 9.11 compares the flow profiles on the monitor positions, as shown in Figure 9.5, for the case L_{s2} with the original collected data and with the reconstructed data from VAE; good agreement is found between them. The maximum difference in the mean velocity ratio is only about 2% in Figure 9.11(a) and the difference in the turbulence intensity is about 7.4%. This implies that the turbulence is well reproduced.

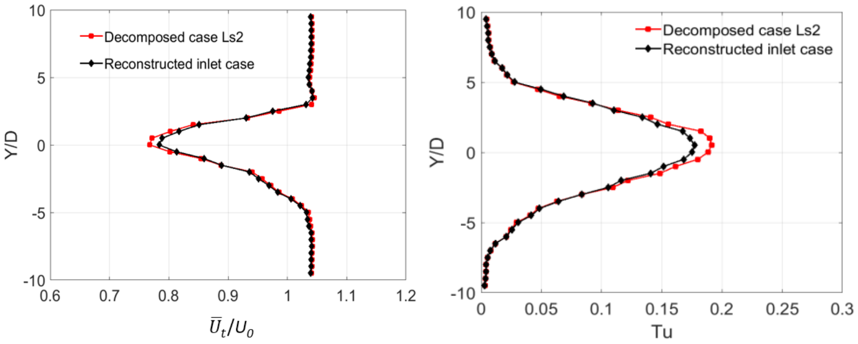

(a) $\overline{U}_t/U_0$ (b) Tu

Figure 9.19 Comparison of statistical flow profiles of the decomposed case L_{s2} and the reconstructed inlet case

Table 9.5 lists the statistical results of the force coefficients of the downstream cylinder calculated by different generation methods of inflow data. These differences in the flow field and in the force coefficients are due to the reconstruction error of the neural network, as discussed in section 9.2.2. Corrections of the mean and rms values of the inflow velocity on every pixel can be used to further improve the simulation results.

Table 9.5 The flow parameters of the downstream cylinder of the model L_{s2} with original collected data and the reconstructed data

case	C_d	$C_{d,rms}$	$C_{l,rms}$
L_{s2}	1.084	0.244	0.750
Reconstructed inlet case	1.150	0.221	0.758
Difference	6.1%	9.4%	1%

The mean statistical parameters above are well reproduced by using the reconstructed inflow data. However, as shown in Figure 9.20(a), the instantaneous pressure coefficient ($Cp(t)$) is not as smooth as the original result. Figure 9.20(b) shows its PSD. Although good agreement is found at low frequency (below 100 Hz), there is a large deviation at the high frequencies. The reconstruction error is believed the cause of the high frequency oscillations. More specifically, the reconstruction error destroys the divergence-free state of the inlet velocity field; then the pressure associated with the inlet velocity field has to generate some numerical fluctuations to satisfy the momentum conservation (Kondo et al. 1997; Poletto et al. 2011; Kim et al. 2013; Patruno and Ricci 2018).

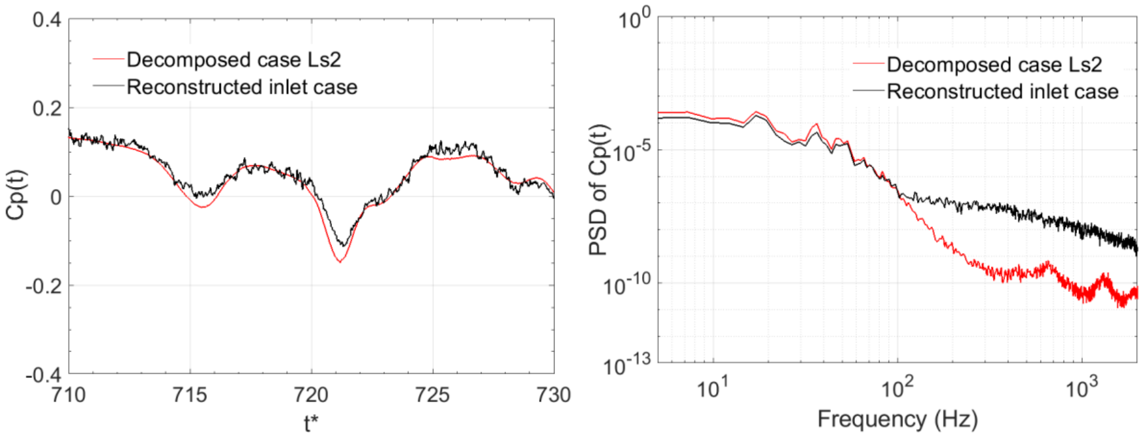

(a) a part of the time history (b) spectra

Figure 9.20 *Cp*(*t*) at the monitor on the central line in Figure 9.5 and its PSD

When using the VAE neural network, the stored latent vectors are imported to the encoding section and the decoder section, as shown in Figure 9.15, to reconstruct the inflow data. The time spent on the reconstruction by VAE is only 11 minutes per 100*t** with 20 processors and it is 192 minutes when using the data sampling model to generate the same length of inflow data. Therefore, the using of VAE can save around 94.3% time compared with using the data sampling model.

9.3 Application of the decomposition method

9.3.1 Decomposition of the leading car model

Figure 9.21 shows the half width model of the leading car of a high-speed train, which has also been used in Chapter 7. The Case standard is used as the complete model to be a reference for the results obtained by application of the decomposition method. Its computational domain is shown in Figure 9.21(a).

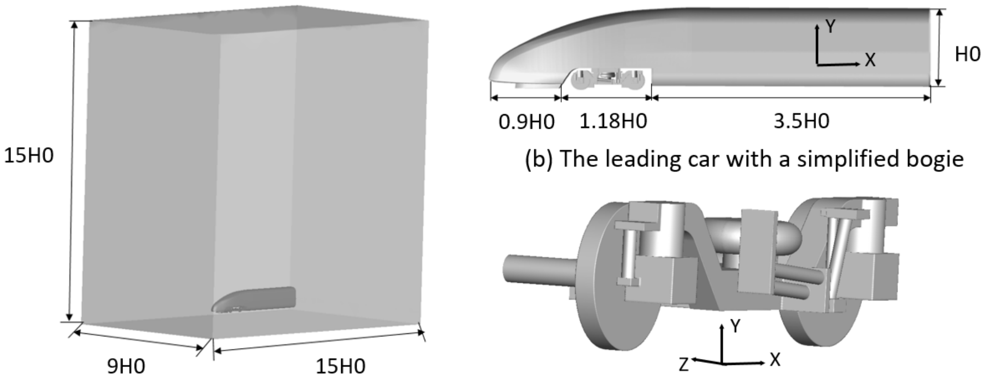

(a) Computational domain

(b) The leading car with a simplified bogie

(c) The half-width simplified bogie

Figure 9.21 The 3D model of the half-width leading car model used in Chapter 7

To calculate the cases described in Chapter 7, in which the lateral position of the bogie is changed, the grid of the whole model had to be regenerated for every case, which is very inconvenient and time-consuming. Therefore, at first, to reduce the grid generation work, the complete computational domain shown in Figure 9.21(a) is divided into four zones, as shown in Figure 9.22. Zone A contains the inlet section of the domain, the train nose and the front part of the cowcatcher beneath the nose. Zone B includes the train shoulder and the upper part of the car body. Zone C consists of the rear part of the cowcatcher and the lower part of the car body. These common zones, A, B, and C, can be reused in all four cases shown in Chapter 7. Zone D, the cavity region within Zone C, is considered separately so as to reduce the meshing time if the geometry of the bogie components in the cavity needs to be changed. Zone D1, which will be used in the boundary sampling case, is empty, whereas Zone D2 contains a bogie and is in the decomposed leading car model shown in Figure 9.23(a). Therefore, the complete model (Case standard in Chapter 7) is modularized.

For a decomposed model (Zone C+D2), as shown in Figure 9.23(a), it only needs to change Zone D2 if the geometry of the bogie is changed. The computational time is expected to be saved by simulating the decomposed model instead of the whole one (Zone A+B+C+D2) and the inflow data stored by the VAE neural network can be reused for many times.

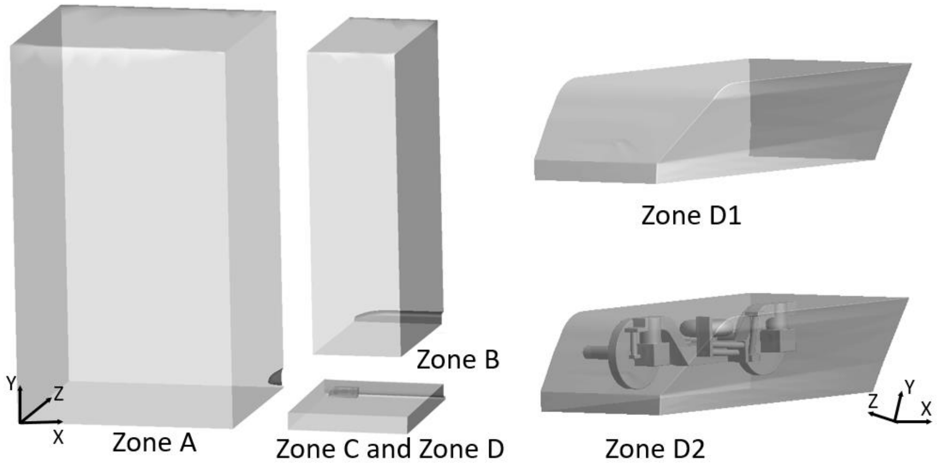

Figure 9.22 Schematic diagram of the modularization of the complete model in Figure 9.21

Before simulating the decomposed model shown in Figure 9.23, which consists of Zone C and Zone D, the data sampling model, with no bogie in the cavity (Zone D1), needs to be calculated to provide inflow data, which also can be stored by the VAE. The flow properties, including the velocity and the turbulence viscosity, on the interfaces, which are planes Ⅰ, Ⅱ and Ⅲ as shown in Figure 9.23(b), are recorded at every time step. Figure 9.24 shows the grid distribution on the typical interfaces. The grid distribution is set to be identical on both sides of the interface between two zones. On the one hand, this minimizes the numerical error due to the data exchange on the interfaces. On the other hand, each decomposed zone is modularized and the block containing components to be modified can be easily replaced, which also excludes the effect from the different grid distribution on the interfaces.

(a) the decomposed leading car (b) the decomposed zone

Figure 9.23 The decomposed zone (Zone C and Zone D) that will be simulated

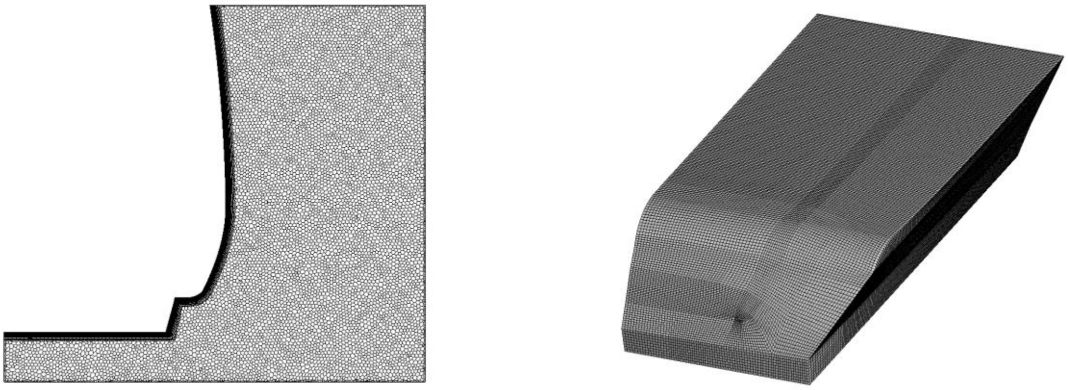

(a) Grid distribution on Plane Ⅰ (b) Grid distribution on the interface of zone C and zone D

Figure 9.24 The grid distribution on the interfaces of the zones

Table 9.6 shows the number of cells in the modularized model and the decomposed model. The size of the decomposed model is reduced by around 27%.

Table 9.6 The zones and total number of cells in three models

Case	Data sampling model	Modularized model	Decomposed model
Consist of zones	Zone A+B+C+D1	Zone A+B+C+D2	Zone C+D2
Total number of cells	9.24 M	15.1 M	10.8 M

Figure 9.25 illustrates the boundary conditions applied on the decomposed model. The flow field around the bogie is mainly affected by the incoming flow turbulence from upstream. Therefore, a time-varying inlet boundary condition is applied on the red section (Plane Ⅰ as shown in Figure 9.23(b)). For the boundary conditions on Planes Ⅱ and Ⅲ, the turbulence intensity is smaller and has much less influence on the flow field around the bogie, and thus the time-averaged boundary conditions are used. The solid surfaces of the car body and bogie are specified as no-slip walls. The boundary layer that develops on the ground is not considered in this chapter and it is specified as a slip wall. Zero pressure is specified on the outlet boundary, which is the same as that of the complete model.

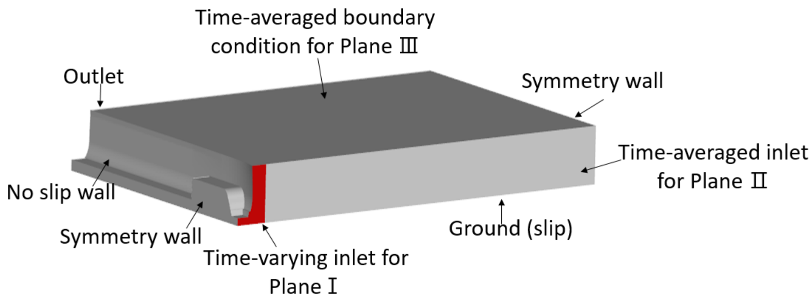

Figure 9.25 The boundary conditions of the decomposed model

9.3.2 Results assessment

Before simulating the decomposed model shown in Figure 9.25, the Data sampling model listed in Table 9.5 is simulated to allow sampling of the inflow data, as listed in Table 9.2. The inflow data sampling begins at 0.8 s, the total collected length is about 3.5 s, corresponding to 95 flow-through times of the cavity length. The initial flow field of the decomposed model is interpolated from the time-averaged flow field of the complete model. The collection of results from the decomposed model begins at 1.0 s and the total collection time is about 40 flow-through times of the cavity length.

Table 9.7 shows the computation times of the modularized model and the decomposed model for every 10 flow-through times of the cavity length. The computational time of the decomposed model is about 9% smaller than the modularized model.

Table 9.7 The comparison of the estimated computational time (10t^* with 640 processors) of the modularized model and the decomposed model

Case	Modularized model	Decomposed model	Time saved
Simulation time	18.4 hours	16.7 hours	9.2%

Four monitors, as shown in Figure 9.26, are placed at the entrance to the cavity and the instantaneous velocity histories at the monitors are recorded. Figure 9.27 shows the time-averaged total velocity and the turbulence intensity at the monitors. For the mean streamwise velocity, the values from the decomposed model are 1.3% greater than those of other three models. It is believed that this is caused by the difference between the mass flux of Plane Ⅰ of the modularized model and the data sampling model. The differences in the turbulence intensity, as shown in Figure 9.26(b), are very small. The results indicate that the flow properties are very similar in the three models.

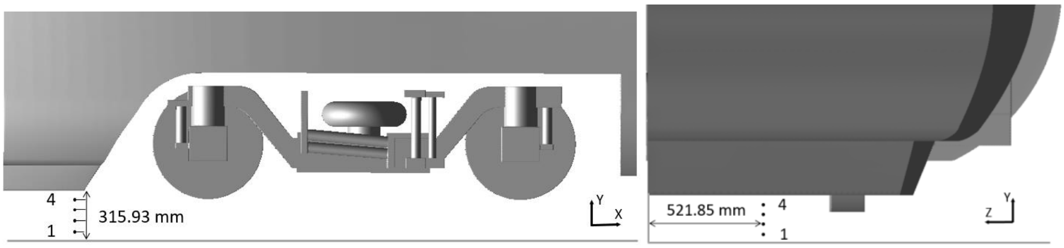

(a) Side view (b) Front view

Figure 9.26 The position of the monitors at the entrance of the cavity

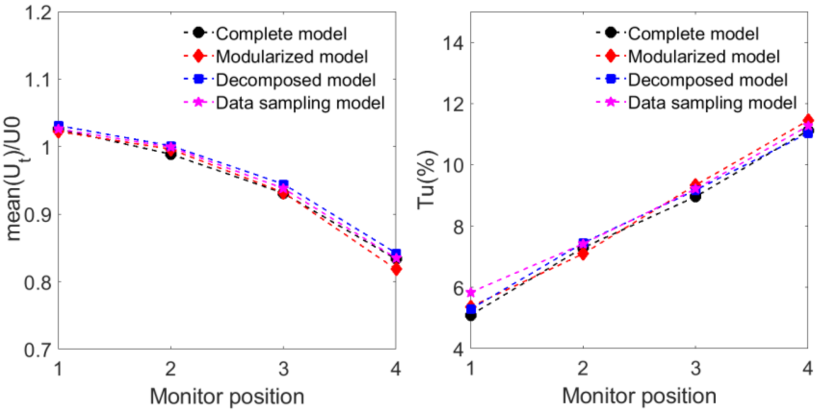

(a) $\overline{U}_t/U_0$ (b) turbulence intensity

Figure 9.27 Comparison of the flow properties at the monitors

Table 9.8 compares the statistical results for the bogie in the complete model, the modularized model and the decomposed model. The difference in C_d and C_l, which are defined in the section 4.1.3 and the reference area is the cross-section area of the car body, brought about by the modularization is significant. It is because their values are very small that can be easily affected by the numerical errors. Besides, the difference in $C_{l,rms}$ and $C_{s,rms}$ between the modularized model and the complete model are around 14.7% and 11.7%. The values from the modularized model and the decomposed model are very similar except for $C_{l,rms}$ which has a difference of about 10%. Figure 9.28 shows the PSDs of the force coefficients. A good agreement is found over the whole frequency range.

Table 9.8 The force coefficients of the bogie of three computed models

case	C_d	C_l	C_s	$C_{d,rms}$	$C_{l,rms}$	$C_{s,rms}$
Complete model	-0.00120	0.00458	0.010	0.0048	0.0075	0.0094
Modularized model	-0.00183	0.00436	-0.0103	0.0044	0.0064	0.0083
Decomposed model	-0.00140	0.00383	-0.0095	0.0043	0.0070	0.0082

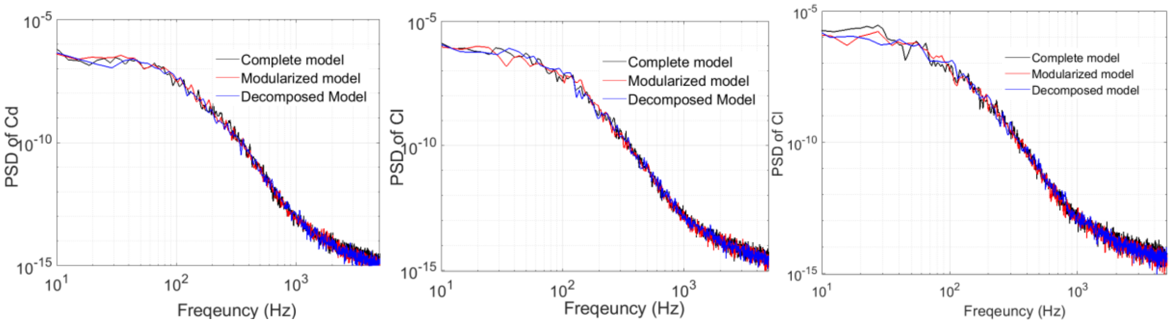

(a) Cd (b) Cl (c) Cs

Figure 9.28 The PSDs of the force coefficients from the three models

The noise is calculated at a number of receivers shown in Figure 5.18 that are set around the bogie at a distance from the centre of the bogie of 20 m. The noise results are converted to correspond to the full-width model and scaled back to the full size and full speed (400km/h) by using equation (5.1) and (5.2). Figure 9.29 shows the noise spectra and the directivities obtained with the three models. The noise spectra in Figure 9.29(a) show good agreement at all frequencies apart from a difference of about 2.5 dB difference in the frequency range 600-1000 Hz. The directivities are shown in Figure 9.29(b) and the shapes and values match well. The maximum difference between the noise levels of the complete model and the decomposed model is only about 0.5 dB. Therefore, the results of the noise simulation of the decomposed model have good agreement with those of the complete model and modularized model.

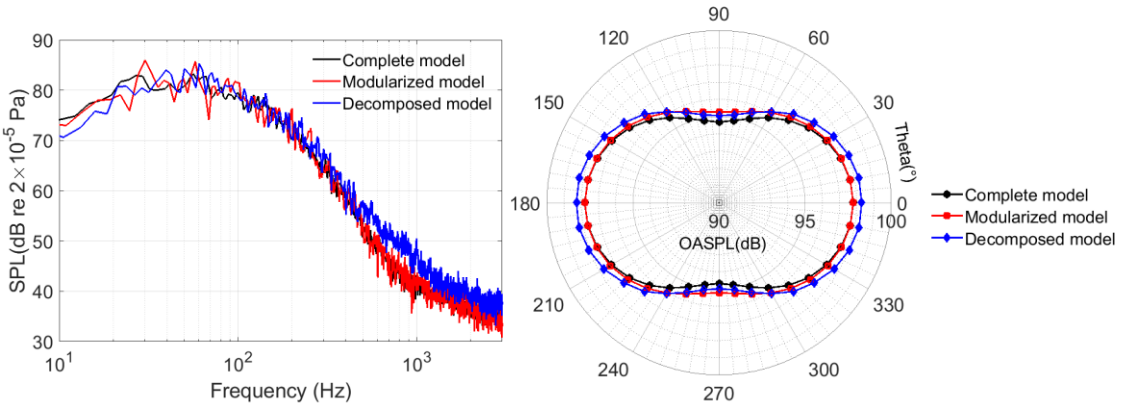

(a) spectra at side receiver (b) directivities

Figure 9.29 The noise of the bogie of the three models

9.3.3 Boundary data storage

The total length of the collected inflow data is about 95 flow-through times of the cavity length, corresponding to the MATLAB file size of around 142.5 GB, which is very large compared with the size of the decomposed model itself (0.9 GB). Therefore, to compress the data to an acceptable size, the VAE neural network tested in section 9.2 is adopted. The whole length of the collected data is too large for the memory of a single GPU and thus, it is divided into pieces to feed the neural network. A piece of inflow data with 6700 time steps is used to give an example of the compression calculation. Figure 9.30 is an example of the preparation of the training data, which is used to feed the neural network. Figure 9.30 (a) shows the original data on Plane Ⅰ, which is a hybrid grid, as shown in Figure 9.24(a), and the sequence of its nodes is irregular. Therefore, as shown in Figure 9.30(b), a 2D structured grid is used to convert the original data into a regular image (Figure 9.30 (c)), which is expressed in terms of 348×100 pixels. It can be noticed that the flow variables change significantly near the solid boundary, the side d in Figure 9.30(b). Thus, the interpolation grid, which has 34800 nodes and nearly twice the number of the original Plane Ⅰ, is greatly refined near the side d in Figure 9.30(b), which makes the boundary layer area appear magnified as the blue area shown in Figure 9.30(c). The collected variables, such as the normal gradient of *nusgs*, $\tilde{v}$, and *U*, are all interpolated to the structured grid; the size of the training array is 6,700×348×100×5.

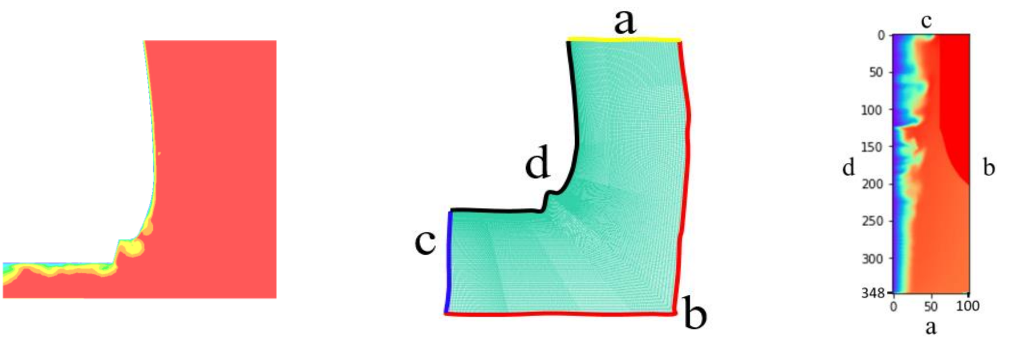

(a) original data (b) interpolation grid (c) converted regular image

Figure 9.30 The preparation of the training data for the VAE neural network applied for the decomposed leading car model

The architecture of the VAE network is the same as that illustrated in Figure 9.16 except for the pixel size of the input image which becomes 348×100 and the latent space is 200. The training step is set to 1000. The whole training time is about 2.5 hours. Table 9.9 lists the file size of the example training data and the estimated compression ratio. It is noticed that the current compression ratio is 9.4, which is only about 1/7th of that in Section 9.2.2 because the interpolation grid has twice as many points as the original interface grid. In addition, there are only 6700 time steps of inflow data used to train the VAE; if more training data are used, the compression ratio will increase.

Table 9.9 Estimated compression ratio of VAE used for decomposed leading car model

	MATLAB data	VAE data	Compression ratio
Data size	3.88 GB	423 MB	9.4

Figure 9.31 shows an example of the comparison of the original velocity images with the reconstructed ones. No noticeable difference can be found by eye between Figure 9.31(a) and Figure 9.31(b). The location of the normalized errors in Figure 9.31(c) is similar to that in Figure 9.18(c), which appears at the area with largest gradient. As discussed in section 9.2.3, the simulation is extremely sensitive to the divergence-free state of the velocity field, which may be violated by the reconstruction error, thus causing some unphysical pressure fluctuations near the inlet section of the decomposed model. However, as discussed in section 9.2, the current reconstructed inflow data can still be used to carry out the time-averaged statistical calculations, e.g. the drag and lift simulation and the time-averaged flow field simulation. Further research is required to correct the inflow velocity components to satisfy the divergence-free condition.

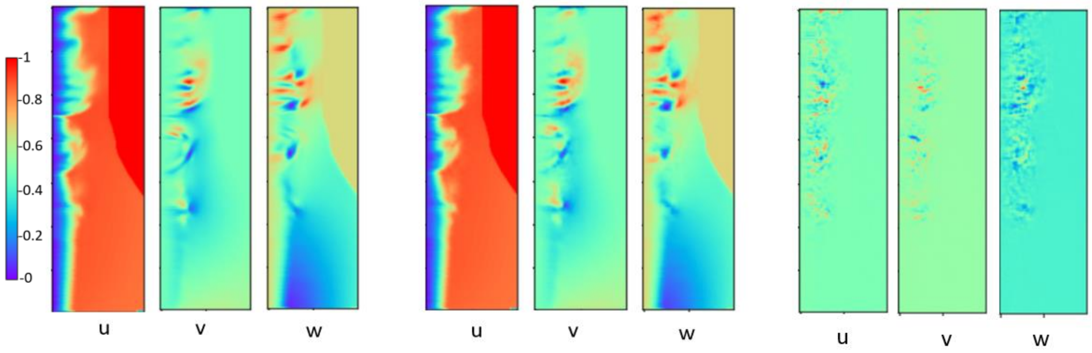

(a) original velocity (b) reconstructed velocity (c) normalized reconstruction error

Figure 9.31 An example of the original and reconstructed velocity components of the inlet velocity of the decomposed leading car model; the colour is normalized by equation (9.3)

9.4 Summary

A novel decomposition method for CFD simulation is proposed for reducing the computational time of a large model. Firstly, the complete model is modularized by dividing it into several zones according to the research aims and the characteristics of the geometry. The decomposed model, which contains the targeted region, is one of the zones. When discretizing the zones, the grid distribution on their interfaces is specified to be identical, which can minimize the error of the data exchange. Only the grid of one zone needs to be replaced to study changes in its geometry and the other grids can remain unchanged. The turbulence properties on the inlet boundaries of the decomposed model can be collected from a data sampling model. The simulation time of the decomposed model is less than that of the complete modularized model and the reduced simulation time is determined by the relative grid sizes of the decomposed model and the complete modularized model. In order to reduce the boundary condition data sampling time, a neural network (VAE), which is trained by the already collected data, can be used to generate new boundary conditions.

The method is first validated by a tandem square cylinder case. The computational time of the decomposed model is reduced by about 30%. The flow field in the decomposed model is well reproduced and the results of the force coefficients and the aerodynamic noise show a good agreement with those of the complete model. These results imply that the model decomposition method has a good performance in the simulation. To reduce the stored file size, a neural network called VAE is used to compress the data size and its compression ratio achieves 63. However, when applying the reconstructed data from the neural network, unphysical pressure fluctuations are found in the flow field, especially near the inlet section. The reason is believed to be that the reconstruction error destroys the divergence-free state of the velocity on the inlet plane.

The decomposition method is then applied to a half-width model of a bogie under the leading car. The model is split into four zones and the decomposed model, which is simulated separately, contains the bogie and a part of the car body. A model of the leading car without the bogie is calculated and the boundary condition data is collected and applied to the decomposed model. Good agreement is found in the comparison of the aerodynamic and aeroacoustic results. In the compression of the inflow data, the compression ratio of a dataset with 6700 time steps is 9.4 but there is greater potential when the length of the inflow data is increased. The reconstruction flow velocity field still contains some noise that may cause unphysical oscillation in the pressure field.

Chapter 10 Conclusions and future work

10.1 Conclusions

The aim of this research is to enhance understanding of the aerodynamic noise generation mechanisms of a high-speed train bogie and to identify the key factors influencing the noise. As the geometry of the bogie is extremely complex, numerical simulation is very challenging in the study of bogie aerodynamic noise. To overcome this, three strategies covering different aspects of the numerical simulations are proposed in this thesis. First, a hybrid grid system has been developed to reduce the mesh size and generate meshes with good quality. This discretises the boundary layer using a hexahedral grid with good quality and the rest of the volume by a good quality polyhedral grid. Second, the model size is scaled down by reducing the Reynolds number within the self-similarity region and, meanwhile, keeping the Strouhal number the same by using a reduced incoming flow velocity. Third, appropriately simplified models are used in different simulations, e.g. the symmetric bogie used in the half-width model without the motors and gears. By applying these measures, the characteristics of the flow field and aerodynamic noise of the bogie have been studied. A flow control technique has been proposed to reduce the noise of the leading car of a train, which has shown promising potential to reduce noise from train bogies. Finally, a novel decomposition CFD method has been explored to reduce the computational cost further. All the simulations are run with OpenFOAM 2.4.0 using the DDES method with S-A turbulence model to calculate the aerodynamics of the model and the pressure fluctuations, which are fed to the FW-H equation for far field noise prediction.

To validate the developed approach, the hybrid grid generation procedure is first tested for circular and square cylinders. The results of the aerodynamic parameters including force and pressure coefficients, and radiated noise showed a good agreement with other simulation results which used a structured grid (Liu 2017). The aerodynamic noise of a more complex component of the bogie, an isolated wheelset used in Zhu (2015), was also calculated by using the hybrid system. The noise spectra calculated by the hybrid grid successfully captured the vortex shedding peaks and matched very well with Zhu’s numerical and experimental results. The validation results showed that the hybrid grid system can capture the local flow features that have a vital effect on the simulation of the aerodynamic noise and, meanwhile, its grid size is comparable with the structured grid.

Simulations were run for a bogie in a simplified cavity. It was found that the shear layer detached from the upstream cavity rims and the turbulent wake downstream of the front components are two influencing factors on the generation of the aerodynamic noise by the bogie and its cavity. By identifying the noise sources using dp/dt, it was shown that the components, such as rear part of the bogie and the rear corners of the cavity, that are immersed in the wake or the detached shear layer, have strong pressure fluctuation intensity. The far field noise showed that the spectra have no aeolian tone and the noise is dominated by low frequencies (20-200 Hz). It was also found that the noise levels generated by the cavity are up to 10 dB greater than those generated by the bogie. For the contributions of the bogie components, it has been shown that components at the rear part of the bogie produce higher noise levels, which was also confirmed by the calculated pressure fluctuation intensity.

The aerodynamics and aeroacoustics of a bogie under a more detailed leading car were investigated. For the analysis of the aerodynamic force coefficients, it is found that the bogie contributes less to the mean and the fluctuation of the forces than the car body. This is due to the fact that most parts of the bogie are shielded from the flow by the cavity. In the analysis of the flow field, it was shown that the wake flow separated from the front edge of the cowcatcher and the detached shear layer at the two sides of the cavity are critical to the generation of the noise. This was confirmed by the calculation of the pressure fluctuation intensity. It was found that the bottom of the cowcatcher and the bogie, the cavity rear surface, and the side dampers, which are directly impinged by the highly turbulent wake and the detached shear layer, form strong pressure fluctuations. In the calculation of the far field noise, it was also found that the noise generated by the bogie is much lower (5 dB) than that by the car body but the difference is much smaller than that in the simplified cavity case. In addition, from the comparison of the noise contribution of different bogie components, it was found that the upstream and downstream wheelsets contribute most to the bogie noise in the lateral direction, while the frame surface has the greatest contribution in the vertical direction. It was also found that the cavity and ground emit the highest sound power, whereas the bogie and the train nose produce about 3 dB lower sound power than each of these two sources. For the contributions of the bogie components, the wheelsets, the lateral damper, and the frame surface contribute most of the sound power.

The effect is investigated of the positions of the bogie’s side components on the aerodynamics and aeroacoustics of the train. It is found that protruded side components disrupt the detached shear layer from upstream, which would otherwise impinge on the rear part of the cavity. The pressure fluctuation on the side components increases, but that acting on the rear surface of the cavity, especially at the arc corner near the rear surface, is reduced. This resulted in significantly increased noise levels of the bogie in the vertical direction while the noise levels of the car body in the horizontal direction were reduced. However, the total SWLs of the four cases were very similar.

Simulations of the bogie under a leading car showed that the wake flow that separates from the front edge of the cowcatcher and the detached shear layer at the two sides of the cavity are vital to the noise generation of the bogie and its cavity. Based on this, a jet is used as a mitigation method to disturb the wake and shear layer to prevent them from impinging directly on the downstream components. First, the noise generated by the jet itself at full scale with a Mach number of 0.32 (full speed of the train, 400 km/h) was estimated and the result showed that it can be neglected compared with the noise generated by the car model. After the comparison of the half-width car model with different jets applied, a dual staggered jet was applied on the full width model and the air collection nozzle was set up at the front surface of the cowcatcher. The aerodynamic results showed that the wake at the bottom and the detached shear layer at the two sides of the cavity were pushed away from the car body by the jets, which significantly reduces the pressure fluctuation on the bottom and side components of the bogie and the rear surface of the cavity. Besides, the pressure fluctuation at the bottom of the cowcatcher is also reduced because of the suction of the air flow by the air collection nozzle. The comparison of the noise spectra at the side receiver showed that the noise levels are reduced by the jet at almost all frequencies (30-2000 Hz) except for the very low frequencies. The SPL values are reduced by up to about 3.5 dB for the bogie and 2 dB for the car body. The total SWL is reduced by 3.5 dB and almost every component is reduced except for the rear part of the car body, which is affected by the turbulent wake from upstream which is strengthened by the jet flow.

To reduce the computational cost further, a novel decomposition method for CFD simulation was developed. It was tested by a model of tandem square cylinders, giving good agreement for the aerodynamic and aeroacoustic results between the decomposed model and the complete model. It was found that the computational time of the decomposed model is 30% less than that of the original one. A VAE neural network was used to compress the collected inflow data, achieving a compression ratio of 63. The decomposition method was then applied to simulations of a half-width model of a bogie under the leading car. The results of the decomposed model showed good agreement with those of the original models. Although, the computational time was only reduced by about 9%, this approach still has great potential in the simulation models where more car bodies and bogies are included. In the compression of the inflow data, the compression ratio of a limited data length (6700 time steps) was 9.4; however it would be much higher when the length of the inflow data increases.

10.2 Future work

In the aerodynamic simulations of the bogie in the simplified cavity and under a leading car, the ground was modelled as a flat plane, the ballast, the sleepers, and the rails, which may change the flow field at the bottom of the model, were not considered. This may affect the noise generated at the bottom. Hence, it will be worth carrying out a simulation of the model with more detailed features at the bottom to investigate the noise generated by the local flow. In addition, in the current simulation, only the aerodynamic noise of the first bogie was calculated. It will be interesting to investigate the characteristics of noise generated by the downstream bogies.

The simulations of the aerodynamic noise were calculated by the FW-H equation using the free space Green's functions without considering the scattering effect of the train on the sound propagation. The bogie itself, the cavity, and the ground as well as the flow itself are expected to affect the characteristics of the noise in the far field. Hence, it will be necessary to use Finite Element Method (FEM) or Boundary Element Method (BEM) to simulate the sound propagation. Then, experimental research needs to be carried out to validate the calculated far field noise. Moreover, only the dipole sources were calculated in the simulation, considering that the Mach number is only 0.32 at the maximum train speed considered (400 km/h). However, as the simulations showed, the local speed at the bottom of the cowcatcher is around 30% greater than the freestream velocity. Thus, it is worth calculating a model that considers the quadruple noise sources at the bottom area of the cowcatcher.

In the noise control study, although the numerical results show a good noise reduction, experimental work needs to be carried out to test the technique. In addition, the optimization of the jet slots, such as the pitch length of the staggered slots, the distance between the dual slots, and the outlet shape of the jet slots, should be carried out by more numerical and experimental research. A model with a finer grid at the jet slots should be developed in the optimization study. The jet air collection system should be investigated, including the possible path from the collection nozzle to the jet slots, the pressure loss of the system, and the detailed parameters of the air collection nozzle. Moreover, the effect of the jet flow on the slipstream of the train should be assessed, and some parameters of the jet, e.g. the jet direction, should be further optimized. Other flow control measures, such as changing the shape of the rear cavity surface and installing some turbulence absorbing or sound absorbing material at the rear cavity surface, are interesting to investigate.

For the decomposition method, the prime future work should be to explore a method to correct the unphysical pressure fluctuation found in the simulation with the reconstructed inflow data. It is interesting to develop a new correction algorithm to ensure divergence-free inlet velocity field. Moreover, benefit of the decomposition method has not been fully realized because of the requirement for an interpolation process on the inlet surface that happens at every time step in the boundary condition function 'time varying mapped fixed value' in OpenFOAM. This slowed down the speed of the calculations, which resulted in a much smaller percentage reduction of the computation time. Hence, in the future, it is worth developing a function that can directly impose the inlet data to the nodes of the inlet surface. In addition, in the current simulations, the neural network was only applied as a data compression tool. It is also interesting to apply more advanced neural networks to make it have more functions, such as generating some flow field with physical meaning between two large time steps, scaling the turbulent flow field of low Reynolds number to higher ones, and generating some general turbulence by specifying its parameters.

Appendix A

Illustration of the components of the computational model used in Chapter 6.

Bogie under a leading car body

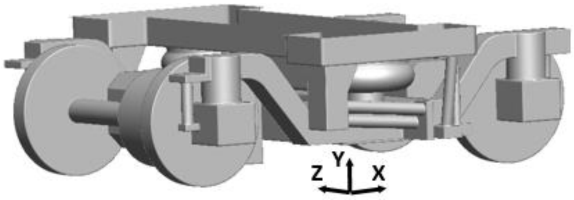

Bogie

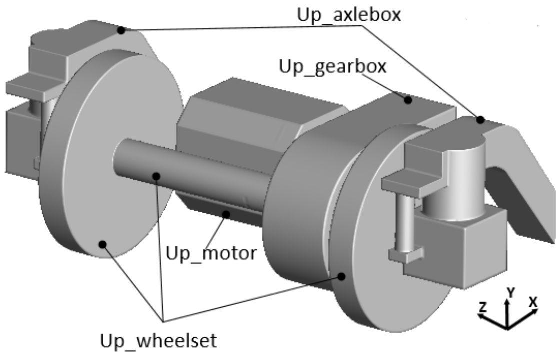

Upstream dynamic system

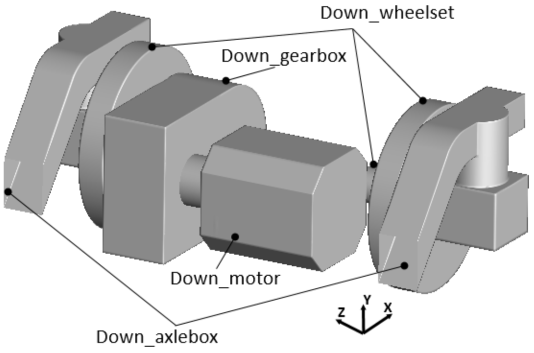

Downstream dynamic system

Appendix A

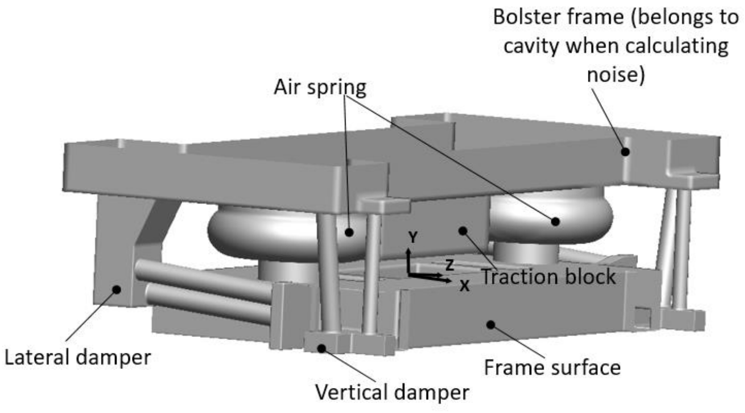

Frame system

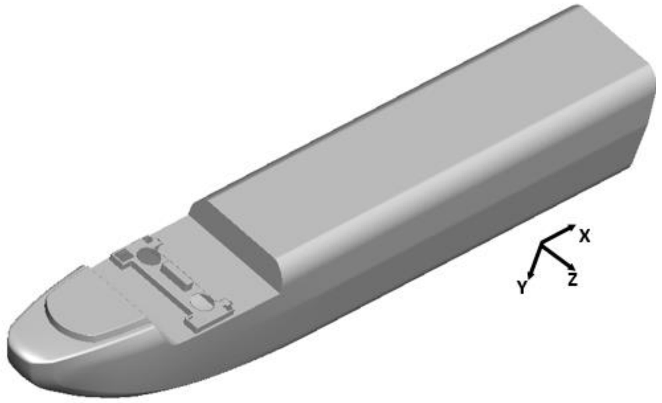

Car body

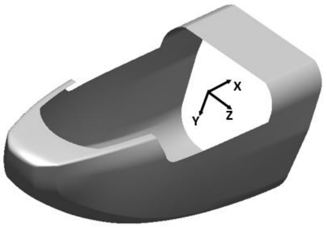

train nose

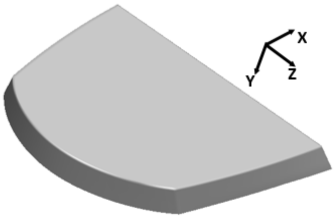

cowcatcher

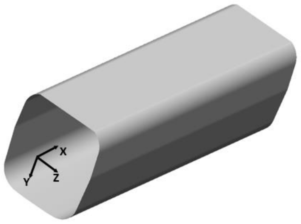

rear car body

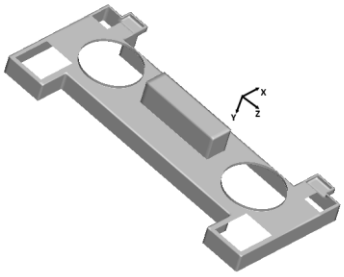

boster

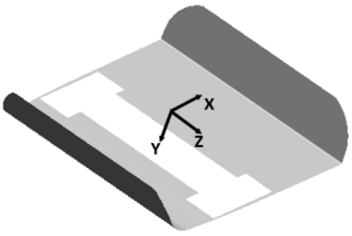

cavity

References

Abdelmwgoud, M. and Mohany, A. (2021). "Control of the self-sustained shear layer oscillations over rectangular cavities using high-frequency vortex generators." Physics of fluids **33**(4): 045115.

Abedi, M., Sun, B. and Zheng, Z. (2019). "A sinusoidal-hyperbolic family of transforms with potential applications in compressive sensing." IEEE Transactions on Image Processing **28**(7): 3571-3583.

Ahmed, N., Natarajan, T. and Rao, K. R. (1974). "Discrete cosine transform." IEEE transactions on Computers **100**(1): 90-93.

Albawi, S., Mohammed, T. A. and Al-Zawi, S. (2017). Understanding of a convolutional neural network. 2017 international conference on engineering and technology (ICET), Ieee:1-6.

Ali, J. M., Omar, A. A., Ali, M. A. B. and Baseair, A. R. B. M. (2017). Numerical Investigation of Aerodynamic Characteristics of High Speed Train. IOP Conference Series: Materials Science and Engineering, IOP Publishing **184 :**012015.

Arunajatesan, S., Kannepalli, C., Sinha, N., Sheehan, M., Alvi, F., Shumway, G. and Ukeiley, L. (2009). "Suppression of cavity loads using leading-edge blowing." AIAA journal **47**(5): 1132-1144.

Arunajatesan, S., Shipman, J. and Sinha, N. (2002). Hybrid RANS-LES simulation of cavity flow fields with control. 40th AIAA Aerospace Sciences Meeting & Exhibit.

Asperti, A. and Trentin, M. (2020). "Balancing reconstruction error and Kullback-Leibler divergence in Variational Autoencoders." IEEE Access **8**: 199440-199448.

Baker, C., Johnson, T., Flynn, D., Hemida, H., Quinn, A., Soper, D. and Sterling, M. (2019). Chapter 3 - Testing techniques. Train Aerodynamics. C. Baker, T. Johnson, D. Flynn et al., Butterworth-Heinemann**:** 35-51.

Baker, C. J. and Brockie, N. J. (1991). "Wind tunnel tests to obtain train aerodynamic drag coefficients: Reynolds number and ground simulation effects." Journal of Wind Engineering and Industrial Aerodynamics **38**(1): 23-28.

Baldi, P. (2012). Autoencoders, unsupervised learning, and deep architectures. Proceedings of ICML workshop on unsupervised and transfer learning, JMLR Workshop and Conference Proceedings: 37-49.

Bearman, P. and Obasaju, E. (1982). "An experimental study of pressure fluctuations on fixed and oscillating square-section cylinders." Journal of Fluid Mechanics **119**: 297-321.

Becker, K., Heitkamp, K. and Kügeler, E. (2010). Recent progress in a hybrid-grid CFD solver for turbomachinery flows. Proceedings fifth European conference on computational fluid dynamics ECCOMAS CFD.

Bottou, L. (2010). Large-scale machine learning with stochastic gradient descent. Proceedings of COMPSTAT'2010, Springer**:** 177-186.

Breuer, M. (1998). "Large eddy simulation of the subcritical flow past a circular cylinder: Numerical and modeling aspects." International journal for numerical methods in fluids **28**(9): 1281-1302.

Brun, C., Aubrun, S., Goossens, T. and Ravier, P. (2008). "Coherent Structures and their Frequency Signature in the Separated Shear Layer on the Sides of a Square Cylinder." Flow, Turbulence and Combustion **81**(1): 97-114.

Cattafesta III, L. N., Song, Q., Williams, D. R., Rowley, C. W. and Alvi, F. S. (2008). "Active control of flow-induced cavity oscillations." Progress in Aerospace sciences **44**(7-8): 479-502.

Cattafesta, L., Alvi, F., Williams, D. and Rowley, C. (2003). Review of active control of flow-induced cavity oscillations. 33rd AIAA Fluid Dynamics Conference and Exhibit.

Chawdhury, S. and Morgenthal, G. (2016). "Flow reproduction using Vortex Particle Methods for simulating wake buffeting response of bluff structures." Journal of Wind Engineering and Industrial Aerodynamics **151**: 122-136.

Cheli, F., Giappino, S., Rosa, L., Tomasini, G. and Villani, M. (2013). "Experimental study on the aerodynamic forces on railway vehicles in presence of turbulence." Journal of Wind Engineering and Industrial Aerodynamics **123**: 311-316.

Chen, H., Zhou, X., Feng, Z. and Cao, S.-J. (2022). "Application of polyhedral meshing strategy in indoor environment simulation: Model accuracy and computing time." Indoor and Built Environment **31**(3): 719-731.

Chen, Y., Ding, W. and Bian, R. (2021). "Performance studies on cavitation-resistance turbine flow sensor based on experiment and CFD simulation." Flow Measurement and Instrumentation **79**: 101918.

Cheng, W., Pullin, D. I., Samtaney, R., Zhang, W. and Gao, W. (2017). "Large-eddy simulation of flow over a cylinder with Re from 3900 to 850000 : a skin-friction perspective." Journal of Fluid Mechanics **820**: 121-158.

Comte, P., Daude, F. and Mary, I. (2008). "Simulation of the reduction of unsteadiness in a passively controlled transonic cavity flow." Journal of Fluids and Structures **24**(8): 1252-1261.

Courant, R., Friedrichs, K. and Lewy, H. (1928). "Über die partiellen Differenzengleichungen der mathematischen Physik." Mathematische Annalen **100**(1): 32-74.

Curle, N. (1955). "The influence of solid boundaries upon aerodynamic sound." Proc. R. Soc. Lond. A **231**(1187): 505-514.

Curtiss, C. F. and Hirschfelder, J. O. (1952). "Integration of stiff equations." Proceedings of the National Academy of Sciences **38**(3): 235-243.

Dai, Y., Kobayashi, T. and Taniguchi, N. (1994). "Large eddy simulation of plane turbulent jet flow using a new outflow velocity boundary condition." JSME International Journal Series B Fluids and Thermal Engineering **37**(2): 242-253.

Demir, O., Çelik, B. and Güleren, K. M. (2021). "Noise Reduction of Open Cavities by Passive Flow Control Methods at Transonic Speeds using OpenFOAM." Journal of Aeronautics and Space Technologies **14**(2): 193-208.

Deng, L. (2012). "The mnist database of handwritten digit images for machine learning research [best of the web]." IEEE signal processing magazine **29**(6): 141-142.

Doersch, C. (2016). "Tutorial on variational autoencoders." arXiv preprint arXiv:1606.05908.

Dong, T., Liang, X., Krajnović, S., Xiong, X. and Zhou, W. (2019). "Effects of simplifying train bogies on surrounding flow and aerodynamic forces." Journal of Wind Engineering and Industrial Aerodynamics **191**: 170-182.

Ffowcs Williams, J. E. and Hawkings, D. L. (1969). "Sound generation by turbulence and surfaces in arbitrary motion." Philosophical Transactions of the Royal Society of London. Series A, Mathematical and Physical Sciences **264**(1151): 321-342.

Fröhlich, J. and Rodi, W. (2004). "LES of the flow around a circular cylinder of finite height." International Journal of Heat and Fluid Flow **25**(3): 537-548.

Galindo, J., Hoyas, S., Fajardo, P. and Navarro, R. (2013). "Set-up analysis and optimization of CFD simulations for radial turbines." Engineering Applications of Computational Fluid Mechanics **7**(4): 441-460.

Garimella, R. V., Kim, J. and Berndt, M. (2014). Polyhedral mesh generation and optimization for non-manifold domains. Proceedings of the 22nd International Meshing Roundtable, Springer**:** 313-330.

Goldstein, M. E. (2003). "A generalized acoustic analogy." Journal of Fluid Mechanics **488**: 315-333.

Greenshields, C. J. (2015). "Openfoam user guide." OpenFOAM Foundation Ltd, version, 3(1).

Guo, Z., Liu, T., Chen, Z., Xia, Y., Li, W. and Li, L. (2020). "Aerodynamic influences of bogie's geometric complexity on high-speed trains under crosswind." Journal of Wind Engineering and Industrial Aerodynamics **196**: 104053.

Harwood, A. R. and Dupère, I. D. (2016). "Numerical evaluation of the compact acoustic Green's function for scattering problems." Applied Mathematical Modelling **40**(2): 795-814.

Harwood, A. R. G. (2014). "Numerical evaluation of acoustic Green's functions." PhD Thesis,University of Manchester.

Howe, M. (1975). "Contributions to the theory of aerodynamic sound, with application to excess jet noise and the theory of the flute." Journal of Fluid Mechanics **71**(4): 625-673.

Huffman, D. A. (1952). "A method for the construction of minimum-redundancy codes." Proceedings of the IRE **40**(9): 1098-1101.

ICEM, A. (2019). The american scholar. ANSYS Inc. ANSYS ICEM User Guide, Release 14.0.

Izawa, S., Lerner, J. and Boldes, U. (2011). "Active and passive control of flow past a cavity." Wind Tunnels and Experimental Fluid Dynamics Research: 369-394.

Jayasankar, U., Thirumal, V. and Ponnurangam, D. (2021). "A survey on data compression techniques: From the perspective of data quality, coding schemes, data type and applications." Journal of King Saud University - Computer and Information Sciences **33**(2): 119-140.

Juretić, F. and Gosman, A. (2010). "Error analysis of the finite-volume method with respect to mesh type." Numerical heat transfer, part B: fundamentals **57**(6): 414-439.

Kattan, A. (2010). Universal intelligent data compression systems: A review. 2010 2nd Computer Science and Electronic Engineering Conference (CEEC), IEEE.

Kim, H., Hu, Z. and Thompson, D. (2020). "Effect of cavity flow control on high-speed train pantograph and roof aerodynamic noise." Railway Engineering Science **28**(1): 54-74.

Kim, S. J., Huang, W.-X. and Sung, H. J. (2020). "The reduction of noise induced by flow over an open cavity." International Journal of Heat and Fluid Flow **82**: 108560.

Kim, Y., Castro, I. P. and Xie, Z.-T. (2013). "Divergence-free turbulence inflow conditions for large-eddy simulations with incompressible flow solvers." Computers & Fluids **84**: 56-68.

Kingma, D. P. and Welling, M. (2013). "Auto-encoding variational bayes." arXiv preprint arXiv:1312.6114.

Knowles, K., Khanal, B., Bray, D. and Geraldes, P. (2010). Passive control of cavity instabilities and noise. 27th International congress of the aeronautical sciences.

Kolmogorov, A. N. (1941). "The local structure of turbulence in incompressible viscous fluid for very large Reynolds numbers." Cr Acad. Sci. URSS **30**: 301-305.

Kondo, K., Murakami, S. and Mochida, A. (1997). "Generation of velocity fluctuations for inflow boundary condition of LES." Journal of Wind Engineering and Industrial Aerodynamics **67**: 51-64.

Kurita, T. (2011). "Development of external-noise reduction technologies for Shinkansen high-speed trains." Journal of Environment and Engineering **6**(4): 805-819.

Kwon, H.-b., Park, Y.-W., Lee, D.-h. and Kim, M.-S. (2001). "Wind tunnel experiments on Korean high-speed trains using various ground simulation techniques." Journal of Wind Engineering and Industrial Aerodynamics **89**(13): 1179-1195.

Lamp, A. M. and Chokani, N. (1997). "Computation of cavity flows with suppression using jet blowing." Journal of Aircraft **34**(4): 545-551.

Latorre Iglesias, E. (2015). "Component-based model to predict aerodynamic noise from high-speed trains." PhD thesis, University of Southampton.

Latorre Iglesias, E., Thompson, D. J., Smith, M., Kitagawa, T. and Yamazaki, N. (2017). "Anechoic wind tunnel tests on high-speed train bogie aerodynamic noise." International Journal of Rail Transportation **5**(2): 87-109.

Laubscher, R. and Rousseau, P. (2020). "Application of generative deep learning to predict temperature, flow and species distributions using simulation data of a methane combustor." International Journal of Heat and Mass Transfer **163**: 120417.

Lauterbach, A., Ehrenfried, K., Kröber, S., Ahlefeldt, T. and Loose, S. (2010). Microphone array measurements on high-speed trains in wind tunnels. Berlin Beamforming Conference, Citeseer.

Lauterbach, A., Ehrenfried, K., Loose, S. and Wagner, C. (2012). "Microphone Array Wind Tunnel Measurements of Reynolds Number Effects in High-Speed Train Aeroacoustics." International Journal of Aeroacoustics **11**(3-4): 411-446.

LeCun, Y. and Bengio, Y. (1995). "Convolutional networks for images, speech, and time series." The handbook of brain theory and neural networks **3361**(10): 1995.

LeCun, Y., Boser, B., Denker, J. S., Henderson, D., Howard, R. E., Hubbard, W. and Jackel, L. D. (1989). "Backpropagation applied to handwritten zip code recognition." Neural computation **1**(4): 541-551.

LeCun, Y., Bottou, L., Bengio, Y. and Haffner, P. (1998). "Gradient-based learning applied to document recognition." Proceedings of the IEEE **86**(11): 2278-2324.

Lee, S. Y. (2015). "Polyhedral mesh generation and a treatise on concave geometrical edges." Procedia Engineering **124**: 174-186.

Li, B., Ye, C.-C., Wan, Z.-H., Liu, N.-S., Sun, D.-J. and Lu, X.-Y. (2020). "Noise control of subsonic flow past open cavities based on porous floors." Physics of fluids **32**(12): 125101.

Lighthill, M. J. (1952). "On sound generated aerodynamically I. General theory." Proc. R. Soc. Lond. A **211**(1107): 564-587.

Liu, W., Guo, D., Zhang, Z., Chen, D. and Yang, G. (2019). "Effects of Bogies on the Wake Flow of a High-Speed Train." Applied Sciences **9**(4): 759.

Liu, X. (2017). "Aerodynamic noise from components of a train pantograph and its reduction." PhD thesis, University of Southampton.

Liu, X., Thompson, D. J. and Hu, Z. (2019). "Numerical investigation of aerodynamic noise generated by circular cylinders in cross-flow at Reynolds numbers in the upper subcritical and critical regimes." International Journal of Aeroacoustics **18**(4-5): 470-495.

Liu, X., Zhang, J., Thompson, D. J., Latorre Iglesias, E., Squicciarini, G., Hu, Z., Toward, M. and Lurcock, D. (2021). "Aerodynamic noise of high-speed train pantographs: Comparisons between field measurements and an updated component-based prediction model." Applied Acoustics **175**: 107791.

Liu, Y., Long, Z. and Liu, W. (2022). "A semi-empirical mesh strategy for CFD simulation of indoor airflow." Indoor and Built Environment: 1420326X221089825.

Lockard, D., Khorrami, M., Choudhari, M., Hutcheson, F., Brooks, T. and Stead, D. (2007). Tandem cylinder noise predictions. 13th AIAA/CEAS Aeroacoustics Conference (28th AIAA Aeroacoustics Conference).

Lyrintzis, A. S. (2003). "Surface integral methods in computational aeroacoustics—From the (CFD) near-field to the (Acoustic) far-field." International Journal of Aeroacoustics **2**(2): 95-128.

Mancini, G., Malfatti, A., Violi, A. G. and Matschke, G. (2001). Effects of experimental bogie fairings on the aerodynamic drag of the ETR 500 high speed train. Proc. of the World Congress on Railway Research (WCRR 2001).

Martens, A., Wedemann, J., Meunier, N. and Leclere, A. (2009). "High speed train noise-sound source localization at fast passing trains." Sociedad Espanola de Acoustica, SEA.

Martin, R., Soria, M., Rodriguez, I. and Lehmkuhl, O. (2022). "On the Flow and Passive Noise Control of an Open Cavity at Re= 5000." Flow, Turbulence and Combustion **108**(1): 123-148.

Mary, I. and Lê, T.-H. (2005). Large-Eddy Simulation of a Controlled Flow Cavity. Engineering Turbulence Modelling and Experiments 6, Elsevier**:** 565-573.

Masson, E., Paradot, N. and Allain, E. (2012). The Numerical Prediction of the Aerodynamic Noise of the TGV POS High-Speed Train Power Car. Noise and Vibration Mitigation for Rail Transportation Systems, Tokyo, Springer Japan.

Menter, F. and Kuntz, M. (2004). Adaptation of eddy-viscosity turbulence models to unsteady separated flow behind vehicles. The aerodynamics of heavy vehicles: trucks, buses, and trains, Springer**:** 339-352.

Menter, F. R., Kuntz, M. and Langtry, R. (2003). "Ten years of industrial experience with the SST turbulence model." Turbulence, Heat and Mass Transfer **4**(1): 625-632.

Meskine, M., Perot, F. and Kim, M.-S. (2013). Community noise prediction of digital high speed train using LBM. 19th AIAA/CEAS Aeroacoustics Conference.

Minelli, G., Yao, H. D., Andersson, N., Höstmad, P., Forssén, J. and Krajnović, S. (2020). "An aeroacoustic study of the flow surrounding the front of a simplified ICE3 high-speed train model." Applied Acoustics **160**: 107125.

Mockett, C., Perrin, R., Reimann, T., Braza, M. and Thiele, F. (2010). "Analysis of Detached-Eddy Simulation for the Flow Around a Circular Cylinder with Reference to PIV Data." Flow, Turbulence and Combustion **85**(2): 167-180.

Moin, P. and Kim, J. (2006). "Numerical investigation of turbulent channel flow." Journal of Fluid Mechanics **118**: 341-377.

Morris, S. C. (2011). "Shear-layer instabilities: particle image velocimetry measurements and implications for acoustics." Annual Review of Fluid Mechanics **43**: 529-550.

Munoz-Paniagua, J. and García, J. (2020). "Aerodynamic drag optimization of a high-speed train." Journal of Wind Engineering and Industrial Aerodynamics **204**: 104215.

Munro, S. and Ahuja, K. (2003). Aeroacoustics of a high aspect-ratio jet. 9th AIAA/CEAS Aeroacoustics Conference and Exhibit:3323.

Nagakura, K. (2006). "Localization of aerodynamic noise sources of Shinkansen trains." Journal of Sound and Vibration **293**(3): 547-556.

Nakahashi, K. and Obayashi, S. (1987). "FDM-FEM zonal method for viscous flow computations over multiple-bodies." NASA STI/Recon Technical Report N **88**: 11069.

Nicoud, F. and Ducros, F. (1999). "Subgrid-Scale Stress Modelling Based on the Square of the Velocity Gradient Tensor." Flow, Turbulence and Combustion **62**(3): 183-200.

Niu, J., Liang, X. and Zhou, D. (2016). "Experimental study on the effect of Reynolds number on aerodynamic performance of high-speed train with and without yaw angle." Journal of Wind Engineering and Industrial Aerodynamics **157**: 36-46.

Norberg, C. (1993). "Flow around rectangular cylinders: Pressure forces and wake frequencies." Journal of Wind Engineering and Industrial Aerodynamics **49**(1): 187-196.

Norberg, C. (2001). " Flow around a circular cylinder: aspects of fluctuating lift." Journal of Fluids and Structures **15**(3): 459-469.

Norberg, C. (2003). "Fluctuating lift on a circular cylinder: review and new measurements." Journal of Fluids and Structures **17**(1): 57-96.

O'Shea, K. and Nash, R. (2015). "An introduction to convolutional neural networks." arXiv preprint arXiv:1511.08458.

Oerlemans, S. and De Bruin, A. (2009). Reduction of landing gear noise using an air curtain. 15th AIAA/CEAS Aeroacoustics Conference (30th AIAA Aeroacoustics Conference):3156.

Okamoto, T. and Yagita, M. (1973). "The experimental investigation on the flow past a circular cylinder of finite length placed normal to the plane surface in a uniform stream." Bulletin of JSME **16**(95): 805-814.

Paradot, N., Masson, E., Poisson, F., Grégoire, R., Guilloteau, E., Touil, H. and Sagaut, P. (2008). "Aero-acoustic Methods for High-speed Train Noise Prediction." WCRR (World Congress on Railway Research), Seoul, Korea.

Patruno, L. and Ricci, M. (2018). "A systematic approach to the generation of synthetic turbulence using spectral methods." Computer Methods in Applied Mechanics and Engineering **340**: 881-904.

Peric, M. and Ferguson, S. (2005). "The advantage of polyhedral meshes." Dynamics **24**: 45.

Plentovich, E. B., Stallings Jr, R. L. and Tracy, M. B. (1993). "Experimental cavity pressure measurements at subsonic and transonic speeds. Static-pressure results."

Poletto, R., Revell, A., Craft, T. J. and Jarrin, N. (2011). Divergence free synthetic eddy method for embedded LES inflow boundary conditions. Seventh international symposium on turbulence and shear flow phenomena, Begel House Inc.

Pope, S. B. (2000). Turbulent flows, Cambridge university press.

Richardson, L. F. (1922). Weather prediction by numerical process, University Press.

Rosenblatt, F. (1958). "The perceptron: a probabilistic model for information storage and organization in the brain." Psychological review **65**(6): 386.

Rossiter, J. (1964). "Wind-tunnel experiments on the flow over rectangular cavities at subsonic and transonic speeds."

Rumelhart, D. E., Hinton, G. E. and Williams, R. J. (1985). Learning internal representations by error propagation, California Univ San Diego La Jolla Inst for Cognitive Science.

Saddington, A. J., Thangamani, V. and Knowles, K. (2016). "Comparison of passive flow control methods for a cavity in transonic flow." Journal of Aircraft **53**(5): 1439-1447.

Sarkar, S. and Hussaini, M. Y. (1993). Computation of the sound generated by isotropic turbulence, No. ICASE-93-74.

Sawamura, Y., Uda, T. and Kitagawa, T. (2018). "Wind tunnel study on measurement and reduction of aerodynamic noise generated from the bogie section of high-speed trains." The Proceedings of the Symposium on Environmental Engineering **2018.28**: 109.

Schewe, G. (1983). "On the force fluctuations acting on a circular cylinder in crossflow from subcritical up to transcritical Reynolds numbers." Journal of Fluid Mechanics **133**: 265-285.

Shaw, J. and Peace, A. (2002). "Simulating three-dimensional aeronautical flows on mixed block-structured/semi-structured/unstructured meshes." International journal for numerical methods in fluids **39**(3): 213-246.

Showkat Ali, S. A., Azarpeyvand, M. and Ilário da Silva, C. R. (2018). "Trailing-edge flow and noise control using porous treatments." Journal of Fluid Mechanics **850**: 83-119.

Shuanbao, Y., Dilong, G., Zhenxu, S., Guowei, Y. and Dawei, C. (2014). "Optimization design for aerodynamic elements of high speed trains." Computers & Fluids **95**: 56-73.

Shur, M., Spalart, P., Strelets, M. and Travin, A. (1999). Detached-eddy simulation of an airfoil at high angle of attack. Engineering turbulence modelling and experiments 4, Elsevier**:** 669-678.

Sima, M., Gurr, A. and Orellano, A. (2008). Validation of CFD for the flow under a train with 1: 7 scale wind tunnel measurements. Proceedings of the BBAA VI International Colloquium on Bluff Bodies Aerodynamics and Applications, Milano, Italy.

Smagorinsky, J. (1963). "General circulation experiments with the primitive equations: I. The basic experiment." Monthly Weather Review **91**(3): 99-164.

Spalart, P. and Allmaras, S. (1992). A one-equation turbulence model for aerodynamic flows. 30th aerospace sciences meeting and exhibit**:** 439.

Spalart, P., Jou, W. H., Strelets, M. and Allmaras, S. (1997). Comments on the Feasibility of LES for Wings, and on a Hybrid RANS/LES Approach.

Spalart, P. R. (2000). "Strategies for turbulence modelling and simulations." International Journal of Heat and Fluid Flow **21**(3): 252-263.

Spalart, P. R., Deck, S., Shur, M. L., Squires, K. D., Strelets, M. K. and Travin, A. (2006). "A New Version of Detached-eddy Simulation, Resistant to Ambiguous Grid Densities." Theoretical and Computational Fluid Dynamics **20**(3): 181.

Spalart, P. R. and Streett, C. (2001). "Young-person's guide to detached-eddy simulation grids." No. NAS 1.26: 211032.

Talotte, C. (2000). "Aerodynamic noise: a critical survey." Journal of Sound and Vibration **231**(3): 549-562.

Thompson, D. J., Latorre Iglesias, E., Liu, X., Zhu, J. and Hu, Z. (2015). "Recent developments in the prediction and control of aerodynamic noise from high-speed trains." International Journal of Rail Transportation **3**(3): 119-150.

Torii, A. and Ito, J. (2000). "Development of the series 700 Shinkansen train-set (improvement of noise level)." Japanese railway engineering.

Travin, A., Shur, M., Strelets, M. and Spalart, P. (2000). "Detached-eddy simulations past a circular cylinder." Flow, Turbulence and Combustion **63**(1-4): 293-313.

Tysell, L. (2010). "Hybrid grid generation for complex 3D geometries."

Uda, T., Yamazaki, N., Kitagawa, T., Nagakura, K. and Wakabayashi, Y. (2018). Estimation of Aerodynamic Bogie Noise Through Field and Wind Tunnel Tests. Noise and Vibration Mitigation for Rail Transportation Systems: Proceedings of the 12th International Workshop on Railway Noise, 12-16 September 2016, Terrigal, Australia, Springer. **139:** 377-387.

Vickery, B. J. (1966). "Fluctuating lift and drag on a long cylinder of square cross-section in a smooth and in a turbulent stream." Journal of Fluid Mechanics **25**(3): 481-494.

Wang, M., Freund, J. B. and Lele, S. K. (2005). " Computational prediction of flow-generated sound " Annual Review of Fluid Mechanics **38**(1): 483-512.

Weidman, P. (1968). Wake transition and blockage effects on cylinder base pressures, Diss. California Institute of Technology.

West, G. S. and Apelt, C. J. (1993). "Measurements of Fluctuating Pressures and Forces on a Circular Cylinder in the Reynolds Number Range 10^4 to 2.5×10^5." Journal of Fluids and Structures **7**(3): 227-244.

Willemsen, E. (1997). "High Reynolds number wind tunnel experiments on trains." Journal of Wind Engineering and Industrial Aerodynamics **69-71**: 437-447.

Witkowska, A., Juvé, D. and Brasseur, J. (1997). "Numerical study of noise from isotropic turbulence." Journal of Computational Acoustics **5**(03): 317-336.

Yamashita, R., Nishio, M., Do, R. K. G. and Togashi, K. (2018). "Convolutional neural networks: an overview and application in radiology." Insights into imaging **9**(4): 611-629.

Yamazaki, N., Uda, T., Kitagawa, T. and Wakabayashi, Y. (2019). "Influence of Bogie Components on Aerodynamic Bogie Noise Generated from Shinkansen Trains." Quarterly Report of RTRI **60**(3): 202-207.

Yang, H. x. and Liu, D. (2017). "Numerical study on the aerodynamic noise characteristics of CRH2 high-speed trains." Journal of Vibroengineering **19**(5): 3953-3967.

Yoo, S. P. and Lee, D. Y. (2007). Experimental study on the time-delayed-phase-control for reduction of open cavity noise. 2007 International Conference on Control, Automation and Systems, IEEE.

You, J., Chen, Y. and Yang, Z. (2015). "Influence of the wheel rotation on underbody flow and aerodynamic forces of high speed train." Procedia Engineering **126**: 399-404.

Young, D. F., Munson, B. R., Okiishi, T. H. and Huebsch, W. W. (2010). A brief introduction to fluid mechanics, John Wiley & Sons.

Yu, D., Ali, M. and Lee, J. H. (2006). "Multiple tandem jets in cross-flow." Journal of hydraulic engineering **132**(9): 971-982.

Yu, G., Yu, B., Sun, S. and Tao, W.-Q. (2012). "Comparative study on triangular and quadrilateral meshes by a finite-volume method with a central difference scheme." Numerical heat transfer, part B: fundamentals **62**(4): 243-263.

Zeiler, M. D. and Fergus, R. (2014). Visualizing and understanding convolutional networks. European conference on computer vision, Springer, Cham:818-833.

Zhang, J., Wang, J., Wang, Q., Xiong, X. and Gao, G. (2018). "A study of the influence of bogie cut outs' angles on the aerodynamic performance of a high-speed train." Journal of Wind Engineering and Industrial Aerodynamics **175**: 153-168.

Zhang, X. (2012). "Aircraft noise and its nearfield propagation computations." Acta Mechanica Sinica **28**(4): 960-977.

Zhao, K., Alimohammadi, S., Okolo, P. N., Kennedy, J. and Bennett, G. J. (2018). "Aerodynamic noise reduction using dual-jet planar air curtains." Journal of Sound and Vibration **432**: 192-212.

Zhao, K., Liang, Y., Yue, T., Wang, Y. and Bennett, G. J. (2019). Rectangular Cavity Flow Noise Suppression Using Chevron Treatment to the Front Edge at Subsonic Speeds. 25th AIAA/CEAS Aeroacoustics Conference.

Zhao, K., Neri, E., Okolo, P., Kennedy, J. and Bennett, G. J. (2015). Landing gear noise reduction by Double jet air curtain configuration. The 22nd International Congress on Sound and Vibration (ICSV22), Florence, Italy.

Zhao, K., Yang, X., Okolo, P. N., Wu, Z. and Bennett, G. J. (2017). "Use of dual planar jets for the reduction of flow-induced noise." AIP Advances **7**(2): 025312.

Zhu, J. (2015). "Aerodynamic noise of high-speed train bogies." PhD thesis, University of Southampton.

Zhu, J., Hu, Z. and Thompson, D. (2014). "Flow simulation and aerodynamic noise prediction for a high-speed train wheelset." International Journal of Aeroacoustics **13**(7-8): 533-552.

Zhu, J., Hu, Z. and Thompson, D. (2017). "The effect of a moving ground on the flow and aerodynamic noise behaviour of a simplified high-speed train bogie." International Journal of Rail Transportation **5**(2): 110-125.

Zhu, J., Hu, Z. and Thompson, D. (2018). "The flow and flow-induced noise behaviour of a simplified high-speed train bogie in the cavity with and without a fairing." Proceedings of the Institution of Mechanical Engineers, Part F: Journal of Rail and Rapid Transit **232**(3): 759-773.

Zhu, J., Hu, Z. and Thompson, D. J. (2016). "Flow behaviour and aeroacoustic characteristics of a simplified high-speed train bogie." Proceedings of the Institution of Mechanical Engineers, Part F: Journal of Rail and Rapid Transit **230**(7): 1642-1658.

Zhuang, N., Alvi, F. S., Alkislar, M. B. and Shih, C. (2006). "Supersonic cavity flows and their control." AIAA journal **44**(9): 2118-2128.

Ziegler, H. and Woller, P. (1973). Analysis of stratified and closely spaced jets exhausting into a crossflow, **NASA** report No. NASA-CR-132297.

Ziv, J. and Lempel, A. (1977). "A universal algorithm for sequential data compression." IEEE Transactions on information theory **23**(3): 337-343.